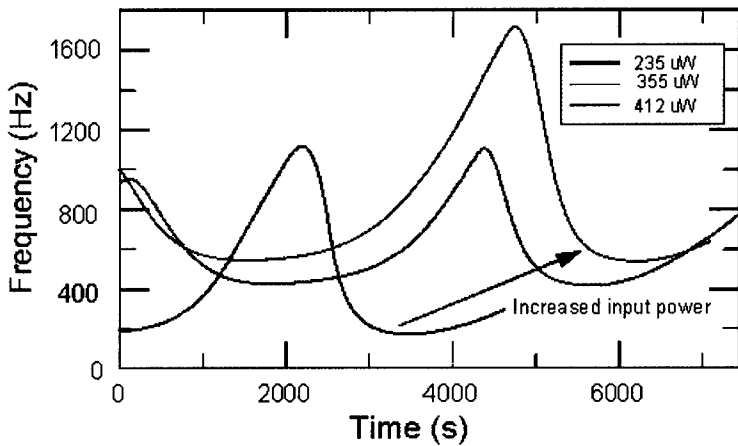
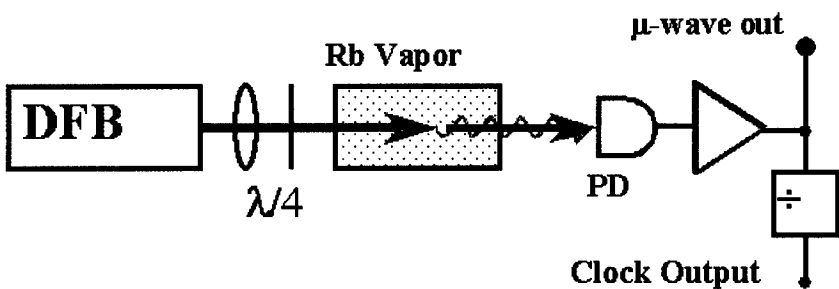


Trends in Optics and Photonics

TOPS Volume XXXI

Diode Laser Atomic Clock



Advanced Semiconductor Lasers and Their Applications

DISTRIBUTION STATEMENT A

Approved for Public Release

Distribution Unlimited

DTIC QUALITY INSPECTED

20000626 074

OSA
Optical Society of America

Edited by Leo Hollberg and Robert J. Lang

REPORT DOCUMENTATION PAGE

AFRL-SR-BL-TR-00-

Public reporting burden for this collection of information is estimated to average 1 hour per response, including gathering and maintaining the data needed, and completing and reviewing the collection of information. Send comments, including suggestions for reducing this burden, to Washington Headquarters Services, 1204 Davis Highway, Suite 1204, Arlington, VA 22202-4302, and to the Office of Management and Budget, Paperwork Reduction Project (0704-0188), Washington, DC 20503.

0241

es,
this
son

1. AGENCY USE ONLY (Leave blank)			2. REPORT DATE	3. REPORT TYPE AND DATES COVERED
			15 Jan 99 to 30 Nov 99 Final	
4. TITLE AND SUBTITLE			5. FUNDING NUMBERS	
ORGANIZATION OF THE 1999 PHOTONIC SCIENCE TOPICAL MEETINGS			61102F 2301/AX	
6. AUTHOR(S)			8. PERFORMING ORGANIZATION REPORT NUMBER	
Dr Thorner				
7. PERFORMING ORGANIZATION NAME(S) AND ADDRESS(ES)			10. SPONSORING/MONITORING AGENCY REPORT NUMBER	
Optical Society of America 2010 Massachusetts Ave NW Washington, DC 20036				
9. SPONSORING/MONITORING AGENCY NAME(S) AND ADDRESS(ES)			F49620-99-1-0101	
AFOSR/NE 801 North Randolph Street Rm 732 Arlington, VA 22203-1977				
11. SUPPLEMENTARY NOTES				
12a. DISTRIBUTION AVAILABILITY STATEMENT			12b. DISTRIBUTION CODE	
APPROVAL FOR PUBLIC RELEASED; DISTRIBUTION UNLIMITED				
13. ABSTRACT (Maximum 200 words)				
<p>This volume of Trends in Optics and Photonics (TOPS) collects the papers from the 3rd ASLA conference, held July 21-23, 1999, in Santa Barbara, California. Continuing the tradition of diversity of this conference, the papers presented covered wavelengths from the visible to sub-millimeter, with spectral properties ranging from oscillations and chaos to high-purity single-mode operation. A particularly strong application area as always was sensing and spectroscopy; here, new sensor configurations were demonstrated in parallel with, or making use of, new diode laser characteristics. We hope you find these papers interesting and useful in your own work, and look forward to seeing you at the next ASLA meeting in 2001.</p>				
14. SUBJECT TERMS			15. NUMBER OF PAGES	
			16. PRICE CODE	
17. SECURITY CLASSIFICATION OF REPORT	18. SECURITY CLASSIFICATION OF THIS PAGE	19. SECURITY CLASSIFICATION OF ABSTRACT	20. LIMITATION OF ABSTRACT	
UNCLASSIFIED	UNCLASSIFIED	UNCLASSIFIED	UL	

**OSA Trends in Optics
and Photonics Series**

Series Editor
Tingye Li *AT&T Labs.*

Volume 31

**ADVANCED
SEMICONDUCTOR
LASERS AND THEIR
APPLICATIONS**

AIR FORCE OFFICE OF SCIENTIFIC
RESEARCH (AFOSR)
NOTICE OF TRANSMITTAL TO DTIC. THIS
TECHNICAL REPORT HAS BEEN REVIEWED
AND IS APPROVED FOR PUBLIC RELEASE
IWA AFR 190-12. DISTRIBUTION IS
UNLIMITED.
YONNE MASON
STINFO PROGRAM MANAGER

Trends in Optics and Photonics Series

Tingye Li, Series Editor

Vol. 33 Bragg Gratings, Photosensitivity, and Poling in Glass Wavelengths, *E. Joseph Friebele, Raman Kashyap, and Turan Erdogan, eds.*

Vol. 32 Photonics in Switching, *Paul R. Prucnal & Daniel J. Blumenthal, eds*

Vol. 31 Advanced Semiconductor Lasers and Their Applications, *Leo Hollberg and Robert J. Lang, eds.*

Vol. 30 Optical Amplifiers and Their Applications (1999)
Susumu Kinoshita, Jeff C. Livas, and Gerlas Van den Hoven, eds.

Vol. 29 WDM Components
Daniel A. Nolan, ed.

Vol. 28 Ultrafast Electronics and Optoelectronics (1999)
John Bowers and Wayne Knox, eds.

Vol. 27 Advances in Photorefractive Materials, Effects and Devices
Peter E. Andersen, Per M. Johansen, Henrik C. Pedersen, Paul M. Petersen, and Mark Saffman, eds

Vol. 26 Advanced Solid-State Lasers (1999)
Martin M. Fejer, Hagop Injeyan, and Ursula Keller, eds.

Vol. 25 Optical Amplifiers and Their Applications (1998)
Douglas M. Baney, Katsumi Emura, and Jay M. Wiesenfeld, eds.

Vol. 24 Fabrication and Testing of Aspheres
John S. Taylor, Mark Piscottty, and Arne Lindquist, eds.

Vol. 23 Symposium on Electro-Optics: Present and Future
Hermann A. Haus, ed.

Vol. 22 joint volume - Biomedical Optical Spectroscopy and Diagnostics / Therapeutic Laser Applications (1998)
Eva Sevick-Muraca, Joseph Izatt, and Marwood N. Ediger, eds.

Vol. 21 Advances in Optical Imaging & Photon Migration (1998)
James G. Fujimoto and Michael S. Patterson, eds

Vol. 20 Optical Networks and Their Applications
Richard A. Barry, ed.

Vol. 19 Advanced Solid State Lasers (1998)
Walter R. Bosenberg and Martin M. Fejer, eds.

Vol. 18 Radiative Processes and Dephasing in Semiconductors
D. S. Citrin, ed.

Volumes 1-17 Contact OSA Customer Service for more information

**OSA Trends in Optics
and Photonics Series**

Volume 31

**ADVANCED
SEMICONDUCTOR
LASERS AND THEIR
APPLICATIONS**

Edited by
Leo Hollberg
and
Robert J. Lang

**From the Topical Meeting on
Advanced Semiconductor Lasers and Their
Applications
July 21-23, 1999
Santa Barbara, California**

Sponsored by
Optical Society of America

In cooperation with
US Air Force Office of Scientific Research
and
Electronics Society of IEICE of Japan
IEEE/Lasers and Electro-Optics Society

Optical Society of America
2010 Massachusetts Avenue, NW
Washington, DC 20036-1023
(202) 223-8130

Articles in this publication may be cited in other publications. In order to facilitate access to the original publication source, the following form for the citation is suggested:

Name of Author(s), Title of Paper, *OSA Trends in Optics and Photonics*
Vol. 31, Advanced Semiconductor Lasers and Their Applications, Leo Hollberg
and Robert J. Lang, eds. (Optical Society of America, Washington, DC 2000),
pp. xx-xx.

Cover art courtesy of Kiyoshi Nakagawa, Yamagata University:
Optical amplifiers cover the entire fiber transmission band. (see pp. 2-9)

ISSN Number 1094-5695

ISBN Number 1-55752-605-2

LC Number 99-60567

Copyright © 2000, Optical Society of America

Individual readers of this publication and libraries acting for them are permitted to make fair use of the material in it, as defined by Sections 107 and 108 of the U.S. Copyright Law, such as to copy an article for use in teaching or research, without payment of fee, provided that such copies are not sold. Copying for sale or copying for use that exceeds fair use as defined by the Copyright Law is subject to payment of copying fees. The code 1-55752-605-2/\$15.00 gives the per-article copying fee for each copy of the article made beyond the free copying permitted under Sections 107 and 108 of the U.S. Copyright Law. The fee should be paid through the Copyright Clearance Center, Inc., 21 Congress Street, Salem, MA 01970.

Permission is granted to quote excerpts from articles in this publication in scientific works with the customary acknowledgment of the source, including the author's name, name of the publication, page, year, and name of the Society. Reproduction of figures and tables is likewise permitted in other articles and books provided that the same information is printed with them, and notification is given to the Optical Society of America. Republication or systematic or multiple reproduction of any material in this proceedings, including contents and abstracts, is permitted only under license from the Optical Society of America; in addition, the Optical Society may require that permission also be obtained from one of the authors. Electrocopying or electrostorage of any material in this publication is strictly prohibited. Address inquiries and notices to the Director of Publications, Optical Society of America, 2010 Massachusetts Avenue, NW, Washington, DC 20036. In the case of articles whose authors are employees of the United States Government or its contractors or grantees, the Optical Society of America recognizes the right of the United States Government to retain a nonexclusive, royalty-free license to use the author's copyrighted article for United States Government purposes.

The views and conclusions contained in this publication are those of the author(s) and should not be interpreted as necessarily representing endorsements, either expressed or implied, of the editors or the Optical Society of America.

Printed in the USA

Advanced Semiconductor
Lasers and Their Applications
Contents

Preface	ix
---------	----

High-Power, High-Brightness Semiconductor Lasers

Progress in the development of broad-waveguide high-power 0.97-2.3 μm diode lasers and CW room temperature 2.3-2.7 μm mid-infrared lasers <i>Dmitrii Garbuзов</i>	2
>90mW CW superluminescent output power from single-angled facet-ridge waveguide diode at 1.5 μm <i>S.H. Cho, I.K. Han, Y. Hu, J.H. Song, P.J.S. Heim, M. Dagenais, F.G. Johnson, D.R. Stone, H. Shen, J. Pamulapati and W. Zhou</i>	5
Performance and reliability of high-power 670-690 nm CW laser diode bars grown by solid-source molecular beam epitaxy <i>P.J. Corvini, P.A. Bournes, F. Fang, M. Finander, M. Jansen, R.F. Nabiev, M. Widman, S. Orsila, M. Saarinen, A. Salokatve, P. Savolainen, M. Toivonen and P. Uusimaa</i>	10
Large spot size single mode Bragg waveguide vertical cavity surface emitting lasers <i>M.G. Greatly, J. Masum, M.J. Adams, M.J. Steer, J.E.F. Frost, J.S. Roberts and J. Woodhead</i>	13
Large spatial mode, single frequency semiconductor lasers using two dimensional gratings <i>Srinath Kalluri, Timothy Vang, Robert Lodenkamper, Michael Nesnidal, Michael Wickham, David Forbes, Johanna Lacey, Larry Lembo and John Brock</i>	16

Diode-Laser Spectroscopy: 1

Laser diode-based lidar and applications <i>James B. Abshire</i>	20
Diode-laser absorption sensors for industrial process monitoring and control <i>D.S. Baer, S.I. Chou, S. Sanders, M.E. Webber, S.D. Wehe and R.K. Hanson</i>	22
Quantitative wavelength modulation spectroscopy with diode lasers <i>Jes Henningsen and Harald Simonsen</i>	25
Overview of sensitive detection and multiplexing techniques for tunable diode laser absorption spectroscopy <i>Michael B. Frish</i>	32
Low-cost, single-frequency sources for spectroscopy using conventional Fabry-Perot diode lasers <i>Gary L. Duerksen and Michael A. Krainak</i>	35

Diode-Laser Spectroscopy: 2

An overview of external-cavity diode lasers for use in spectroscopy and WDM applications <i>Robert Shine, Jr.</i>	40
Diode lasers, DFG and molecules <i>D.G. Lancaster, D. Richter, R.F. Curl and F.K. Tittel</i>	43
Open air detection of CO ₂ , CO, and H ₂ S with a DFB laser at 1.57 μm <i>Jes Henningsen and Harald Simonsen</i>	47
Development of a near-IR TDL probe for rapid species measurements in large pool fires <i>Christopher R. Shaddix, Philip J. Santangelo, Peter D. Ludowise, Sarah W. Allendorf and David K. Otteson</i>	50
Diode laser-based detector for fast detection of binary gas mixtures <i>Kevin L. McNesby, R. Reed Skaggs, Andrzej W. Misiolek, Jeffrey B. Morris, Brian Kennedy and Ian A. McLaren</i>	53

Coherence Control and Modeling

Compact external-cavity diode laser at 633 nm with a transmission grating <i>M. Merimaa, I. Tittonen, E. Ikonen, H. Talvitie, P. Laakkonen and M. Kuittinen</i>	56
Semiconductor lasers with broadband tunability <i>Chinh-Fuh Lin, Bor-Lin Lee and Min-Jang Chen</i>	58
Relaxation oscillation frequency properties in injection-locked semiconductor lasers <i>Y. Hong and K.A. Shore</i>	61
Coherence collapse in semiconductor diode lasers with phase conjugate feedback <i>J.S. Lawrence and D.M. Kane</i>	64
Suppression of coherence collapse in semiconductor diode lasers with short external cavities <i>J.S. Lawrence, D.M. Kane and P.S. Spencer</i>	67
Communication with chaotic external cavity diode lasers <i>S. Sivaprakasam and K.A. Shore</i>	70
Reprint from IEEE Journal of Quantum Electronics 35, 5, pp. 788-793. Transition to pulsed operation in short external-cavity FM semiconductor lasers <i>P.S. Spencer, D.M. Kane and K.A. Shore</i>	73
Reprint from IEEE Journal of Lightwave Technology 17, 6, pp. 1072-1078. Coupled-cavity effects in FM semiconductor lasers <i>P.S. Spencer, D.M. Kane and K.A. Shore</i>	79
Evaluation of comb bandwidth parameters for frequency-shifted feedback semiconductor lasers <i>K.A. Shore and D.M. Kane</i>	86
Self-consistent analysis of carrier transport and carrier capture dynamics in quantum cascade intersubband semiconductor lasers <i>K. Kálna, C.Y.L. Cheung, I. Pierce and K.A. Shore</i>	89

Modeling spatiotemporal dynamics of high power semiconductor lasers: microscopically computed gain and device simulation

R.A. Indik, J. Hader, J.V. Moloney and S.W. Koch

92

Microwave and Frequency-Conversion Devices

Faraday-configured mode-locked p-Ge laser and p-Ge far-infrared amplifier

R.E. Peale, A.V. Muraviov, S.H. Withers, R.C. Strijbos, S.G. Pavlov and V.N. Shastin

96

A three-diode-laser, terahertz-difference-frequency synthesizer and its applications toward far-infrared spectroscopy of ammonia and water

Pin Chen, John C. Pearson, Herbert M. Pickett, Shuji Matsuura and Geoffrey A. Blake

103

A compact microwave frequency reference using diode lasers

N. Vukičević, A.S. Zibrov, L. Hollberg, F. Walls and J. Kitching

106

Frequency shifting of four-wave mixing of picosecond optical pulses in semiconductor optical amplifiers

J.M. Tang and K.A. Shore

109

Single and multiple wavelength conversion using double pump four-wave-mixing in a semiconductor optical amplifier

Abhik Ghosh, Guang-Hua Duan, Guoxi Sun and Mario Dagenais

112

Efficient generation of tunable mid-infrared radiation in a channel waveguide

Douglas J. Bamford, Konstantin P. Petrov, Arti P. Roth and Thomas L. Patterson

119

Difference-frequency radiation around 4.3 μm for high sensitivity and sub-Doppler spectroscopy of CO_2

D. Mazzotti, G. Giusfredi, P. De Natale, J. Mitchell and L. Hollberg

122

VCSELs and Applications

Micromachined tunable optoelectronic devices for spectroscopic applications

James S. Harris, Jr., Chien-Chung Lin, Wayne Martin, Fred Sugihwo, Michael Larson, and Barbara Paldus

130

Nonlinear spectroscopy using a current-modulated VCSEL

C. Affolderbach, W. Kemp, S. Knappe, A. Nagel and R. Wynands

135

Commercial gas sensing with vertical cavity lasers

Mark Paige

141

Transverse mode selection in index-guided VCSELs

A. Valle, L. Pesquera, P. Rees and K. A. Shore

144

Injection locking of shear-strain photonic lattices based on VCSEL arrays

T. Fishman, A. Hardy, E. Kapon and H. Pier

147

Quantum Cascade and Interband IR Lasers

High performance quantum cascade lasers for trace gas analysis <i>Federico Capasso and Claire Gmachl</i>	156
High-temperature continuous-wave operation of optically-pumped W lasers with $\lambda = 3 \mu\text{m}$ to $7.1 \mu\text{m}$ <i>W.W. Bewley, I. Vurgaftman, C.L. Felix, D.W. Stokes, L.J. Olafsen, E.H. Aifer, J.R. Meyer, M.J. Yang, B.V. Shanabrook, H. Lee, R. U. Martinelli, J.C. Connolly and A.R. Sugg</i>	158
Optical gain calculations for $1.55 \mu\text{m}$ unipolar intersubband semiconductor lasers <i>C.Y.L. Cheung, I. Pierce, P. Rees and K.A. Shore</i>	161
Relative intensity noise of unipolar intersubband semiconductor lasers <i>N. Mustafa, L. Pesquera and K. Alan Shore</i>	164

Novel Semiconductor Lasers

Blue nitride lasers: physics of operation and opportunities in vertical-cavity devices <i>Arto V. Nurmikko and Y.-K. Song</i>	168
Quantum dot laser diodes <i>S. Fafard, C. Ni. Allen, K. Hinzer and Z.R. Wasilewski</i>	175
Narrow-linewidth complex-coupled DFB lasers with gain coupling induced by vertical emission <i>Nguyen Hong Ky, J. Robadey, J. -D. Ganière, C. Gourgon, D. Martin, B. Deveaud and F.K. Reinhart</i>	178
Quantum dot semiconductor optical amplifiers <i>Richard P. Mirin and Daniel J. Blumenthal</i>	183
100 GHz frequency step-tunable hybrid laser based on a vernier effect between a Fabry-Perot cavity and a sampled fiber Bragg grating <i>Jean-François Lemieux, Antoine Bellemare, Christine Latrasse and Michel Tétu</i>	186
Characterization and coupling of diode lasers by photorefractive wave mixing <i>Peter Pogany and Hans J. Eichler</i>	189
Comparison between performance of SG and BSG DBR semiconductor lasers <i>M. Gioannini, V. Guja and I. Montrosset</i>	192
A simple polarization insensitive scheme for four-wave mixing using one semiconductor optical amplifier and single pump source <i>J.M. Tang and K.A. Shore</i>	200
How to have narrow-stripe semiconductor lasers self-pulsate <i>Shahram M. Shahruz</i>	203
Author Index	215
Subject Index	217

Preface

Since the first demonstration of semiconductor lasers in the 1960s, the diode laser has steadily expanded its wavelength range, power output, spectral capabilities, and reliability. Along the way, the unique capabilities provided by diode lasers has opened up new application after new application, enabling billion-dollar industries in data storage and fiber optics communications and countless smaller markets in sensors, materials processing, printing, and scientific instrumentation, to name but a few. The Advanced Semiconductor Lasers Applications meeting (ASLA) was started in 1995 and runs every two years with joint and alternating sponsorship of the OSA and the IEEE.^{**} ASLA has uniquely brought together laser device and applications scientists, providing a forward look at both semiconductor lasers themselves and their future uses.

This volume of Trends in Optics and Photonics (TOPS) collects the papers from the 3rd ASLA conference, held July 21-23, 1999, in Santa Barbara, California. Continuing the tradition of diversity of this conference, the papers presented covered wavelengths from the visible to sub-millimeter, with spectral properties ranging from oscillations and chaos to high-purity single-mode operation. A particularly strong application area as always was sensing and spectroscopy; here, new sensor configurations were demonstrated in parallel with, or making use of, new diode laser characteristics. We hope you find these papers interesting and useful in your own work, and look forward to seeing you at the next ASLA meeting in 2001.

Leo Hollberg
Program Co-chair
National Institute of Standards & Technology
Boulder, Colorado

Robert J. Lang
Program Co-chair
SDL, Inc.
San Jose, California

July 23, 1999

^{**} Previous Volumes
1995 Technical Digest Series, Vol. 20, OSA
1997 Digest of the LEOS Summer Topical Meetings, IEEE

High-Power,
High-Brightness
Semiconductor Lasers

Progress in the Development of Broad-Waveguide High-Power 0.97-2.3 μm Diode Lasers and CW Room Temperature 2.3 - 2.7 μm Mid-Infrared lasers

D. Z. Garbuzov

Sarnoff Corporation CN-5300
Princeton, New Jersey, 08543-5300

Recent investigations [1-6] demonstrate that increase of the waveguide thickness in separate confinement-heterostructure quantum-well (SCH-QW) diode lasers significantly decreases internal losses, leading to record high output powers. The maximum output power levels achieved in continuous wave (CW) operation are listed in Table 1 for 100-200 μm wide aperture (S) lasers based on GaAs [3,4], InP [2,6] and GaSb [5] lattice-matched structures. All tested devices had anti-reflective quarter-wavelength Al_2O_3 coatings on the emitting facets and 95% high-reflective coatings on the rear facets. The devices had 1-2 mm long cavity lengths and were mounted p-side down on copper heatsinks.

Table 1. Broad Waveguide SCH QW laser Record Parameters

Structure	λ μm	W μm	S μm	η_d	CW P_{CW} (W)	I_M (A)
InGaAsP/GaAs SCH, 2QW	0.98	1.3	100	0.86	10.6*	13.0
InGaAsP/GaAs SCH, 2QW	0.98	1.3	200	0.86	16.8*	20.5
InGaAsP/InP SCH, 3QW	1.47	1.3	200	0.64	5.2	12.0
InGaAsP/InP SCH, 3QW	1.83	1.1	100	0.51	1.75	8

*In cooperation with University of Wisconsin-Madison

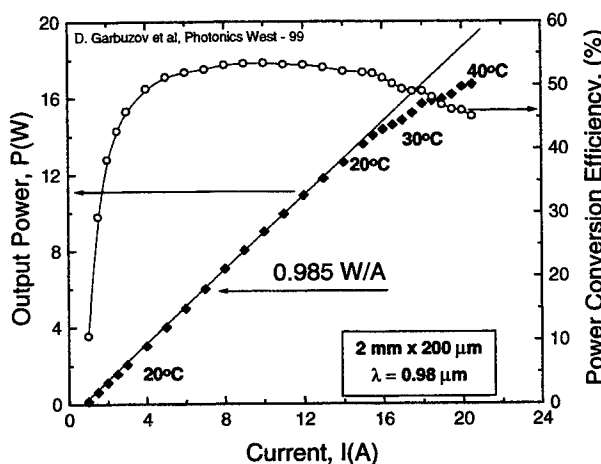


Fig.1. Power conversion efficiency and output power for an Al-free laser with 2 mm cavity length and 200 μm aperture.

All devices listed in Table 1 have the waveguide thicknesses, W, to about 0.8-1.3 μm ; that is 3-4 times larger than what is normally used in conventional SCH-QW laser structures. Our calculations [1,2,5]

show that waveguide broadening changes the transverse lasing mode distribution, dramatically decreasing the fraction of the mode propagating in the highly doped cladding layers. The increased mode confinement in the undoped waveguide region significantly decreases internal losses normally associated with free-carrier absorption in the doped cladding regions. An example of the BW structure output power capability for InGaAsP/GaAs devices is shown in Fig. 1. The results are for 2 mm long devices, mounted p-side down on copper heatsinks. Output powers of 16.8 W and 22.3 W at 980 nm were obtained for devices with an 200- μm wide aperture in CW and QCW operation, respectively [4]. The corresponding results for lasers with 100- μm aperture are 11W (CW) and 14.3 W (QCW) [3].

In the second part of this paper we describe recent progress in the development of mid-infrared quantum well diode lasers which has led to the expansion of their CW-operating range up to 2.7 μm [7-9]. The broad waveguide SCH QW laser diodes were grown by MBE in system InGaAsSb/AlGaAsSb using n-GaSb substrate. The first version of such lasers, emitting in 2 μm range demonstrated record for this wavelength parameters [5]. In these lasers, $\text{In}_{0.17}\text{Ga}_{0.83}\text{Sb}_{0.98}\text{As}_{0.02}$ 1% compressively strained compositions were used as a material for QWs. To achieve the longer wavelength operation and keep 1% strain in QWs the compositional values for both of In and As in QW material should be increased simultaneously. However, at wavelength exceeding $\lambda > 2.1 \mu\text{m}$ the performance of such devices suffers significantly since QW material quality degrades rapidly as the miscibility gap is approached. In an effort to eliminate material quality degradation associated with miscibility gap we grew structures with heavily-strained, quasi-ternary InGaAsSb(As) quantum wells. The compositions of these QWs were outside the miscibility gap. About ten laser structures were grown whose the only composition parameter varied was the In (0.25 to 0.4) in the Double QW active region. We estimated that the As concentration for all these structures was less than 3 %. The QW thickness were in the range of 10 – 20 nm. The compressive strain in QWs increased from 1.5 to 2.3% with increasing In content.

Figure 2 shows differential efficiency (η_d) and threshold current density (J_{th}) for 2-mm-long-cavity diodes prepared from the five wafers with increasing In composition in the QWs. For lasers with In compositions in the QWs exceeding 35% ($\lambda = 2.7 \mu\text{m}$) a sharp increase of J_{th} and fast decrease of η_d caused by the strain relaxation and the generation of dislocations near the QWs. .

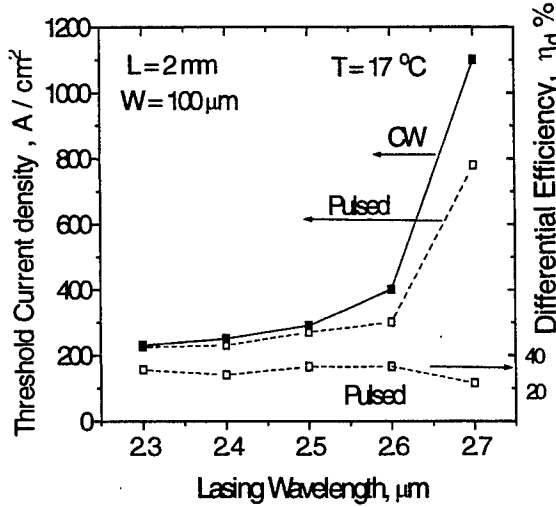


Fig.2. Laser parameters versus wavelength.

For lasers with wavelengths shorter than 2.7 μm at $T \leq 20^\circ\text{C}$ the laser parameters are weakly dependent on QW composition. The threshold current density in the pulsed regime only increases from 230 to 300 A/cm², as the wavelength increases from 2.3 to 2.6 μm . The corresponding increase of J_{th} in the CW regime is slightly higher, from 230 to 400 A/cm². Output power characteristics (P-I) measured in the

pulsed regime are linear up ten times the threshold current. Corresponding values of η_d (dashed line in Fig. 2) are independent of wavelength in the wavelength range of 2.3 - 2.6 μm and are close to 30% for all 2-mm-long-cavity devices. CW efficiency and powers for these lasers are presented in Tab. 2.

Table 2. Broad Waveguide Mid-Infrared SCH Lasers with Heavily-Stained Quasi Ternary QWs

Structure	λ μm	W μm	S μm	η_d	CW	
					P_{CW} (W)	I_M (A)
AlInGaAsSb/GaSb SCH, 1QW	2.0	0.9	200	0.53	1.9	8.5
AlInGaAsSb/GaSb SCH, 2QW	2.3	0.9	100	0.3	0.5	5
AlInGaAsSb/GaSb SCH, 2QW	2.5	0.9	100	0.25	0.4	5
AlInGaAsSb/GaSb SCH, 2QW	2.7	0.9	100	0.1	0.03	2

In conclusion we demonstrated that broad waveguide AlGaAsSb/InGaAsSb/GaSb diode lasers with heavily-strained quasi-ternary InGaAsSb QWs with In compositions of 25-38% operate CW at room-temperature in the wavelengths range from 2.3 to 2.7 μm . For lasers with emission wavelengths from 2.3 - 2.6 μm at room temperature J_{th} and η_d weakly depend on wavelength ($J_{\text{th}} \approx 300 \text{ A/cm}^2$ and $\eta_d \approx 30\%$). Maximum output powers of 500, 250 and 160 mW were obtained at room temperature for 100- μm -wide stripe lasers emitting at wavelengths of 2.3, 2.5 and 2.6 μm , respectively.

The overall effectiveness of the BW-SCH-QW approach has been demonstrated in four different material systems (AlGaAs/GaAs, InGaAsP/GaAs, InGaAsP/InP, and AlInGaAsSb/GaSb), thereby providing a method for achieving high output power within a wavelength range suitable for most medical and industrial applications.

References

1. D. Garbuzov, J. Abeles, N. Morris, P. Gardner, A. Triano, M. Harvey, D. Gilbert, and J. Connolly, Proc. SPIE, 2682, 20 (1996).
2. D. Garbuzov, L. Xu, S. R. Forrest, R. Menna, R. Martinelli, and J. C. Connolly, Electron. Lett. 32, 1717 (1996).
3. Al-Muhanna, L. Mawst, D. Botez, D. Garbuzov, R. Martinelli, and J. Connolly, Appl. Phys. Lett. 73, 1182, (1998).
4. D. Garbuzov, M. Maiorov, V. Khalfin, M. Harvey, A. Al-Muhanna, L. Mawst, D. Botez, and J. Connolly
5. D. Garbuzov, R. Menna, H. Lee, R. U. Martinelli, J. C. Connolly, L. Xu, and S. R. Forrest, Conference on InP and Related Compounds, Hyannis, MA, 11 May, 1997, 551-554.
6. D. Garbuzov, R. Menna, R. Martinelli, J. Abeles, and J. Connolly, Electron. Lett. 33, 1635, (1997).
7. D. Garbuzov, H. Lee, V. Khalfin, R. Martinelli, R. Menna, and J. C. Connolly, CLEO/EUROPE – European Quantum Electronics Conference, Glasgow, Scotland, United Kingdom, 1998, paper CWL2.
8. D. Garbuzov, H. Lee, V. Khalfin, L. DiMarco, R. Martinelli, R. Menna, and J. C. Connolly, SPIE Photonics West Conference'99, San Jose, CA, 1999, Paper 3625-93.
9. D. Garbuzov, R. Menna, M. Maiorov, H. Lee, V. Khalfin, L. DiMarco, D. Capewell, R. Martinelli, G. Belenky, and J. Connolly, SPIE Photonics West Conference'99, San Jose, CA, 1999, Paper 3628-32.

>90mW CW Superluminescent Output Power from Single-Angled Facet-Ridge Waveguide Diode at 1.5 μ m

S. H. Cho, I. K. Han, Y. Hu, J. H. Song, P. J. S. Heim and M. Dagenais

Department of Electrical engineering, University of Maryland, College Park, MD 20742

Phone: (301) 405-3684, Fax: (301) 314-9281, e-mail:

chosh@eng.umd.edu, ikhan@eng.umd.edu, yhu@eng.umd.edu, jhsong@eng.umd.edu, heim@eng.umd.edu, dage@eng.umd.edu

F. G. Johnson, and D. R. Stone

Laboratory for Physical Sciences, College Park, MD 20740

fred@lps.umd.edu, den@lps.umd.edu

H. Shen, J. Pamulapati, and W. Zhou

Army Research Laboratory, Adelphi, MD 20783

Abstract :

More than 90 mW CW of superluminescent power in a \sim 65 nm bandwidth (full width at half maximum) with less than 1.5 dB spectral modulation was obtained from a single-angled facet ridge waveguide at 1.5 μ m. The output beam was measured to be in a single spatial mode. This high superluminescent output power was realized by optimizing both the epitaxial layer and the waveguide designs and the device mounting.

OCIS Codes : 140.5960 (Key words: Semiconductor lasers, Multi-Quantum Wells, Superluminescent diodes)

Introduction

Superluminescent diodes (SLD's) have recently found numerous uses, in particular, in applications requiring broad band sources such as fiber optic-gyrosopes, optical sensors, optical coherence tomography [1], WDM passive components characterization, and spectrum-sliced wavelength division multiplexed metropolitain area networks [2]. Some of the largest reported superluminescent optical powers have been obtained in tapered laser structures. Tapered broad area stripe amplifiers at a wavelength of 0.85 μ m [3] and 1.5 μ m [4] have been shown to be capable of delivering superluminescent CW powers in excess of several hundred mW's in a near-diffraction-limited beam. Several bulk lenses, or micro-lenses, are typically used to remove the intrinsic astigmatism in these laser structure before coupling the light from the tapered amplifier into a single mode fiber. In other approaches favoring monolithic integration, re-growth can be used to integrate a waveguide lens with the laser. An interesting approach for producing a high optical power, broad spectrum, source uses a diode-pumped rare-earth-doped fiber. Such a source can produce powers in excess of 100 mW in a single mode fiber at 1.5 μ m [2], but is typically bulky and costly.

In this paper, we report having produced more than 90 mW of CW superluminescent power in a 65 nm bandwidth (FWHM) spectrum with less than 1.5 dB spectral modulation. Our approach uses a single-angled-facet ridge waveguide laser structure. Because of the single-mode nature of the narrow ridge laser structure, almost no astigmatism is present. This will lead to high coupling efficiencies to single-mode fibers using simple optics or lens fibers.

Experimental Results

The devices were fabricated from a four multiple quantum well wafer, grown by solid source molecular beam epitaxy (MBE). The epitaxial layer structure consists of four 0.9% compressively strained quantum wells and a single-step separate confinement heterostructure (SCH), as shown in Figure 1. The n-type cladding and core region consist of 1.0 μm InP cladding layer with $n \sim 5 \times 10^{17} \text{ cm}^{-3}$ on the highly doped n-type InP substrate and four 10 nm $\text{In}_{0.73}\text{Ga}_{0.27}\text{As}_{0.82}\text{P}_{0.18}$ quantum wells surrounded by 10 nm $\text{In}_{0.73}\text{Ga}_{0.27}\text{As}_{0.57}\text{P}_{0.43}$ lattice matched barriers. The SCH region is reduced to 50 nm of $\text{In}_{0.73}\text{Ga}_{0.27}\text{As}_{0.57}\text{P}_{0.43}$ in order to expand the mode in the transverse direction. The QW and the SCH regions are undoped. The hetero-interface between the SCH region and the p-type InP cladding layer is doped heavily with the doping level of $\sim 1 \times 10^{18} \text{ cm}^{-3}$ in order to minimize the reduction of the barrier height at the high carrier injection level [5,6]. The p-type cladding layer consists of 0.4 μm p-type InP cladding layer with $p \sim 3 \times 10^{17} \text{ cm}^{-3}$ above the SCH region followed by 15 nm $\text{In}_{0.73}\text{Ga}_{0.27}\text{As}_{0.57}\text{P}_{0.43}$ etch-stop layer and 1.1 μm graded p-doped InP cladding layer from $p \sim 5 \times 10^{17} \text{ cm}^{-3}$ to $1 \times 10^{18} \text{ cm}^{-3}$. A 0.15 μm $\text{In}_{0.53}\text{Ga}_{0.47}\text{As}$ p⁺-doped cap layer with $p \sim 1.5 \times 10^{19} \text{ cm}^{-3}$ is used for p-contact.

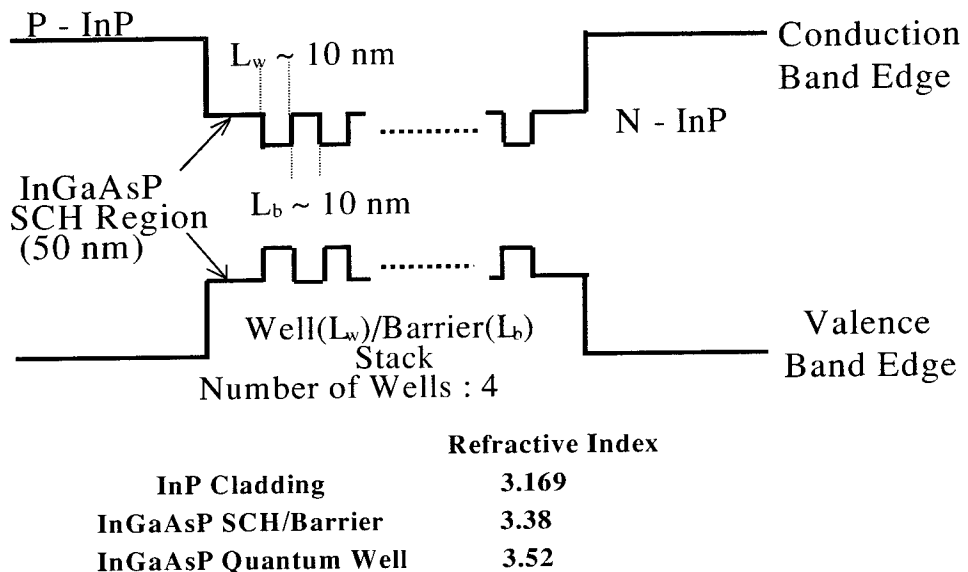


Figure 1. Band edge profile of InGaAsP/InP based multiple quantum wells with a single step heterostructure (SCH).

This epitaxial structure was designed to have a relatively large transverse spot size. A large transverse mode leads to a higher saturation power enabling a higher optical power density on the laser facets. A $1/e^2$ transverse diameter of 1.2 μm was obtained. In order to obtain the maximum output power, the length of the single-angled-facet ridge waveguide structure was optimized. The device was mounted p-side down on a copper heat sink.

The schematic design of the single-angled-facet-ridge amplifier [7] is shown in Figure 2. The device consists of 1mm long single-angled-facet-ridge waveguide followed by 0.3 mm long straight

single mode ridge waveguide section. The single mode curved waveguide traverses an arc along the 1mm length, with a constant radius of ~ 1 cm, intersecting the angled-facet at an angle of $\sim 8^\circ$ relative to the normal of the facet. There were no differences on the threshold current and the slope efficiency between a straight and a double bent 2 mm long ridge laser. This indicates that there is almost no bending loss due to the curved ridge waveguide in this device. A low facet reflectivity on the order $\sim 10^{-5}$ was achieved from the angled-facet. An additional anti-reflection coating was deposited on the both facets to further reduce the spectral modulation.

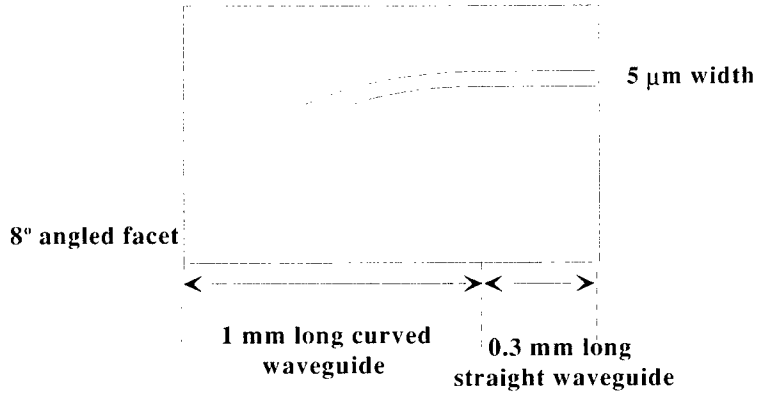


Figure 2. Schematic design of the single-angled-facet-ridge waveguide

Figure 3 (a) and (b) shows the superluminescent light-current (L-I) curve and the spectrum obtained for different current levels. The output power starts rolling over above the current level of 400 mA and is saturated at 800 mA current due to the thermal effect, as shown from L-I curve in Figure 3 (a). An optical power of more than 90 mW CW with a spectral bandwidth (FWHM) in excess of 65 nm was obtained with relatively low spectral modulation (1.5 dB) from the angled facet side of the device.

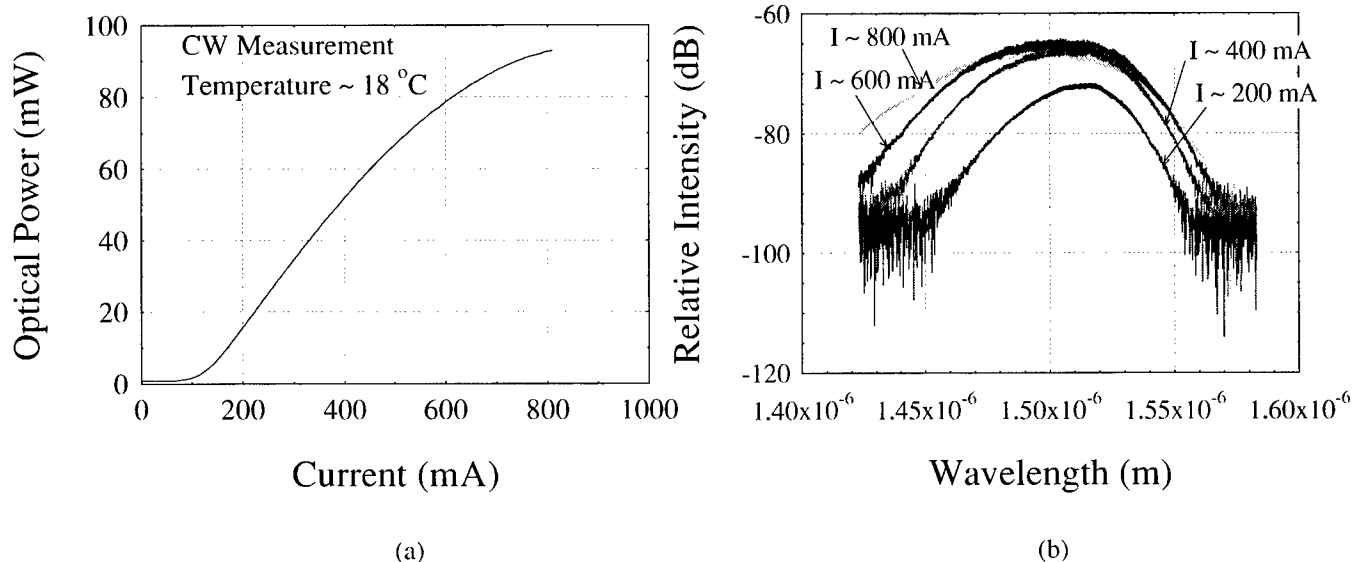


Figure 3. a) Superluminescent light-current curve from the angled facet side
b) Spectrum at the different current levels

Figure 4 shows the lateral far-field profiles at different power levels, which indicates the spatially single mode output beams at the high output powers. In order to investigate the temperature dependence of the L-I curves of this singled-facet ridge waveguide source, the heat sink temperature was varied from 18 °C to 50 °C. Figure 5 shows the superluminescent L-I curves at the different temperatures. Even at the temperature of 50 °C, more than 3 mW of the superluminescent output power was obtained at the current level of ~400 mA.

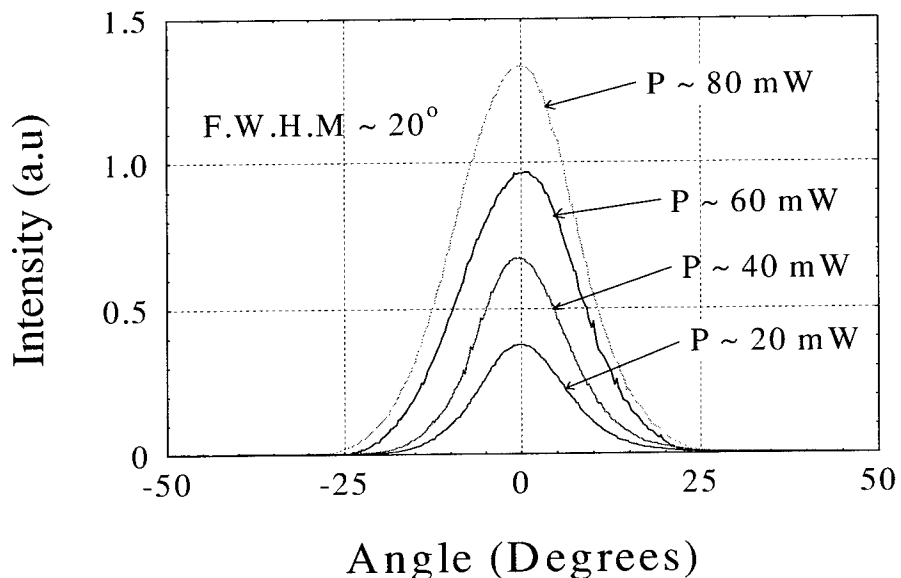


Figure 4. Lateral far-field profiles at the different power levels at 18°C

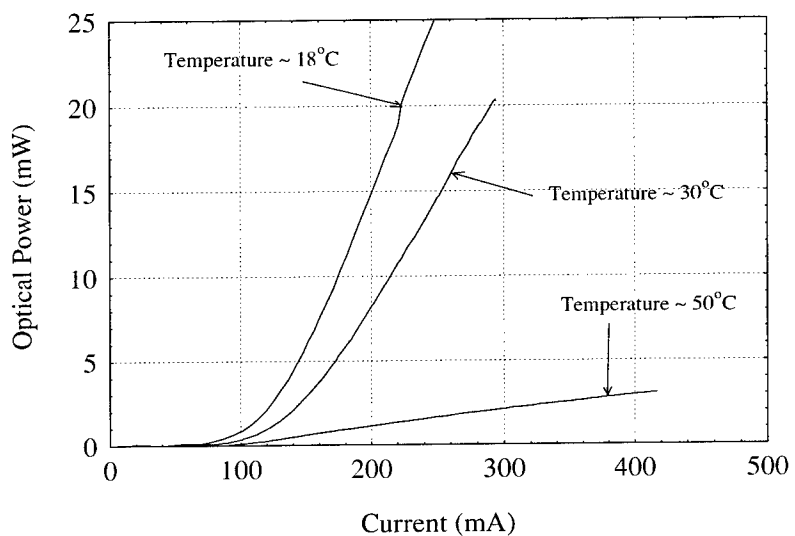


Figure 5. Superluminescent light-current curves at the different temperatures.

In summary, we have demonstrated the operation of a high power 1.5 μm superluminescent diode with a spectral bandwidth in excess of 65 nm. This was achieved by implementing a single-angled-facet, single-mode, ridge waveguide laser structure. An optical power of 90 mW was demonstrated, which is a record for a single-mode semiconductor superluminescent laser structure operating at 1.5 μm . We expect that this structure can be easily fabricated and that it will find numerous applications.

References, Notes, and Links

1. David Huang, Eric A. Swanson, Charles P. Lin, Joel S. Schuman, William G. Stinson, Warren Chang, Michael R. Hee, Thomas Flotte, Kenton Gregory, Carmen A. Puliafito, James G. Fujimoto, "Optical coherence tomography," *Science*, Vol. 254, pp. 1178-1181, 1991.
2. D. D. Sampson and W. T. Holloway, "100mW spectrally-uniform broadband ASE source for spectrum-sliced WDM systems," *Electron Lett.*, Vol. 30, pp. 1611-1612, 1994.
3. L. Goldberg and D. Mehuys, "High power superluminescent diode source," *Electron Lett.*, Vol. 30, pp. 1682-1684, 1994.
4. F. Koyama, K.-Y. Liou, A. G. Dentai, T. Tanbun-ek, and C. A. Burrus, "Mutiple-quantum-well GaInAs/GaInAsP tapered broad-area amplifiers with monolithically integrated waveguide lens for high-power applications," *IEEE Photonics Tech. Lett.*, Vol. 5, pp. 916-919, 1993.
5. Gregory L. Belenky, C. L. Reynolds, Jr., R. F. Kazarinov, V. Swaminathan, Serge L. Luryi, and John Lopata, "Effect of p-doping profile on performance of strained multi-quantum-well InGaAsP-InP lasers," *IEEE J. Quantum Electron.*, vol. 32, pp. 1450-1455, 1996.
6. I. K. Han, S. H. Cho, P. J. S. Heim, D. H. Woo, S. H. Kim, J. H. Song, F. G. Johnson, and M. Dagenais, "Dependence of the light-current characteristics of 1.55 μm broad area lasers on different p-doping profiles," Submitted to *IEEE Photonics Tech. Lett.*
7. Peter J. S. Heim, Z. Frank Fan, S. H. Cho, Keeyol Nam, Mario Dagenais, F. G. Johnson, and Rich Leavitt, "Single-angled-facet laser diode for widely tunable external cavity semiconductor lasers with high spectral purity," *Electron. Lett.*, Vol. 33, pp.1387-1389, 1997.

Performance and reliability of high-power 670-690 nm CW laser diode bars grown by solid source molecular beam epitaxy

P.J. Corvini, P.A. Bourns, F. Fang, M. Finander, M. Jansen, R.F. Nabiev, and M. Widman
Coherent Semiconductor Group, 5100 Patrick Henry Dr., Santa Clara CA 95054 USA
tel: +1 408 764-4231; fax: +1 408 764-4182; email: pat_corvini@cohr.com

S. Orsila, M. Saarinen, A. Salokatve, P. Savolainen, M. Toivonen, and P. Uusimaa
Nordic Epitaxy, P.O. Box 692, FIN-33101 Tampere, Finland
tel: +358-3-3652994; fax: +358-3-3652995; email: Seppo.Orsila@nordicepitaxy.com

High-power AlGaInP laser diodes in the 670-690 nm range are needed for a variety of applications, including pumping, illumination, displays, and medicine. Solid-source molecular beam epitaxy (SSMBE), which provides both good control over and safe handling of the Group V sources [1,2], is a promising technique for manufacturing these devices. We have previously reported on red single emitters fabricated on SSMBE-grown material [3]. Here, we extend this work and report on the performance and reliability of 670- and 690-nm bars made by SSMBE.

Structures were grown in two reactors, both configured with multi-zone valved cracking cells for generation of As and P fluxes. (A description of the growth system and procedures has been given elsewhere [4].) Group III elements and the dopants Si and Be were evaporated from conventional effusion cells. Substrates and chamber were both outgassed extensively prior to growth.

The epitaxial layer design is a conventional graded-index separate confinement heterostructure. All devices contain a single, undoped, 7-nm-thick GaInP quantum well under compressive biaxial strain, and a symmetric, undoped, continuously-graded AlGaInP waveguide. Cladding material is also AlGaInP. A GaInP barrier-reduction layer is used on the *p*-side to improve hole transport in the structure. All structures were grown on exact-cut (100) *n*-GaAs substrates. As has been discussed elsewhere [5], growth on off-axis substrates to suppress ordering of the GaInP does not appear to be necessary in SSMBE growth of this material.

Wafers were processed into 19-element 1-cm bars suitable for fiber coupling. Element spacing is 500 μm center to center. Emitter width is 50 μm . In most of the work shown here, each element consists of a single 50- μm emitter, for an overall fill factor of 10%. Bars were cleaved to a cavity length of 1 mm, and standard anti-reflection/high-reflection coatings were applied to the facets. Bars are soldered *p*-side down onto copper heatsinks.

Light-current characteristics for a typical 10%-fill-factor 685-nm bar, measured after burn-in, are shown in Figure 1. Lasing threshold is about 3.5 A; slope efficiency is 1 W/A. The power conversion efficiency at 5 W light power is 31%. Figure 2 shows a spectrum for the same bar, measured at 5 W and 25 °C. The spectrum is narrow, with a full width at half maximum (FWHM) of 1.1 nm, indicating good uniformity among the emitters. (Spectral width for single emitters packaged from the same wafer is typically 0.8 nm).

Two similar 685-nm bars have been lifetested at 5 W; results to date are shown in Figure 3. The test is run at constant current, at a heatsink temperature of approximately 25 °C. Both bars were burned in for 100 hours prior to lifetesting. During the 1700 hours of lifetest, one bar showed no degradation and may have improved slightly. The second bar showed less than 1% degradation in the 1700 hours. (This second bar exhibited a weak parasitic shunt path before burn-in that may be due to a material defect.)

Reliability of bars at shorter wavelengths is measurably poorer than that of bars near 690 nm, but still very good. Figure 4 shows a lifetest of two 10%-fill-factor 670-nm bars, again conducted in constant current mode at 25 °C. These bars were operated for 1100 hours at 3 W, and then turned up to 5 W for another 1000 hours. During the 1000 hours at 5 W, total degradation (i.e. change in output power for fixed current) was approximately 3%.

These 670-nm bars were tested again after the above lifetest, with typical results shown in Figures 5 and 6. From the light-current characteristics (Figure 5), lasing threshold is about 4 A and slope efficiency 1 W/A at 25 °C. Power conversion efficiency is 28% at 5 W light power out. A spectrum from the same bar, measured at 5 W at 25 °C, is shown in Figure 6; FWHM is 0.8 nm. Again, the narrow spectrum indicates good uniformity among the emitters.

The 19-element geometry is chosen for convenience in fiber coupling. Emitter width was chosen based on single-emitter reliability. With these constraints, increased power (and increased brightness for the same fiber dimensions) can be obtained by clustering emitters within each element. Figures 7-9 show preliminary results for a 20%-fill-factor structure, with 19 pairs of 50- μm emitters.

Light-current characteristics are shown in Figure 7. The bar was tested to 15 W at 15 °C, with 28% power conversion efficiency at 15 W. Figure 8 shows a spectrum for the same bar, measured at 10 W light output power at 15 °C. FWHM is 1.2 nm. Figure 9 shows the near-field distribution for a similar bar. The 38 emitters are clearly resolved. (Near-field was measured at 3 W due to limitations in the measurement setup.)

In summary, good reliability has been demonstrated for 10%-fill-factor 5-W CW bars fabricated from SSMBE-grown 670- and 690-nm material. Preliminary results on 20%-fill-factor 670-nm bars are encouraging: 15-W CW operation with minimal thermal rollover indicates the feasibility of making reliable 10-W CW fiber-coupled arrays.

References:

- [1] J.N. Baillargeon, A.Y. Cho, and R.J. Fischer, *J. Vac. Sci. Technol.* **13**, 64 (1995).
- [2] M. Pessa, M. Toivonen, M. Jalonens, P. Savolainen, and A. Salokatve, *Thin Solid Films* **306**, 237 (1997).
- [3] S. Orsila, M. Toivonen, P. Savolainen, V. Vilokkinen, P. Melanen, M. Pessa, M. Saarinen, P. Uusimaa, P. Corvini, F. Fang, M. Jansen, and R. Nabiev, *Photonics West '99*, San Jose, California, *SPIE Proceedings* **3628-25** (1999).
- [4] M. Toivonen, M. Jalonens, A. Salokatve, J. Nappi, P. Savolainen, M. Pessa, and H. Asonen, *Appl. Phys. Lett.* **67**, 2332 (1995).
- [5] P. Savolainen, M. Toivonen, M. Pessa, P. Corvini, M. Jansen, and R.F. Nabiev, "Red lasers grown by all-solid-source molecular beam epitaxy," accepted for *Semicon. Sci. Tech.* (1999).

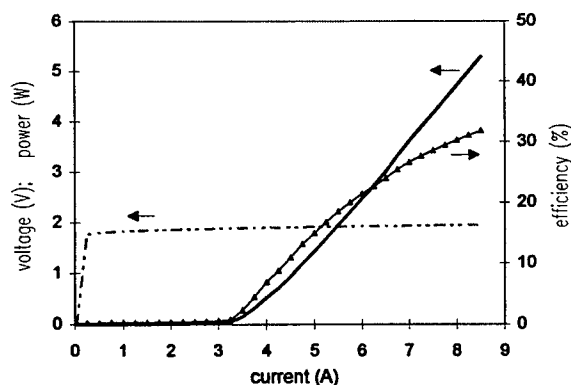


Figure 1. Forward voltage (broken line), light power output (solid line), and power conversion efficiency (triangles) vs. current for 10%-fill-factor 685-nm bar after burn-in. Measurement is at 25 °C.

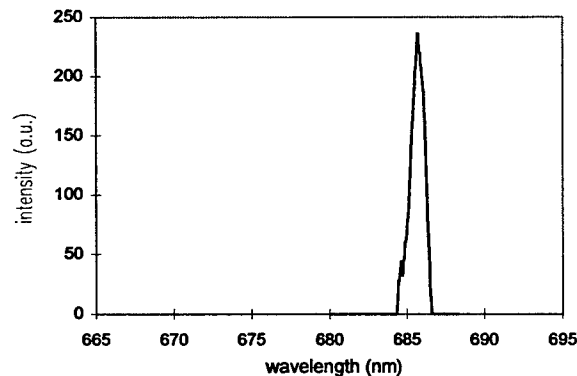


Figure 2. Spectrum of same 685-nm bar as in Figure 1, measured at 5 W at 25 °C. FWHM is 1.1 nm.

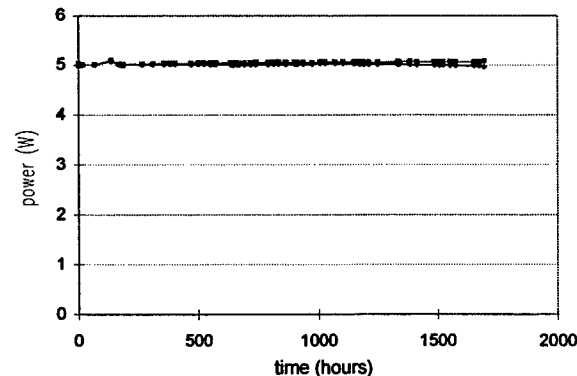


Figure 3. Constant-current lifetest of two 685-nm bars running at 5 W CW at 25 °C. After 1700 hours, one bar shows no measurable degradation. Second bar, which had an electrical anomaly before burn-in, shows <1% degradation.

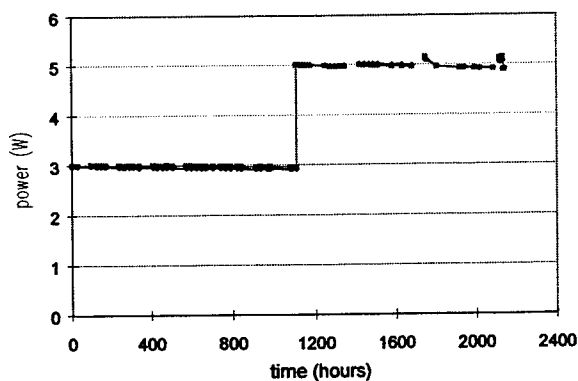


Figure 4. Constant-current lifetest of two 670-nm bars at 25 °C. Initial power was 3 W; after 1100 hours, power was increased to 5 W. Degradation was approximately 3% in 1000 hours at 5 W. (Discontinuities correspond to excursions in the cooling-water temperature.)

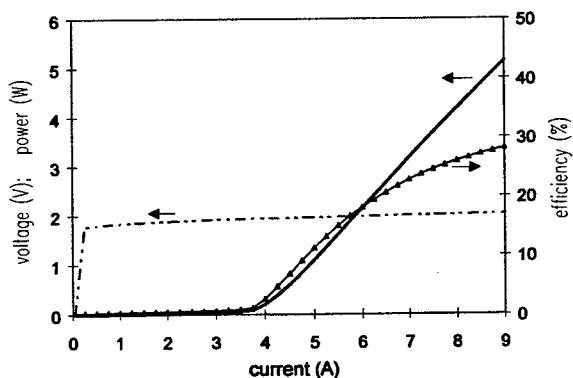


Figure 5. Forward voltage (broken line), light power output (solid line), and power conversion efficiency (triangles) vs. current for 670-nm bar after 2000 hours' lifetest as shown in Figure 4. Measurement is at 25 °C.

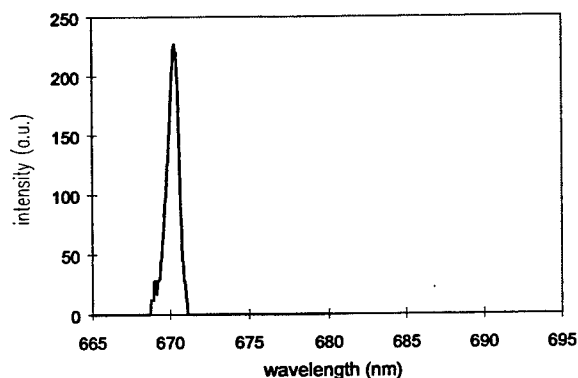


Figure 6. Spectrum of same 670-nm bar as in Figure 5, measured at 5 W at 25 °C after lifetest. FWHM is 0.8 nm.

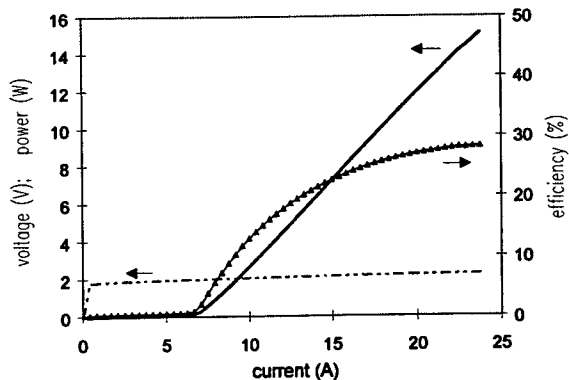


Figure 7. Forward voltage (broken line), light power output (solid line), and power conversion efficiency (triangles) vs. current for 20%-fill-factor 670-nm bar before burn-in. (Threshold current normally improves during burn-in.) Measurement is at 15 deg C.

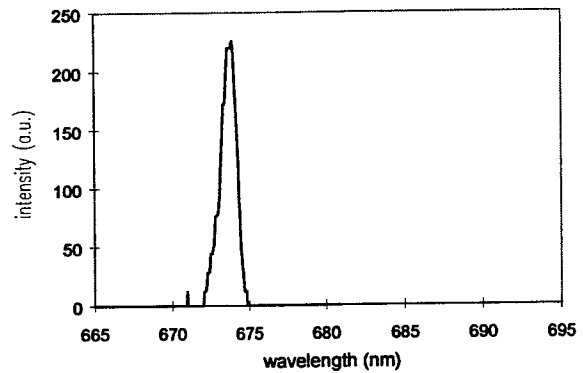


Figure 8. Spectrum for 20%-fill-factor bar of Figure 7. Measurement is made at 10 W light output power at 15 °C. FWHM is 1.2 nm.

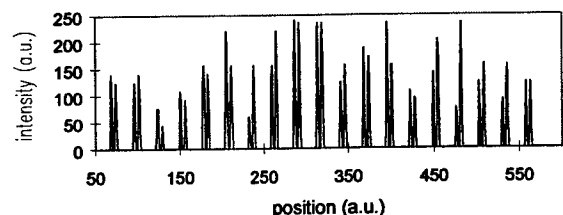


Figure 9. Near-field for 20%-fill-factor 670-nm bar. Measurement is made at 3 W light output power at 25 °C. Bar contains 19 pairs of emitters spaced on 500-μm centers. Each pair comprises two 50-μm emitters separated by 50 μm.

Large Spot Size Single Mode Bragg Waveguide Vertical Cavity Surface Emitting Lasers

M.G. Greatly, J. Masum, and M.J. Adams.

*Department of Physics, University of Essex, Wivenhoe Park,
Colchester CO4 3SQ, UK.
greatly@essex.ac.uk.*

M.J. Steer, J.E.F. Frost, J.S. Roberts and J. Woodhead,

*Department of Electrical and Electronic Engineering, University of Sheffield, P.O. Box 600, Mappin
Street, Sheffield S1 4DU, UK.
M.J.Steer@sheffield.ac.uk*

Introduction

The pursuit for a high-power single-mode Vertical Cavity Surface Emitting Laser (VCSEL) is currently generating considerable interest. The highest power reported for a single-mode device is for an 860nm oxide aperture VCSEL¹ with a 3.5 μ m aperture which delivered a maximum power of 4.8mW before becoming multi-mode. We have designed and fabricated a novel VCSEL device which incorporates a cylindrical Bragg waveguide (BW) across the VCSEL.

A cylindrical Bragg waveguide is composed of a series of concentric annuli of alternating high and low refractive indices surrounding a central core². Unlike a conventional step-index waveguide, a BW will support a fundamental mode within a core of arbitrary radius and refractive index. We have induced such a lateral waveguide across a 980nm VCSEL by patterning the top distributed Bragg reflector (DBR). This device therefore has two main advantages: the potential for large spot size single-mode devices and no requirement for regrowth.

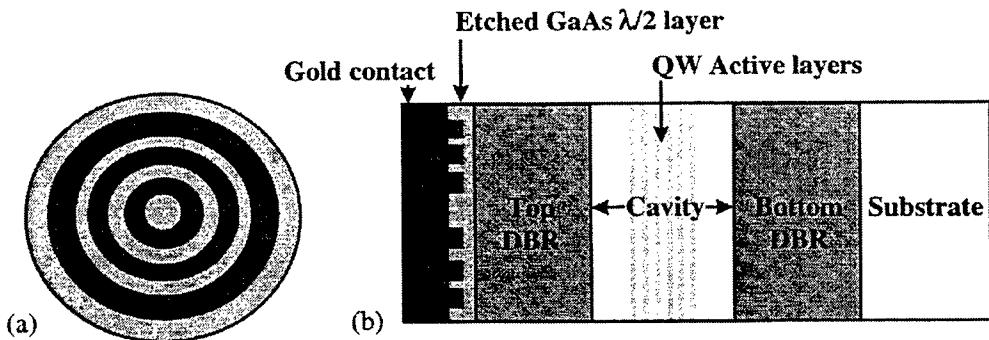


Fig. 1 A schematic diagram of the top (a) and side view (b) of a VCSEL with a patterned reflector.

BW VCSEL Design

A conventional bottom emitting VCSEL (shown in fig.1) consists of an active region placed in a cavity between top and bottom DBRs. The reflectivity of the top DBR is increased significantly above that of the bottom DBR by the addition of a gold film which also acts as an electrical contact. A half-wavelength GaAs phase-matching layer separates the top DBR from the gold. It is this half-wavelength phase-matching layer that is etched into concentric rings, prior to gold deposition, which induces the cylindrical Bragg waveguide across the VCSEL cavity.

We have developed a waveguide model to design a cylindrical BW for a 980nm bottom emitting VCSEL inducing transverse mode confinement for the HE₁₁ fundamental mode.^{3,4} The effective index approximation⁵ is employed to calculate the change in effective index (Δn), across the VCSEL cavity. Etching away part of the $\lambda/2$ layer results in a shift, $\Delta\lambda$, in the resonance wavelength, λ , of the VCSEL cavity. The shift in cavity resonance is related to the change in the effective index of the cavity, n_{cav} , by $\Delta n = n_{cav} \Delta\lambda / \lambda$. The value of $\Delta\lambda$, and therefore Δn , is determined as a function of

etch depth using the transmission matrix method,⁶ as shown in fig 2. The value of Δn can then be used to design the BW for a VCSEL, by applying the Yeh and Yariv² design method for a cylindrical Bragg fibre.

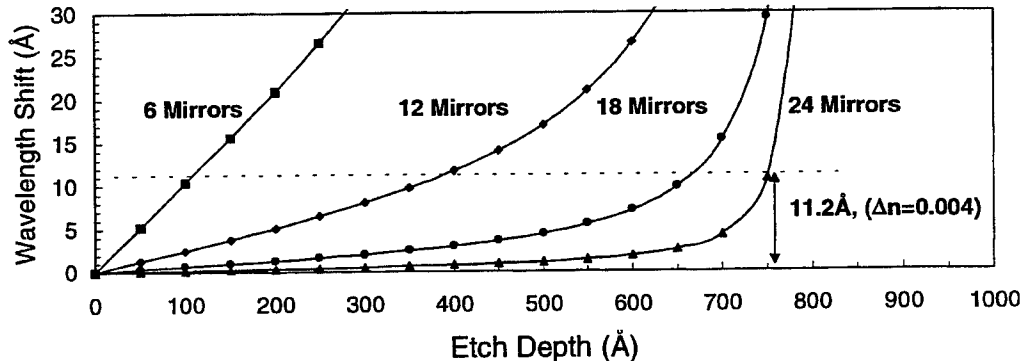


Fig. 2 Theoretical data from transmission line modeling showing the wavelength shift, $\Delta\lambda$ as a function of etch depth into the top $\lambda/2$ GaAs phase matching layer. The position of the required etch depth for devices with $\Delta n=0.004$ is indicated. Results are shown for devices with 6,12,18 and 24 mirror pairs in the top DBR.

Fabrication and Results

We have fabricated a series of BW VCSELs from a MOCVD grown structure designed to operate at a wavelength of 980nm. This was based on conventional AlGaAs/GaAs stepped DBRs with six InGaAs quantum wells within a 2λ cavity. The BW designs were designed assuming a Δn value of 0.004 since this leads to minimum feature sizes of $1.3\mu\text{m}$ which are suitable for the standard photolithography used here. Larger values of Δn would lead to better confinement, but the smaller features make fabrication more difficult. For a 980nm VCSEL, $\Delta n=0.004$ corresponds to a wavelength shift $\Delta\lambda$ of 11.2\AA .

Figure 2 shows that this magnitude of shift can be achieved for a wide range of structures, but we have chosen to use 12 periods for the top DBR since this provides good tolerance to etch depth variations since $\Delta\lambda$ is only a shallow function of etch depth for this structure at the target depth. The figure shows that the etch depth required for the Bragg rings was therefore 380\AA , which can be achieved by wet chemical etching without undue distortion due to undercutting. The etch depth was checked by measuring $\Delta\lambda$ directly via the difference in lasing wavelength of test VCSELs on the chip which were etched over either all or none of their surface. The bottom DBR for these structures comprised 31 periods, chosen to provide good reflectivity and reasonable output coupling efficiency.

Figure 3(a) shows the LI curve for a device having a central core of radius $3.4\mu\text{m}$. The total radius of this laser is $50\mu\text{m}$, which encompasses 6 periods of the Bragg structure. The LI and spectral data reported here were recorded under pulsed conditions with pulse lengths of 200ns and a repetition rate of 50kHz.

The threshold current of this device is 11.5mA and spectral measurements indicate that the output is initially single mode (figure 3(b)). This behaviour is maintained up to 14.5mA where the output power is $60\mu\text{A}$. Above this, weaker higher order modes appear in the spectra. In principle, such modes should not be supported in a Bragg waveguide structure and the nature of the guiding leading to these modes is not yet clear.

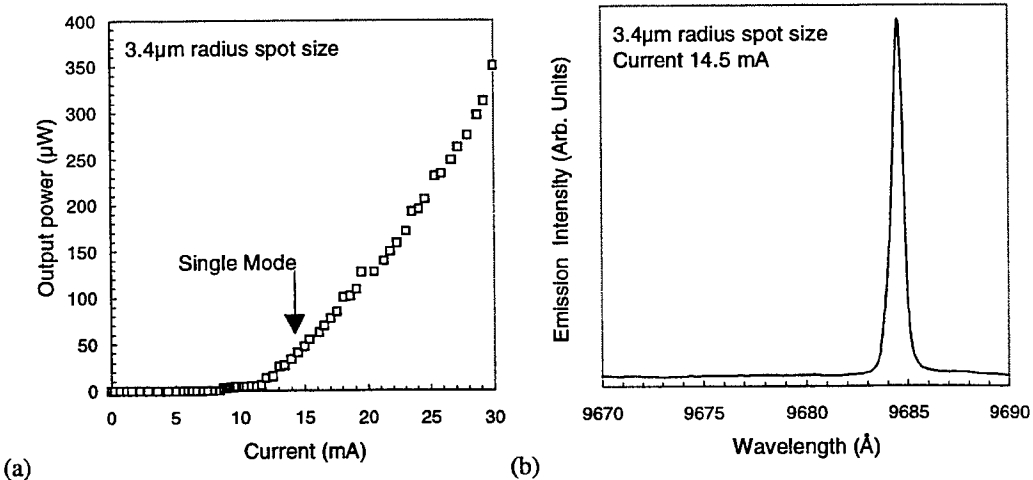


Fig. 3 (a) LI curve for a BW VCSEL (b) Single mode spectra with current = 14.5mA.

Single mode behaviour has been observed in many types of VCSEL, so to demonstrate that the BW controls the fundamental mode we show the beam profile in figure 4. This confirms that lasing is occurring from the centre of the device, roughly coincident with the central core. This agrees with our expectations, since the modelling suggests that the optical field of the BW mode is small beyond the first guiding ring. Above 14.5mA, where higher order modes appear, these modes are also concentrated in the central core but their detailed nature remains unclear.

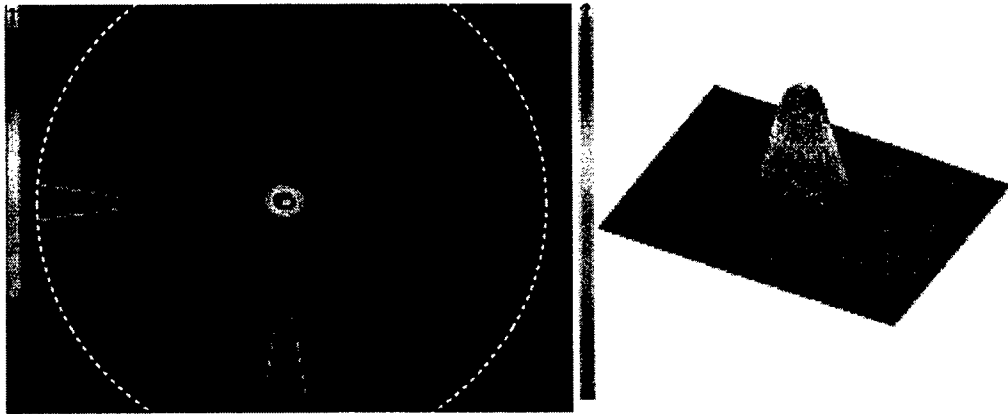


Fig. 4 Beam profile images of BW VCSEL devices. The edge of the device is also indicated.

Conclusions

In summary, we have produced a new type of single mode VCSEL whose guiding is controlled by a Bragg waveguide structure. The fundamental mode observed is concentrated in the central core and is clearly controlled by the Bragg waveguide. Unfortunately, other unexpected modes are also supported which appear at currents above threshold. The BW VCSEL potentially offers high power single mode output, but further studies of the inadvertent guiding mechanisms is required before this potential can be realised.

References

1. C.Jung *et al.* Elect. Lett. **33**, 1790 (1997).
2. P.Yeh and A.Yariv J. Opt. Soc. Am. **68**, 1196 (1978).
3. M.G. Greally *et al.* International Semiconductor Laser Conference 1998, TuE14, P121-122.
4. M.G. Greally *et al.* To be published.
5. G. R. Hadley, Opt. Lett. **20**, 1483 (1995).
6. P.Yeh, *Optical Waves in Layered Media*, New York: Wiley, Chapter 5, 1988.

Large spatial mode, single frequency semiconductor lasers using two dimensional gratings

Srinath Kalluri, Timothy Vang, Robert Lodenkamper, Michael Nesnidal, Michael Wickham, Doyle Nichols, David Forbes, Johanna Lacey, Larry Lembo, John Brock

TRW
One Space Park, DJ-1024
Redondo Beach, CA 90278
tel: (310) 813-3502 fax: (310) 812-8983
srinath.kalluri@trw.com

Abstract: We demonstrate single mode operation of laser diode cavities up to 200 μ m wide using 2-D Bragg gratings for simultaneous longitudinal and lateral mode control.

OCIS codes: (140.2020) Diode lasers; (140.3490) Lasers, distributed feedback; (140.3570) Lasers, single mode; (140.5960) Semiconductor lasers.

Introduction

Broad area devices that can produce large and stable diffraction limited beams are desirable for delivering high optical powers. Novel approaches that use antiresonant narrow-stripe arrays [1], angled 1-D gratings [2], master oscillator/power amplifier lasers [3] and many others have been demonstrated in the literature for achieving high powers from large apertures. Some of these approaches have also demonstrated single frequency operation. We present here a novel technique for expanding the spatial mode size while maintaining both a large, diffraction limited output beam and single longitudinal mode emission.

Most commercial single frequency, near infra-red diode lasers use one dimensional Bragg gratings for longitudinal mode control. We demonstrate that the concept of mode control using gratings can be extended to two-dimensions for simultaneous control of both the longitudinal and lateral modes. Longitudinal mode control permits narrow linewidth operation while lateral mode control permits lateral expansion of the fundamental spatial mode. Two-dimensional grating feedback lasers have been discussed in the literature [4-6], however, to our knowledge, this work is the first to demonstrate true 2-D DFB operation in semiconductor laser diodes.

Design and Fabrication

The transverse waveguide structure of our 2-D broad area laser is a conventional separate confinement, multi-quantum well heterostructure. All the epitaxial layers were lattice matched to the n type InP substrate and grown by MOCVD. The active region is composed of 8, 50 \AA , InGaAsP quantum wells. A three-layer structure grown on top of the active region was used to define the gratings. This structure consists of a 75 nm thick layer of InGaAsP sandwiched between two thin layers of InP. The two dimensional gratings were written in photoresist by E-beam lithography and chemically etched into the InGaAsP grating layer by using the upper InP as an etch mask and the lower InP layer as an etch stop. Thus the thickness of the epitaxially grown InGaAsP grating layer precisely controls the depth of the grating. Gratings with long periods, Λ_L , of 880 nm and 1100 nm (the short period, Λ_S is 220 nm for both designs) were written in 100 μ m and 200 μ m wide columns. These widths define the width of the 2-D

broad area laser cavity. The rest of the device fabrication steps include the regrowth of an InP upper cladding and p+ InGaAs Ohmic layer, followed by p metallization over the grating columns, lapping and n backside metallization. Finally, 800 μ m long devices were cleaved and anti-reflection (AR) coated for testing.

Figure 1 shows an atomic force microscope (AFM) image of a typical 2-D grating fabricated on the active region of our laser. The periods Λ_s and Λ_L of this grating are 220nm and 1100nm respectively, which is a grating period aspect ratio of 1:5. Figure 2 shows a k vector schematic for this grating. In addition to the two degenerate 1-D modes, k_+ and k_- , typical of a conventional DFB laser; the two-dimensional grating couples four other degenerate modes k_A , k_B , k_C and k_D . Other vectors coupled by the grating lie outside the gain spectrum of the semiconductor material. The 2-D mode at the facet of the device is a superposition of these four modes. The periods and the aspect ratio of the periods in the orthogonal directions determine the angle and magnitude of the k vectors. Note that the length of the k vectors for the two kinds of mode also determines the feedback wavelengths; with the 1-D wavelength slightly red shifted (smaller $|k|$) from the 2-D wavelength (larger $|k|$). The k vector predictions for the 1-D (λ_{1D}) and 2-D (λ_{2D}) wavelengths and the expected internal (θ_I) and external angles (θ_{EXT}) for the two grating period aspect ratios in our design are listed in Table 1. Note that we use the wavelength separation between the 1-D and 2-D wavelengths to design the material gain peak to overlap the 2-D feedback wavelength and thus prefer it for lasing. Finally, AR coatings on the facets suppress any Fabry-Perot modes.

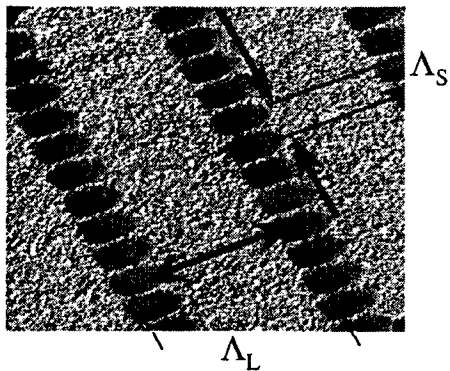


Fig. 1. AFM image of a grating written on top of the active region. Λ_L and Λ_s are the long (1100nm) and short periods (220nm) respectively.

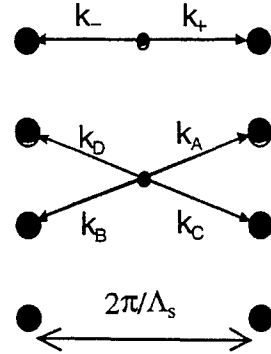


Fig. 2. k vector schematic showing the four 2-D coupled modes, k_A , k_B , k_C and k_D and the two 1-D modes k_- and k_+ .

Table 1. Expected Emission Parameters for Two Different 2-D Grating Laser Designs

Aspect Ratio	λ_{1D}	λ_{2D}	θ_I	θ_{EXT}
1:4	1436 nm	1393 nm	14°	52.3°
1:5	1436 nm	1408 nm	11.3°	39.8°

Device Results

Lasers were tested in our pulsed current injection setup. The optical spectrum of the device was collected at both normal incidence and at the angle of peak 2-D emission (see Table 1). The amplified spontaneous spectrum at normal incidence for the 1:5 sample shows a small 1-D feedback feature at 1435 nm but no lasing modes. The spectrum collected at 40° for the same injection current is shown in Figure 3. The laser

was single mode to within the 1 Å resolution bandwidth of our spectrum analyzer with up to 40 dB of side mode suppression. The ratio of the 2-D emission wavelength at 40° and the 1-D feature in the ASE at normal incidence match the predictions of the k vector geometry shown in Figure 2. Similarly consistent results were obtained for the 1:4 laser.

The lateral far-field of a 200 μm wide \times 800 μm long device with a grating period aspect ratio of 1:5 is shown in Figure 4. Note that the far field emission is peaked at the external angles of $\pm 40^\circ$ in close agreement with the predictions of Table 1. We have achieved similarly consistent results for the 1:4 two-dimensional grating lasers with the far field peaked at $\pm 52.7^\circ$. Figure 5 shows a high resolution scan of the far-field around an external angle of $+40^\circ$ for the 1:5 device at 1.9 times the threshold current. The far field is ~ 1.6 times the diffraction limit for a 200 μm aperture; however in these initial demonstrations, no effort was made to prevent lateral current spreading in the p doped upper cladding.

We have also developed a two-dimensional coupled mode theory to model these structures. Previous

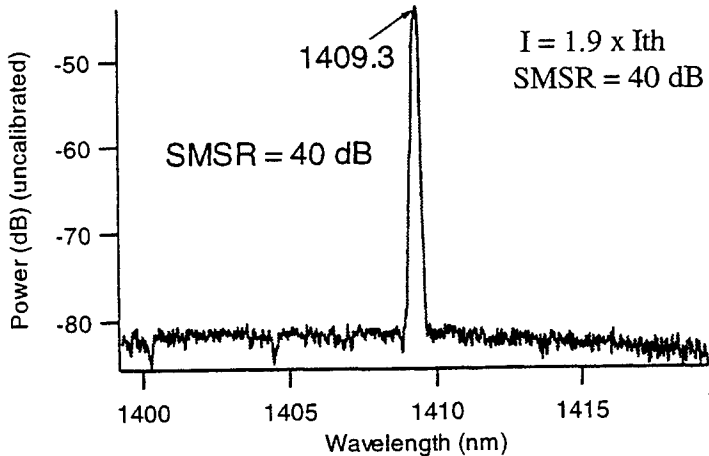


Fig. 3. Optical spectrum of the 1:5 laser at 40 degrees angle of incidence. The emission wavelength is 1409 nm.

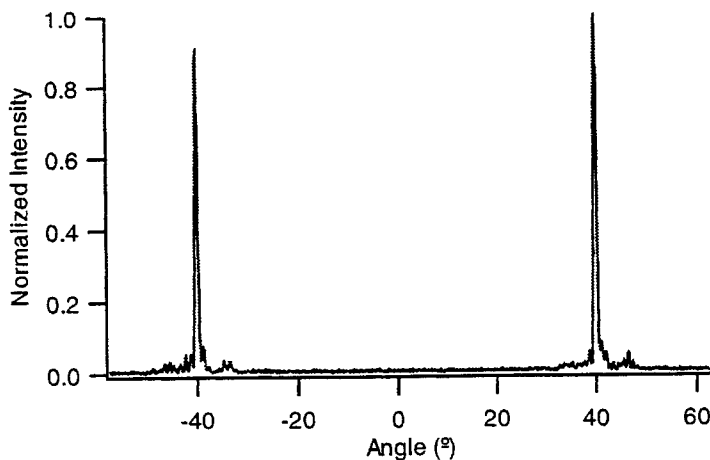


Figure 4: Far-field scan of a 1:5 grating period aspect ratio laser of length 800 μm and width 200 μm .

approaches [5,6] were appropriate for cases where the 2-D grating could be considered as two orthogonal 1-D gratings. Our model can handle more general structures where the 2-D gratings cannot be reduced to 1-D gratings. The far-field results match the predictions of the theory quite well. We have also used the theory to model structures where the gratings are tilted with respect to the facet for normal emission (instead of emission at $\pm \theta$). The model predicts that for the tilted structure, the lowest order mode maintains a low threshold and has good threshold discrimination.

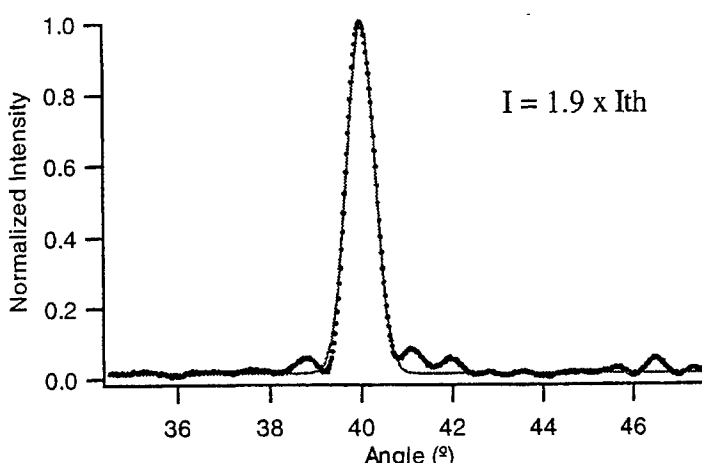


Figure 5: Far field pattern near 40° incidence for a 1:5 laser 800 μ m long and 200 μ m wide. The beam waist of 0.4° is 1.6 times the diffraction limit for a 200 μ m aperture. Dots are measured data, solid line is a gaussian fit.

Doyle Nichols is currently at the CIENA Corporation, Linthicum, Maryland. Michael Nesnidal is with Focused Research, Wisconsin. Paul Maker is with the Jet Propulsion Laboratory.

References

1. H Yang, L J Mawst, M Nesnidal, J Lopez, A Bhattacharaya, D Botez; Electron. Lett., Vol. 33, p. 136, 1997
2. R J Lang, K Dzurko, A A Hardy, S Demars, A Schoenfelder, D Welch; IEEE J. Quantum Electron., Vol. 34, (11), pp. 2196-2210
3. L Goldberg, D Mehuys; Appl. Phys. Lett., Vol 61, p. 633, 1992
4. S Wang, S Sheem; Appl. Phys. Lett., Vol.22, (9), p. 460, 1973
5. M Toda; IEEE J. Quantum Electron., Vol. 28, (7), p. 1653, 1992
6. H Han, J J Coleman; IEEE J. Quantum Electron., Vol. 31, (11), p. 1947, 1995

In conclusion, the lateral far-field and spectral characteristics of a novel true two-dimensional distributed feedback broad area laser were used to demonstrate the simultaneous control of lateral and longitudinal modes. Narrow linewidth lasers with apertures as wide as 200 μ m were demonstrated.

Acknowledgements

The authors would like to thank Po-Hsin Liu, Carol Namba and Paul Maker for Electron beam lithography; Roosevelt Johnson, Fernando Alvarez for help in fabrication and testing and Moshe Sergant for his AFM expertise.

Diode-Laser
Spectroscopy: 1

Laser Diode-based Lidar and Applications

James B. Abshire

NASA-Goddard Space Flight Center, Laser remote Sensing Branch, Greenbelt MD
20771

James.Abshire @gsfc.nasa.gov

Diode lasers have many properties which make them attractive for use in small laser remote sensing instruments. These include very small size and low mass, good average power, high electrical efficiency, and very high power/mass ratio. Other advantages are direct high speed modulation, flexibility in modulation format, and ease in wavelength tunability. Diode lasers can be selected with wavelengths which overlap with both sensitive photon counting detectors and the absorption bands of atmospheric water vapor, O₂, and CO₂.

There are several space and Earth laser remote sensing applications which benefit from these properties. They include satellite to satellite ranging systems for scientific measurements as well as for satellite rendezvous and station keeping. Diode transmitters are also attractive for miniature atmospheric lidar. A small aerosol diode lidar was selected is part of the payload for NASA's Mars 1998 Lander. A longer term goal for our group at Goddard is to develop a small landed planetary lidar for Mars atmospheric water vapor and high altitude aerosol measurements.

Earth-based applications also benefit from measurements from small diode lidar instruments. Desired features are that they low cost, rugged, operate autonomously, eye safe and power efficient. Some examples include small networks of lidar to monitor water vapor transport for the NOAA GCIP program and monitoring polar atmospheric transmissions and polar cloud cover over remote sites in Antarctica and Greenland. Future applications include small lidar for measuring upper tropospheric water vapor from small unmanned aerial vehicles (UAV's) and for downward looking lidar on planetary orbiters. Orbital applications depend on further development of diode power scaling approaches.

With the low peak powers typically available from diode lasers, important issues are modulation waveforms and collecting enough signal photons to make useful measurements. To date the applications have been compatible with long integration times (minutes to hours) for signal accumulation. An important question is how best to modulate the diode source within this integration time. Intensity modulation techniques which have been applied include monopulse modulation with kHz pulse rates, and using time-extended modulation formats, such as multi-frequency tones and pseudo-noise codes.

There are possibilities to extend these applications. Issues to be addressed include better stabilizing and controlling the diode's center emission wavelength under modulation, and techniques to increase the output power of the diode transmitter through power scaling or combining. Sub-nm bandwidth receivers are also needed. For space use, there are the issues of vibration, vacuum compatible materials and ionizing radiation. Instrument developers also face the issues of incentives for researchers and manufacturers to produce the needed specialized laser diode devices in (at least initially) small numbers while still achieving the properties needed in reliable devices. These applications, approaches and issues will be addressed in the talk.

Diode-laser absorption sensors for industrial process monitoring and control

D.S. Baer, S.I. Chou, S. Sanders, M.E. Webber, S.D. Wehe, R.K. Hanson

High Temperature Gasdynamics Laboratory

Department of Mechanical Engineering

Stanford University, Stanford, CA 94305

doug.baer@stanford.edu

Diode-laser absorption sensors have been developed for measurements and control of critical gas parameters in process streams including combustion, incineration, and semiconductor systems. These sensors employed tunable (distributed feedback and external cavity) diode lasers as narrow-bandwidth light sources for high-resolution absorption measurements of H_2O (near 1.4 μm), HBr (2.0 μm), K (near 0.77 μm), and NH_3 (near 1.52 μm). Gas temperature was determined from the ratio of measured absorbances. Species concentrations were determined from the measured absorbance of a single transition and the gas temperature. Gas velocity was determined from Doppler-shifted absorption lineshapes. This paper will review recent progress in the development of diode laser sensors at the High Temperature Gasdynamics Laboratory for various industrial applications.

In the first project, a sensor system was developed measurements of gas temperature and H_2O concentration in combustion flows generated by a pulse detonation engine facility operated in the propulsion laboratory at the Naval Postgraduate School (NPS). A simplified schematic of the sensor system is shown in Fig. 1 (left). The PDE facility is, at present, a pre-detonation tube suited for exploration of detonation concepts in liquid-fueled systems. For these initial measurements, an optical test section that included ports for fiber-optic couplers and pressure taps was built at Stanford and subsequently attached to the pre-detonation tube at NPS. A set of four tunable diode lasers operating at selected resonant (1.34 μm , 1.39 μm) and non-resonant (1.65 μm) wavelengths were amplitude modulated at high frequencies, multiplexed and directed to the test section using fiber-optic components. The laser transmission through the PDE flow was recorded using a high-bandwidth photodetector with subsequent filtering to separate the intensities associated with each laser wavelength. Water-vapor concentration and temperature values were determined from the absorption measurements after subtracting contributions due to scattering and beam-steering effects. For emission measurements, a fiber-coupled lens was attached to the optical test section to collect radiation due to particles (soot) and gaseous radicals (especially CH). The emission signal was directed onto three spectrally filtered detectors to enable determination of temperature through two-color pyrometry (650 nm, 1060 nm) and CH emission (430 nm).

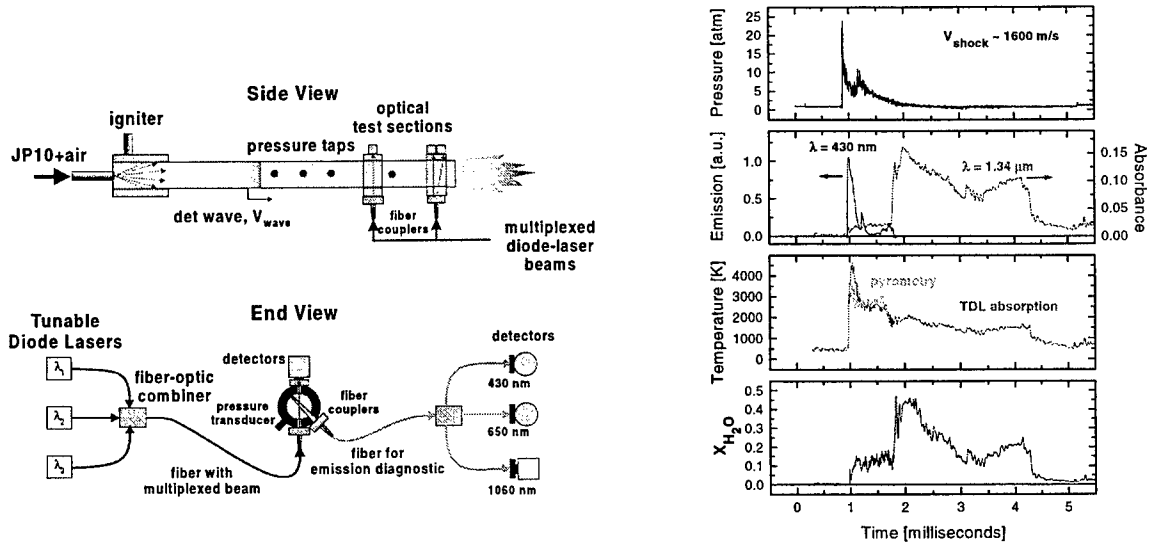


Fig. 1 (left) Optical diagnostics setup in pre-detonation tube at NPS. (right) Measurements of pressure (pitot probe), gas temperature, soot temperature, water vapor mole fraction, and UV emission.

Some of the results of the initial visit to NPS are shown in Fig. 1. (right) which illustrates measurements of pressure, temperature (determined from TDL absorption and 2-wavelength soot pyrometry), H_2O mole fraction, and CH emission in the pre-detonation tube operating on $\text{JP10}+\text{O}_2$. Of particular note is the ability of the diode laser sensors to record important parameters over a wide range of temperatures and pressures in this complex combustion flow.

In the second project, an external-cavity diode laser operating near $1.52 \mu\text{m}$ was used to record high-resolution measurements of NH_3 spectra at elevated temperatures for sensitive *in situ* concentration measurements of ammonia slip above flat-flame burner operated on $\text{C}_2\text{H}_4+\text{air}+\text{NH}_3$. Measured spectra, recorded in a heated static cell, were compared with calculations to verify the HITRAN96 database and used to determine optimum transitions for species detection. Individual lineshape measurements were used to determine fundamental spectroscopic parameters including the line strength and line-center frequency.

Figure 2 illustrates measurements of NH_3 mole fraction in exhaust gases above the burner for various NH_3 flow rates (seeded into the fuel flow to simulate Thermal DeNOx applications). For these measurements the laser beam was directed across the flow in a multi-pass arrangement to yield a 1.65-meter path. A sensitivity of approximately 10 ppm was demonstrated using a direct absorption strategy.

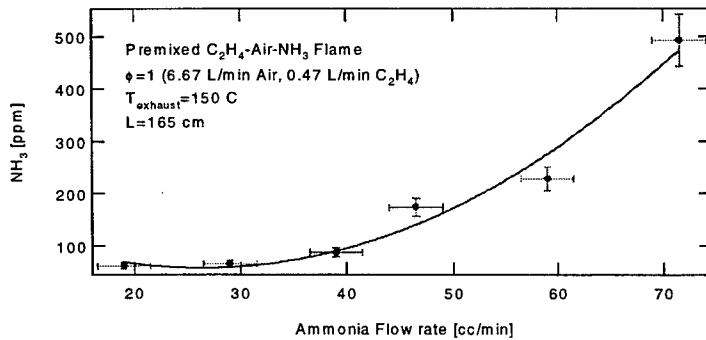


Fig. 2 NH_3 concentrations above a burner determined from absorption lineshapes near $1.52 \mu\text{m}$.

The third project involves the development and implementation of a compact sensor that capitalizes on the natural presence of chemically frozen potassium (K) for the determination of gas velocity from measurements of Doppler-shifted absorption lineshapes in high-velocity flowfields. The sensor was applied for velocity measurements in the Calspan 96-inch Hypersonic Shock Tunnel (Buffalo, NY). The design of the sensor is based on a larger version developed previously for simultaneous near-infrared H₂O absorption measurements of temperature, species concentration, and velocity in hypersonic flows. The probe was installed directly into the flowfield, 25 cm below the nozzle centerline, to minimize complications due to boundary layers and facility vibration. Values of gas velocity (typically ~4.2 km/s) were determined from lineshapes obtained every 0.1 msec by repetitively tuning the wavelength of a (AlGaAs) diode laser across the D₁ transitions near 770 nm (see figure 3). The measured gas velocities were consistent with (temporally averaged) values obtained from conventional tunnel measurements. The sensor is currently being applied for velocity measurements in hypersonic flows generated in the Stanford Expansion Tube and the results will be presented at the meeting.

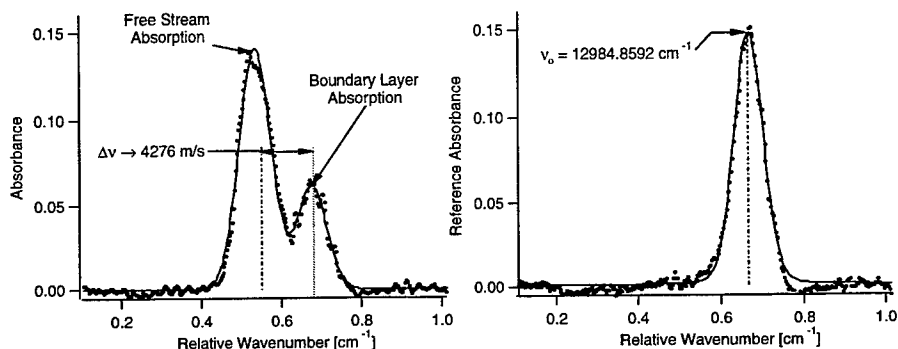


Fig. 3 Single-sweep potassium absorption lineshapes (770.11 nm) obtained during a 9.53-MJ/kg test. The left (right) trace was obtained from a beam directed at a 43.8° (90°) angle with respect to the bulk gas flow.

In the fourth project, wavelength modulation spectroscopy techniques were applied for sensitive measurements of HBr and H₂O concentrations for semiconductor processing applications. DFB lasers operating near 2.0 μm and 1.4 μm , modulated at 20.5 MHz, were tuned over HBr and H₂O absorption features, respectively, to record high-resolution 2f lineshapes. Species concentrations and gas temperature values were determined from measured absorption features recorded in an etch reactor operating over a range of conditions (1-100 mTorr, 300-800 K). Results from recent measurements will be presented at the meeting.

Quantitative wavelength modulation spectroscopy with diode lasers

Jes Henningsen and Harald Simonsen

Danish Institute of Fundamental Metrology, Bld. 307, Anker Engelunds Vej 1,
DK2800 Lyngby, Denmark
jh@dfm.dtu.dk, hs@dfm.dtu.dk

Abstract: Laser spectroscopy with wavelength modulation and second harmonic detection is used as a sensitive and highly selective technique for trace gas monitoring. Usually, the unknown concentration is derived by comparing with a certified reference mixture. We here present algorithms which will enable the quantitative analysis of the second harmonic signal to within $\pm 10\%$ without reference to a calibration gas. The algorithms are validated by measurements with an extended cavity diode laser on pure CO_2 , and with a DFB laser on atmospheric CO_2 .

OCIS codes: (280.1120) Air pollution monitoring; (300.6380) Spectroscopy, modulation;

Introduction

Modulation spectroscopy with room temperature near infrared diode lasers is widely used for monitoring molecules through detection of overtone or combination band transitions [1,2]. In wavelength modulation spectroscopy (WMS) the laser frequency is modulated in the kHz range and the response is detected at one of the harmonics of the modulation frequency, most often the second. In the limit of small modulation depth where the modulation amplitude is much smaller than the line width, the second harmonic response is proportional to the second derivative of the absorbance. However, in order to maximize the signal, the modulation amplitude must be comparable to the line width, and both the magnitude of the response and the line shape then depend critically on the modulation amplitude. For a Voigt line profile a numerical analysis of the second harmonic response for a range of combinations of modulation amplitude and line width shows that the response can be well modeled by three analytic functions, which depend on the ratio of modulation amplitude to line width [3]. The implications of this result are studied through measurements with an extended cavity diode laser on pure CO_2 , and with a DFB laser on atmospheric CO_2 , using different transitions in the combination band centered at 1575 nm.

Theory

Radiation travelling over a path length L in a medium with absorption coefficient α suffers an exponential decay $\exp(-\gamma)$ where $\gamma = \alpha L$ is denoted the absorbance. In the vicinity of an absorption line centered at frequency ν_0 , the absorbance is given by

$$\gamma = L N S g(\nu - \nu_0) \quad (1)$$

where N is the number density of absorbing molecules, S is the line strength of the absorption line, and $g(\nu - \nu_0)$ is the area normalized line shape function. The power reaching the detector is given by

$$P = P_0 \kappa \cdot \exp(-\gamma) \approx P_0 \kappa (1 - \gamma) \quad (2)$$

where P_0 is the power launched into the absorption path, the factor κ accounts for all losses except those associated with the absorption line, and the last expression holds for $\gamma \ll 1$.

The laser frequency is modulated according to $v(t) = v + v_m \sin(\omega_m t)$, and the response is detected with a lock-in amplifier. Using 2f demodulation, the lock-in detector will recover the rms value of the second harmonic Fourier component. Assuming a linear detector, and noting that only the term containing γ is modulated, we find that the lock-in output normalised with respect to the DC detector voltage can be written as

$$u = \frac{1}{\sqrt{2}} LNS \cdot \frac{1}{\pi} \int_0^{2\pi} g(v + v_m \sin(\omega_m t) - v_0) \cos(2\omega_m t) d(\omega_m t) \quad (3)$$

In the weak modulation limit the line shape function can be Taylor expanded, and this leads to the usual result that the second harmonic is proportional to the second derivative of the line profile. However, if maximum second harmonic response is desired, as is the case in monitoring, the modulation amplitude will be way beyond the limit where the Taylor expansion applies, and the integral must be evaluated numerically.

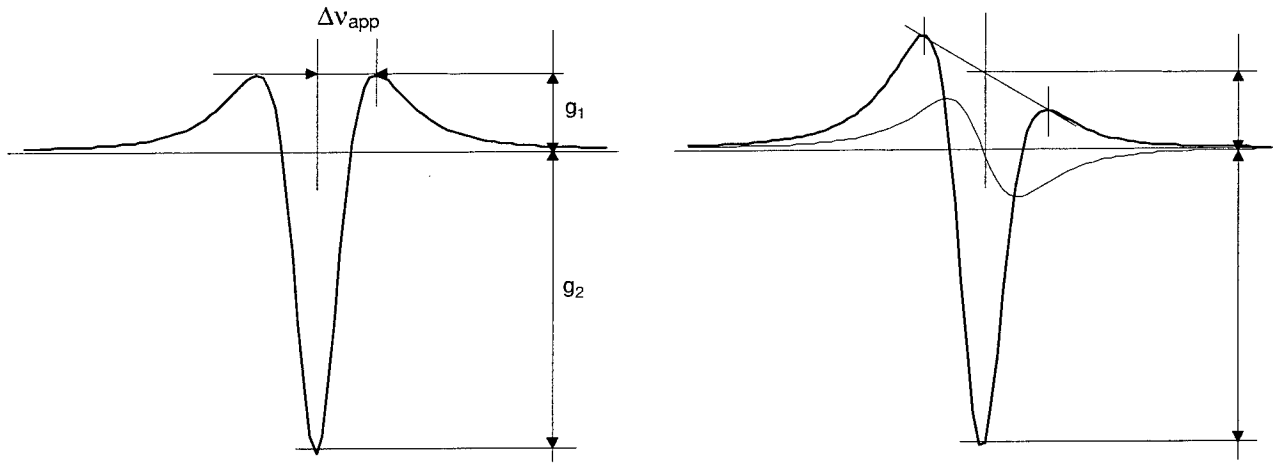


Fig.1. Second harmonic profiles for pure frequency modulation (left) and for simultaneous frequency and amplitude modulation (right).

The line shape function in general is a Voigt profile, characterized by a Doppler width Δv_D , and a Lorentz width Δv_L , and we shall approximate the overall line width by the expression

$$\Delta v = (\Delta v_L^2 + \Delta v_D^2)^{1/2} \quad (4)$$

Generic second harmonic profiles are shown in Fig.1. Introducing the modulation depth $b \equiv v_m / \Delta v$ we find that for a wide range of combinations of v_m and Δv , the amplitudes g_1 and g_2 , and the apparent line width Δv_{app} can be expressed in terms of functions $F(b)$, $G(b)$, and $H(b)$ as follows

$$(g_1 + g_2)\pi\Delta\nu = F(b) \quad (5)$$

$$g_2 / g_1 = G(b) \quad (6)$$

$$\Delta\nu_{app} / \Delta\nu = H(b) \quad (7)$$

Fig. 2 summarizes the results of numerical integration of Eq. 3 for line widths $\Delta\nu$ in the range 0.5 to 2.5 GHz, and modulation amplitudes ν_m in the range 0.1 to 5 GHz, corresponding to the range $0.04 < b < 10$. The solid lines represent analytical model functions

$$F(b) = 1.02 \cdot \frac{-0.52b^{0.12} + 1}{0.55b^{0.12} + b^{-2}} \quad (8)$$

$$G(b) = \frac{0.30b^{1.656} + 4}{0.47b^{1.656} + 1} \quad (9)$$

$$H(b) = (0.89b^2 + 1)^{1/2} \quad (10)$$

which are tailored to provide a good representation in the range $0.1 < b < 10$.

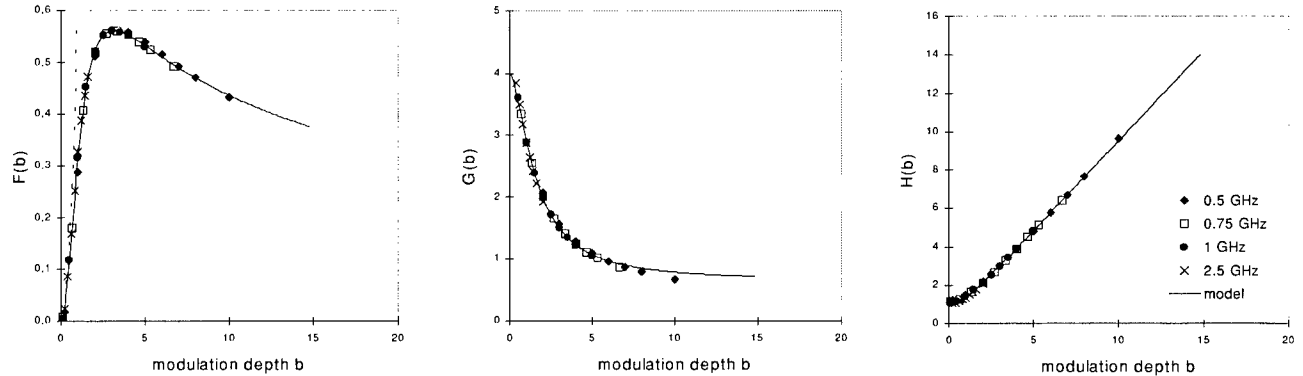


Fig.2. Functions $F(b)$, $G(b)$, and $H(b)$ characterizing amplitude and width of a strongly modulated Voigt line profile.

Making use of these results, we may then write the overall amplitude u of the 2. harmonic line profile as

$$u = c \cdot 2.173 \cdot 10^{20} L[m] \frac{p[Pa]}{T[K]} S[cm/mol] \frac{1}{\sqrt{2}} \frac{F(b)}{\pi\Delta\nu[GHz]} \quad (11)$$

where we have expressed the number density N in terms of the concentration c , the pressure p , and the temperature T , and where the numerical constant is the combined effect of Boltzmanns constant and all the conversion factors needed in order to reconcile the different units. In the Lorentz limit, where the peak value of the line shape function is given by

$$g(0) = \frac{1}{\pi \Delta v} \quad (12)$$

a simple relationship exists between the peak absorbance $\gamma(0)$ and the overall amplitude u of the normalized second harmonic signal

$$u = \frac{1}{\sqrt{2}} \gamma(0) F(b) \quad (13)$$

The results apply directly when using an extended cavity laser where modulation applied to the grating results in almost pure frequency modulation. For a DFB laser modulated through the injection current, an additional amplitude modulation must be taken into account. If the laser power depends linearly on the injection current, the amplitude modulation index α_m is a constant during the scan over the line, and we may then multiply the integrand in Eq.3 by a factor $(1+\alpha_m \sin(\omega_{mt}))$. The amplitude modulation will give rise to a term, which in the low modulation limit is proportional to the first derivative of the line profile, and which will in general be antisymmetric with respect to the line center. Thus, if the overall amplitude of the second harmonic is defined in accordance with the right hand side of Fig.1, the expressions of Eqs. 8-10 remain good approximations.

Experiment

The theoretical results were validated through measurements on CO₂ lines of the 300012←00001 overtone band centered at 6347.9 nm. A New Focus extended cavity laser was used in conjunction with a 127 cm absorption cell for measurements on R42 at 6374.376 cm⁻¹, and a full description of the experimental setup is found in [3]. The upper part of Fig. 3 shows the absorbance at 116 and 994 mbar and we see that the maximum absorbance of 3% satisfies the condition of Eq. 2. Measurements were performed at 8 pressures between 50 and 1000 mbar, and following the procedure of [3], the line strength $S=0.226 \cdot 10^{-23}$ cm/mol and the self broadening parameter $\gamma_L=2.253$ MHz/mbar were determined after subtracting the two hot band lines located at the left edge of the tuning window, and taking into account the Lorentz tails of the neighboring lines R40 and R44. For both parameters the estimated standard uncertainty is less than 2%. For the collision broadening parameter our result agrees with the value quoted in the 1996 version of the Hitran database to within about 1% [4]. However, our result for the line strength is about 25% below the Hitran value, and this large discrepancy will be the subject of a more detailed investigation. The lower part of Fig. 3 shows the corresponding second derivative spectra recorded at a modulation frequency of 319 Hz and a modulation amplitude of 0.69 GHz. The wavelength was modulated through a piezoelectric transducer, and the symmetry of the second harmonic spectrum is the signature of pure frequency modulation.

As a first step in the analysis of the second derivative spectra, the apparent line width Δv_{app} is read, and the line width Δv and the modulation depth b are determined from Eq. 7, Eq. 10, and the definition of b . Next, $F(b)$ is evaluated from Eq. 8, and the line strength is determined from the peak-to-peak amplitude of the second harmonic spectra in conjunction with Eq. 9. The results obtained for 8 pressures are shown in Fig. 4, where the solid lines are the results of the absorbance measurements.

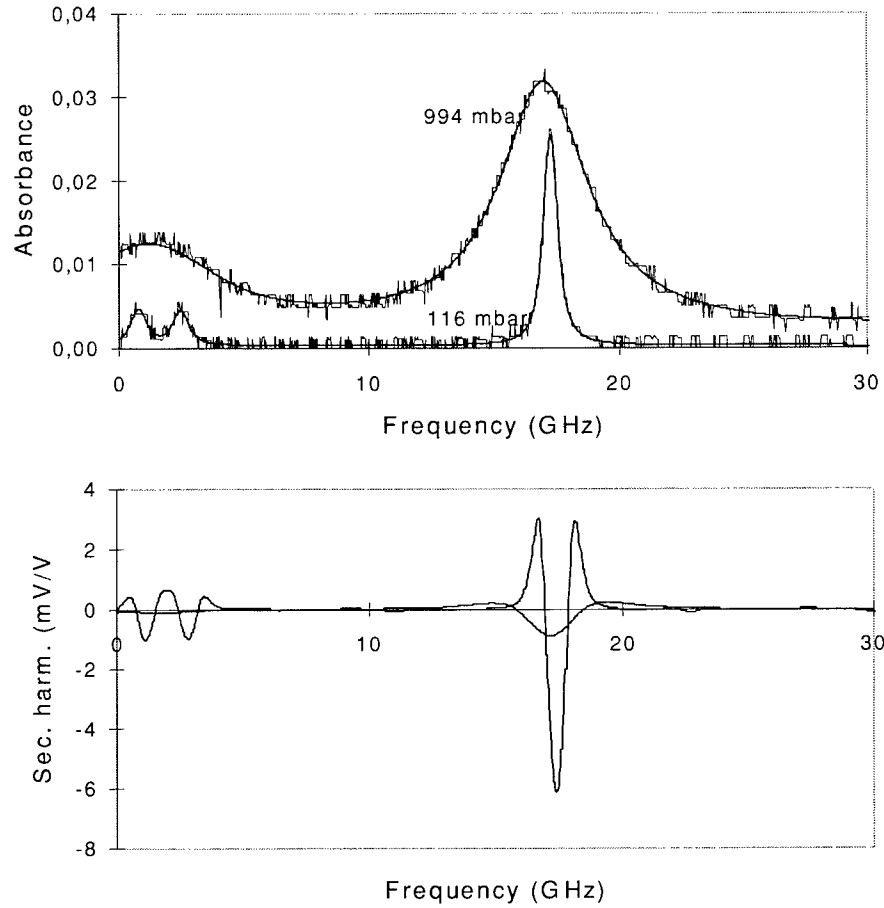


Fig.3. Absorbance spectra and second harmonic spectra for R42 at pressures of 116 and 994 mbar.

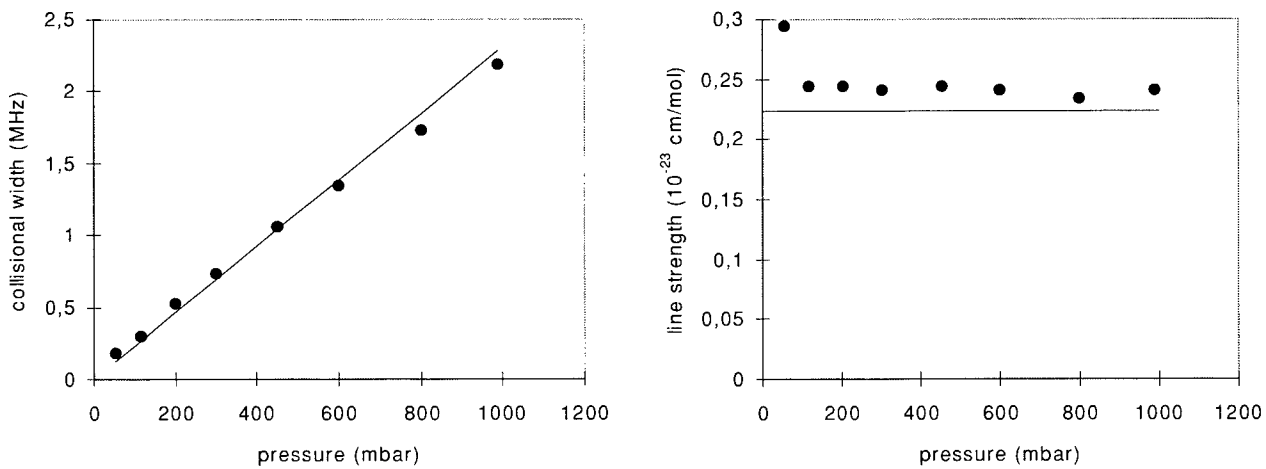


Fig. 4. Self broadening and line strength for R42, determined from second harmonic spectra. Solid lines are from absorbance measurements.

The results for different pressures are generally consistent. For the line width we find good agreement with the result of absorbance measurements, whereas the line strength is overestimated by about 10%. This discrepancy disappears if the modulation depth used in the analysis is taken as 0.71 GHz instead of 0.69 GHz, and this suggests a small systematic error in the measurement of frequency modulation amplitude versus modulation voltage amplitude.

Measurements on atmospheric CO₂ were carried out in R12 at 6357.312 cm⁻¹ with a DFB laser from Sensors Unlimited. The line strength and the self broadening parameter were determined as for R42 with the results $S=1.634 \cdot 10^{-23}$ cm/mol and $\gamma_L=3.040$ MHz/mbar, and the scaling from self broadening to

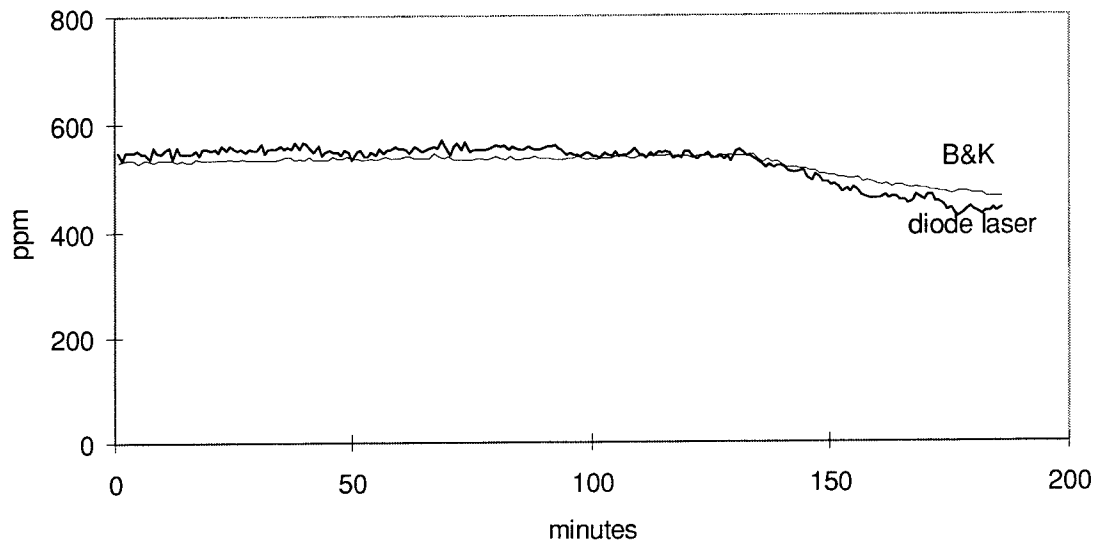


Fig.5. Concentration of CO₂ in laboratory air, determined with wavelength modulation spectroscopy and with a Brüel and Kjaer photoacoustic gas analyzer

air broadening was taken from Hitran, resulting in an air broadening parameter of $\gamma_{\text{air}}=2.196$ MHz/mbar. The laser was modulated through the injection current at 319 Hz with a modulation amplitude of 4.1 GHz, corresponding to a modulation depth of $b \approx 1.87$ at ambient pressure. The concentration was determined from the amplitude of the second harmonic signal observed over 48 m path length, obtained by 3 double passes over an 8 m distance in the laboratory, using Eqs.8-9 with the known value for the line width. Fig. 5 shows the result as compared over 3 hours with the readings of a Brüel and Kjaer photoacoustic gas monitor BK1302, calibrated with a certified 400 ppm gas mixture.

Conclusion

We have demonstrated that wavelength modulation spectra recorded over a pressure range from 100 to 1000 mbar can be quantitatively analyzed to produce line strengths or trace gas concentrations with an accuracy of about 10%. The analysis requires a knowledge of the pressure, the temperature, and the absorption path length, coupled with a well controlled frequency tuning of the laser in order to provide a reliable frequency axis and frequency modulation amplitude. For absorption lines with known line strength the analysis enables the determination of trace gas concentrations without reference to calibration with certified gas mixtures.

References

1. H. I. Schiff, G. I. Mackay, J. Bechara, "The use of tunable diode laser absorption spectroscopy for atmospheric measurements," *Chemical Analysis Series*, Vol. 127 (Wiley, New York, 1994).
2. P. Werle, "A review of recent advances in semiconductor based gas monitors," *Spectrochimia Acta A*54 197-236 (1998).
3. J. Henningsen, H. Simonsen, "Quantitative wavelength modulation spectroscopy without certified gas mixtures", *Appl. Phys. B* (submitted).
4. L. S. Rothman, C. P. Rinsland, A. Goldman, S. T. Massie, D. P. Edwards, J.-M. Flaud, A. Perrin, C. Camy-Perot, V. Dana, J.-Y. Mandin, J. Schroeder, A. McCann, R. R. Gamache, R. B. Wattson, K. Yoshino, K. V. Chance, K. W. Jucks, L. R. Brown, V. Nemtchinov, P. Varanasi, "The HITRAN molecular spectroscopic database and HAWKS (HITRAN Atmospheric WorK Station): 1996 edition, *J. Quant. Spectrosc. Rad. Transf.* 60 665-710 (1998).

Overview of sensitive detection and multiplexing techniques for tunable diode laser absorption spectroscopy

Michael B. Frish

Physical Sciences Inc., 20 New England Business Center, Andover, MA 01810
(978)689-0003 p.,(978)689-3232 f., frish@psicorp.com

Tunable Diode Laser Absorption Spectroscopy (TDLAS) has become a popular and powerful technique for accurately, reliably, and continuously measuring trace concentrations of selected gases entrained in a gas mixture. Until recently, TDLAS for gas analysis was suitable for laboratory use only, requiring highly trained individuals to operate high-maintenance devices and provide expert interpretation of the outputs. Over the past five years, however, the technology has emerged from the laboratory to become a reliable, robust, and commercially available means for continuously measuring and, in some cases, controlling extremely small concentrations of selected trace gas species. The virtues of TDLAS are several: The probe beam need not physically contact the gas sample of interest, time response can be fast, the technique can be made exquisitely sensitive to very low target gas concentrations, and it offers the potential to accurately measure specific target gases free of cross-species sensitivities to other gases.

TDLAS instruments rely on well-known spectroscopic principles and recently-perfected sensitive detection techniques, coupled with advanced diode lasers and optical fibers developed by the telecommunications industry. The principles are straightforward: Gas molecules absorb energy at specific wavelengths in the electromagnetic spectrum. At wavelengths slightly different than these absorption features there is essentially no absorption. By: (1) transmitting a beam of light through a gas mixture sample containing a (usually trace) quantity of the target gas; and (2) tuning the beam's wavelength to one of the target gas's absorption features; and (3) accurately measuring the absorption of that beam, one can deduce the concentration of target gas molecules integrated over the beam's path length. This measurement is usually expressed in units of ppm-m.

In TDLAS instruments, tunable diode lasers serve as a light source having a well-defined but adjustable wavelength. Herein, we limit the discussion to near-infrared (<2 μ m) TDLs. These single chip solid state lasers are readily be coupled to optical fibers, and offer linewidths of less than 100 MHz, considerably narrower than molecular absorption linewidths which are typically 3 GHz at atmospheric pressure. The lasers are typically packaged with pre-aligned fiber optic couplers, as well as thermoelectric coolers and thermistors that permit the laser temperature to be regulated to better than 10 mK. Accurate control of the laser temperature, combined with accurate control of the electrical current that powers the laser, provides the means for precisely tuning the laser wavelength to a specific molecular absorption feature. Typically, the absorption feature is selected to be free of interfering absorbances from other molecules.

Unlike many other types of spectroscopic gas analyzers, in TDLAS the laser wavelength is not set to stably reside upon the center of a selected gas absorption feature, but instead is rapidly and repeatedly scanned across the feature. While this scanning occurs, the fraction of emitted laser power that is transmitted through the gas mixture is monitored with a photodetector. Measurement of the change in

amplitude of the signal output by the detector as the wavelength sweeps through the absorption feature yields a precise and highly sensitive measure of the target gas concentration integrated along the path transited by the laser beam.

To obtain this precision and sensitivity, it is important to utilize a detection technique that diminishes the effects of laser noise, which is characterized by a 1/f spectrum. Two basic techniques for overcoming laser noise have been developed. They are known as wavelength modulation spectroscopy (WMS) and Balanced Ratiometric Detection (BRD).

In Wavelength Modulation Spectroscopy (WMS) the laser wavelength is continually scanned back and forth across the selected gas absorption line at a frequency, typically 1 MHz or greater, that exceeds the frequencies in which most of the system noise reside. Each time the laser wavelength crosses an absorption line of the gas through which the laser beam is transmitted, the power received by the detector is diminished. Thus, the presence of absorbing gas causes a periodic distortion of the detector signal. The average amplitude of one Fourier component of the distortion is measured using phase-sensitive detection. The averaging is performed for as long or as short a period as required to provide a system response time commensurate with the measured process. The resulting averaged signal is proportional to both the power of the transmitted beam and the path-integrated concentration of the absorbing gas. The average beam power is usually measured separately, and subsequently utilized for normalization. The resulting ratio is proportional only to path-integrated concentration. The proportionality constant is determined by calibration using a known gas concentration standard.

TDLAS systems using WMS typically incorporate a mechanism for stabilizing the laser wavelength, known in the literature as “linelocking”. An additional set of modulations and demodulations is performed to generate an “error” signal that is zero when the laser wavelength sweeps symmetrically around the center of the absorption line, and is non-zero if any asymmetry occurs. A feedback loop adjusts the average laser drive current to remove any asymmetry, thereby eliminating drift of the average laser wavelength in response to external events such as changes in ambient temperature. The spectral drift of a linelocked system can readily be made less than 100 MHz.

In the BRD technique, laser amplitude noise is eliminated by measuring it independently. The output of the laser is split into two paths. One path directs the beam through the gas sample to be analyzed and thence onto the photodetector, while in the second path the beam impinges directly onto another photodetector. Electronic circuitry senses the ratio of the currents generated by the two detectors. Any common mode signals, specifically those originating prior to the beam splitter, are automatically eliminated from the ratio signal. Like WMS, the BRD is typically employed in conjunction with circuitry that scans the laser wavelength across the selected molecular absorption feature, although the scanning may be performed more slowly than in WMS. Any constant broadband extinction, that is, an absorption or scattering of the laser beam that is independent of wavelength across the width of the spectral feature and does not change during the scanning period, results in a constant signal output by the BRD. Any absorption by the target gas appears as a signal superimposed on the background.

To obtain a gas concentration measurement using a BRD-based system, the output of the BRD is digitized and recorded as the laser wavelength is scanned. The wavelength scan is wide enough to assume that there is no significant molecular absorption by the target gas near the beginning and end of the scan. The signals measured in these so-called “wings” therefore represent the constant “baseline” due to broadband absorption or equivalent effects. This baseline value is subtracted from all points in the scan. The subtraction may be performed electronically, via a high-pass filter, or numerically after

digitization. The residual provides an accurate and detailed representation of the complete spectral feature shape. Target gas concentrations are deduced by numerical analyses of the spectral feature shapes.

Many TDLAS practitioners have adopted an architecture that capitalizes upon the flexibility offered by optical fibers. The architecture separates the instrument into two distinct yet interconnected components, which are called the System Console and the Measurement Path. The laser beam originates within the System Console. The beam is brought via optical fiber to the Measurement Path. At the beginning of the Measurement Path, the laser beam exits the fiber and is transmitted into the sample gas. At the opposite end of the Measurement Path, the laser beam impinges upon the photodetector which converts it, and the information it carries, into an electrical signal that is returned to the System Console via electrical cable. At the System Console, the signal is processed and the path-integrated target gas concentration is reported.

The fiber optic architecture enables the construction of highly-multiplexed systems, wherein several lasers are coupled together to sense several gas species in each of many measurement paths. Beams from several lasers, one for each target gas species, are initially combined onto a single fiber. The single fiber is subsequently split into multiple fibers, each of which serves a Measurement Path. (If BRD is utilized, the comparison beam is also split among the Measurement Paths.) Thus, each Measurement Path receives light from each laser. The output of the detector is de-multiplexed, and in WMS demodulated, to deduce the concentrations of each target gas. The multiplexing and de-multiplexing techniques are the same as those used in telecommunications including time, frequency, and wavelength division multiplexing.

In time multiplexing, timing circuitry activates the lasers sequentially. This technique has been successfully implemented in a 3-species BRD-based systems as follows: Laser 1 is turned on, and held at a wavelength corresponding to the beginning of its scan for nominally 1 ms. During the next 2 ms, the wavelength is scanned to the other end of its range, and then the laser is shut off. The output during the scanning period is a waveform representative of the target gas absorption feature, with an amplitude representative of the gas concentration. Starting 0.3 ms later, Laser 2 follows the same sequence, followed by Laser 3. Thus, every 10 ms, all three lasers are scanned in sequence.

Time multiplexing has also been successfully applied to WMS. However, WMS more naturally lends itself to frequency multiplexing techniques. Frequency multiplexing is the process of transmitting concurrently several signals of different frequencies to a single receiver, and then separating the signals at the receiver to analyze one at a time, or to utilize several receivers to analyze several signals concurrently. It is the essence of virtually all broadcast telecommunications systems. Though frequency multiplexed TDLAS is complicated by the need to pay careful attention to cross-channel interference, it is starting to be utilized in practical TDLAS systems.

Both BRD and WMS can, in principle, take advantage of Wavelength Division Multiplexing (WDM) technologies being developed by the telecommunications industry. WDM is simply the concept of combining several laser wavelengths into a single fiber, as described previously, transmitting them through the Measurement Path, and then separating the wavelengths back into separate beams each of which impinges on its own detector and signal analyzer. This technique has not yet found much application in TDLAS because the wavelengths of interest in a multiplexed system may have very irregular spacings. The design of a widely applicable WDM receiver for TDLAS may prove to be impractical.

Low-cost, single-frequency sources for spectroscopy using conventional Fabry-Perot diode lasers

Gary L. Duerksen, Dept. of Elec. Eng., Univ. of Maryland, College Park, MD 20742
Michael A. Krainak, Code 554, NASA/Goddard Space Flight Center, Greenbelt, MD 20771

The wide bandwidth characteristic of the gain media of diode lasers makes them good sources for spectroscopy. In order to achieve the required spectral purity, however, either a DFB or DBR device must be fabricated, which incurs significant development costs for every target wavelength. Conversely, conventional Fabry-Perot diode lasers can be fabricated relatively cheaply, and their design does not preclude operation at any wavelength within the gain bandwidth. Unfortunately, their laser oscillations do not stabilize at one single-frequency, hopping chaotically between modes instead. This instability has been circumvented previously by two methods that employ a grating in an extended cavity configuration^{1,2}. Here we demonstrate stable, CW, single-frequency operation from a non-AR coated Fabry-Perot laser diodes using only fiber-Bragg-grating (FBG) optical feedback.

The basis for this frequency-stabilization experiment lies in the nature of the light reflected from a fiber Bragg grating. In the standard coupled-mode formalism³, the reflection spectrum of a FBG is derived from two counter-propagating modes, which are constrained by the structure of the two coupled differential equations to take the following form (in the notation of Erdogan⁴):

$$\begin{aligned} R(z) &\equiv A(z) \exp i(\delta z - \phi / 2) \\ S(z) &\equiv B(z) \exp -i(\delta z - \phi / 2) \end{aligned} \quad (1)$$

where $\phi/2$ is the phase of the incident beam at $z = 0$, the middle of the FBG. When light is reflected from a mirror, the phase of the reflected light is always π out-of-phase with respect to the incident light. However, the phase of light reflected from a FBG, is given by the ratio R/S at $z = -L/2$, $\rho \exp -i(\delta L - \phi)$, where L is the length of the grating:

$$\rho = \frac{-\kappa \sinh(\sqrt{\kappa^2 - \hat{\sigma}^2} L)}{\hat{\sigma} \sinh(\sqrt{\kappa^2 - \hat{\sigma}^2} L) + i\sqrt{\kappa^2 - \hat{\sigma}^2} \cosh(\sqrt{\kappa^2 - \hat{\sigma}^2} L)} \quad (2)$$

Moving the source of the incident light induces a shift in the incident phase, $\phi \rightarrow \phi + \Delta\phi$, under which the phase of the two modes transforms as:

$$\begin{aligned} R(z) &\rightarrow \exp(-i\Delta\phi / 2) R(z) \\ S(z) &\rightarrow \exp(i\Delta\phi / 2) S(z) \end{aligned} \Rightarrow \rho \rightarrow \exp(-i\Delta\phi) \rho \quad (3)$$

In other words, the spatial variation of the phase of the reflected beam is conjugate to that of the incident beam (modulo the phase of $B(-L/2)$, which depends only on wavelength). This property can be reconciled conceptually by regarding the phenomenon as one-dimensional four wave mixing where the hologram has been written permanently during an earlier exposure.

At the short-wavelength band edge ($\delta = +\kappa$) the phase of ρ is zero (κ is real for single-mode fiber), so that light reflected at this wavelength will interfere constructively at its source, regardless of the (1-dimensional) location of the source. If a diode laser is temperature or current tuned so that the wavelength of the an axial mode coincides precisely with the short-wavelength band edge of a FBG, the reflected light will seed the laser with feedback that constructively reinforces only that axial mode, phase-locking the laser oscillations.

We coupled a nominally 935 nm Fabry-Perot laser diode (Sensors Unlimited) into an angle-cleaved, ultra narrow-band (18 pm), 16% reflectivity FBG (Kromafibre, Inc.) with a reflection peak at 935.625 nm using the configuration depicted in Fig. 1. The laser temperature was controlled by an analog TEC with 1 mK resolution (Wavelength Electronics HTC 3000). The emission at the laser facet was imaged 1:64 onto a beam profiler (BeamScan), and the spectrum

characterized using an OSA (HP 7000A), a wavemeter (Burleigh WA-1500), and a scanning Fabry-Perot étalon (Burleigh). The optical-heterodyne measurement of the single-frequency linewidth used a Si-PIN detector (ThorLabs DET 210) and an RF spectrum analyzer (HP 8590A).

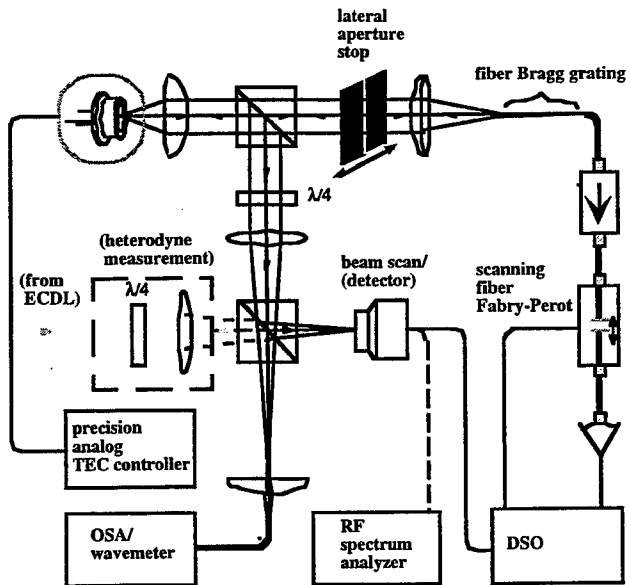


FIG. 1. Experimental setup including linewidth measurement (dashed lines)

For best coupling into single-mode fiber, the astigmatic laser beam was collimated on the fast axis, placing the virtual beam waist of the slow axis 5 μm behind the facet. To accommodate the resulting mode mismatch with the anastigmatic feedback signal, we used a variable aperture stop on the slow (lateral) axis of the collimated beam. This displaced the lateral focus of the feedback signal⁵ to coincide with that of the laser for a slit width of 1.45 mm.

We tuned the laser wavelength, subject to feedback from the FBG, by varying its temperature (Fig. 2A). The spectral purity of the laser, measured by side-mode suppression ratio, tracks the reflectance curve of the FBG, offset about -3 pm to the band edge of the grating (Fig. 2B):

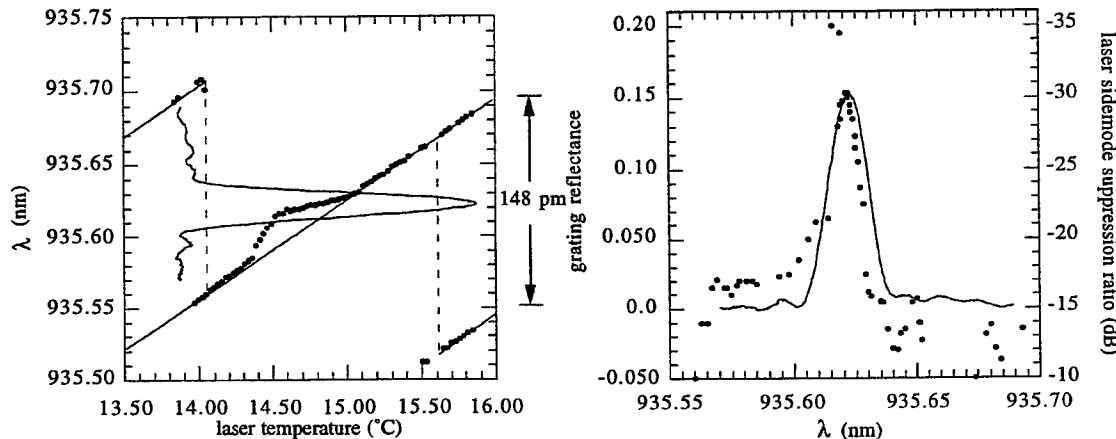


FIG 2A. Laser output vs. T overlaid on reflectance spectrum of FBG

FIG. 2B. Laser spectral purity overlaid on reflectance spectrum of FBG

Detailed examination of the laser output reveals the spectra in figure 3: Off the band edge, the spectrum is broad; Slightly off the band edge (the points at the top of fig 2B), the spectrum

comprises several phase-stabilized submodes that span about 7 GHz--the approximate bandwidth of the FBG; True single-frequency operation results precisely on the band edge.

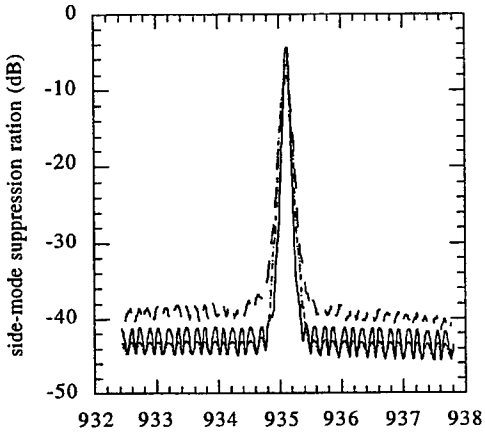


FIG 3A. OSA spectra of off-band-edge, near-band-edge, and on-band-edge tuned laser

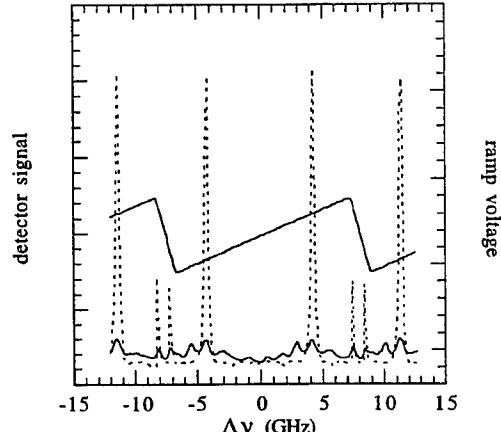


FIG 3B. Scanning Fabry-Perot spectrum of single-frequency (dotted line) and phase-stabilized spectrum

We characterized the linewidth of the laser by mixing the laser output at 935.625 nm with the output from an ECDL⁶ tuned to 935.624 nm and measuring the RF spectrum of the power beat note at the detector. The instantaneous (20 ms) linewidth was about 225 kHz and the time-averaged (2 s) linewidth was about 470 MHz (Fig. 4).

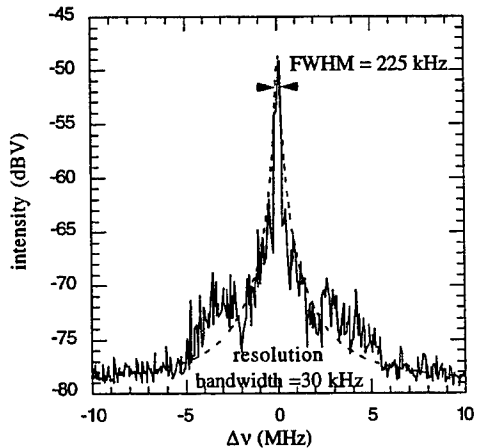


FIG 4A. Instantaneous (20 ms) RF spectrum

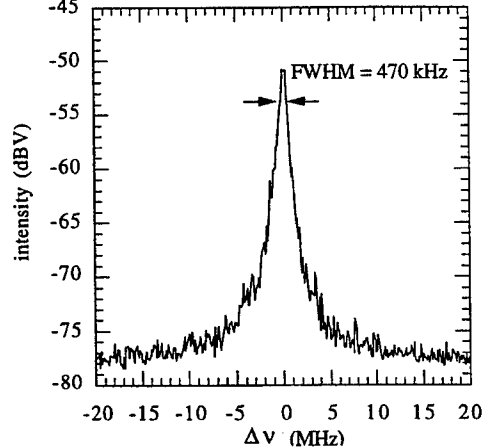


FIG 4B. Time averaged (2 s) RF spectrum

The P-I characteristic curve (not shown) reveals that single-frequency operation lowers the lasing threshold by 15% and increases the slope efficiency by 5%.

This experiment also was repeated using 0.1 nm FBG's with an SDL 5431 high-power laser at 825 nm and an SDL 7311 buried heterostructure laser at 666 nm. Stable single-frequency operation was achieved for both lasers: In the first case, the slope efficiency was doubled, while the second case did not require a lateral aperture for stop single-frequency operation (-50 dB side-mode suppression). We infer from this result that rigidly confining the gain region within the confines of the waveguide sufficiently reduces spatial variation of the gain profile to nearly eliminate astigmatism and the associated mode-mismatch phase ambiguity.

1. D. M. Bird, J. R. Armitage, R. Kashyap, R. M. A. Fatah, K. H. Cameron, Electron. Lett. **27**, 1115 (1991).
2. S. N. Atutov, E. Moriotti, M. Meucci, P. Bicchi, C. Marinelli, L. Moi, Opt. Comm. **107**, 83-87 (1994).
3. A. Yariv, IEEE J. Quantum Electron. **QE-9**, 919 (1973).
4. T. Erdogan, J. Lightwave Tech. **15**, 1277 (1997).
5. C. J. R. Sheppard, P. Török, Opt. Lett. **23**, 1803 (1998)
6. G. W. Switzer, J. L. Carlsten, submitted to App. Opt.

Diode-Laser
Spectroscopy: 2

An Overview of External-Cavity Diode Lasers for use in Spectroscopy and WDM applications

Robert Shine, Jr.

New Focus, 2630 Walsh Ave., Santa Clara, CA 95051

bshine@newfocus.com

Lasers that exhibit wide and continuous wavelength tunability are desirable for use in applications such as high-resolution spectroscopy, WDM telecommunications network development, and environmental monitoring. A diode laser itself can be tuned over its large gain spectrum by adjusting its operating temperature. However, because of the semiconductor laser's broad gain spectrum, more than one mode will often operate simultaneously, resulting in multiple output wavelengths and a broad spectral linewidth. By placing the diode laser in an external cavity, the system can be forced to operate in a single-mode. With careful design, the external-cavity diode laser (ECDL) will also tune continuously over a wide wavelength range. The ease-of-use, continuous tunability and wide choice of wavelengths have allowed ECDLs to move from research to industrial applications in a very short time.

External-cavity tunable diode laser design principles are similar to those used for dye lasers, so the ideas developed to achieve wide tunability in dye laser systems can be applied directly to ECDLs. The most common cavity configuration for an ECDL is the Littman-Metcalf design, as shown in Figure 1 [1]. For optimum performance in this cavity, the laser diode cavity (chip) modes must be suppressed with a very good anti-reflection (AR) coating. An example of the diode laser output before and after AR coating is shown in Figure 2. With the diode laser providing a wide gain spectrum, the operating wavelength is selected by the external cavity, consisting of a collimating lens, diffraction grating and a mirror. The double-pass scheme coupled with grazing incidence on the grating results in a very narrow spectral pass band and therefore excellent wavelength selectivity. Tuning is achieved by adjusting the angle of the mirror, which selects a unique diffracted wavelength. Continuous tuning is only obtained if the same cavity mode remains under the diffraction grating pass band as the mirror is rotated. This can be achieved by carefully selecting the pivot point about which the mirror rotates [2]. The reflected zero-order beam from the diffraction grating is the output beam.

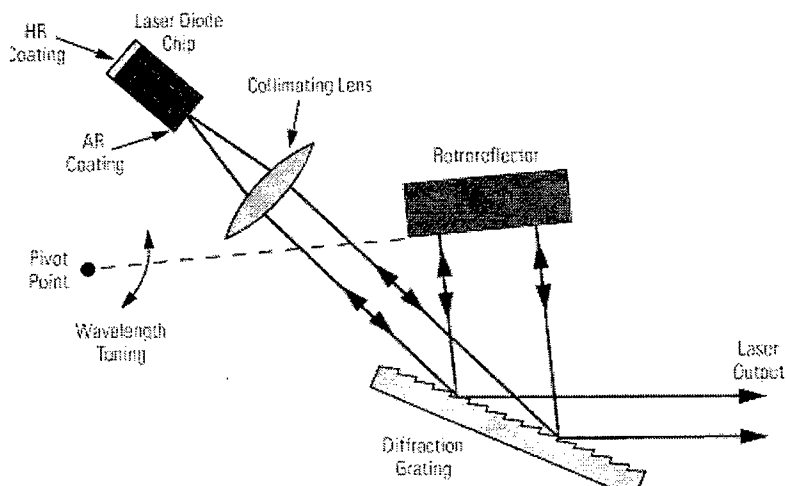


Figure 1. Schematic of the Littman-Metcalf cavity

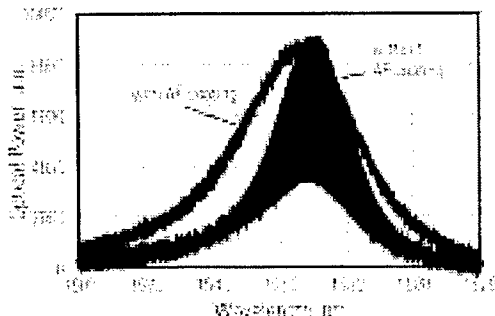


Figure 2: Diode laser fluorescence output before and after AR coating. Note the large modulation due to the cavity (chip) modes without the AR coating.

Since the ECDL design is based on well-developed, commercially-available Fabry-Perot diode lasers, ECDL manufacturers can offer products in a wide range of wavelengths. Currently available wavelengths span the range from 630 nm to beyond 1630 nm, which covers many important wavelengths for atom trapping, spectroscopy, telecommunications and metrology. New wavelengths can also be added very quickly following the advances in semiconductor design and fabrication. New Focus has worked with the Sarnoff Corporation to develop ECDLs in the 2 μ m range and beyond. Researchers at Sarnoff designed and fabricated a new strained-layer InGaAs/InP quantum-well ridge-waveguide semiconductor laser. Tensile strain was added in the barrier region to extend the operating wavelength to 2 μ m. This diode laser was then AR-coated and placed in an external cavity. This laser tunes continuously from 1960 nm to 2040 nm as shown in Figure 3. Current work is underway to extend this wavelength range to 2.3 μ m and beyond using antimonide-based semiconductor lasers. The 2.0, 2.3 and 2.7 μ m ranges are especially interesting for spectroscopy of molecular species such as CO₂, H₂O, N₂O, and NH₃ for combustion diagnostics and environmental monitoring, and for HBr for in-situ gas phase substrate etching for the semiconductor industry.

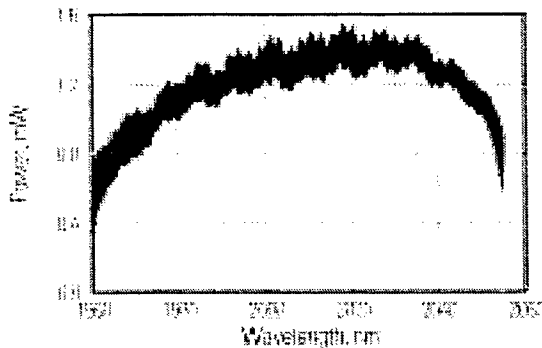


Figure 3: Tuning curve of an ECDL operating in the 2 μ m range.

On the other end of the spectrum, Nichia Corporation in Japan has taken the lead in developing blue and violet diode lasers and have recently announced lifetimes of 10,000 hours under cw operation at room temperature. This level of performance is adequate for many commercial applications, and once these diode lasers are commercially available, a blue ECDL is sure to follow. While the significant driver for diode lasers at this wavelength is the CD market for increased storage density, the 400 nm region is very interesting spectroscopically. The shorter wavelength can also improve the resolution in metrology applications.

The voracious appetite for bandwidth created by the Internet has driven the development of ECDLs in the 1550 nm region for test and measurement of WDM systems. Applications range from simulating channels in the design of a WDM system to characterizing components such as filters, splitters and MUX/DEMUXs. As the channel spacing of WDM systems has moved from 200 GHz to 50 GHz or even narrower, the truly continuous tunability and the accurate wavelength control of ECDL have become critical in testing components. With the explosive growth in the number of narrow-band components to test, new measurement techniques are also being investigated. While very accurate wavelength characterization can be obtained by the "step & measure" technique, this method can be extremely time consuming. A new technique using an extremely linear wavelength scan can obtain the spectra in a second. By using a known wavelength marker and the extremely linear wavelength scan of the laser, narrow-band components can be characterized in a single scan.

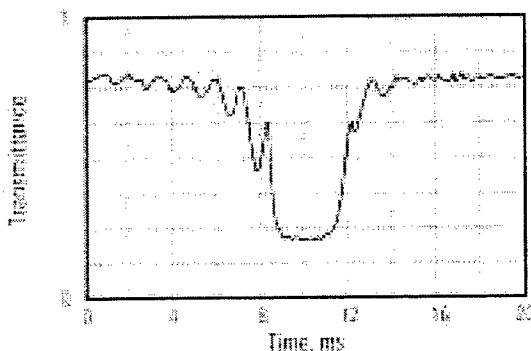


Figure 4: Transmission of a fiber Bragg grating measured with a single scan of a linearly swept ECDL.

As ECDL technology enters industrial and manufacturing environments such as those mentioned for testing WDM components, the additional requirement of reliability is added to the technical performance specifications. The ECDL has now been through as much as four product generations and can meet the reliability specifications of the most demanding customers. The current generation of New Focus ECDLs is designed to meet stringent shock, vibration, temperature and humidity specifications.

While the ECDL technology has only been available at a variety of wavelengths for about 5 years, it has very rapidly gained acceptance as a tool in spectroscopy and telecommunications applications. A key to this success has been the availability of highly-reliable Fabry-Perot semiconductor diode lasers at a wide variety of wavelengths, with recent advances extending the range both into the 2 μ m range and in the blue-violet region. Product reliability improvements allow the ECDL to penetrate into manufacturing environments with tremendous growth in WDM component testing. While the majority of current applications for the ECDL are in telecommunications and spectroscopy, tunability in an easy-to-use package will enable many other applications in the near future.

References:

- [1] M. Littman and H. Metcalf, *Appl. Opt.* 17, 2224 (1978).
- [2] New Focus Patent #5,319,668.
- [3] G.S. Feller, I-f Wu, T. Day, R.J. Menna, R.U. Martinelli, and J.C. Connolly, *Laser Applications to Chemical and Environmental Analysis* (March 9-11, 1998), paper LTuA6.

Diode lasers, DFG and Molecules

D. G. Lancaster, D. Richter, R.F. Curl, F.K. Tittel

*Rice Quantum Institute
Rice University, Houston, TX 77251-1892
phone: (713) 527 4833, fax: (713) 524 5237
davelanc@rice.edu, fkt@rice.edu*

Abstract: The development and characteristics of compact diode laser pumped mid-infrared difference frequency gas sensors are reported. One such tunable cw sensor operates in the 3.3 to 4.4 μm spectral region and uses a diode-seeded fiber amplifier. Results show that fiber coupled sensors are capable of real-time, highly selective and sensitive measurements of numerous trace gas species in ambient air, presently CH_4 , H_2CO , HCl , CO_2 , N_2O , and H_2O

OCIS codes: 280.3420, 300.6340, 190.2620, 060.2320

Introduction

Significant developments in tunable diode laser technology and nonlinear optical materials have led to the demonstration of compact optical gas sensors operating in the 3-5 μm spectral region based on difference frequency generation (DFG). The characteristics of these sensors have been shown to be suitable for the sensitive, selective and real-time detection of numerous molecules with rovibrational spectra in the mid-infrared fingerprint region. Since CW DFG was first demonstrated using two low power single longitudinal mode laser diodes [1] (generating several nW), improvements in diode laser pump sources and nonlinear optical materials (eg. periodically poled LiNbO_3 , PPLN) has increased the DFG power to tens of μW 's, thereby yielding minimum detectable absorbances of $< 10^{-4}$ (or ppb concentrations) with the use of low noise thermo-electrically cooled infrared detectors (NEP $\sim \text{pW}(\text{Hz})^{-1/2}$). Suitable DFG pump sources include distributed feedback (DFB) and distributed Bragg reflector (DBR) diode lasers, extended cavity diode lasers (ECDLs), semiconductor master oscillator power amplifiers (MOPAs), diode-pumped non-planar ring Nd: YAG lasers and more recently, diode laser seeded rare earth doped fiber amplifiers.

Portable and tunable DFG sensors have been demonstrated to be suitable for real-time trace gas sensing [2]. A sensor based on discrete optics (measuring 30x30x60 cm^3), generated mid-infrared radiation near 3.5 μm by difference frequency mixing a 100 mW Fabry-Perot laser and Nd: YAG laser. Such a sensor measured ppb levels of CO and H_2CO gas over a period of several weeks in a human rated simulation chamber located at NASA-Johnson Space Center for ground verification measurements for the life support system of the international space station program [3].

In recent DFG work, the emphasis has been on improved sensor robustness against vibrations and temperature drifts by using optical fiber for beam delivery, combining and amplification. Furthermore, attention has been paid to using diode laser pump sources that are fiber coupled ('pigtailed'), or can be fiber coupled. Fiber pump delivery also facilitates the efficient use of the wide gain bandwidth commercially available ytterbium and erbium doped fiber amplifiers. Diode laser

pump sources we have used include telecom DFB diode lasers near $1.55\text{ }\mu\text{m}$ (telecom ITU grid), DBR diodes available near $1\text{ }\mu\text{m}$, α -DFB high power $1.064\text{ }\mu\text{m}$ diode lasers, and broadly tunable ECDLs. These diode lasers have characteristics that are desirable for high-resolution spectroscopy for field gas concentration measurements. Characteristics include inherent frequency stability, narrow linewidth, direct current modulation, and cw single frequency pump powers from 2-500 mW.

Sensor configuration

A portable DFG sensor that is continuously tunable from 3.25 - $4.40\text{ }\mu\text{m}$ is shown schematically in Fig 1. This device uses as pump sources an ECDL ($P=20\text{ mW}$, $\lambda=814$ to 870 nm) and a distributed Bragg reflector (DBR, $P=50\text{ mW}$, $\lambda=1083\text{ nm}$) diode laser seeded Ytterbium doped fiber amplifier pumped by a 975 nm , $P=2\text{ W}$ diode laser [4,5]. The fiber amplifier boosts the seed pump power of 10 mW at 1083 nm to 540 mW . Both lasers are coupled into a single mode fiber and combined by a wavelength division multiplexer (WDM). The linear polarization output from the fiber for a $e+e\rightarrow e$ nonlinear mixing process in the PPLN crystal is maintained by using two polarization controllers in the fiber delivery system. Coarse tuning is achieved by rotation of the feedback mirror in the Littman style ECDL. Fine tuning and scanning of single or multi-component absorption lines of up to $\sim 25\text{ GHz}$ is accomplished by current modulation of the DBR diode laser ($\sim 50\text{ Hz}$). The sensor, including driver electronics, optics and an 18 m multi-pass cell, was mounted on a breadboard ($45 \times 45 \times 12\text{ cm}^3$).

An achromat lens ($f=10\text{ mm}$; 0.25 NA) was used for imaging the fiber output (terminated with a FC-APC connector) into the PPLN crystal. A 19 mm long, 0.5 mm thick PPLN crystal with a broadband AR-coating applied to both end faces contained 8 quasi-phasmatching channels (0.5 mm wide) from 22.4 - $23.1\text{ }\mu\text{m}$ in $0.1\text{ }\mu\text{m}$ increments. In fig. 2 the mid-infrared power (DFG idler) as a function of wavelength is shown (right axis) with up to $\sim 3\text{ }\mu\text{W}$ generated. The conversion efficiency is also plotted in fig. 2 (left axis) with a peak efficiency of 0.82 mW/W^2 ($0.08\%/\text{W}$) at a wavelength of $3.5\text{ }\mu\text{m}$. This value compares reasonably with a theoretically predicted DFG conversion efficiency of 1.4 mW/W^2 .

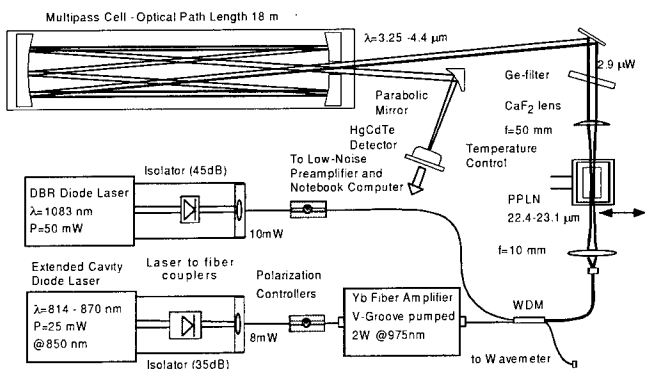


Fig. 1: Optical setup of a fiber coupled widely tunable DFG spectrometer.

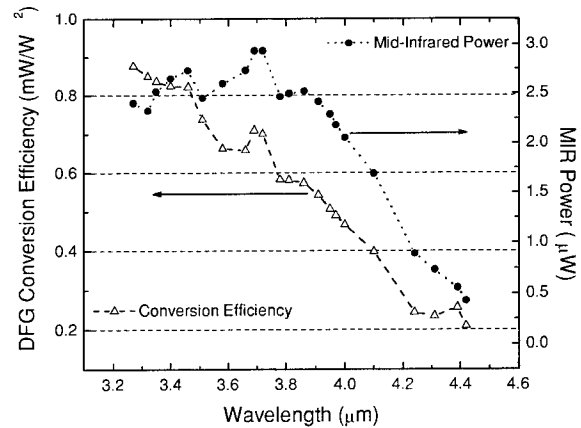


Fig. 3: DFG conversion efficiency and DFG power as a function of mid-IR wavelength

Spectroscopic performance

Shown in Fig. 3 is a Doppler broadened spectrum obtained from a 1 torr CH_4 sample (Doppler FWHM=270 MHz) in a 3 cm cell (20 averages over 0.2 s). The measured Gaussian absorption linewidth indicates a DFG linewidth of 42 ± 5 MHz (assuming a Gaussian DFG lineshape).

To characterize the detection sensitivity, prepared low concentration calibration mixtures of gases could be drawn through the multi-pass spectroscopic cell at reduced pressures (90-100 torr). For instance, using a 860 ± 43 ppb mixture of H_2CO in air (Scott Specialty gases) a concentration of 887 ± 19 ppb was measured (1 measurement every minute for 40 minutes, $\lambda=3.53 \mu\text{m}$). Using a 1773 ± 1 ppb CH_4 in air mixture a concentration of 1830 ± 15 ppb was measured, which is within 3.1 % of the calibrated concentration (1 measurement every 8.7 s for 19 minutes, $\lambda=3.29 \mu\text{m}$). These measurements

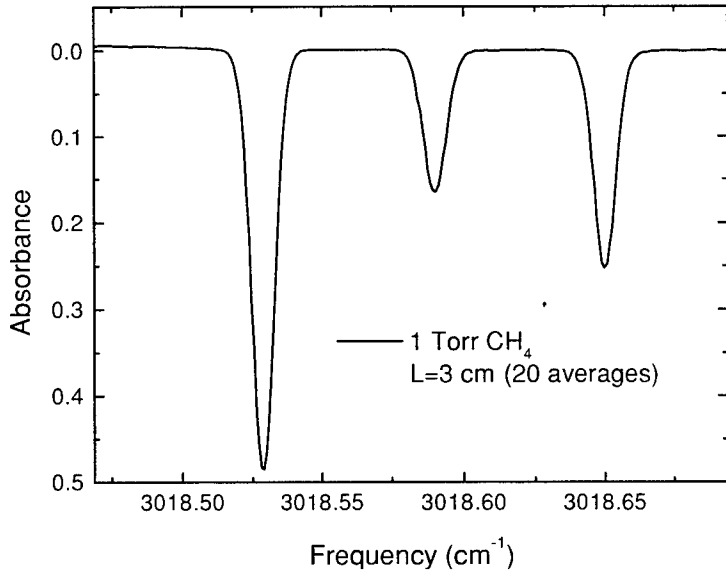


Fig.3: . Doppler broadened Q-branch CH_4 spectrum near $3.3 \mu\text{m}$.

agree closely with the calibrated gas mixture concentrations if the ± 2 % uncertainty in the path length of the multi-pass gas cell is taken into account. Absorption cross sections used were from Ref [6] and Hitran96 respectively. Fig. 4 shows the detected methane concentration and the generated mid-IR power as a function of time. The ambient concentration was measured at ~ 2 ppm, with higher concentration spikes which are attributed to the intermittent operation of the central air-conditioning. This long-term experiment shows reliable operation of the fiber coupled spectroscopic source of both the generated mid-IR power as well as the inherent frequency stability for a time interval of 18 hours. In similar fashion, CO_2 ($4.2 \mu\text{m}$), N_2O ($3.9 \mu\text{m}$), NO_2 ($3.5 \mu\text{m}$), H_2CO ($3.5 \mu\text{m}$) and HCl ($3.5 \mu\text{m}$) have also been investigated.

In recent experiments using a new DFG sensor architecture, we have addressed the issues of increased power and sensitivity. The sensor, which is based on difference frequency mixing seeded $1\mu\text{m}$ Yb and $1.5 \mu\text{m}$ Er/ Yb fiber amplifiers in PPLN, has produced up to 0.7 mW [7]. Furthermore we have demonstrated the use of a dual beam detection configuration which allows optical noise to be

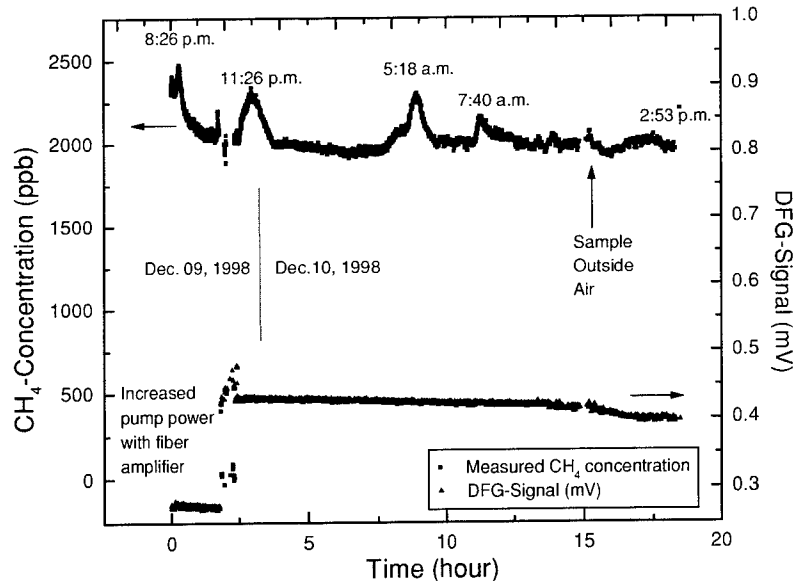


Fig.5: Long-term sampling of laboratory and outside air (upper trace) and mid-IR power for a 18 hour time interval

cancelled out by use of a reference beam, which is obtained by a beam splitter placed in front of the multi-pass cell, and directed to a second detector. Using this technique we have demonstrated an increased optical sensitivity of $\pm 2.8 \times 10^{-5}$ ($L = 100$ m in a multi-pass cell) which implies, for instance, sub-ppb level CH_4 detection.

In conclusion, robust, compact and widely tunable fiber coupled diode laser pumped mid – IR sensors suitable for the real-time detection of various trace gases have been reported. The same sensor DFG architecture is also suitable for difference-frequency generation of longer IR wavelengths (> 5 μm) using quasi-phase matched GaAs with a transparency range from $2 \mu\text{m}$ to $16 \mu\text{m}$ [8].

References:

1. U. Simon, C. E. Miller, C. C. Bradley, R. G. Hulet, R. F. Curl, and F. K. Tittel, "Difference frequency generation in AgGaS_2 using single-mode diode laser pump sources", Opt. Lett. **18**, 1062-1064 (1993)
2. T. Töpfer, K.P. Petrov, Y. Mine, D. Jundt, R.F. Curl, F.K. Tittel, "Room temperature mid-infrared laser sensor for trace gas detection", Appl. Opt. **36**, 8042-8049 (1997)
3. D.G. Lancaster, D. Richter, R.F. Curl, F.K. Tittel, "Real-time measurements of trace gases using a compact difference-frequency-based sensor at $3.5 \mu\text{m}$ ", Appl. Phys B **67**, 339-345 (1998)
4. L. Goldberg, J. Koplow, Dahv A. V. Kliner, "Compact 1-W Yb-doped double-cladding fiber amplifier using v-groove side pumping", IEEE Phot. Tech. Lett. **10**, 6, 793 (1998)
5. D. G. Lancaster, D. Richter, F.K. Tittel, "Portable fiber coupled diode laser based sensor for multiple trace gas detection, Appl. Phys. B (accepted June 1999)
6. A. Fried, B. Henry, B. Wert, S. Sewell, J.R. Drummond, "Laboratory, ground-based, and airborne tunable diode laser systems: performance characteristics and applications in atmospheric studies", App. Phys. B, **67**, 317-330 (1998)
7. D. G. Lancaster, D. Richter, R.F. Curl, F.K. Tittel, L. Goldberg, J. Koplow, submitted to Opt. Lett. (July, 99)
8. D.Zheng, L.A. Gordon, Y.S. Wu, R.S. Feigelson, M.M. Fejer, R.L. Byer, "16- μm infrared generation by difference-frequency mixing in diffusion-bonded-stacked GaAs", Optics Letters **23**, 1010-1012 (1998)

Open air detection of CO₂, CO, and H₂S with a DFB laser at 1.57 μ m

Jes Henningsen and Harald Simonsen

Danish Institute of Fundamental Metrology, Bld.307, Anker Engelunds Vej 1, DK-2800 Lyngby, Denmark
jh@dfm.dtu.dk, hs@dfm.dtu.dk

The use of DFB lasers oscillating around 1.57 μ m for the detection of molecules having overtone or combination bands in this region has been the subject of numerous publications over the last 10 years. However, in almost all cases the schemes applied have relied on flowing samples of the gas to be analysed through multipass absorption cells of the White or Herriot type. The absorption is determined by normalising the transmitted signal with respect to the signal admitted to the cell, since in the absence of absorption the ratio between these signals is in principle constant. When monitoring over a long path in open air, the radiation travels one or several double passes between a launching module and a retroreflector. One problem is associated with the lack of control over the signal returning to the detector after the travel in open air. The return signal is influenced by turbulence and scattering, and it is strongly affected by lack of stability of the retroreflector relative to the launching module. A second problem is that it is not possible to remove the target molecules from the measuring volume by evacuation, and therefore the determination of a zero reference becomes troublesome.

We here describe an open air monitor capable of the simultaneous detection of CO₂, CO, and H₂S. The monitor uses wavelength modulation spectroscopy (WMS) where the laser frequency is modulated in the kHz range and the response is detected at the second harmonic. We give a realistic assessment of the detection limit and conclude that for practical monitors WMS is not inferior to other detection schemes such as frequency modulation spectroscopy (FMS), where the modulation frequency is chosen in the MHz range, and two-tone frequency modulation spectroscopy (TTFMS) where modulation frequencies in the GHz range and the MHz range are applied simultaneously [1].

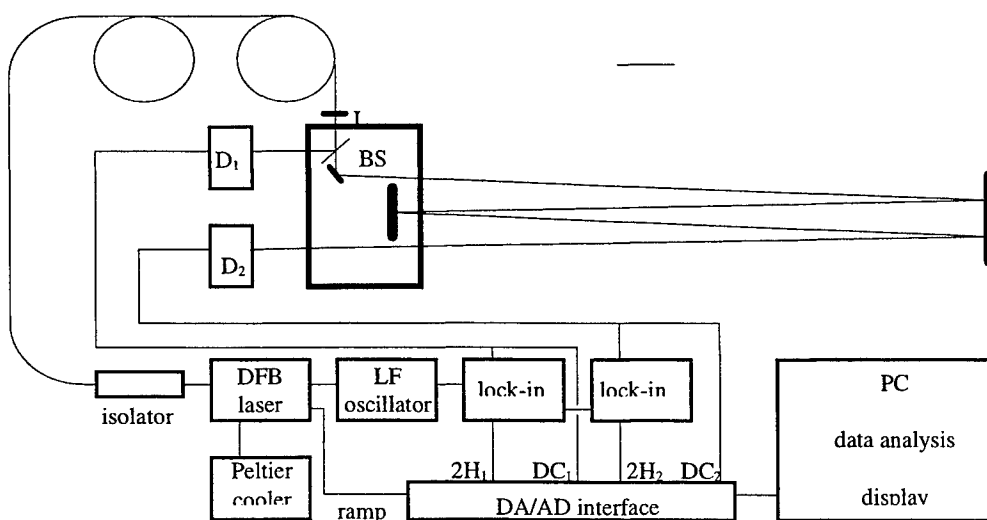


Fig.1 Schematic diagram of open path DFB laser monitor.

A schematic diagram of the monitor is shown in Fig.1. Radiation at 1572.9 nm from a DFB laser (Sensors Unlimited) is conducted through 50 m of single mode optical fiber to the launching unit, and after leaving the fiber the radiation is collimated by an AR coated lens with 75 mm focal length (L). It next passes through a pellicle beam splitter (BS) which diverts about 10% to the reference detector D_1 , and then performs a number of passes between two flat mirrors before arriving at the signal detector D_2 . The base length of the absorption path is 8 m, and with mirror dimensions of $100 \times 75 \text{ mm}^2$ and $75 \times 50 \text{ mm}^2$ for the far and near mirror respectively, a total path length of 16, 32, 48 or 64 m can be achieved by simply rotating the 45° launching mirror in a horizontal plane. The detectors are $5 \times 5 \text{ mm}^2$ Ge photodiodes, and preamplifiers are integrated in the detector mounts. The laser current is ramped to provide a linear frequency scan of 30 GHz, and at the same time modulated at 313 Hz with a modulation index large enough to optimize the signal to noise ratio. The detector signals are sent to two identical lock-in amplifiers (Stanford Research SR530) and the second harmonic signals as well as the input signals to the lock-ins are digitized with an AD/DA card (Data Translation DT2802).

A single scan consists of 200 steps. For each step, the two 2. harmonic signals are normalized with respect to the DC signals, and the normalized reference signal is subtracted from the normalized transmitted signal. The integration time of the lock-ins is set at 10 ms, and a delay is introduced so that the total time consumption amounts to about 15 ms per step, leading to 3 s per scan. The final signal is taken as a running average over 10 scans, leading to an effective time resolution of about 30 s. The progression in the data analysis is shown in Fig.2, where we show from top to bottom the 2. harmonic signals recorded by the signal detector and the reference detector, the single-scan result of normalization and subtraction, and the 10-scan average. When performing the normalization it must be taken into account that the 313 Hz current modulation leads to a substantial amplitude modulation in addition to the frequency modulation. Normalizing with respect to the instantaneous value of the DC signals would lead to disaster since these signals contain the effect of the amplitude modulation sampled at times which are random with respect to

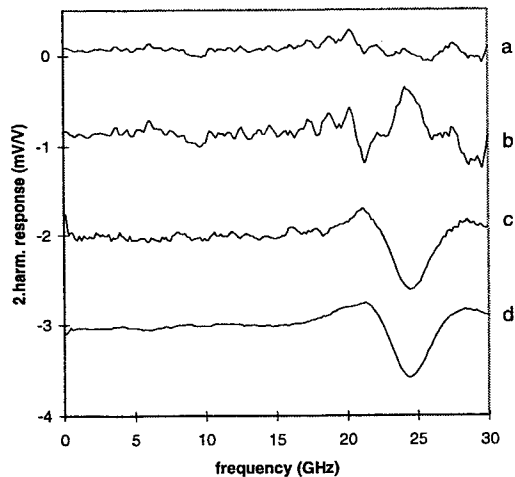


Fig.2 2. harmonic from signal detector D_2 (a) and reference detector D_1 (b), single scan after normalization and subtraction (c), and 10-scan average (d). The line is R12 in CO_2 at 1572.992 nm

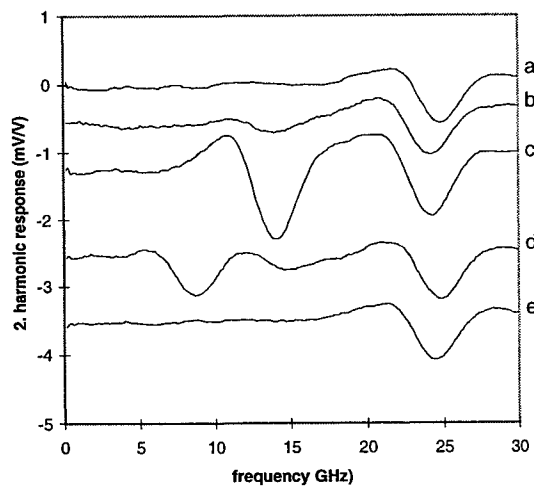


Fig.3 Lab air including about 500 ppm of CO_2 (a), lab air + simulated content of 18 ppm H_2S (b), lab air + simulated 150 ppm of H_2S (c), lab air + simulated 18 ppm of H_2S + 800 ppm of CO (d) and lab air (e). The scan range is as in Fig.2

the modulation cycle. We suppress this effect by normalizing with respect to a sliding average over 20 steps. The normalization routine ensures that the resulting spectrum becomes insensitive to variations in the return signal on a time scale longer than 0.3 s. The subtraction routine eliminates spectral features which might be present in the laser signal when it arrives at the beam splitter, i.e. features which originate in the laser itself, or from imperfect fiber connectors, fiber splitters, etc.

Scans corresponding to different gas compositions are seen in Fig.3. The laser can be temperature tuned over the range 1571 – 1575 nm, and if the 30 GHz current tuning window is centered at 1572.9 nm, it is possible to cover the R12 line of the $2v_1+2v_2+v_3$ band of CO₂ at 1572.992 nm (at \approx 25 GHz), the R1 line of the 3v overtone band of CO at 1572.868 nm (at \approx 9 GHz), and a strong absorption at 1572.912 nm which is the combined absorption in H₂S of the transitions 818 \leftarrow 717 and 808 \leftarrow 707 of the $v_1+v_2+v_3$ band (at \approx 15 GHz). Since the poisonous gases CO and H₂S cannot be released in the laboratory, the different concentration levels are simulated by 15 cm sealed cells of 25 mm clearance, each filled with a mixture of the appropriate gas and N₂, at a concentration scaled by the ratio between the transmission path length 6400 cm and the cell path length 15 cm. In all cases the N₂ concentration is high enough that the line shape is determined by N₂ collisions, so that the line profile is the same as would be observed if the gases were released in the lab. The sealed cells are positioned immediately in front of the detector D₂ in order to ensure that all of the radiation reaching the detector has also passed through the cell.

The minimum detectable signal is determined by residual noise in the compensated signal. From the peak-to-peak value of this noise we arrive for 64 m path length at a minimum detectable absorbance of $5 \cdot 10^{-4}$ which translates into about 40 ppm CO₂, 50 ppm CO, and 5 ppm H₂S. For CO₂ and H₂S this is near optimum in this spectral region, since we are using lines with line strength comparable to the strongest lines. For CO, however, the line strength of R1 is about 38% of the strongest line R7 at 1568.036 nm, and the detection limit can therefore be improved by about a factor of 2.5 by optimum choice of line.

The use of WMS might seem somewhat archaic in view of the fact that numerous reports exist on absorbance limits down to $5 \cdot 10^{-8}$ using either FMS or TTFMS [1]. However, in our point of view those reports neglect the presence of long term drift, a complication which invariably has to be dealt with if the monitors are to have a future outside the laboratory [2]. Increasing the modulation frequency only improves the signal to noise ratio if the dominant noise source is the laser itself, and this is probably rarely the case in real life. In our case the limiting factor is fringe-like structures such as that seen below 20 GHz in Fig.3 (a), reflecting imperfect cancellation of spectral features in the radiation leaving the collimating lens. Although such structures may be repeatable over several minutes, they exhibit drift over time intervals of hours and hence introduce an unpredictable contribution to the signal.

- [1] Peter Werle, "A review of recent advances in semiconductor laser based gas monitors", *Spectrochimica Acta Part A* 54 (1998) 197-236.
- [2] A.M. Ballangrud, "Diode laser spectroscopy for gas monitoring and environmental pollution and for industrial process and emission control", Thesis, University of Oslo, Norway, (1993).

Acknowledgements

This work has been supported by the European Commission under contract no. OG 269/95, and by the Danish Science Research Council under grant no. 9600860

Development of a near-IR TDL probe for rapid species measurements in large pool fires

Christopher R. Shaddix, Philip J. Santangelo, Peter D. Ludowise,
Sarah W. Allendorf, and David K. Ottesen

Combustion Research Facility
Sandia National Laboratories

7011 East Avenue
Livermore, CA 94550
crshadd@sandia.gov

Introduction

Researchers at Sandia have been experimentally and numerically investigating large-scale pool fires for several years, because of the risk that these fires pose to critical engineered systems during transport accident scenarios. Experimental measurements in large fire research have traditionally been limited to thermocouples, heat-flux gauges, and bidirectional velocity probes, due to the difficulty of fielding optical measurement techniques in this turbulent, optically thick, high-temperature environment. Recently, Sandia developed and successfully implemented an insulated, water-cooled fiber optic probe that utilized a combined HeNe-laser-absorption, 2-color emission technique to determine soot volume fraction distributions and soot temperatures over a 2-cm sampling distance in a 6-meter diameter JP-8 pool fire [1]. Photographs of the probe and the type of fire it is used in are shown in Figure 1. This probe system has now been affixed to a rail system on the bottom of the pool, allowing optical measurements to be performed as a function of radial distance at a given height in these fires. With the collection and analysis of soot property data, attention has turned to the measurement of gas-phase species concentrations (together with soot properties), in order to evaluate mixing phenomena, gas-phase radiation interactions, and soot formation and oxidation chemistry in these large fires.

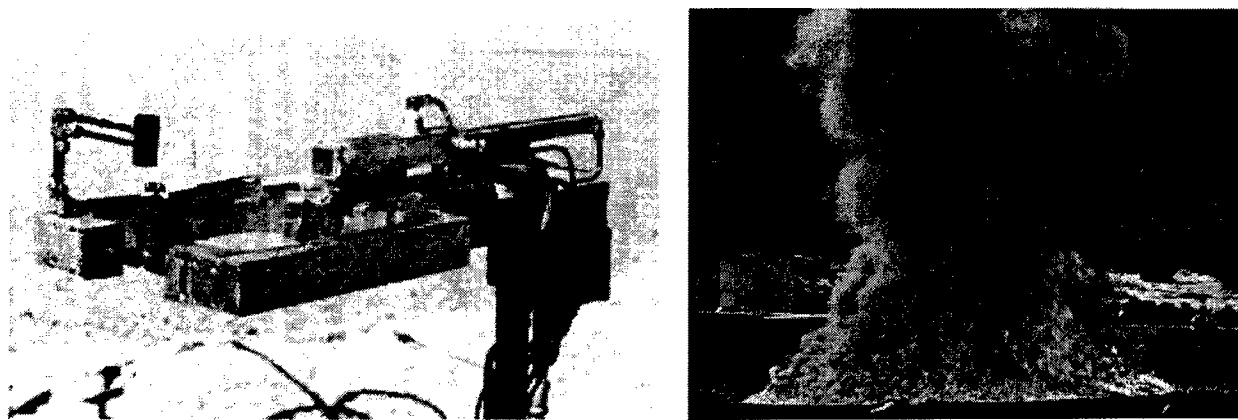


Figure 1. The photograph on the left shows a fiber-optic probe design for local optical measurements in large fires. The entire probe is wrapped in fire-proof insulation, with the small protruding line-of-sight tubes (front, left) defining the sample volume. Water cooling and a small nitrogen gas purge protect the fiber optic cabling and associated optics. A typical experimental flame system is a 5-m diameter pool fire of JP-8, shown here in the photo on the right.

Near-IR tunable diode laser (TDL) absorption spectroscopy appears to be the most promising technique currently available for performing the requisite species measurements, because of the narrow linewidths of TDLs (discriminating against spectral interferences), the sensitivity of TDL measurement systems, and the ready-coupling of TDLs to low-cost, highly transmissive fiber optic cabling. In addition, laser tuning by means of injection current ramping allows very fast spectral scans to be performed by TDLs over absorption features of interest, effectively freezing the local flowfield that is being probed. In spite of these favorable features of near-IR TDLs, performing quantitative species measurements in fires remains a formidable challenge, due to the very weak overtone and combination band rovibrational transitions in the near-IR, the highly transient flowfield, and the time-dependent beam steering, optical attenuation, and thermal emission effects from the sampled flame volume. These considerations, coupled with our desire to multiplex four or more lasers over a given sample volume, have necessitated a laboratory-based research program to elucidate the optimal design choices in fabricating a TDL system for applications to the fire environment. The major components of our research program and our findings to date are summarized below.

High-Temperature Spectroscopy

The end-goal of Sandia's research program into large pool fires is to develop both an experimental understanding and a modeling capability to realistically describe heat transfer to 3-dimensional objects situated near or within the fire. To achieve this goal, one would like to measure the local fuel, oxygen, and combustion product concentrations (to determine the local mixture fraction), as well as species specifically associated with gaseous radiative transport and with soot formation and oxidation. This list includes, as a minimum, O₂, CO₂, H₂O, CO, C₂H₂, OH, and an indicator fuel species. If we choose CH₄ as the indicator fuel species, then all of these species may be detected, in principle, with near-IR TDLs. However, oxygen detection is via the electronic A-band transitions at 760 nm, necessitating the use of a separate fiber optic cable and detector for its measurement. OH radical concentrations do not correlate well with mixture fraction in diffusion flames, so such measurements appear to be of less value than those of the other listed species. Consequently, we have focussed our attention on evaluating the prospects of detecting CO₂, H₂O, CO, C₂H₂, and CH₄ in pool fires.

Because of the incompleteness and errors associated with HiTran/HiTemp [2] calculations of absorption spectra at high temperatures in the near-IR, we have used a low-pressure flat flame/FTIR facility to measure absorption spectra. Unfortunately, the need to multipass the incoherent IR beam through the flame to achieve sufficient FTIR sensitivity compromised the temperature definition of the captured spectra. Improved spectra for CO₂ and H₂O have been obtained by utilizing external-cavity TDLs and distributed-feedback (DFB) TDLs in a multipass configuration above an atmospheric-pressure burner in an optical chimney. Taken together, these measurements provide a unique experimental database for choosing optimal transitions of CO₂, H₂O, CO, C₂H₂, and CH₄ to probe at high temperature in the near-IR. In particular, we have evaluated water and CO₂ interferences with respect to detecting the other species of interest.

In Situ Multipassing

Because of the weak absorption linestrengths and the need to limit the physical sample volume to a length of a few cm, multipassing of the TDL beam over the sample volume is desired. However, maintaining optical alignment in an open-path setup, particularly with the unavoidable heating of the probe during fire experiments, may prove to be difficult. Also, beam steering across the flame sheets in the probe volume may be exacerbated by multipassing, and the exponential increase in beam attenuation with pathlength through a sooty region ultimately compromises the benefits of multipassing. We are presently experimenting with multipassing through a turbulent, buoyant diffusion flame in order to improve our understanding of these effects.

High-Frequency wms/Multiplexing

The two most common techniques to sensitively perform TDL absorption spectroscopy are to use high-frequency wavelength modulation spectroscopy (wms) or to apply balanced ratiometric detection (BRD) with a reference detector. Similar sensitivities (typ. detection limit of 10^{-6} absorbance) have been reported with these two techniques in steady-state laboratory experiments. However, the BRD approach does not respond well to transient variations in the measured light intensity and therefore is not well suited for measurements in the pool fire environment. In order to properly interpret the 2nd harmonic (2f) signal from a wavelength-modulated TDL spectral scan, the characteristic scan time across the absorption feature of interest must be less than any of the time scales characterizing the flowfield across the probe volume. Experimental measurements show that these time scales can be less than 1 ms. Therefore, in order to apply wms to kHz frequency spectral scans, modulation frequencies > 1 MHz must be used. Such frequencies are easily achieved, but commercial diode controllers are limited to 2 MHz modulation and commercial rf lock-ins are expensive and have time constants on the order of 100 μ s, which are insufficient to suitably resolve kHz-level spectral scans. Consequently, we are evaluating the relative merits of utilizing modulation frequencies of up to 5 MHz, with 2f detection via the use of custom rf lock-ins (consisting of standard electrical components such as frequency doublers, filters, amplifiers, and mixers).

Several options exist for a multiplexed TDL system with all of the incident laser light combined into a single fiber, including “temporal stagger”, “grating separation”, and “distinct frequency” approaches. For this application, with the incumbent need for high-frequency wms, the “distinct frequency” approach appears to be most favorable, although there are important considerations such as saturation of the detector and 2f crosstalk. Our experiments have demonstrated that laser crosstalk can easily be avoided at 1 MHz level modulation with frequency separations of 100 kHz or more, depending on the relative magnitude of the 2f signals on the different channels.

Lineshape Fitting

In order to deduce species concentration information from measured 2f spectral scans, the gas temperatures must be known. With this information, correlations of peak 2f signal versus temperature may be used (accounting for the dependencies on linestrength, collisional broadening, and gas density), or else the best fit to the entire measured 2f feature may be calculated. We plan on implementing 2-line H₂O thermometry to measure the gas temperature through the probe volume. We are also investigating the relative benefits of detecting the wms signal using other harmonics (esp. 1f or 3f), with respect to optimizing the S/N for the weak spectral absorptions.

Reference

1. Gritzo, L.A., Sivathanu, Y.R., and Gill, W., “Transient measurements of radiative properties, soot volume fraction and soot temperature in a large pool fire”, *Combustion Science and Technology* 139:113, 1998.
2. Rothman, L.S., Rinsland, C.P., Goldman, A., Massie, S.T., Edwards, D.P., Flaud, J.M., Perrin, A., Campeyret, C., Dana, V., Mandin, J.Y., Schroeder, J., McCann, A., Gamache, R.R., Wattson, R.B., Yoshino, K., Chance, K.V., Jucks, K.W., Brown, L.R., Nemtchinov, V., and Varanasi, P., “The HiTran molecular spectroscopic database and HAWKS (HiTran Atmospheric Workstation): 1996 Edition”, *J. Quant. Spectros. Rad. Trans.* 60:665–710, 1998.

Diode laser-based detector for fast detection of binary gas mixtures

Kevin L. McNesby, R. Reed Skaggs, Andrzej W. Mizolek, Jeffrey B. Morris, Brian Kennedy

U.S. Army Research Laboratory
Aberdeen Proving Ground, MD 21005-5066
Tel/Fax 410-278-6163/6150
Email: mcnesby@arl.mil

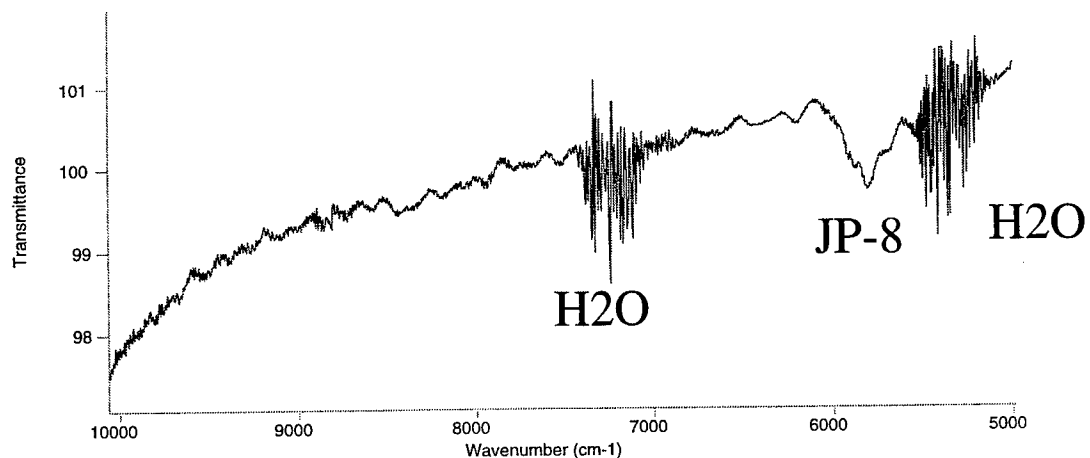
Ian A. McLaren
McLaren Research, Mountain View, CA 94043

For many automated fire suppression systems onboard military vehicles, the nominal time-to-fire-out, after detection by thermal or light sensors, is 250 milliseconds. Because of this critical requirement, detailed evaluation of new fire suppression systems installed onboard military vehicles requires measurements of fuels, oxidizers, fire suppressants, and combustion products with a time resolution of 10 milliseconds or better. Because of the extreme hostility of the testing environment, the measurement system needs to be capable of remote operation, and the sensing probe needs to be inexpensive and readily replaceable.

Wavelength modulation spectroscopy (WMS) is typically used for concentration measurements of molecules with narrow, well resolved ro-vibrational absorption lines, such as hydrogen fluoride gas. Large and/or heavy molecules may not possess well resolved ro-vibrational absorption bands because of overlap between fundamental, combination, and overtone vibrations, and because of rotational constants which may be less than typical gas phase linewidths. Figure 1 shows the near-infrared vapor phase absorption spectrum of the hydrocarbon-based turbine fuel JP-8. For this molecule, the absorption spectrum near 5881 cm⁻¹ is essentially a continuous hump. Because of this, conventional WMS is not a practical method for determination of vapor phase concentration of JP-8 fuel.

The talk will focus on the development and characterization of near-infrared tunable diode laser-based gas sensor to simultaneously measure concentrations of oxygen and the vapor from a series of volatile organic compounds. Signal processing is performed digitally, and control of the sensor and electronics, data collection, and real time readout is by a laptop computer. The discussion will focus on the methods used for laser selection, phase sensitive detection, data storage, and concentration measurements for species which do not possess well resolved rotational-vibrational spectra.

- JP8 fuel
- 13 cm path length
- Vapor above liquid at 82C (355K)
- 4 cm⁻¹ resolution
- Bomem DA-8 Spectrometer
- 256 scans



NIR JP-8 transmission is a minimum
at 5801 cm⁻¹ (1723.8 nm)

Figure 1: The near infrared absorption spectrum of JP-8 fuel at 355 K.

This work is supported by the Next Generation Fire Suppression Technology Program (NGP).

Coherence Control and Modeling

Compact external-cavity diode laser at 633 nm with a transmission grating

M. Merimaa, I. Tittonen, and E. Ikonen

Helsinki University of Technology, Metrology Research Institute,
P.O. Box 3000, FIN-02015 HUT, Finland.

Mikko.Merimaa@hut.fi, Ilkka.Tittonen@hut.fi, Erkki.Ikonen@hut.fi
Phone: +358 9 451 2185 Fax: +358 9 451 2222

H. Talvitie

Presently with Vaisala Oyj, P.O. Box 26, FIN-00421 Helsinki, Finland.
Hannu.Talvitie@vaisala.com

P. Laakkonen and M. Kuittinen

University of Joensuu, Department of Physics,
P.O. Box 111, FIN-80101 Joensuu, Finland.

Pasi.Laakkonen@joensuu.fi, Markku.Kuittinen@joensuu.fi

Diode lasers are widely used in experiments in optical and atomic physics and increasingly in spectroscopy and frequency stabilization. Their small size, high power, low price and simple operation account for their popularity, but they nevertheless have their drawbacks. Poor tunability, large linewidth and operation on multiple longitudinal modes mainly restrict the usability of solitary diode lasers. It is widely known that these properties can be improved by operating the diode laser in a longer external cavity which provides frequency selective optical feedback [1,2].

A traditional external-cavity diode laser is based on a reflective diffraction grating in the Littrow configuration as shown in Fig. 1 (a) [3]. A significant improvement can be obtained by using a transmittive grating, as shown in Fig. 1 (b), as it totally removes the problem of turning the output beam while tuning the laser wavelength, which is a major drawback in the reflection geometry. Transmittive gratings have not been used before due to the difficulty of obtaining 15-20 % diffraction back to the laser without significant power loss to other diffraction orders or reflections. We report on construction of a novel external-cavity diode laser based on a low-loss transmission diffraction grating. The grating has been designed and manufactured at the Physics Department of the University of Joensuu.

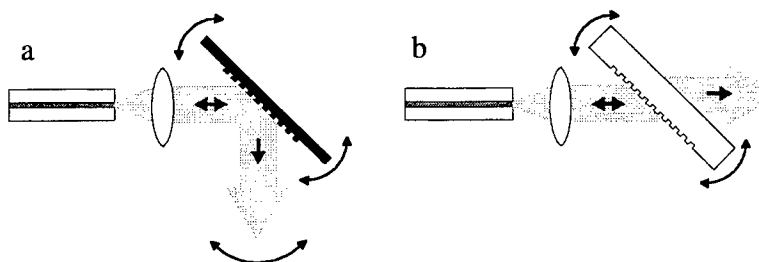


Figure 1. External-cavity lasers. The traditional reflection geometry (a) and the novel transmission geometry (b). Note that in (b) the output beam direction does not change.

The mechanical structure of the laser is shown in Fig. 2. The optical length of the cavity is 32 mm, yielding free spectral range of 4.7 GHz, which is enough to give robust single mode operation. The laser source is an AR-coated 15 mW laser diode (SDL-7501). The transmission grating is fabricated onto a

SiO_2 substrate with electron beam lithography and reactive ion etching with the optimized grating parameters: period 447.6 nm (~2200 lines/mm), height 122 nm and fill factor 0.5. The grating is coated with a 76 nm thick TiO_2 layer using vacuum evaporation. The grating transmits 80 % of the power, diffracts 15 % back to the laser and only 5 % of the power is lost. These experimental values compare favorably to the theoretical calculations which give 17.3 % diffraction and 76.6 % transmission, indicating excellent mastering of the manufacturing process. Three independent piezoelectric transducers are used to control the grating rotation and the cavity length to achieve wide continuous tuning range [4].

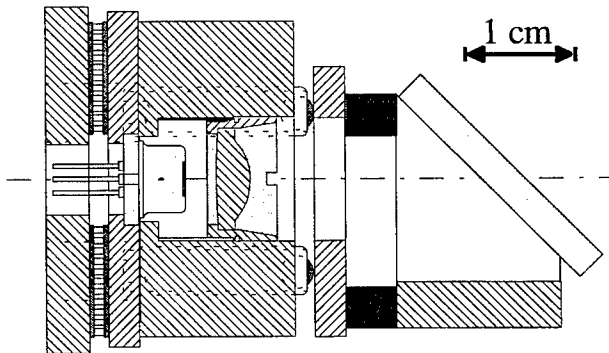


Figure 2. Mechanical structure of the external-cavity laser based on a transmission grating.

When the laser is properly adjusted, the threshold current is 44 mA and the differential efficiency is as high as 0.47 mW/mA. The total tuning range of the laser is ± 4 nm around 632 nm with a continuous tuning range of 12 GHz. The spectral purity of the laser is very good; the linewidth is 360 kHz and the side-mode suppression is 40 dB. The laser intensity noise is only two times the shot noise at frequencies higher than 5 kHz at the output power of 8.5 mW. Thus the relative intensity noise (RIN) is -155 dB/Hz.

The results prove that the transmission configuration provides excellent performance without the problem of directional variation of the output beam. The transmission configuration is also suitable for making extremely compact external-cavity lasers.

References

- [1] C. E. Wieman and L. Hollberg, "Using diode lasers for atomic physics," *Rev. Sci. Instrum.*, vol. 62, pp. 1-20, 1991.
- [2] A. S. Arnold, J. S. Wilson, and M. G. Boshier, "A simple extended-cavity diode laser," *Rev. Sci. Instrum.*, vol. 69, pp. 1236-1239, 1998.
- [3] H. Talvitie, A. Pietiläinen, H. Ludvigsen and E. Ikonen, "Passive frequency and intensity stabilization of extended-cavity lasers," *Rev. Sci. Instrum.*, vol. 68, pp. 1-7, 1997.
- [4] J. Mellis, S. A. Al-Chalabi, K. H. Cameron, R. Wyatt, J. C. Regnault, W. J. Devlin and M. C. Brain, "Miniature packaged external-cavity semiconductor laser with 50 GHz continuous electrical tuning range," *Electron. Lett.*, vol. 24, pp. 988-989, 1988.

Semiconductor Lasers with Broadband Tunability

Ching-Fuh Lin, Bor-Lin Lee, and Miin-Jang Chen

Institute of Electro-Optical Engineering

and

Department of Electrical Engineering

National Taiwan University

Taipei, Taiwan, ROC

Tel: 886-2-23635251 ext. 339/Fax: 886-2-23638247

Email: cflin@cc.ee.ntu.edu.tw

Semiconductor lasers have potential applications in many areas due to their compact size, low cost, integration possibility with electronics, and so on. For many applications such as optical communication and spectroscopy, wide-range tunability is important. Conventional semiconductor-laser materials have a gain bandwidth around 50 meV, which is the major limitation for tunability. The gain bandwidth can be broadened by several methods such as stacking twin active layers with different bandgaps,¹ using $n=1$ and $n=2$ transitions in the same quantum well simultaneously,² and using multiple quantum wells of different widths.³⁻⁵ In this work, we demonstrate the use of asymmetric dual quantum wells to broaden the gain bandwidth and achieve broadband tunability. The broadband tunability is achieved for single-wavelength, dual-wavelength, and actively mode-locked operations with 90 nm, 55.7 nm, and 62 nm tuning ranges, respectively.

The semiconductor laser material used in this work has two quantum wells with their widths 40 Å and 75 Å, respectively. The widths are chosen to make their $n=1$ transition energies separate for 50 meV. In addition, the $n=2$ transition energy in 75 Å well also separates from the $n=1$ transition energy in 40 Å well for 50 meV. Thus, the overall gain bandwidth is more than two times wider than conventional ones. Superluminescent diodes (SLD's) fabricated on such material show that their emission spectra are 2~3 times wider than conventional SLD's fabricated on substrate with two QWs of the same width. The

SLD's are used in the laser cavity for tuning experiments. The SLD's have a ridge waveguide tilted at 7° from the normal of the cleaved facet to eliminate the gain ripple.⁶ The single-wavelength, dual-wavelength, and actively mode-locked operations will be described separately as follows.

A ring cavity was set up for single-wavelength operation. Fig.1 shows the experimental setup. The ring cavity using the tilted-stripe SLD's provides two advantages over the linear cavity. First, because the cross section of the active region is very small and both facets of the SLD have a very small retro-reflectivity, the alignment of ring cavity is easier than a linear cavity. Second, one arm of the output beams, beam (a), has significantly reduced amplified spontaneous emission (ASE) noise because the ASE noise is first spatially dispersed by the grating and then filtered out by the mirror mount M1. In the conventional linear cavity, the ASE noise is spatially overlapped with the oscillation mode.

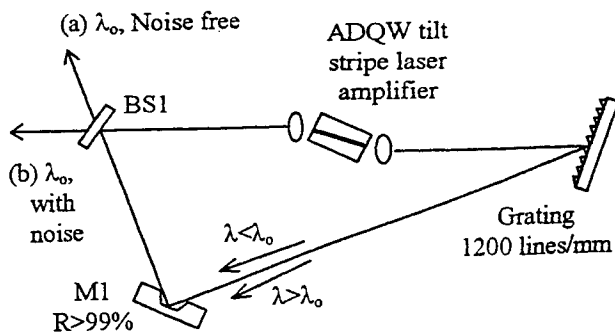


Fig. 1 The experimental setup of ring cavity.

SLD's of different lengths had been used in the cavity. The tuning characteristics are shown in Figs. 2(a) and (b). The tuning ranges are 90, 70, and 48 nm for the 400-, 700-, and 1000- μ m devices. In the experiment, the operation current was limited to below 400 mA. Further increase of injection current should increase the tuning range, but not much, because the threshold current increases significantly at the two sides of the tuning curve. The wide tuning range of using the 400- μ m SLD indicates that the $n=1$ and 2 transitions in 75 \AA well and $n=1$ transition in 40 \AA well could all contribute to the lasing operation.

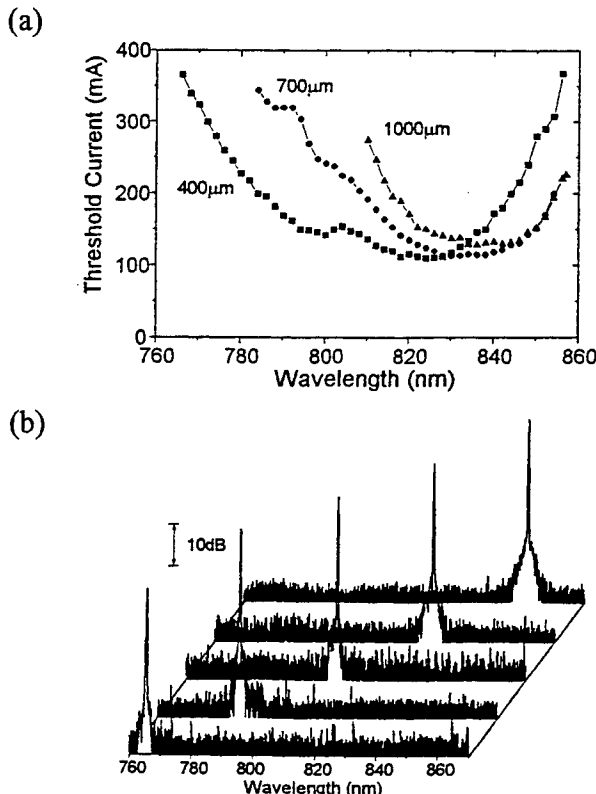


Fig. 2 (a) Threshold current vs. tuning wavelength. (b) The spectra measured from the beam (a) at different wavelengths.

For dual-wavelength operation, the cavity schematically shown by Fig. 3 was used. A reflection-type grating telescope⁷ was used on one side of the SLD. Double slits were inserted in front of the mirror for the selection

of the oscillation wavelengths.

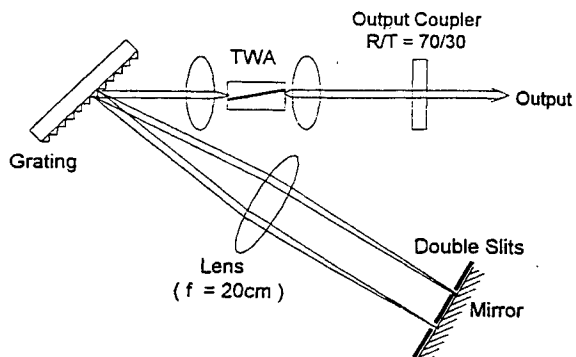


Fig. 3 Schematic of the experimental setup for dual-wavelength operation.

The two oscillation wavelengths can be almost randomly selected within a large spectral range over 30 nm. In the experiments, the spectral spacing had been varied from 5 to 55.7 nm for injection current not larger than 210 mA. A narrower spacing should be possible as long as the slit spacing is reduced.

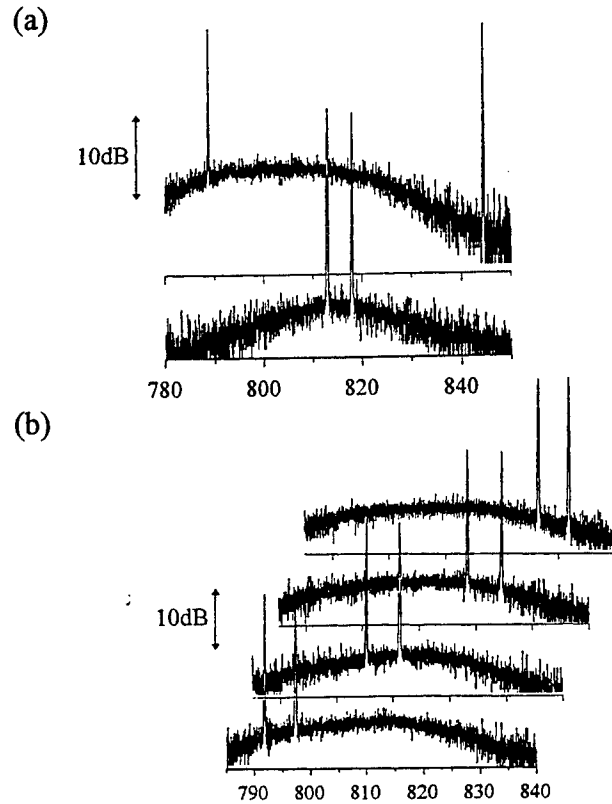


Fig. 4 (a) Measured spectra of two wavelengths at two spacings: 5 nm and 55.7 nm. (b) Tuning spectra of two wavelengths at fixed spacing.

The maximum spectral current could also increase if the injection current is larger. Other tuning situations had also been experimented. For example, simultaneous tuning of the two wavelengths at a constant spacing had been achieved. In addition, experiments had shown that one wavelength could be varied with the other wavelength fixed. Figs. 4 (a)-(b) show the tuning characteristics in different situations.

In the mode-locking experiment, the ring cavity similar to the one shown in Fig. 1 was used for the advantages mentioned previously. In addition, the pulse train travelling in the ring cavity can be more easily synchronized with the RF modulation signal than in the linear cavity. Fig. 5 shows the lasing threshold, DC bias, and RF modulation frequency vs. tuning wavelength in the experiment. The RF modulation was maintained at 0.5 I_{th} for the entire tuning range. The mode-locked pulse shape is sensitive to the variation of modulation frequency. In order to maintain the measured autocorrelation trace with a well-behaved shape, the RF modulation frequency can be varied only within 0.3 MHz. This trace could be well fitted by the single-sided exponential shape, as shown in Fig. 6. The mode-locked spectral width is about 2-4 Å, which is limited mainly by the grating. The pulse width is 10-15 ps and is in general decreases with decreasing laser wavelength. The pulses are highly chirped and could be possibly compressed to 1-2 ps.

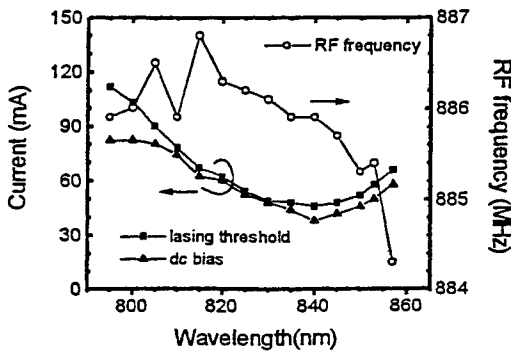


Fig. 5 Lasing threshold, DC bias and RF modulation frequency vs. tuning wavelength.

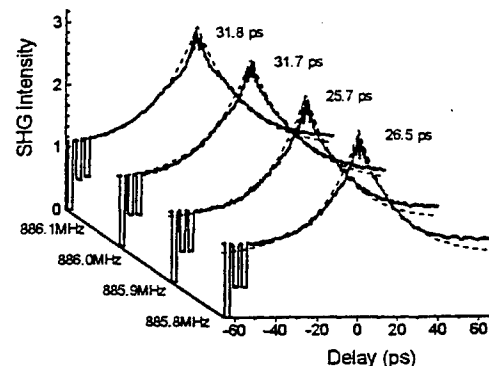


Fig. 6 The autocorrelation trace of the mode-locked pulses at different modulation frequency. (Autocorrelation widths are indicated and dotted lines are fitted by single-sided exponential functions.)

In summary, wide-range tunability is achieved in single-wavelength, dual-wavelength, and actively mode-locked operations of semiconductor lasers due to the broadened gain bandwidth using asymmetric dual quantum wells.

References:

1. O. Milkami, H. Yasaka, and N. Noguchi, *Appl. Phys. Lett.* vol. 56, pp. 987-989, 1990.
2. A. T. Semenov, V. R. Shidlovski, and S. A. Safin, *Electron. Lett.* vol. 29, pp. 854-857, 1993.
3. C.-F. Lin, B.-L. Lee, and P.-C. Lin, *IEEE Photon. Technol. Lett.* vol. 8, pp. 1456-1458, 1996.
4. X. Zhu, D. T. Cassidy, M. J. Hamp, D. A. Thompson, B. J. Robinson, Q. C. Zhao, and M. Davies, *IEEE Photon. Technol. Lett.* vol. 9, pp. 1202-1204, 1997.
5. C.-F. Lin, and B.-L. Lee, *Appl. Phys. Lett.* vol. 71, pp. 1598-1560, 1997.
6. G. A. Alphonse, D. B. Gilbert, M. G. Harvey, and M. Ettenberg, *IEEE J. Quantum Electron.* vol. 24, pp. 2454-2457, 1988.
7. C.-L. Wang, and C.-L. Pan, *Appl. Phys. Lett.* vol. 64, pp. 3089-3091, 1994.

Relaxation Oscillation Frequency Properties in Injection-Locked Semiconductor Lasers

Y. Hong and K. A. Shore

University of Wales, Bangor, School of Electronic Engineering & Computer Systems
BANGOR LL57 1UT, Wales, UK

Tel: +44(1248)382618. Fax: +44(1248)361429
e-mail: alan@sees.bangor.ac.uk

Direct modulation of semiconductor lasers has attracted considerable attention in recent years. Semiconductor lasers with a large modulation bandwidth have potential applications in both digital and analog optical transmission links. Several theoretical studies have predicted that modulation bandwidth in injection-locked semiconductor lasers can be significantly improved relative to the free running case^[1]. There has also some experimental work on the modulation bandwidth of intramodal injection-locked semiconductor lasers^[2] when the frequency injected by the master laser(ML) is close to the slave laser(SL) free-running frequency. However, to author's knowledge, there is little experiment on the modulation bandwidth of intermodal(side-mode) injection-locked semiconductor lasers when the injection occurs in the vicinity of a nonlasing longitudinal sidemode.

The modulation bandwidth of a semiconductor laser is approximately proportional to the relaxation oscillation frequency. This paper is focused on an experimental study of relaxation oscillation frequency(ROF) in an injection-locked semiconductor laser. It is shown that relaxation oscillation frequency in an injection-locked semiconductor laser is related to injection power and the wavelength of the injection target mode.

In the experiment, the ML is a tunable laser diode (SDL-TC10-850) with more than 20nm tuning range, the SL is a commercial laser diode with >20dB sidemode suppression. An isolator of >40dB attenuation inserted between the ML and the SL was used to ensure that no light was injected into the ML. Two other isolators of >40dB attenuation were used to eliminate the feedback from the optical spectrum analyzer and the Fabry-Perot interferometer, which used to obtain the spectra characteristics of the SL output. A variable optical attenuator was used to change the launched probe power. A half-wave plate was used to match the polarization of the probe and pump beams. A power meter was employed to monitor the injection power. The SL was biased at 1.2 times threshold current and operated wavelength of 829.2nm. The launched probe power was evaluated from the photocurrent induced in the SL at zero bias and are assumed an internal quantum efficiency of 0.9.

In the experiment, the definition of stable locking is that the side peaks of relaxation oscillation or spurious free-running slave modes are less than 20dB of the locked main peak in the SL spectrum. The ROF of the laser under injection locking was measured at the upper limit of the

stable locking range where the relaxation oscillation frequency was strongly enhanced^[3]. Negative mode numbers correspond to long wavelength side of the free-running spectrum.

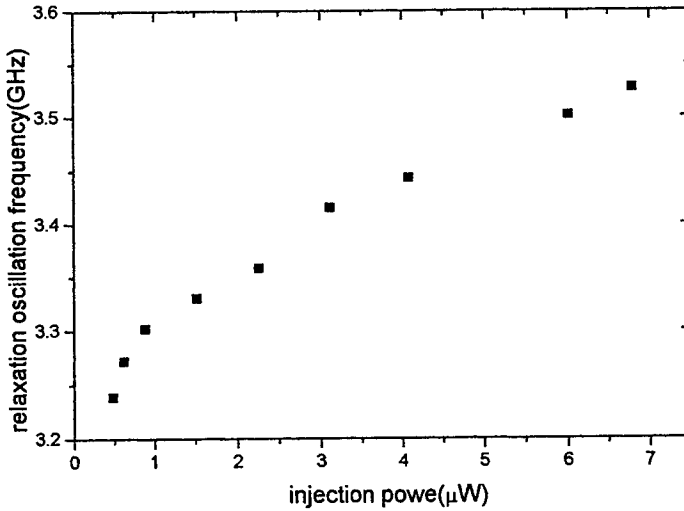


Fig. 1 Relaxation oscillation frequency versus the injection power

Fig. 1 shows the relaxation oscillation frequency versus the injection power. The result was obtained for intermodal injection locking at mode +1, which the ML is detuned to the one cavity resonance frequency higher with respect to the SL free running frequency. It is shown that the ROF increase with the increasing injection power, similar result in the intramodal injection locking have been theoretically predicted^[2]. Same results in the other side mode have also been observed.

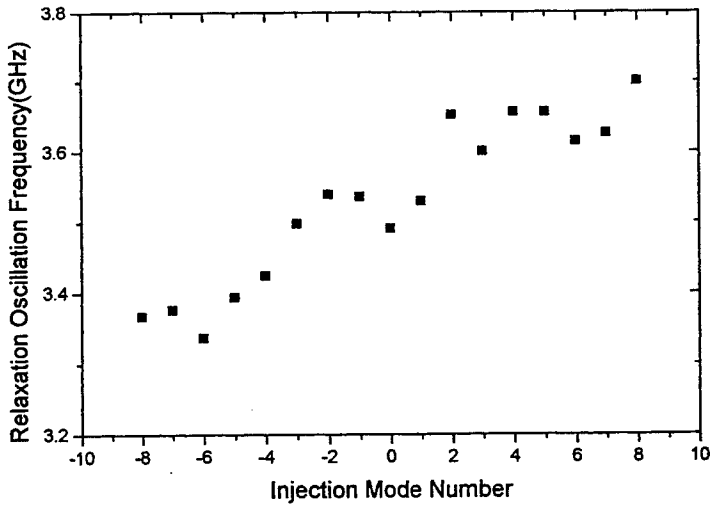


Fig. 2 Relaxation oscillation frequency versus injection target modes

In order to observe the influence of the target injection mode on the ROF in the injection-locked diode lasers, we fixed the injection power at $p_{in} = \sim 19 \mu\text{W}$ and changed the target injection mode from mode -8 to mode +8, the result is shown in Fig. 2. It can be seen that the relaxation

oscillation frequency is increased when the injection wavelength is detuned to the short wavelength side of the free-running wavelength, while the relaxation frequency is decreased when the injection wavelength is set to the long wavelength side of the free-running wavelength, which is qualitative agreement with the theoretical predictions^[4].

The results show that semiconductor lasers with a large modulation bandwidth may be achieved in injection-locked diode lasers by increasing the injection power and appropriately choosing the target injection mode. An additional benefit in a injection-locked semiconductor laser is that the optical injection enhances the field damping, thereby narrowing the spectral linewidth, increasing modal stability and reducing the dynamic frequency chirp during direct modulation.

Acknowledgments

This work is supported by EPSRC under grant GR/L03262.

Reference

1. J. Wang, M. K. Haldar, L. Li and F. V. C. Mendis, "Enhancement of modulation bandwidth of laser diodes by injection locking", *IEEE Photon. Technol. Lett.*, **8**, 34-36, 1996
2. J. M. Liu, H. F. Chen, X. J. Meng and T. B. Simpson, "Modulation bandwidth, noise, and stability of a semiconductor laser subject to strong injection locking", *IEEE Photon. Technol. Lett.* **9**, 1325-1327, 1997
3. I. Petitbon, P. Gallion, G. Debarge and C. Chabran, "Locking bandwidth and relaxation oscillations of injection-locked semiconductor laser", *IEEE J. Quant. Electron.*, **24**, 148-154, 1988
4. J. M. Luo and M. Osinski, "Multimode small-signal analysis of side-mode injection-locked semiconductor lasers", *Jpn. J. Appl. Phys.*, **31**, L685-L688, 1992

Coherence collapse in semiconductor diode lasers with phase conjugate feedback

J. S. Lawrence and D. M. Kane

Physics Department, Macquarie University, Sydney 2109, Australia
ph: 61 -2 9850 7901, fax: 61 -2 9850 8983
jl@ics.mq.edu.au, debkane@mpce.mq.edu.au

Semiconductor diode lasers when operated with conventional optical feedback (COF) can exhibit various dynamic instabilities. At low levels of feedback (regime III) the diode laser operates in a stable single longitudinal mode (the narrowest linewidth mode) with constant power. As the feedback is increased the relaxation oscillation of the diode laser becomes undamped, resulting in periodic oscillation of the output power. Further increase in the feedback level ultimately leads to an unstable chaotic output state (typically through a series of bifurcations). This chaotic state is known as coherence collapse (or regime IV) and is characterised by a dramatically broadened noise spectrum, and an optical frequency spectrum which is predominantly multi-mode. This coherence collapsed region is bounded by another stable single mode region of strong feedback (regime V).

A number of theoretical studies on diode lasers with phase conjugate feedback (PCF) have shown that the spatial and temporal phase reversal induced by the PCM induces dynamic instabilities which are much richer than for COF [1],[2]. These models, however, because they are based on the Lang-Kobayashi rate equations, are only applicable for very weak feedback; and thus do not predict behaviour throughout the entire coherence collapse regime. Previous experimental studies on diode lasers with phase conjugate feedback (PCF) have been primarily concerned with the spatial attributes of the phase conjugation, and the ability to achieve mode locking, beam coupling, and phase locking; particularly for laser diode arrays and broad area diodes. PCF on single mode laser diodes has been found to induce a coherence collapsed state, and also linewidth narrowing and side mode suppression according to the feedback level [3],[4],[5]. However, no systematic investigation of the dynamic or spectral behaviour or comparison to the case of COF has been reported, to our knowledge.

In the current work the regime of coherence collapse for a single mode diode laser subject to PCF is experimentally investigated, and compared to the same diode with mirror feedback. In particular, critical feedback levels which result in transitions between stable and unstable regimes are, for a number of different cavity lengths, compared for the two cases. Also, the evolution of the optical frequency spectrum, the intensity noise spectrum and the real time power spectrum, with increasing feedback level are observed. Feedback is introduced into a single mode 850 nm quantum well index guided diode laser. The phase conjugate mirror is an internal reflection geometry self pumped Rhodium doped BaTiO₃ crystal.

It is found that the transition between stable single mode regime III and coherence collapse occurs at a lower feedback fraction for PCF than for COF. Also the transition from unstable coherence collapse to stable strong feedback regime V occurs at higher feedback fractions for PCF than for COF. Feedback fraction is defined as the ratio of the emitted power from the front facet of the diode to the reflected power entering the front facet of the diode. Considering the coupling efficiency for the PCF system is significantly higher than for the COF system, then the range of feedback levels giving stable operation is much larger for the COF system.

Another difference between the two systems occurs near the regime IV \rightarrow V high feedback transition. This transition from chaotic to stable operation is interrupted by a region of low frequency fluctuations (LFF) for both COF and PCF. However, the LFF for the case of PCF (which has not previously been observed, and is shown in figure 1) is much easier to excite than for COF, and occurs over a much larger range of feedback levels.

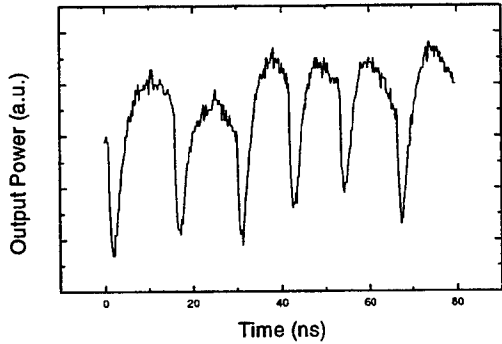


Figure 1: Low frequency fluctuations induced by phase conjugate feedback; near the transition from coherence collapse to stable single mode high feedback regime V.

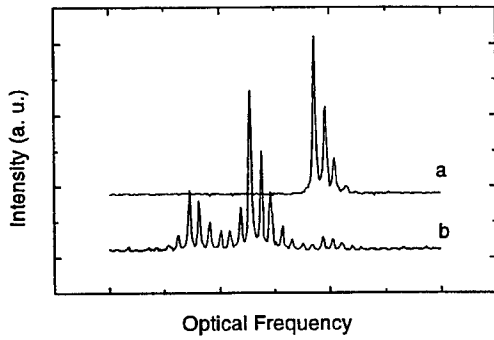


Figure 2: Optical frequency spectra for the coherence collapsed state for (a) PCF, and (b) COF. Each spectrum shows the excitation of a number of the solitary diode longitudinal modes- spaced by approximately 150 GHz.

The evolution of the chaotic state, as determined through the intensity noise and optical frequency spectra has also been compared for the two systems. Figure 2 shows a comparison of the optical frequency spectrum for the diode laser with PCF and COF. Both spectra are taken at the same injection current and cavity length, and a feedback level well within the coherence collapse region. The chaotic state for COF is shown to comprise significantly more and larger solitary diode side modes than that for the PCF chaotic state. This is a general comparative characteristic of the two types of feedback in this regime.

Figure 3 shows the comparison of intensity noise spectra. In plots (a) the laser system noise is below the detection system dark noise. In plots (b) the external cavity modes are excited for both COF and PCF- indicating a periodic oscillation of the output power. As the feedback is increased for the case of COF the noise spectrum dramatically broadens and develops a large number of peaks with a much smaller frequency spacing. The spectrum does not significantly change through the region of coherence collapse until the transition to stable operation at strong feedback (g), although we can see an increased noise at low frequencies (in f) indicating LFF. The noise spectra for PCF shows distinct differences. The spectra do not broaden as much and at high feedback levels the external cavity modes are once again excited. The low frequency noise is also significantly larger for the PCF; indicating the larger range of feedback levels giving rise to LFF for PCF.

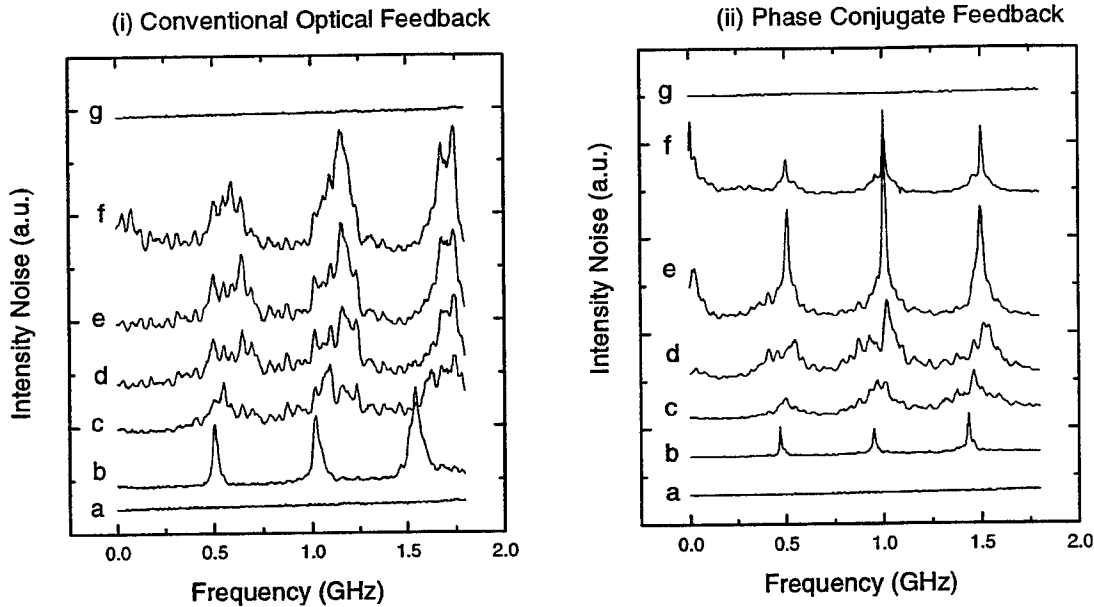


Figure 3: Intensity noise spectra for the cases of (i) COF and (ii) PCF. Each graph shows the evolution of the noise spectrum as the feedback fraction is increased from the stable regime III in (a), through the region of periodic oscillations in (b), coherence collapse (c-f) and stable regime V in (g). The external cavity length is 330 mm. All spectra are plotted on identical vertical scales which are shifted vertically for clarity.

In conclusion, the differences between phase conjugate feedback and conventional optical feedback on the output characteristics for a single mode diode laser are investigated experimentally. It is found that the region of feedback levels giving stable output is much larger for the case of COF than for PCF. However, the coherence collapsed state for the case of COF is significantly more multi-mode than for PCF and has a much broader noise spectrum. Additionally PCF induces a low frequency fluctuations over a much larger range of feedback levels. The applicability of existing theories to the current experimental data is also considered.

- [1] G. G. Gray, D. Huang, and G. P. Agrawal, Phys. Rev. A, Vol. 49, 2096 (1994).
- [2] D. DeTienne, G. G. Gray, G. P. Agrawal, and D. Lenstra, IEEE J. Quantum Electron. 33, 838 (1997).
- [3] K. Cronin-Golomb, K. Y. Lam, and A. Yariv, Appl. Phys. Lett. Vol. 47, 567 (1985).
- [4] S. Mailhot and N. McCarthy, Can. J. Phys. Vol. 71, 429 (1993).
- [5] E. Miltenyi, M. O. Ziegler, M. Hoffmann, J. Sacher, W. Elsasser, E. O. Gobel, and D. L. MacFarlane, Opt. Lett. Vol. 20, 734 (1995).

Suppression of coherence collapse in semiconductor diode lasers with short external cavities

J. S. Lawrence and D. M. Kane

Physics Department, Macquarie University, Sydney 2109, Australia

ph: 61 -2 9850 7901, fax: 61 -2 9850 8983

jl@ics.mq.edu.au, debkane@mpce.mq.edu.au

P. S. Spencer

School of Electronic Engineering and Computer Systems,

University of Wales, Bangor, LL57 1UT, UK

pauls@sees.bangor.ac.uk

Introducing optical feedback into semiconductor laser diodes can induce detrimental or advantageous effects, dependent on the level of the feedback. Advantageous effects, such as reduced laser linewidth, reduced operating threshold, and increased side mode suppression, occur for very low or strong feedback (regimes I, III, and V). However, at low to intermediate feedback levels (regime IV) the device operates in a coherence collapsed state, which is characterised by dynamic instabilities, a dramatically broadened noise spectrum, and an optical frequency spectrum which is predominantly multi-moded. In a real optical system there will always be unwanted feedback, arising from, for example, fibre optic end faces, couplers, or optical discs, which may cause such collapse of the coherence of the laser systems' output. Thus, it is important to understand what levels of optical feedback will produce a coherence collapsed state and how this is influenced by the solitary diode operating parameters (such as injection current and temperature) and the characteristics of the feedback field (such as feedback power, external cavity length, and feedback phase). Of particular significance for a number of short cavity applications (such as integrated feedback and frequency modulated devices) is how the coherence state of the diode is influenced by the length of the external cavity.

Based on a numerical analysis of the Lang-Kobayashi rate equations, predictions of the stability of diode lasers subject to optical feedback, dependent on the external cavity length have been reported [1]. The specific system investigated shows a stability which is dependent on the product of the external cavity round trip time (τ_{ext}) to the solitary diode relaxation oscillation frequency (ω_r). When this product is greater than one the critical feedback level for entering the coherence collapse regime (from the low feedback regime III) is independent of the external cavity length. For $\tau_{\text{ext}} \omega_r < 1$, the critical feedback level increases dependent on the external cavity length, until $\tau_{\text{ext}} \omega_r < f_{\text{const}}$ where the coherence collapsed state is suppressed and does not occur for any feedback level (f_{const} is a constant dependent on parameters of the solitary diode laser). Other theoretical analysis of short external cavity diode lasers [2],[3] predict similar behaviour with the addition of regions of high frequency oscillations for cavity lengths approaching the condition for suppression of coherence collapse.

In the present work the transition from both the strong feedback regime V, and the weak feedback regime III, to the coherence collapsed regime IV is examined experimentally. This is the first time, to our knowledge, that experiments examining the IV→V transition, and this suppression of coherence collapse for short external cavity lengths, has been reported. These three regimes have been investigated with an 850 nm quantum well index guided diode laser, which has an anti-reflection coated front facet, and a high reflection coated back facet. A 1300 nm quantum well uncoated diode laser is used to examine the III-IV transition. In particular the dependence of the critical feedback level, for transition to coherence collapse, on the solitary diode injection current, external cavity length, and feedback phase is considered. The theoretical models [1-3] have all been developed for diode lasers with symmetric facet reflectivities, and thus are not necessarily applicable to the high/ low coated 850 nm lasers used in the experiment.

It is found that the transition to chaotic operation from either stable feedback regime (III or V) is suppressed as the cavity length is shortened. The range of external feedback fractions giving chaotic operation is reduced as the external cavity length is reduced until at a particular cavity length no coherence collapse is observed. The length of the external cavity required for suppression of coherence collapse is dependent on the particular diode which is subjected to feedback. The anti-reflection coated diode exhibits no transitions to coherence collapse from either strong or weak feedback regimes for cavities less than 80 mm. This is shown in figures 1 and 2, below. The experimental observation of suppression of coherence collapse is theoretically predicted. However, the magnitude of the cavity lengths producing length dependent critical feedback levels, and suppression of coherence collapse is significantly larger than predicted theoretically. Similar behaviour has been observed for an uncoated diode laser. Cavity lengths responsible for suppression of coherence collapse (<10 mm) are much closer to expected theoretically values in this case. This may indicate the importance of the relative diode laser facet reflectivities. The introduction of coatings strongly influences the system behaviour, and the theory needs to be modified to take account of this.

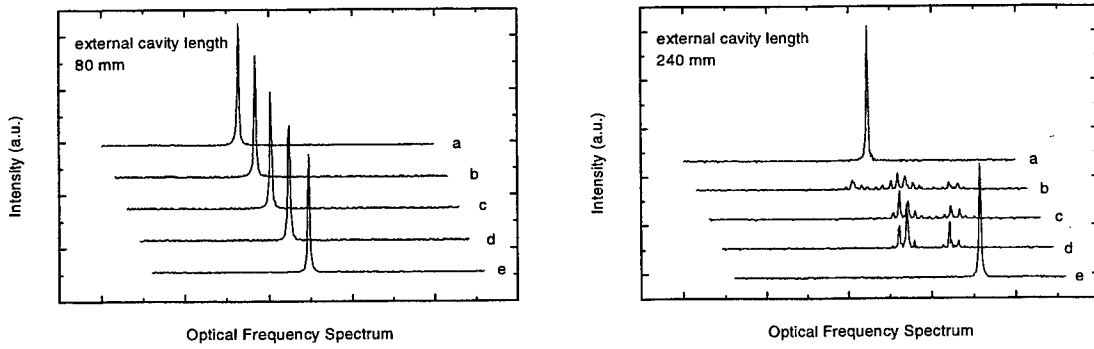


Figure 1: Optical frequency spectrum for different external feedback fractions for two different cavity lengths (80 mm, and 240 mm) at an injection current of 50 mA. The spectra marked a, b, c, d, e refer to feedback fractions of 0.4, 0.04, 0.004, 0.009 and 0.0004 respectively. Each plot shows approximately one free spectral range of 1000 GHz. For the short cavity the output is always stable single mode, no transition to coherence collapse is observed. For the longer cavity, coherence collapse (curves b, c, d) is observed for a large range of feedback fractions.

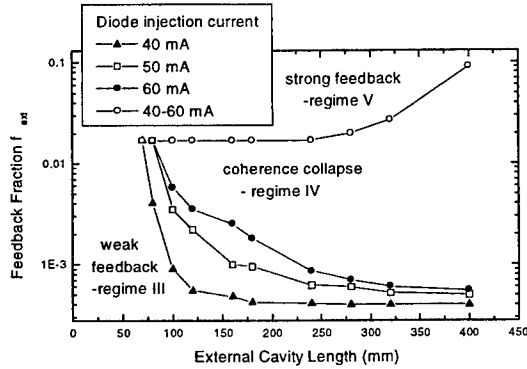


Figure 2 :Critical feedback level for transition to coherence collapse, as a function of external cavity length for a number of different diode injection currents. Feedback fraction is the ratio of emitted power from the front facet to reflected power at front facet.

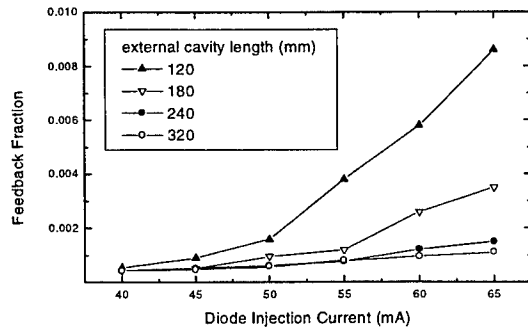


Figure 3: Critical feedback level for transition to coherence collapse -regime IV from stable single mode- regime III as a function of feedback fraction and diode injection current for several external cavity lengths.

The effect of the solitary diode laser operating current on the critical feedback levels for transition to coherence collapse has also been examined (for the high/ low coated diode laser). It is found that the transition between regimes IV and V is independent of the solitary laser diode injection current. The III to IV transition, however is dramatically influenced by the diode laser current, as shown in figures 2 and 3 above. At any particular cavity length, the region of chaotic instability is larger for lower injection currents. As the current is increased the region of stable operation also increases. Thus, at higher currents the external cavity length before transition to coherence collapse is largest. This again demonstrates the discrepancy between the theoretical model (for symmetric diodes) and the experimental data (for asymmetric diodes), as the theory predicts that the external cavity length before transition to coherence collapse should be shorter for higher injection currents because of the higher relaxation oscillation frequency. Thus, there is a need for a model which can account for both asymmetric facet reflectivities and strong feedback.

In conclusion, the critical feedback level for transition to coherence collapse as a function of external cavity length has been experimentally determined. For a high/ low reflectance coated diode laser it is found that for cavity lengths shorter than 80 mm the system is always stable single mode; no transition to coherence collapse is observed. This has important implications for a number of applications-including integrated and frequency modulated short cavity diode lasers. The applicability of existing theories for short cavity symmetric diode lasers to the current experimental observations will be reported [4].

- [1] N. Schunk and K. Petermann, IEEE Photonics Tech. Lett. Vol.1, 49 (1989).
- [2] A. A. Tager and K. Petermann, IEEE J. Quantum Electron. Vol. 30, 1553 (1994).
- [3] A. A. Tager and B. B. Elenkrig, IEEE J. Quantum Electron. Vol. 29, 2886 (1993).
- [4] P. S. Spencer and K. A. Shore, Quantum Semiclass. Opt. Vol. 9, 831 (1997).

Communication with Chaotic External Cavity Diode Lasers

S.Sivaprakasam and K.A.Shore

School of Electronic Engineering and Computer Systems, Dean Street,
University of Wales, Bangor, LL57 1UT, UK.

Tel: +44-1248-382618, Fax: +44-1248-361429
Email: alan@sees.bangor.ac.uk

Secure communication is of great interest in the recent past and efforts have been directed world-wide to develop novel techniques using chaotic lasers[1,2]. The underlying concept for such work is that the message should be encoded within the noise like output of a chaotic transmitter. Extraction of message requires a receiver in which the same chaos is generated as in the transmitter, which can be achieved by synchronization of the transmitter and receiver[2,3]. Because of the ease of operation of semiconductor lasers, it is of great interest to develop a chaotic communication system utilizing these lasers as the source of optical chaos. Useful progress in this direction has already been made by use of a novel form of wavelength chaos, for message encryption and decryption[4]. In the present work use is made of chaos in the laser output intensity.

The experimental arrangement is shown schematically in Figure 1 where two, commercial, single-mode, Fabry-Perot semiconductor lasers emitting at 850 nm have been used. Both the lasers are subjected to optical feedback from external mirrors, and the feedback strength is controlled using continuously variable neutral density filters (NDF1 and NDF2). The optical isolators ensure the lasers are free from back reflection. Isolator (OI1) ensures that the Laser-1 (transmitter) is isolated from Laser-2 (receiver). PD1 and PD2 are two identical fast photodetectors (2.5 nS). The photodetector outputs are stored in a digital storage oscilloscope (Fluke Combiscope PM3394B; 200MHz).

Because of the limitation imposed by the available oscilloscope we consider a part of that chaotic dynamics within a 200 MHz bandwidth of the central frequency. It is noted that the chaotic spectrum is relatively flat around the central frequency, and

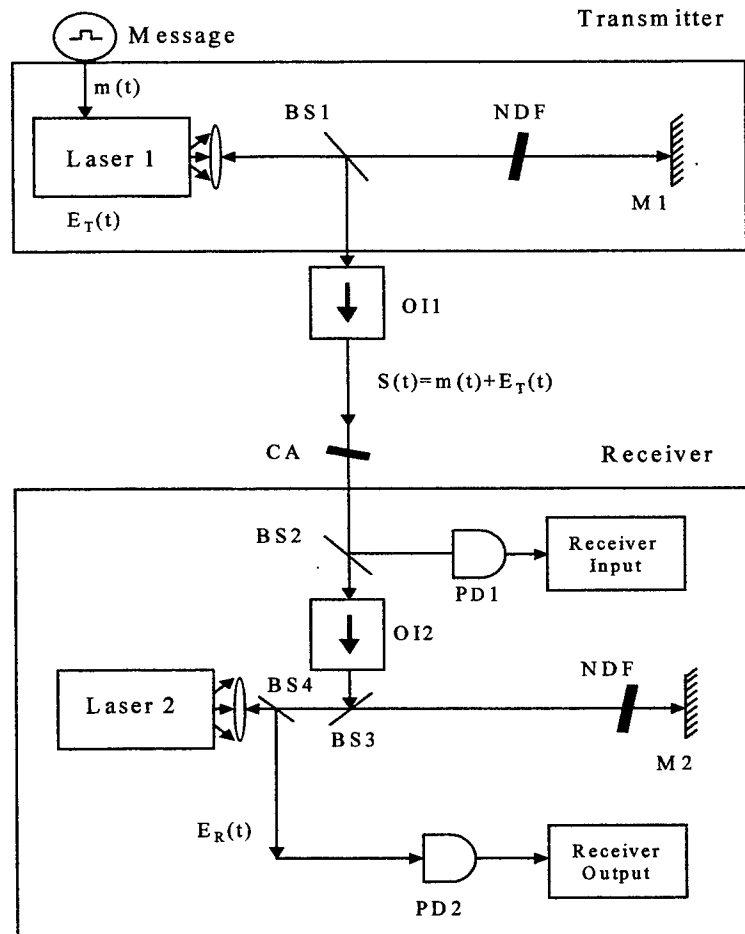


Fig. 1. Schematic diagram of experimental set-up. BS1-BS4, Beam splitters, PD1, PD2, Photodetectors, OI1, OI2, Optical Isolators, NDF, Neutral Density Filter, CA, Coupling Attenuator, M1, M2, Mirrors.

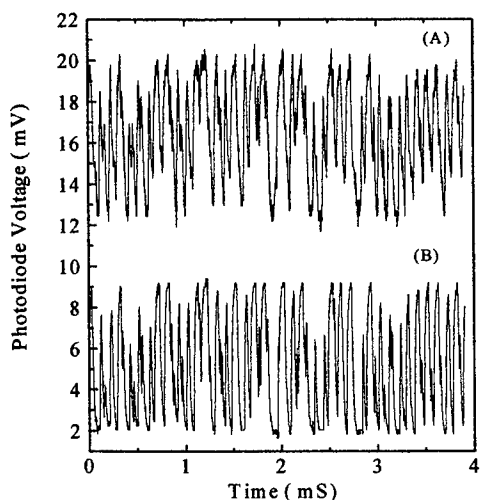


Fig. 2. Time traces of receiver input and output

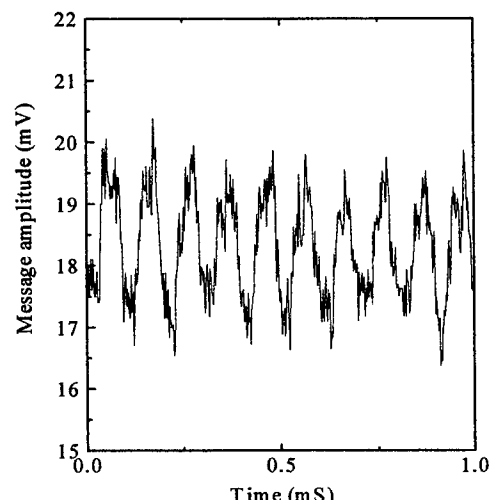


Fig. 3. Decoded message

thus the present measurements are expected to give a good representation of the dynamical behaviour of the lasers.

The output, $E_T(t)$, of the transmitter is rendered chaotic by appropriate optical feedback strength. A 9 KHz square wave, $m(t)$, from a signal generator is encrypted to the chaotic transmitter by amplitude modulation of the transmitter output. The receiver input is coupled to photodetector PD1 and its output is shown in figure 2, trace A. Trace A is shifted vertically for clarity. The receiver set-up is as identical to transmitter set-up as possible. The transmitted message is injected to the receiver by beam-splitter BS3. The receiver output is coupled to the photodetector PD2 and the output is shown in figure 2, trace B.

A similar technique to that followed by Van Wijgeren and Roy [2] is used to decode the message. The transmitted message $S(t) = E_T + m(t)$ is recorded from the output of photodetector PD1 as shown in figure 2, trace A. The intensities at the photodetectors PD1 and PD2 are thus $|E_T + m(t)|^2$ and $|E_R(t)|^2$ respectively. The message and the considered dynamics of diode lasers are on the same time scales, which allows us to recover the message by taking simple difference in the photodiode output intensities, without any filtering. This difference in photodetector intensities is shown in figure 3 and resembles the recovered 9-KHz square wave. Some processing of this signal (as performed in [2]) would be expected to lead to a recovered signal which is closer to the encrypted message.

References

1. S.Hayes, C.Grebogi and E.Ott, Phys. Rev. Lett. **70**, 3031 (1993).
2. G.D.Van Wijgeren and R.Roy, Science **279**, 1198 (1998).
3. S.Sivaprakasam and K.A.Shore, Optics Lett. **24**, April (1999).
4. J.P.Goedgebuer, L.Larger and H.Porte, Phys. Rev. Lett. **80**, 2249 (1998).

Transition to Pulsed Operation in Short External-Cavity FM Semiconductor Lasers

P. S. Spencer, D. M. Kane, and K. A. Shore

Abstract—Conditions are established for the occurrence of a transition from FM operation to pulsed output in short external-cavity FM semiconductor lasers. It is shown that there are dual operating points around which FM operation is possible. The position of the modulation frequency in relation to these two FM operating frequencies determines the type of behavior exhibited by the configuration. In particular, pulsed and mixed pulsed-FM behavior is observed when the modulation frequency is between the two possible FM operating frequencies.

Index Terms—Chaos, frequency modulation, optical feedback, optical pulses, semiconductor lasers.

I. INTRODUCTION

LASER external-cavity configurations have been studied extensively due to their importance for the practical operation of semiconductor lasers in optical fiber communications systems. It is known from such studies that the behavior of the laser can be broadly categorized into five regimes of operation, which are determined by the external environment the laser is subject to and, in particular, upon the strength of the optical feedback to the laser from the external mirror [1]. Such studies of optical feedback effects have generally considered the implications for single-mode lasers which are subject to optical feedback only at the lasing frequency. There are, however, several situations of practical interest where it is required to understand the dynamical and spectral behavior of lasers subject to variable frequency feedback.

One example of a laser system with variable frequency feedback is the frequency-shifted feedback (FSF) laser which is of interest for a number of practical applications. Previous work on FSF diode lasers has been directed at obtaining a high-brightness low-coherence broad-band source [2]–[4]. Broad-band sources would find ready applications in imaging, medical diagnosis, and optical measurements. More recently, the use of FSF has been explored to achieve optical isolation

of diode lasers [5]. It has been noted that some limitations on the performance of FSF laser diodes arise due to the onset of multimode operation at high injection current levels. In such a case, the broad-band lasing would be limited to relatively low output powers. Similar limitations had been reported earlier in connection with FSF effects on red-emitting laser diodes [2]. The challenge posed by that work was to find a practical configuration which would support broad-band operation at higher injection currents. In other laser systems, it has been shown that FSF modifies the spectral properties of the target laser in a characteristic way: a chirped comb of modes is generated [6] which, when time-averaged, appears as a broad-band spectrum which can be used for short pulse generation [7]. Recent work has included the use of a translated grating for FSF-based chirped frequency generation in a diode-pumped microchip laser [8].

It is also known [9], [10] that nonlinearities in semiconductor lasers can lead to the occurrence of self-locked FM lasing action which is a form of multimode operation where well-defined (Bessel function) sidebands are developed around a central frequency. The defining characteristic of such pure FM operation is a sinusoidal modulation of the lasing frequency whilst the total intensity remains constant in time. This is, in fact, a phenomenon which can arise in a number of laser systems. However, it seems to be generally the case that pure FM operation does not occur—some form of amplitude modulation is usually observed in association with the FM lasing. Although, as has just been indicated, self-locked FM lasing may arise in semiconductor lasers, attention has also been given to a range of phenomena which occur when semiconductor lasers are driven into FM operation by the use of external-cavity phase modulation [11]. Such a configuration offers another form of variable frequency feedback which influences the spectral and dynamical behavior of the laser. Applications of such a configuration have been identified for use in optical metrology, laser cooling of atoms, and in optical frequency multiplexing. FM laser operation can also occur in a laser subject to reflections from a moving mirror as may be obtained, for example, in a laser velocimeter configuration.

In order to describe phenomena arising in such a configuration, a general formalism capable of treating the dynamical properties of external-cavity FM laser diodes was developed in previous work [12]. In this work, attention was focused on effects arising due to the need to execute multiple reflections in the external cavity to achieve the enhanced modulation which is a requisite for obtaining broad-band sources. It is known

Manuscript received August 10, 1998; revised January 8, 1999. This work was supported by EPSRC under Grant GR/K80136 and in part by the Royal Society. The work of P. S. Spencer was supported by the Royal Society and Macquarie University which permitted a visit to MPCE, Macquarie University, where part of this work was undertaken. The work of K. A. Shore was supported by Macquarie University through a Visiting Research Scholarship.

P. S. Spencer and K. A. Shore are with the University of Wales, Bangor, School of Electronic Engineering and Computer Systems, Bangor LL57 1UT, Wales, U.K.

D. M. Kane is with the School of Mathematics, Physics, Computing and Electronics, Macquarie University, NSW 2109, Australia.

Publisher Item Identifier S 0018-9197(99)03419-3.

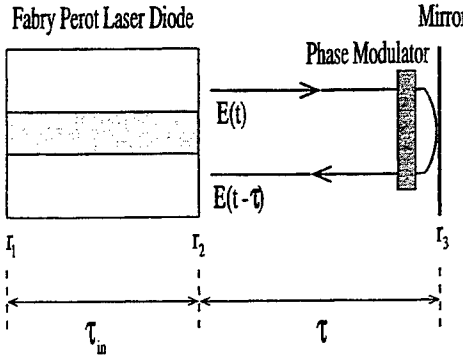


Fig. 1. Schematic diagram of a laser diode subject to optical feedback with a phase modulator inside the external cavity. The amplitude reflectivities of the laser and external cavity are denoted by r_1 , r_2 , and r_3 , respectively.

from experimental studies that, under certain conditions, an FM diode laser undergoes a dramatic change in spectral properties leading to a novel form of coherence collapse [11]. The relevant instability appears to be intrinsically dynamical. Previous studies, [9], [11], [16] have shown that a rather extensive range of phenomena can appear in this laser configuration depending upon the precise operating conditions. Of crucial importance in this respect is the length of the external cavity. Rather different phenomena will arise in the short- and long-cavity cases. A short external cavity is taken to be any cavity where the external cavity round-trip time is only a few tens of times larger than the internal round-trip time of the diode laser cavity. The present contribution will focus on the short-cavity case. Attention will be given to the critical role played by the coupled cavity configuration in the transition from FM operation to pulsed laser output. A further aspect which will be addressed in a parallel contribution is the generalization of the description of the behavior to class-B lasers—notably those where the linewidth enhancement factor is negligible.

II. MODEL

For the experimental situations of interest, the source of the variable frequency feedback is the phase change induced via the external-cavity phase modulation. A generic experimental arrangement is illustrated in Fig. 1 where appropriate (amplitude) reflectivities are indicated. The model described here is developed as a two-fold generalization of previous work on the dynamics of laser diodes subject to strong optical feedback [12]–[14]. In the first place, account is taken of the basic frequency modulation of the laser diode which is established via the phase modulation. Secondly, account is taken of additional phase modulation consequent to multiple passes of the external cavity [10].

The main elements of the iterative scheme used to model the configuration are described here. The iterative model is based on a perturbation approach [14]. The unperturbed state is assumed to be that of a solitary laser and the perturbation is provided by optical feedback. The slowly-varying envelope function of the field A is calculated in steps of the laser diode's

internal round-trip delay τ_{in} and is given by

$$A(t + \tau_{in}) = \frac{e^{G(1+i\alpha)\tau_{in}}}{r_2} \left(r_2 A(t) + r_3(1 - r_2) \right. \\ \left. + \sum_{q=1}^{\infty} (-r_2 r_3)^{q-1} A(t - q\tau) e^{-iq\Phi_E(t)} \right) \quad (1)$$

where $\omega_0 = 2\pi c/\lambda_0$ is the angular frequency of the solitary laser and $G = g_n(n - n_t)/2$. The last term in (1) accounts for multiple reflections and includes a phase term $\Phi_E(t)$ that describes the phase shift that develops between the field in the laser and the field in external cavity

$$\Phi_E(t) = \omega_0 \tau + \left(\Gamma \sin(\omega_m t) + \sum_{p=1}^q \delta_m \sin(\omega_m [t - (p-1)\tau]) \right). \quad (2)$$

The total phase accumulated in the external cavity consists of two main contributions. The first term in (2) describes the phase change associated with the central frequency ω_0 , while the two remaining terms within the parentheses describe the contribution of the phase modulator. The term $\Gamma \sin(\omega_m t)$ arises due to the basic phase modulation where ω_m is the modulation frequency and, following standard theories of FM lasers [15], we identify Γ as the enhanced modulation index. The last term, and the one of primary interest in the present context, is that due to the multiple reflections in the external cavity where on each pass of the cavity an additional phase change governed by the single-pass modulation index δ is impressed upon the laser field. The total phase change is then obtained via a summation over the number of multiple reflections p [12]. The third term in (2) accounts for the fact that, unlike other FM laser configurations based on gas and solid-state lasers, the facet reflectivity of the semiconductor laser facing the external reflector is appreciable and cannot be ignored.

The carrier density equation is incorporated into an iterative scheme by using a second-order Taylor expansion

$$n(t + \tau_{in}) \simeq n(t) + \tau_{in} \frac{dn}{dt} + \frac{\tau_{in}^2}{2} \frac{d^2n}{dt^2}. \quad (3)$$

The first-order derivative is simply the well-known standard carrier rate equation and the second order is found by differentiation

$$\frac{dn(t)}{dt} = \frac{I(t)}{eV} - \frac{n(t)}{\tau_e} - g_n(n - n_o)S(t). \quad (4)$$

In these equations, $S(t) = |A(t)|^2$ is the photon density inside the laser cavity. It is well appreciated that, in general, delay-differential equations such as (1) do not allow analytical solutions. Consequently, a full treatment of the phenomena arising in the configuration of interest requires a numerical solution of the equations.

TABLE I
DESCRIPTION AND VALUES OF LASER PARAMETERS

Symbol	Description	Value
r_1	Laser Facet Reflectivity	0.9
r_2	Laser Facet Reflectivity	0.15
r_3	External Facet Reflectivity	0.5 or 0.9
α	Linewidth enhancement factor	3.0
τ_s	Carrier lifetime	1.89 ns
τ_{ph}	Photon Lifetime	1.4 ps
τ_{in}	Laser cavity Round-Trip Delay	9.0 ps
τ	External Round-Trip Delay	0.279 ns
g_n	Differential Gain	$2.125 \times 10^{-12} m^3 s^{-1}$
n_{th}	Threshold Carrier density	$9.9 \times 10^{23} m^{-3}$
n_0	Transparency Carrier Density	$1.3 \times 10^{23} m^{-3}$
ω_0	Wavelength	1.55 μ m
V	Active Region Volume	$1.5 \times 10^{-16} m^3$
f_{ecl}	Axial Freq. of ECL operation	4.472 GHz
f_{ext}	Axial Freq. of EXT operation	3.584 GHz

III. RESULTS

The main parameters used in the following numerical simulation are given in Table I. It has been assumed that the laser is biased at 1.2 times the threshold current of the solitary laser. The output photon density has been normalized with respect to the steady-state value of the external-cavity laser.

A. Dual FM Operating Points

The experimental configuration under consideration is essentially that used by Willis and Kane [11] except that a short external cavity is being considered (see Fig. 1). The laser facet forming the external cavity has an antireflective coating to ensure that the external cavity is strongly coupled to the diode laser cavity. Thus, without the phase modulator in place, the laser configuration is that of an external-cavity laser (ECL). This implies that the laser configuration is operating in Regime V [1]. Without the external mirror, the antireflective-coated laser diode supports one longitudinal mode over a wide injection current range. Thus, the coupled cavity configuration has three characteristic round-trip times: the solitary lasers (τ_{in}), the external cavity (τ), and the external cavity laser ($\tau_{in} + \tau$). It is worth noting that the other laser systems that have exhibited FM operation have generally consisted of one cavity and thus have only one characteristic round-trip time. Hence, such systems show considerably different dynamical behavior from that of the coupled cavity configuration under investigation here.

When the external round-trip time is only a few tens of times larger than the internal round-trip time of the laser diode, the ECL axial frequency $f_{ecl} = 1/(\tau_{in} + \tau)$ and the frequency associated with the external cavity $f_{ext} = 1/\tau$ are sufficiently separated to be discernible. This opens the possibility of inducing FM operation around two operation points:

- modulating around the external-cavity mode frequency $f_{ext} = 1/\tau$;
- modulating around the ECL frequency $f_{ecl} = 1/(\tau_{in} + \tau)$.

It will be shown, using the formalism outlined in Section II, that the relative magnitude of r_3 with respect to r_2 determines

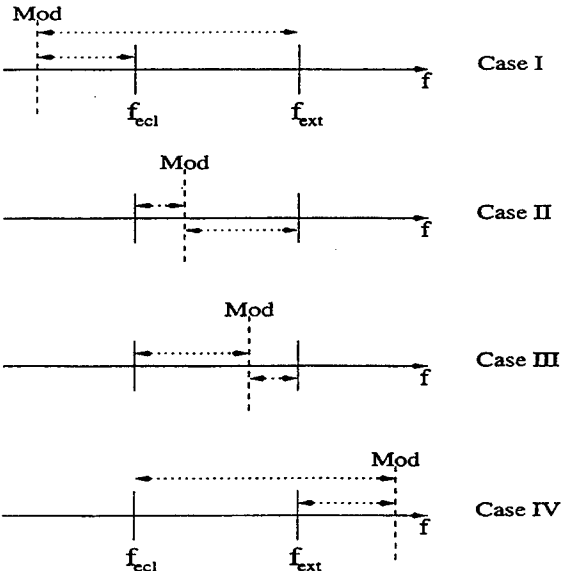


Fig. 2. Frequency diagram showing the position of the modulation frequency (denoted as Mod) in relationship to the dual operating points f_{ecl} and f_{ext} for different cases considered.

the dominant operating point. In the following simulation, the value of r_2 will be kept constant while r_3 is varied. The position of the modulation frequency above or below the dominant operating frequency and the magnitude of the frequency detuning from the operating frequency will be shown to determine whether pulsed or FM operation is obtained.

Four different modulation frequencies and two different values of r_3 will be used to illustrate the behavior described above (see Fig. 2). The position of the modulation frequency relative to f_{ecl} and f_{ext} is shown in Fig. 2. The ECL dominates when r_3 is large, while the external cavity dominates when r_3 is small.

If the value of r_2 is too high, then r_3 cannot be made sufficiently large to make external-cavity operation possible, and the reduced optical coupling from the external cavity this implies drastically reduces the influence of the phase modulator. Lower values of r_2 inhibit operation around f_{ext} but are practically difficult to achieve because alignment of the external optic becomes critical in order to obtain lasing.

B. FM Operation

FM operation is obtained in Case I and Case IV of Fig. 2, but only if the detuning frequencies are sufficiently large. In this case, FM operation is obtained regardless of whether the ECL mode or external-cavity mode is the dominant operating point. Typical spectra and the accompanying photon densities are shown in Figs. 3 and 4, respectively, for $r_3 = 0.5$ and $r_3 = 0.9$. Changing the dominant operating point only changes the FM bandwidth (as determined by the detuning); hence, the bandwidth of Fig. 4(a) is larger than that of Fig. 3(a). At some point, as the modulation frequency is tuned toward f_{ecl} , FM operation is lost when $r_3 = 0.9$ because the modulation frequency is too close to the dominant operating point. However, if the external reflectivity is reduced ($r_3 =$

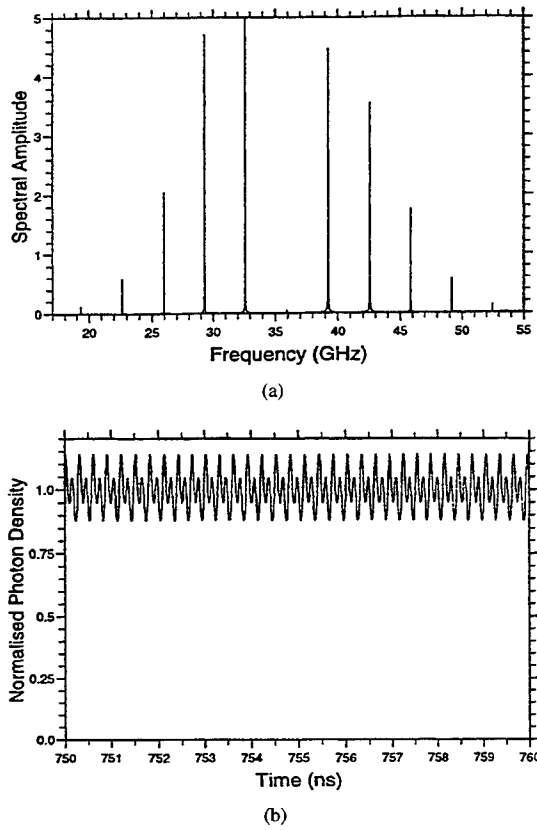


Fig. 3. FM operation is obtained when the modulation frequency is below f_{ext} . (a) Spectral profile when $r_3 = 0.5$ and $f_{\text{mod}} = 3.32$ GHz, and f_{ext} is the dominant operating point. (b) Corresponding temporal evolution of the normalized photon density.

0.5) such that the dominant operating point is now f_{ext} , the detuning is still sufficiently large to allow FM modulation referenced to f_{ext} (see Fig. 2).

The above discussion is also valid for Case IV, except in this case the external-cavity mode is the first to lose FM operation as the modulation frequency is tuned toward f_{ext} .

The temporal evolution of the normalized photon density in both Figs. 3(b) and 4(b) are modulated. The modulation arises because the linewidth enhancement factor α couples the phase and the amplitude of the optical field.

The presence of the external mirror causes a reduction in the threshold of the coupled-cavity configuration, compared to that of the solitary laser. The higher the external mirror reflectivity, the lower the threshold. Additional simulations have been undertaken to ensure that the difference in behavior, exhibited when $r_3 = 0.5$ or $r_3 = 0.9$, is not a consequence of the different thresholds.

C. Intermediate Regime of Mixed FM and Pulsed Operation

The behavior exhibited when the modulation frequency is between f_{ext} and f_{ext} is critically dependent on the frequency detuning relative to the dominant operating point. If the modulation frequency is very close to the dominant operating point (Case II with f_{ext} dominant and Case III with f_{ext} dominant) pulsed operation is obtained (see Fig. 5). As the

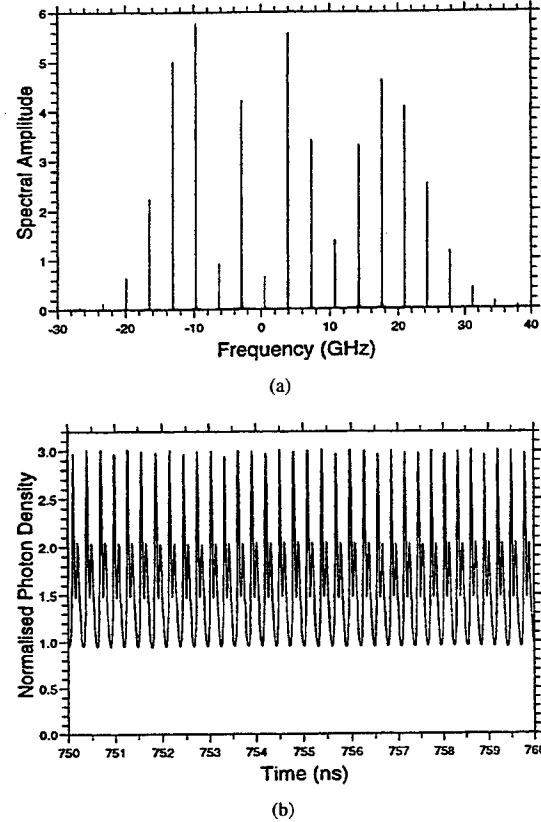
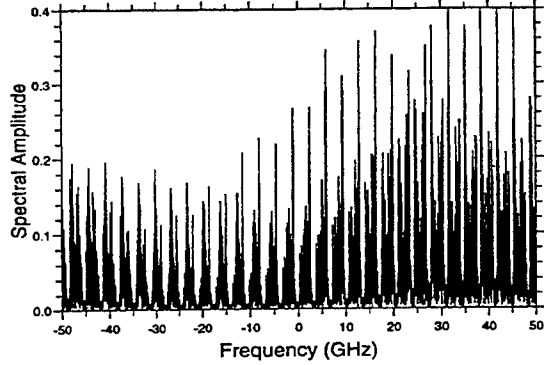


Fig. 4. FM operation obtained when the modulation frequency is below f_{ext} . (a) Spectral profile when $r_3 = 0.9$ and $f_{\text{mod}} = 3.40$ GHz, and f_{ext} is the dominant operating point. (b) Corresponding temporal evolution of the normalized photon density.

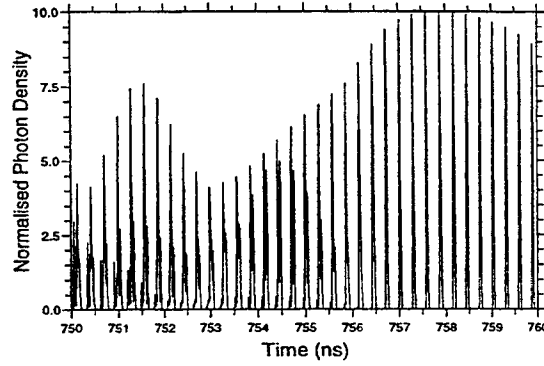
modulation frequency is moved away from the dominant operating point, a narrow intermediate regime can be identified where mixed pulsed and FM-like operation is obtained (see Fig. 6). The mixed behavior occurs because the detuning from the dominant operating point is nearly sufficient to allow FM operation, but it is also sufficiently close to the weaker operating point for its presence to be felt. This effect can be seen in Fig. 6 where side modes around each of the main spectral peaks are evident. The frequency difference between the main mode and the side modes corresponds to multiples of $f_{\text{ext}} - f_{\text{ext}}$. In this intermediate regime, a resonant enhancement-type effect is responsible for increasing the significance of the weaker operating point by inducing frequency pulling that excites modes associated with the weaker operating point.

As the modulation is tuned further toward the weaker operating point, pulsed operation is reestablished. The presence of the dominant operating point is effectively screened because the modulation frequency is so close to the weaker operating point.

A schematic representation of the different regimes of operation is shown in Fig. 7. Fig. 7(a) assumes that f_{ext} is the dominant operating point while Fig. 7(b) assumes that f_{ext} is the dominant frequency. The diagonal hatched regions indicate the operating point with which pulsed operation is associated.



(a)



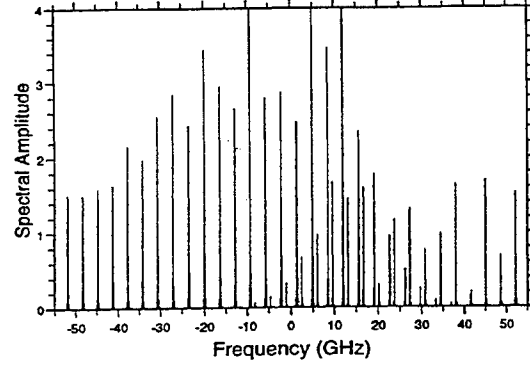
(b)

Fig. 5. Pulsed operation obtained when the modulation frequency is sufficiently close to one of the operating points. In this case, f_{ecl} . (a) Spectral profile when $r_3 = 0.5$ and $f_{\text{mod}} = 3.506$ GHz. (b) Corresponding temporal evolution of the normalized photon density.

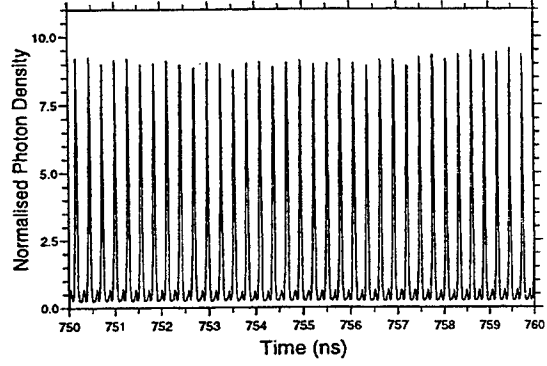
The region between the two pulsed regions denotes the mixed pulsed-FM regime of operation.

The temporal evolution of the normalized photon density shows that a very deep regular modulation is present in the intermediate regime [see Fig. 6(b)]. The modulation actually consists of two sinusoidal oscillations of very different amplitudes, but the same frequency. The frequency is in fact the FM modulation frequency. Each of the oscillations can be associated with one of the operating points, with the dominate point giving rise to the larger oscillation. In the pulsed regime, the repetition rate is f_{ecl} , but the pulse shape varies considerably [see Fig. 5(b)]. The pulse shape distortion can be attributed to two effects: the residual influence of the weaker operating point and amplitude-phase coupling effects mediated by the linewidth enhancement factor.

When the modulation frequency is tuned very close (typically frequency detuning <1 MHz) to either of the operating points, the amplitude of the pulses becomes very irregular when viewed over longer time scales, but the pulse separation remains constant. Apart from the regular spacing between the pulses, the photon density temporal evolution is similar to coherence collapse behavior near threshold. However, the constant pulse separations result in a spectrum that has considerable periodicity and is thus quite different from that seen in the coherence collapse regime. This observation, in



(a)



(b)

Fig. 6. Mixed FM and pulsed operation obtained when the weaker operating inhibits FM operation about f_{ecl} . (a) Spectral profile when $r_3 = 0.9$ and $f_{\text{mod}} = 3.548$ GHz. (b) Corresponding temporal evolution of the normalized photon density.

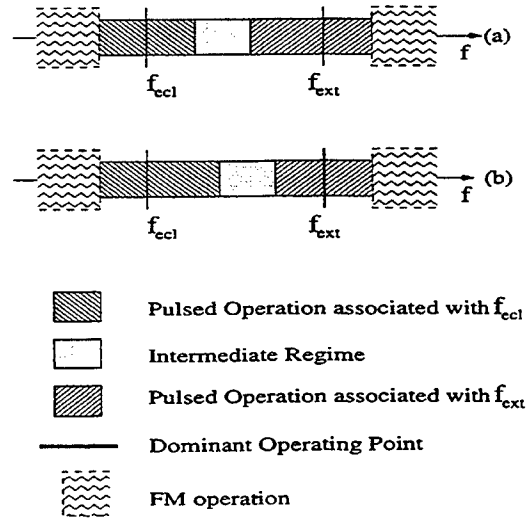


Fig. 7. Frequency diagram showing the position of the pulsed and intermediate regimes when (a) f_{ecl} is the dominant operating point and (b) f_{ext} is the dominant operating point.

conjunction with the fact that all the simulations assumed that the laser diode was biased well above threshold, suggest that coherence collapse, as it usually is understood, is not induced.

The effects described above are only clearly visible in short external cavities since the difference between f_{ecl} and f_{ext} reduces as the external cavity gets larger. Once the two frequencies are no longer discernible, only two types of behavior can occur: FM operation and coherence-collapse-like operation, [1]. Regular pulsed operation is not observed in this case because both operating points are effectively indistinguishable. The ratio between the external and solitary laser round-trip time determines whether the separation between f_{ecl} and f_{ext} is sufficiently large to distinguish these two possible operating points. If, for simplicity, we assume that τ is an integral multiple of τ_{in} , then

$$\frac{f_{\text{ext}}}{f_{\text{ecl}}} = \frac{n}{1+n}. \quad (5)$$

The nearer the ratio $n/(n+1)$ is to unity, the smaller the separation between f_{ext} and f_{ecl} and, hence, the two operating points become degenerate. The two frequencies are only distinguishable if n is sufficiently small.

IV. CONCLUSIONS

This paper has examined in some detail the spectral and dynamical behavior in an external cavity FM laser diode configuration. Attention has been restricted to phenomena arising in the so-called short-cavity case. As indicated above, quite a broad range of phenomena can actually appear in this configuration. In particular, two operating points can be identified, associated with ECL modes and external-cavity modes. The magnitude of the external mirror reflectivity determines the dominant operating point, and the relative position of the modulation frequency in relation to the dominant operating point determines whether pulsed or FM operation is observed. The analysis has indicated under what conditions both pulsed and FM operation can be obtained. Both types of operation have important practical applications [2], [3], [6].

The investigations have also revealed that phenomena arising here are not restricted to semiconductor lasers. Specifically, it has been found that several features of the behavior are independent of the cavity detuning represented via the linewidth enhancement factor of semiconductor lasers. The exploration of such phenomena in more general laser systems will be the subject of a future contribution [17].

REFERENCES

- [1] R. W. Tkach and A. R. Chaplyvny, "Regimes of feedback effects in 1.5 μm distributed feedback lasers," *J. Lightwave Technol.*, vol. 4, pp. 1655-1661, 1985.
- [2] P. I. Richter and T. W. Hänsch, "Diode lasers in external cavities with frequency-shifted feedback," *Opt. Commun.*, vol. 85, pp. 414-418, 1991.
- [3] J. Martin, Y. Zhao, S. Balle, K. Bergmann, and M. P. Fewell, "Visible-wavelength diode lasers with frequency-shifted optical feedback," *Opt. Commun.*, vol. 112, pp. 109-121, 1994.
- [4] A. P. Willis, A. I. Ferguson, and D. M. Kane, "External cavity diode lasers with frequency shifted feedback," *Opt. Commun.*, vol. 116, pp. 87-93, 1995.
- [5] K. W. Benoist, "The influence of external frequency shifted feedback on a DFB semiconductor laser," *IEEE Photon. Technol. Lett.*, vol. 8, pp. 25-27, 1996.
- [6] S. Balle, I. C. M. Littler, K. Bergmann, and F. V. Kowalski, "Frequency shifted feedback dye laser operating at a small frequency shift," *Opt. Commun.*, vol. 102, pp. 166-174, 1993.
- [7] P. D. Hale and F. V. Kowalski, "Output characterization of a frequency shifted feedback laser: Theory and experiment," *IEEE J. Quantum Electron.*, vol. 26, pp. 1845-1851, 1990.
- [8] K. Nakamura, F. V. Kowalski, and H. Ito, "Chirped frequency generation in a translated grating type frequency shifted feedback laser," *Opt. Lett.*, vol. 22, pp. 889-891, 1997.
- [9] K. A. Shore and W. M. Yee, "Theory of self-locking FM operation in semiconductor lasers," *Proc. Inst. Elect. Eng.*, pt. J, vol. 138, pp. 91-96, 1991.
- [10] W. M. Yee and K. A. Shore, "Multimode analysis of self-locked FM operation in laser diodes," *Proc. Inst. Elect. Eng.*, pt. J, vol. 140, pp. 21-25, 1993.
- [11] A. P. Willis and D. M. Kane, "Modulation induced coherence collapse: The collapse of side mode suppression in external cavity diode lasers," *Opt. Commun.*, vol. 111, pp. 577-588, 1994.
- [12] K. A. Shore and D. M. Kane, "Cavity decoupling in external cavity FM diode lasers," *Electron. Lett.*, vol. 33, pp. 50-51, 1997.
- [13] L. N. Langley, K. A. Shore, and J. Mork, "Dynamics and noise properties of semiconductor lasers subject to strong optical feedback," *Opt. Lett.*, vol. 19, pp. 2137-2139, 1994.
- [14] P. S. Spencer and K. A. Shore, "Multimode iterative analysis of the dynamic and noise properties of laser diodes subject to optical feedback," *J. Eur. Opt. Soc. B, Quantum and Semi. Optics*, vol. 9, pp. 819-830, 1997.
- [15] S. E. Harris and O. P. McDuff, "Theory of FM laser oscillation," *IEEE J. Quantum Electron.*, vol. QE-1, pp. 245-262, 1965.
- [16] P. S. Spencer, D. M. Kane, and K. A. Shore, "Coupled-cavity effects in FM semiconductor lasers," *J. Lightwave Technol.*, to be published.
- [17] ———, "FM lasing phenomena in class-B external cavity lasers," unpublished.

P. S. Spencer, photograph and biography not available at the time of publication.

D. M. Kane, photograph and biography not available at the time of publication.

K. A. Shore, photograph and biography not available at the time of publication.

Coupled-Cavity Effects in FM Semiconductor Lasers

P. S. Spencer, D. M. Kane, and K. Alan Shore, *Member, OSA*

Abstract—Numerical simulations of frequency modulated (FM) external cavity semiconductor lasers have been performed and a range of dynamic and spectral phenomena observed. It is shown that FM lasing action can be suppressed due to changes in the FM modulation frequency. Coupled cavity effects are seen to be significant in the development of a broad spectral emission associated with experimentally observed coherence collapse in such a configuration.

Index Terms—FM operation, optical feedback, semiconductor laser.

I. INTRODUCTION

THE study of the effects of optical feedback on the spectral, noise and dynamical properties of semiconductor lasers has been an active area of research for 20 years. Nevertheless, a full characterization of the properties of laser diodes subject to optical injection and optical feedback remains to be achieved and continued efforts are being made toward that aim. Progress on the theory has been reviewed recently in [1] and [2]. Tkach and Chraplyvy [3] have classified the behavior of semiconductor lasers subject to optical feedback according to five regimes of operation—conventionally termed regimes I–V. So, e.g., regime IV is associated with coherence collapse, the appearance of broad spectral features, whilst regime V corresponds to stable external cavity behavior. In regimes I–III the laser properties are, unfortunately, sensitively dependent not only on the strength of the optical feedback but also on the phase of the returned light and thus on the length of the external cavity.

The focus of these efforts has been on single longitudinal mode semiconductor lasers subject to optical feedback, for the purpose of maintaining the spectral purity required, for example, in high bit rate optical communication systems. Additionally, the system of semiconductor laser operated with an external cavity laser (ECL) may lead to output with very different characteristics if the light in the external cavity is modified before being fed back into the laser diode. When the light is phase modulated, (using an electrooptic (EO) phase modulator, in the external cavity), the ECL can provide large bandwidth frequency modulated (FM) output for applications in frequency division multiplexing and optical metrology. In this case the ECL is operated as an FM laser [4]. When the

Manuscript received July 9, 1998; revised February 23, 1999. This work was supported by the EPSRC under GR/K80136. The work of P. S. Spencer was supported by the Royal Society Study Visit Grant and Macquarie University which permitted a visit to MPCE, Macquarie University, where part of this work was undertaken. The work of K. A. Shore was supported as a Macquarie University Visiting Research Scholar.

P. S. Spencer and K. A. Shore are with the School of Electronic Engineering and Computer Systems, University of Wales, Bangor LL57 1UT U.K.

D. M. Kane is with the School of Mathematics, Physics, Computing and Electronics, Macquarie University, NSW 2109 Australia.

Publisher Item Identifier S 0733-8724(99)04513-2.

light is frequency shifted, (using an acoustooptic modulator in an external cavity), then the ECL can give high brightness, low coherence output for applications in imaging, medical diagnostics, and optical measurement. In this case the ECL is a frequency shifted feedback (FSF) laser [5]. If the levels of frequency shifted feedback are very low the FSF laser may be optically isolated from the optical feedback, [6]. Due to coupled cavity effects and the non zero linewidth enhancement factor of semiconductor laser the dynamics of both the FM ECL [7], [8] and the FSF ECL [9]–[12] configurations are found, in practice, to be different to those of the standard FM laser or FSF laser. Thus there are a number of ECL's of practical interest where it is required to understand the dynamical and spectral behavior of semiconductor lasers subject to modified optical feedback. In the present work a model of a FM ECL is implemented.

An FM laser is produced by including an EO phase modulator in the laser cavity. Such an FM laser has an enhanced modulation index, $\Gamma \propto \omega_o/(\omega_o - \omega_m)$, where ω_o is the axial angular frequency and ω_m is the modulation frequency, [4]. It is the enhancement of the modulation index within the laser cavity that gives the opportunity to generate very broadband FM laser output, where well-defined (Bessel function) sidebands are developed around a central frequency. The defining characteristic of such pure FM operation is a sinusoidal modulation of the lasing frequency whilst the total intensity remains constant in time. However, it seems to be generally the case that pure FM operation does not occur—some form of amplitude modulation is usually observed, to a greater or lesser extent, in association with the FM lasing. Additionally, the FM ECL undergoes a dramatic change in spectral properties [7], [8], leading to a novel form of coherence collapse. The relevant instability, which appears to be intrinsically dynamical, is acting on an ECL which is being operated in regime V.

A general formalism capable of treating the dynamical properties of external cavity FM laser diodes was developed in previous work [13]. Attention was focussed on effects arising due to the need to execute multiple reflections in the external cavity in order to achieve the enhanced modulation which is a requisite for obtaining broad-band sources. The aim of our subsequent work has been to broaden the examination of the dynamical and spectral behavior of the device with a view to demonstrating the changes in behavior which may be identified as precursors of the observed coherence collapse. It has been found in these investigations that a rather extensive range of phenomena can appear in the FM ECL configuration, depending upon the precise operating conditions. Of crucial importance in this respect is the length of the external cavity. Rather different phenomena will arise in the short and long cavity cases. Here, a long cavity is taken to be any cavity

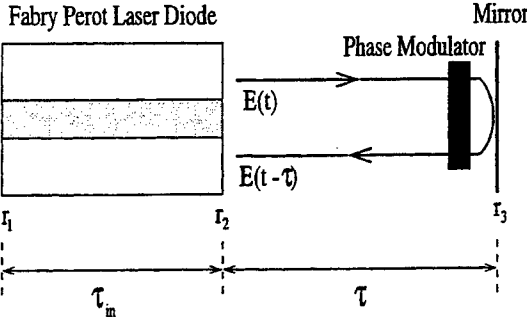


Fig. 1. Schematic diagram of a laser diode subject to optical feedback with a phase modulator inside the external cavity. The amplitude reflectivities of the laser and external cavity are denoted by r_1 , r_2 , and r_3 , respectively.

where the external cavity round-trip time is much greater than the internal round-trip time of the diode laser cavity. The emphasis of the present contribution will be to focus on the long cavity case. In complementary work attention will be given to a transition from FM operation to pulsed laser output in the short cavity case [16].

II. MODEL

For the experimental situations of interest the source of the variable frequency feedback is the phase change induced via the external cavity phase modulation. A generic experimental arrangement is illustrated in Fig. 1 where appropriate (amplitude) reflectivities are indicated. The model described here is developed as a two-fold generalization of previous work on the dynamics of laser diodes subject to strong optical feedback [14], [15]. In the first place, account is taken of the basic frequency modulation of the laser diode which is established via the phase modulation. Second, account is taken of additional phase modulation consequent to multiple passes of the external cavity [13].

The main elements of the iterative scheme used to model the configuration are described here. The iterative model is based on a perturbation approach [15]. The unperturbed state is assumed to be that of a solitary laser and the perturbation is provided by optical feedback. The slowly varying envelope function of the field A is calculated in steps of the laser diode's internal round-trip delay, τ_{in} , and is given by

$$A(t + \tau_{in}) = \frac{e^{G(1+i\alpha)\tau_{in}}}{r_2} \left[r_2 A(t) + r_3 (1 - r_2^2) \cdot \sum_{q=1}^{\infty} (-r_2 r_3)^{q-1} A(t - q\tau) e^{-iq\Phi_E(t)} \right] \quad (1)$$

where $\omega_0 = 2\pi c/\lambda_0$ is the angular frequency of the solitary laser, and $G = g_N (N - N_{th})/2$. The last term in (1) accounts for multiple reflections and includes a phase term, $\Phi_E(t)$ that describes the phase shift that develops between the field in the laser and the field in external cavity

$$\Phi_E(t) = \omega_0 \tau + \Gamma \sin(\omega_m t) + \sum_{p=1}^q \delta_m \sin(\omega_m [t - (p-1)\tau]). \quad (2)$$

TABLE I
DESCRIPTION AND VALUES OF LASER PARAMETERS

Symbol	Description	Value
r_1	Laser Facet Field Reflectivity	0.566
r_2	Laser Facet Field Reflectivity	0.2
r_3	External Facet Field Reflectivity	0.5
α	Linewidth enhancement factor	4.0
τ_s	Carrier lifetime	1.8 ns
τ_{ph}	Photon Lifetime	1.8 ps
τ_{in}	Laser cavity Round-Trip Delay	9.0 ps
τ	External Round-Trip Delay	2.7 ns
g_N	Differential Gain	$2.125 \times 10^{-12} m^3 s^{-1}$
N_{th}	Threshold Carrier density	$9.9 \times 10^{23} m^{-3}$
N_0	Transparency Carrier Density	$1.3 \times 10^{23} m^{-3}$
δ_m	Single pass modulation index	0.02
λ_0	Wavelength	1.55 μm
V	Active Region Volume	$1.5 \times 10^{-16} m^3$

The total phase accumulated in the external cavity consists of two main contributions. The first term in (2) describes the phase change associated with the central frequency, ω_0 . While the two remaining terms describe the contribution of the phase modulator. The term $\Gamma \sin(\omega_m t)$ arises due to the basic phase modulation where ω_m is the modulation frequency and, following standard theories of FM lasers [4], we identify Γ as the enhanced modulation index. The last term, and the one of primary interest in the present context, is that due to the multiple reflections in the external cavity where on each pass of the cavity an additional phase change governed by the single-pass modulation index δ_m is impressed upon the laser field. The total phase change is then obtained via a summation over the number of multiple reflections p .

The carrier density equation is incorporated into an iterative scheme by using a second-order Taylor expansion

$$N(t + \tau_{in}) \simeq N(t) + \tau_{in} \frac{dN}{dt} + \frac{\tau_{in}^2}{2} \frac{d^2N}{dt^2}. \quad (3)$$

The first-order derivative is simply the well-known standard carrier rate equation and the second order is found by differentiation

$$\frac{dN(t)}{dt} = \frac{I(t)}{eV} - \frac{N(t)}{\tau_e} - g_N(N - N_o)S(t). \quad (4)$$

In these equations $S(t) = |A(t)|^2$ is the photon density inside the laser cavity. It is well appreciated that, in general, delay-differential equations such as (1) do not allow analytical solutions. Consequently a full treatment of the phenomena arising in the configuration of interest requires a numerical solution of the equations.

III. DYNAMICS OF EXTERNAL CAVITY FM OPERATION

The parameters used in the numerical simulations (Table I) were chosen to model the experimental arrangement used by Willis and Kane, [8]. In their setup, the laser facet forming the external cavity had an antireflective coating to ensure that the external cavity is strongly coupled to the diode laser cavity. Thus, without the phase modulator in place, the laser configuration is that of an ECL. This implies that the laser configuration is operating in Regime V, [3]. It is worth noting that without the external mirror the antireflective

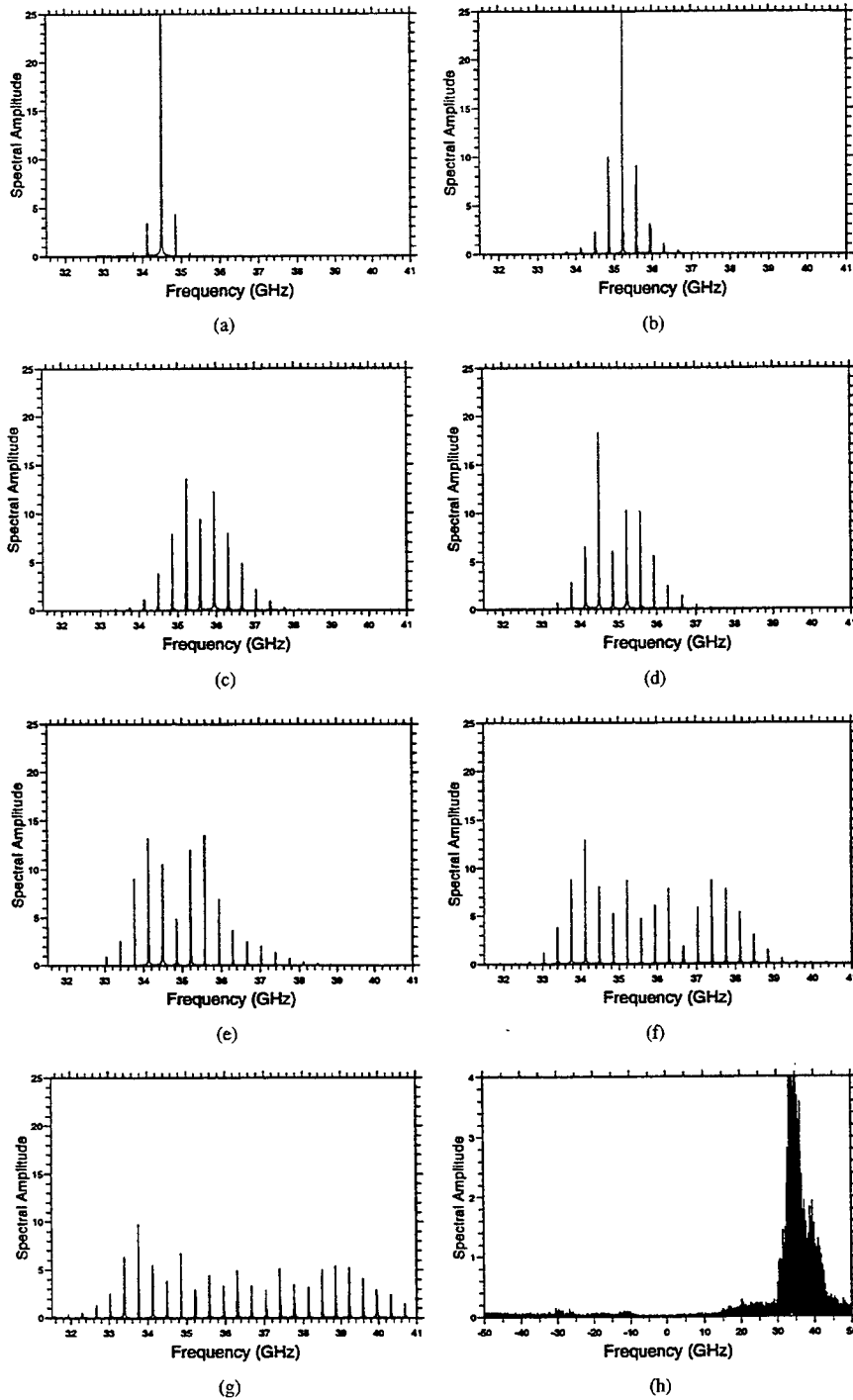


Fig. 2. Spectral profiles obtained as the modulation frequency is tuned toward resonance: (a) unmodulated case, (b) $\omega_m = 351.85$ MHz, (c) $\omega_m = 359.25$ MHz, (d) $\omega_m = 360.37$ MHz, (e) $\omega_m = 362.22$ MHz, (f) $\omega_m = 362.96$ MHz, (g) $\omega_m = 363.88$ MHz, and (h) $\omega_m = 364.07$ MHz.

coated laser diode supports one longitudinal mode over a wide injection current range. Thus, the coupled cavity configuration has three characteristic round-trip times: the solitary lasers, (τ_{in}), the external cavity, (τ), and the external cavity laser, ($\tau_{in} + \tau$). In contrast, the other laser systems that have exhibited FM operation have, generally, consisted of only one cavity and consequently have one characteristic round-

trip time. Hence, such system show considerably different dynamical behavior to that of coupled cavity configuration under investigation here.

Placing a phase modulator in the external cavity of the laser diode causes significant changes in both the spectral features and power dynamics. The numerical results obtained here are in good agreement with the experimental results previously

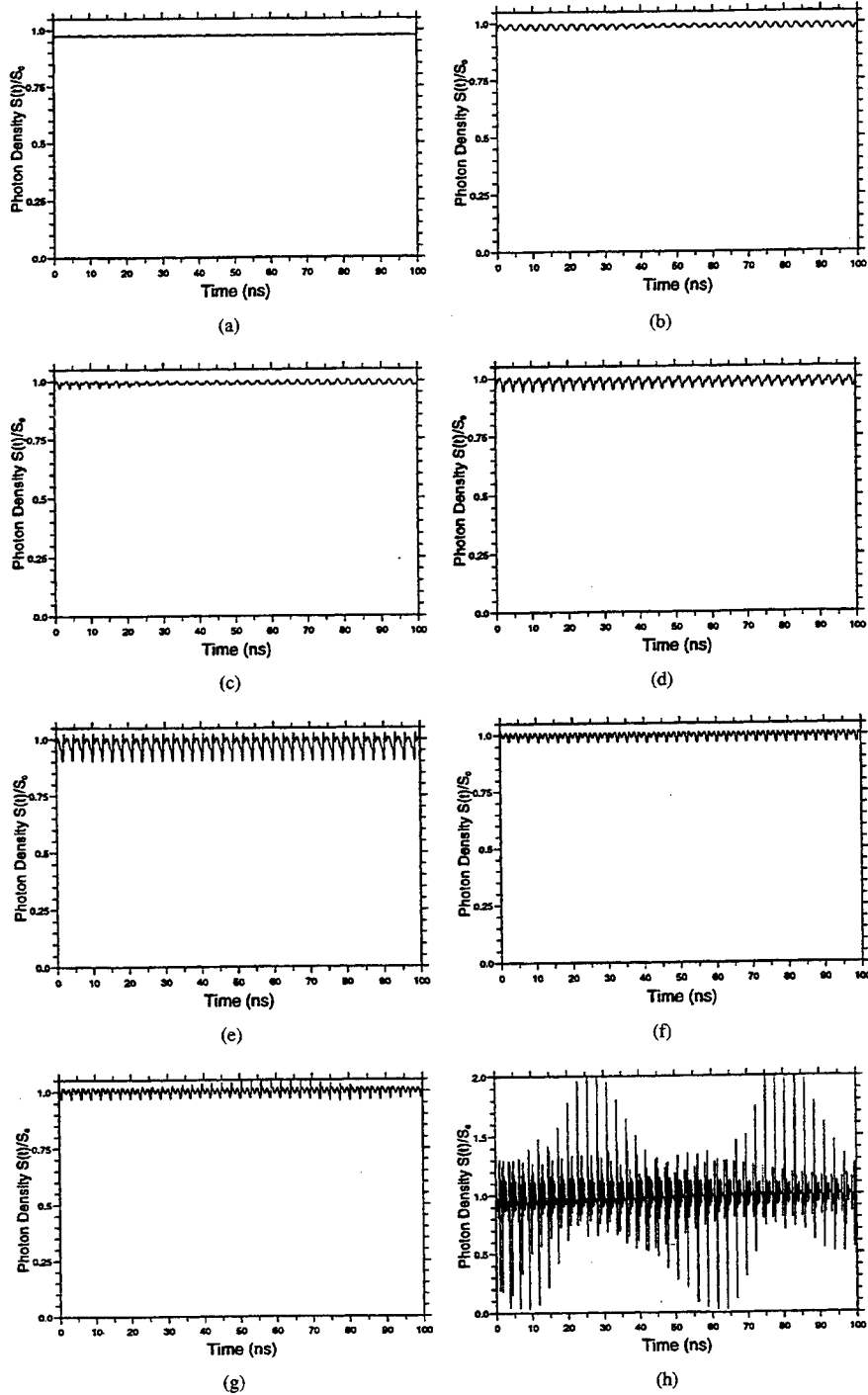


Fig. 3. Temporal scans of the photon density profiles (normalized with respect to ECL steady state value S_0) associated with the spectral profiles of Fig. 2: (a) unmodulated case, (b) $\omega_m = 351.85$ MHz, (c) $\omega_m = 359.25$ MHz, (d) $\omega_m = 360.37$ MHz, (e) $\omega_m = 362.22$ MHz, (f) $\omega_m = 362.96$ MHz, (g) $\omega_m = 363.88$ MHz, and (h) $\omega_m = 364.07$ MHz.

reported by Willis and Kane. In all the simulations that follow the laser is electrically pumped at three time threshold value of the solitary laser.

It is well known from general FM theory that tuning the modulation frequency toward the axial frequency increases the FM bandwidth. This effect can clearly be seen in Fig. 2(a)–(g) where typical FM RF-spectra are observed. Fig. 2(a) shows the

spectrum of the ECL without phase modulation, weak side-modes at $1/\tau$ are evident because the laser facet reflectivity r_2 is not zero. The spectrum is not centred around zero because the external cavity, in conjunction with the linewidth enhancement factor induces a shift in the central laser frequency from that of the solitary laser. It should also be noted that in Fig. 2(a) the graph has been clipped to aid comparison,

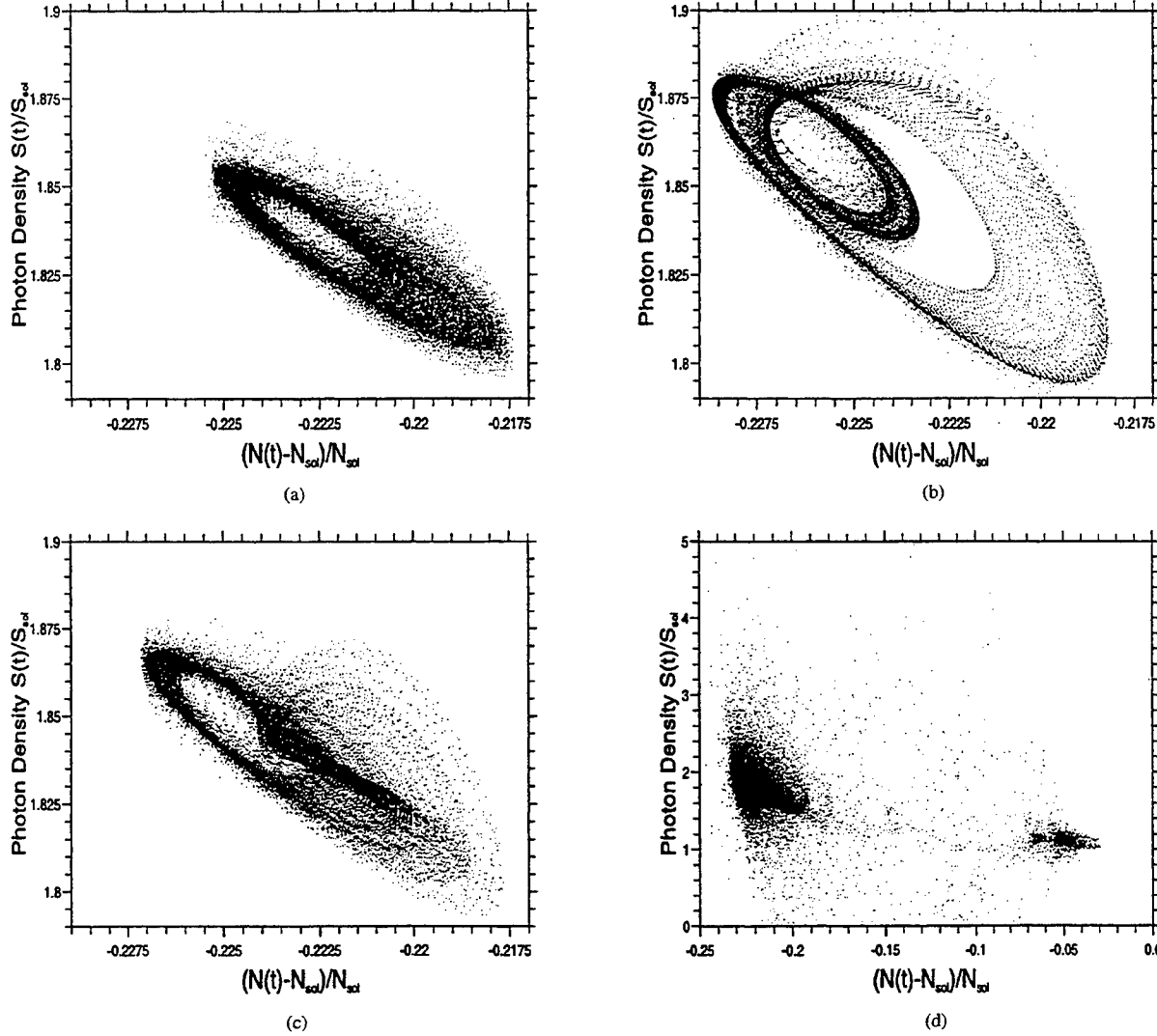


Fig. 4. Phase-plane portraits for four modulation frequencies are shown. The first three are for FM operation cases (a) $\omega_m = 351.85$ MHz, (b) $\omega_m = 359.25$ MHz, (c) $\omega_m = 362.96$ MHz, while the last is for bistable state, and (d) $\omega_m = 364.07$ MHz.

and the central frequency is considerably greater in magnitude than the side-modes.

As expected, the FM bandwidth increases as the modulation frequency is tuned toward the reciprocal of the external round-trip time ($1/\tau = 370.37$ MHz), Fig. 2(b)–(g). The slight asymmetry in the FM spectrum can be attributed to the linewidth enhancement factor, and was also observed experimentally. An abrupt loss of FM operation is observed in Fig. 2(h). The spectrum flattens and broadens drastically; note that both the frequency and amplitude scale have been changed in this figure. Higher harmonics and beat frequency effects, between ω_m and $1/\tau$, can be identified on closer inspection of the spectrum. This drastic loss of FM operation, as a function of modulation frequency, has also been observed experimentally. Further tuning the modulation frequency toward resonance does not result in pulsed FM operation, the spectrum simply broadens further.

The output photon density associated with each spectral plot is shown in Fig. 3. In general there is a small amount of

amplitude modulation. This is expected since the linewidth enhancement factor couples the amplitude and the phase, and thus any phase modulation will always cause amplitude modulation. The abrupt loss of FM operation seen in the spectral domain, Fig. 2(h), is accompanied by a correspondingly drastic change in the temporal behavior of the output photon density, Fig. 3(h). Large quasiperiodic amplitude modulation is obtained, and longer temporal simulation lengths show that the dynamics have an irregular behavior over longer time scales. This type of behavior is reminiscent of coherence collapse seen at lower feedback levels, but shows greater periodic structure than that generally seen in conventional coherence collapse [2], [3].

IV. COUPLED CAVITY PHENOMENA

Insight into the origin of the abrupt loss of FM operation can be obtained by looking at the phase-plane portraits of the normalized photon density versus the normalized carrier density, Fig. 4. Both the photon and carrier density are normalized

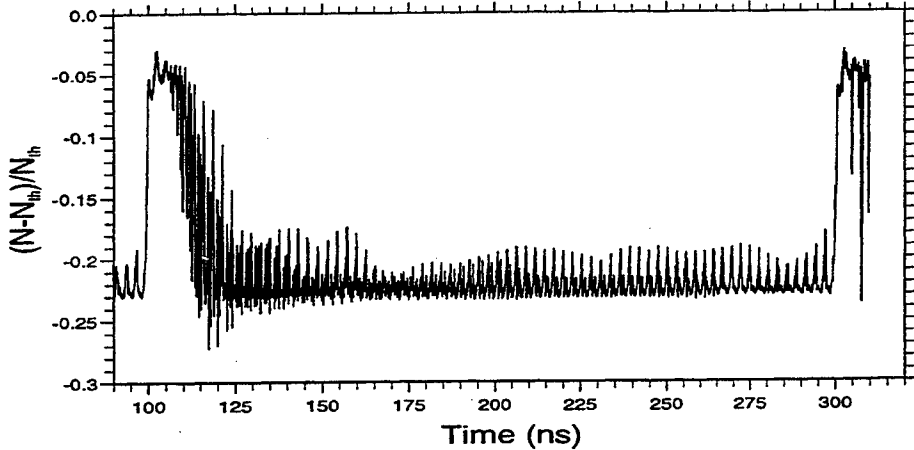


Fig. 5. Time evolution of the carrier density showing that the system switches between the two different states that appear when the system exhibits coherence collapse like behavior, $\omega_m = 364.07$ MHz.

with respect to the solitary laser values. The dynamics of the system are confined to small regions of phase space indicating the existence of stable regions of operation—or, in dynamical system terminology basins of attraction.

The phase-plane portraits for the FM mode of operation are shown in Fig. 4(a)–(c), and shows increasing complexity as the modulation frequency is tuned toward resonance. The observed amplitude fluctuations seen in Fig. 2 translate into “elliptic like” limit cycles seen in Fig. 4(a)–(c). Other frequencies become undamped, with increased phase modulation, allowing the ECL to oscillate at several frequencies, and thus causing the increased complexity seen in Fig. 4(c).

The phase-plane portrait obtained after FM operation is lost indicates that the frequency modulated ECL is hopping between quasi-stable regions of operation (attractors), Fig. 4(d). The larger attractor is centred around the same part of the phase space that the previous portraits occupied. However, the structure seen in the Fig. 4(a)–(c) has been lost and the attractor has weakened and expanded significantly. A second smaller attractor appears near to where the solitary laser would operate. The time evolution of the carrier density (Fig. 5) clearly shows that the system switches between two states. The lifetime of these two states are considerably different. The state associated with the lower carrier density has the longest lifetime and corresponds to the larger of the two attractors evident in Fig. 4(d).

The appearance of a second region of stable operation is attributed to the competition between coupled cavity modes and external cavity modes, where coupled cavity modes are those modes that have frequencies at multiples of approximately $1/(\tau_{in} + \tau)$. At some point, as the modulation frequency is tuned toward $1/\tau$, significant power couples into the coupled cavity modes, causing the development of a second attractor, and simultaneously destroying FM operation.

V. CONCLUSIONS

The present paper has examined in some detail spectral and dynamical behavior in an external cavity FM laser diode

configuration. Attention has been restricted to phenomena arising in the so-called long cavity case. FM operation has been demonstrated and the bandwidth observed to increase as the modulation frequency is tuned toward resonance. However, at some critical frequency FM operation is dramatically lost and coherence collapse like behavior is observed.

The abrupt loss of FM operation has been shown to coincide with the appearance of two quasi-stable state (attractors). The laser hops between these two quasi-stable operating points. This behavior is attributed to mode competition between external cavity modes and coupled cavity modes. The phenomena observed in the numerical simulation are in good qualitative agreement with experimental results [8].

As indicated above, quite a broad range of phenomena can actually appear in this configuration. In particular, in the short cavity case a transition from FM operation to pulsed laser [4] has been demonstrated. Details of this behavior will be described separately [16]. The investigations have also revealed that coupled cavity phenomena arising here are not restricted to semiconductor lasers. Specifically, it has been found that several features of the behavior are independent of the cavity detuning represented via the linewidth enhancement factor of semiconductor lasers. The exploration of such phenomena in more general laser systems will be the subject of a further contribution [17].

REFERENCES

- [1] J. Mork, B. Tromborg, and J. Mark, “Chaos in semiconductor lasers with optical feedback: Theory and Experiment,” *IEEE J. Quantum Electron.*, vol. 28, pp. 93–108, 1992.
- [2] G. van Tartwijk and D. Lenstra, “Semiconductor lasers with optical injection and feedback,” *Quantum. Semiclass. Opt.*, vol. 7, pp. 87–143, 1995.
- [3] R. W. Tkach and A. R. Chaplyvyy, “Regimes of feedback effects in 1.5 μ m distributed feedback lasers,” *J. Lightwave Technol.*, vol. 4, pp. 1655–1661, 1985.
- [4] S. E. Harris and O. P. McDuff, “Theory of FM laser oscillation,” *IEEE J. Quantum Electron.*, vol. 1, pp. 245–262, 1965.
- [5] F. V. Kowalski, P. D. Hale, and S. J. Shattil, “Broadband continuous wave laser,” *Opt. Lett.*, vol. 13, pp. 622–624, 1988.
- [6] B. Furch, A. L. Scholtz, and W. R. Leeb, “Isolation and frequency conversion properties of acoustooptic modulators,” *Appl. Opt.*, vol. 21, pp. 2344–2347, 1982.

- [7] A. P. Willis and D. M. Kane, "Modulation induced coherence collapse in FM diode lasers," *Opt. Commun.*, vol. 107, pp. 65–70, 1994.
- [8] ———, "Modulation induced coherence collapse: The collapse of side mode suppression in external cavity diode lasers," *Opt. Commun.*, vol. 111, pp. 577–588, 1994.
- [9] P. I. Richter and T. W. Hänsch, "Diode lasers in external cavities with frequency-shifted feedback," *Opt. Commun.*, vol. 85, pp. 414–418, 1991.
- [10] J. Martin, Y. Zhao, S. Balle, K. Bergmann, and M. P. Fewell, "Visible-wavelength diode lasers with frequency—Shifted optical feedback," *Opt. Commun.*, vol. 112, pp. 109–121, 1994.
- [11] A. P. Willis, A. I. Ferguson, and D. M. Kane, "External cavity diode lasers with frequency shifted feedback," *Opt. Commun.*, vol. 116, pp. 87–93, 1995.
- [12] K. W. Benoist, "The influence of external frequency shifted feedback on a DFB semiconductor laser," *IEEE Photon. Technol. Lett.*, vol. 8, pp. 25–27, 1996.
- [13] K. A. Shore and D. M. Kane, "Cavity decoupling in external cavity FM diode lasers," *Electron. Lett.*, vol. 33, pp. 50–51, 1997.
- [14] L. N. Langley, K. A. Shore, and J. Mork, "Dynamics and noise properties of semiconductor lasers subject to strong optical feedback," *Opt. Lett.*, vol. 19, pp. 2137–2139, 1994.
- [15] P. S. Spencer and K. A. Shore, "Multimode iterative analysis of the dynamic and noise properties of laser diodes subject to optical feedback," *J. European Optical Soc. B, Quantum and Semi. Optics*, vol. 9, pp. 819–830, 1997.
- [16] P. S. Spencer, D. M. Kane, and K. A. Shore, "Transition to pulsed operation in short external cavity FM semiconductor lasers," *IEEE J. Quantum Electron.*, vol. 35, pp. 788–793, May 1999.
- [17] ———, "FM lasing phenomena in class-B external cavity lasers," in preparation.

P. S. Spencer, photograph and biography not available at the time of publication.

D. M. Kane, photograph and biography not available at the time of publication.

K. Alan Shore, photograph and biography not available at the time of publication.

Evaluation of comb bandwidth parameters for frequency-shifted feedback semiconductor lasers

K. A. Shore

S.E.E.C.S. University of Wales, Bangor
Bangor LL57 1UT, Wales, United Kingdom

D. M. Kane

School of Mathematics, Physics, Computing and Electronics
Macquarie University, NSW 2109, Australia

email: alan@sees.bangor.ac.uk; tel: +44 1248 382618; fax :+44 1248 361429

1 Introduction

The behaviour of lasers subject to frequency shifted optical feedback is of interest in meeting technological requirements for high brightness broadband laser sources and also in fundamental science eg laser cooling of atoms [1-3]. The study of frequency shifted feedback (FSF) has been pursued in a number of laser systems. Initially dye lasers received the greatest attention but more recently semiconductor lasers, fibre lasers and diode-pumped solid state lasers have all been examined for FSF effects [see eg. 4-12]. An examination of the relevant literature reveals that significant scope remains for developing a comprehensive model capable of describing the build-up of FSF effects and the rich behaviours which can arise in such a system - ranging from short pulse generation to broadband emission. The aim of the present contribution is to provide a convenient analytical method for estimating the bandwidth of the frequency comb generated by the application of frequency-shifted feedback (FSF) to semiconductor lasers. The task undertaken here is to obtain an explicit analytical form for the peak frequency and bandwidth of the comb of frequencies generated by FSF. It will be seen that the assumption of a parabolic frequency dependence of the gain readily leads to analytical forms which indicate that GHz bandwidths can be achieved in FSF laser diodes .

2 Spectral intensity in FSF lasers

The basic experimental arrangement for FSF is of a laser subject to optical feedback in an external cavity. The FSF may be provided by an acousto-optic modulator (AOM) located in the external cavity operating at a modulation frequency Ω say. Then if light of frequency ν_i is emitted from the laser the imposition of a frequency shift Ω on each round trip of the external cavity is to generate returned light at frequency $\nu_{i+1} = \nu_i + \Omega$. The strength of the returned light will be determined by a number of experimental parameters but notably the efficiency of the acousto-optic modulator (AOM). For convenience a single parameter, η , is used to incorporate all effects which determine the strength of the frequency shifted light. With successive transits through the external cavity a comb of frequencies is generated. The present paper reports an analysis of FSF in semiconductor lasers. The starting point

for the analysis is a modification of the expression for the spectral intensity, $I(\nu)$, of FSF lasers which was derived in [12] for the case of a diode-pumped solid-state laser.

$$I(\nu) = [\eta G^{net}(\nu)]^{2(\nu-\nu_0)/\Omega} \quad (1)$$

where ν_0 is the emission frequency of the laser and $G^{net}(\nu) = \exp([g(\nu) - \alpha_c]\tau_{in})$ where $g(\nu)$ is the laser gain, α_c is the optical loss, and τ_{in} the round trip time of the laser diode cavity. The first task which has been accomplished here has been to obtain an expression for the peak frequency of the comb i.e. the frequency component with maximum amplitude. This may also be termed the instantaneous oscillation frequency. From that a simple expression is derived for the bandwidth of that frequency comb. The *peak frequency* of the comb is simply the frequency, ν_m , at which $dI/d\nu = 0$. To simplify the representation of the results it is convenient to define a net gain, g_{net} :

$$g_{net} = 1 - \alpha/g_0 + \ln[\eta]/(\tau g_0) \quad (2)$$

Then by utilising a parabolic frequency dependence, $g(\nu) = g_0(1 - g_\nu[\nu_c - \nu]^2/\nu_a^2)$, to represent the semiconductor laser gain it is found that :

$$\nu_m = (2\nu_c + \nu_0)/3 + \sqrt{\{(2\nu_c + \nu_0)/3\}^2/3[\nu_c(2\nu_c + \nu_0) - \nu_a^2(g_{net}/g_\nu)]} \quad (3)$$

In the case that the initial laser emission is located at the centre frequency of the gain, i.e. $\nu_0 = \nu_c$, the following compact expression is obtained:

$$\nu_m = \nu_c + \nu_a(g_{net}/3g_\nu)^{1/2} \quad (4)$$

The *comb bandwidth*, which is defined as the spectral width at half peak intensity, is found, under the assumption that the initial laser emission is located at the centre frequency of the gain ($\nu_0 = \nu_c$), to be given by:

$$\nu_s = \sqrt{\{2\nu_a\Omega\ln(2)/[g_0\tau_{in}(3g_\nu g_{net})^{1/2}]\}} \quad (5)$$

3 Practical implications

The practical implications of the above form of the comb bandwidth are, in fact, quite significant. In [12] it was indicated that a minimum in the oscillation bandwidth would be obtained at a determined g_{net} . In contrast, the present prediction is of a monotonic increase with decreasing g_{net} . That prediction is, however, in accordance with the experimental results reported in [12]. In assessing the performance of the FSF laser it is seen to be desirable to maximise both the comb bandwidth and the output power at which FSF operation can be obtained. The latter requires a high gain which in turn determines the instantaneous frequency. We thus consider, as a figure of merit for the FSF laser, the product

$$\nu_s(\nu_m - \nu_c) = \nu_a^{3/2} \sqrt{\{(g_{net}/3g_\nu)^{1/2} 2\Omega\ln(2)\}/[3g_0\tau_{in}]} \quad (6)$$

The main parameter determining the performance characteristics would now appear to be the material gain bandwidth. From this point of view our expectation is that semiconductor lasers, with their high net gain and ease of operation, will offer significant advantages over other laser systems in applying FSF. In order to illustrate the opportunities available in this context an evaluation of the comb bandwidth has been performed. The principal material parameters required for such an evaluation are the linear gain, g_0 , and the gain bandwidth $\nu_b = \nu_a/g_\nu^{1/2}$ with typical values of 1 ps^{-1} and 10 THz respectively and the cavity round trip time, τ_{in} in which for standard edge emitting lasers is about 5 ps . The net gain, g_{net} , clearly depends significantly on the precise details of the experimental arrangement but a value of 0.3 may be assumed. Then assuming a modulation frequency, Ω , of 110 MHz [9] the comb bandwidth is found to be about 10 GHz which, within the limits defined by the uncertainty in the precise experimental value of the net gain, is seen to be in very good agreement with the measured bandwidth of 6 GHz [9]. Further results indicating the parameter dependence of the salient operating characteristics will be presented. In our view, these results provide strong motivation for undertaking detailed experimental work with a view to determining, in analogy to the work on solid state lasers performed in [12], the dependences of the comb bandwidth on the net gain in Frequency Shifted Feedback on semiconductor lasers.

The analysis reported provides compact expressions which predict the main features of the frequency comb generated by frequency-shifted-feedback on semiconductor lasers. Such expressions may find further applications in the design of laser diode instrumentation for velocity and distance measurements.

References

1. F.V. Kowalski P.D.Hale and S.J.Shattil, Opt.Lett., **13**,622-624,1988
2. I.C.M.Littler and J.H.Eschner , Opt .Comm,**87**,44-52,1992
3. I.C.M.Littler,S.Balle and K.Bergmann ,Opt .Comm,**88**,514-522,1992
4. P.D.Hale and F.V. Kowalski , IEEE,J.Quant.Electron, **26**, 1845-1851,1990
5. P.I.Richter and T.W.Hnsch , Optics. Comm., **85**, 414-418, 1991
6. J.Martin et al ,Optics.Comm., **112**, 109-121, 1994
7. P.I.Richter and T.W.Hnsch , Optics. Comm., **85**, 414-418, 1991
8. J.Martin et al,Optics.Comm., **112**, 109-121, 1994
9. A.P.Willis, A.I.Ferguson and D.M.Kane, Optics Comm., **116**, 87-93, 1995.
10. K.W.Benoist, IEEE Photon.Tech. Lett., **8**, 25-27, 1996
11. H.Sabert and E.Brinkmeyer,IEEE J.Lightwave Technol., **12**,1360-1368,1994
12. K.Kasahara et al ,IEEE J.Quant.Electron.,**QE-34**, 190-203,1998

Self-consistent analysis of carrier transport and carrier capture dynamics in quantum cascade intersubband semiconductor lasers

K. Kálna

Institute of Electrical Engineering, Slovak Academy of Sciences

Dúbravská cesta 9, 842 39 Bratislava, Slovakia

C. Y. L. Cheung, I. Pierce, and K. A. Shore

University of Wales, Bangor

School of Electronic Engineering & Computer Systems

Bangor LL57 1UT, Wales, United Kingdom

email: alan@sees.bangor.ac.uk; tel: +44 1248 382618; fax :+44 1248 361429

1 Introduction

The present contribution describes a theoretical framework for performing calculations of the fundamental time constants which determine the dynamics of carrier transport and carrier capture in intersubband quantum cascade semiconductor lasers. In a recent brief report [1] it was indicated that unipolar lasers have the potential for achieving THz modulation bandwidths and a detailed description of that analysis has been presented elsewhere [2]. All that work was concerned with the dynamical processes occurring in a single triple-quantum well element. In practical intersubband lasers, in order to achieve sufficient optical gain, the active region must contain many copies of such elements so as to achieve the quantum cascade effect which underpins the successful operation of this class of lasers. In order to analyse the dynamical processes at play in such a quantum cascade laser, attention needs to be given to carrier transport and carrier capture processes which will affect, in particular, the achievable direct current modulation frequency of intersubband cascade lasers. In this report, a theoretical framework will be established to perform calculations of the pertinent physical factors which govern carrier transport.

The generic structure which is assumed to form the building block of the active layer of the electrically pumped intersubband laser of interest here has been examined in some detail in previous work [1, 3-6]. The aim of the present work is to study the modifications in predicted dynamical response which arise due to the effects of inter-element carrier transport and the finite time associated with the capture of electrons in the well structure.

The framework for analysis developed here is of general applicability but for the sake of definiteness in prescribing the salient physical processes which are required for accurately predicting the response, the work reported here concerns structures fabricated in the GaAs/AlGaAs system. This material system offers an advantage in terms of the well advanced state of information concerning fundamental material constants. A recent report [7] of the successful demonstration of intersubband lasing in this material system provides particular motivation for analysing this structure.

2 Analysis Technique

The rate equations for carrier densities [1, 3-6] as well as the rate equations for energy densities [8] depend on the intersubband relaxation time τ_s and on the capture time τ_{12} . Both rate equations give the electron volume density N_i and temperature T_{ei} in the each i -th energy subband. These two quantities enter back into the calculations of the electron relaxation times. Hence, it is natural to calculate the electron densities, temperatures and relaxation times self-consistently until the convergence is retained. An iteration process starts with the rate equations for carrier densities and continues with the rate equations for energy densities, and the optical gain [9] and, finally, the required relaxation times are calculated. Then the whole process is repeated. Fortunately, these iterations converge rather fast usually taking no more than 5 cycles or so. Note here that the capture time was not involved in the self-consistent scheme.

2.1 Electron relaxation times

Electron relaxation dynamics in the intersubband lasers are governed predominantly by the electron interaction with polar optical phonons. Nevertheless, in order to verify its contribution we have also taken into account, via the deformation potential interaction, electron scattering by acoustic phonons. Both phonons are considered to be bulklike because incorporation of some phonon confined model affects the overall results to a degree (< 10%) comparable to other fine effects such as non-parabolicity [10].

The electron-phonon rates are calculated using Fermi's golden rule as a transition from the initial subband i with energy E_i to the final subband j with energy E_j . Then the electron rate with an initial energy E can be obtained for the polar optical phonon (pop) scattering as [11, 12]

3 Results and discussion

The quantities found using the self-consistency scheme described in the previous section is utilised to perform calculations of the salient features of the laser dynamics. Results presented here are for the lifetimes calculated self-consistently for the MIR structure [5, 6] while for the lifetimes of the structure described in [7] we have been used the parameters given in that paper.

The electrons in the upper subband levels in the structures of [5, 6] have high enough sheet densities to achieve a population inversion and consequently to participate in a laser action. The sheet density in the highest energy subband (E_1) is also largest. Therefore, we expect that transitions from this level to the lower ones are the most effective. The electron sheet densities in the middle QW indicate that electron transitions between these levels are not as effective as from E_1 . The electron temperatures, as expected, increase with decrease in the subband energies. We have found an intersubband relaxation time of 1.07 ps after the self-consistent calculations. Further, we have calculated the capture time to be 0.28 ps using the self-consistent results for the electron densities and temperatures.

For the structure of Ref. 7, we have been found a relaxation intersubband time of 4.0 ps at the temperature equal to 77 K. The corresponding state lifetimes τ_1 , τ_2 and τ_3 in the active region (see Fig. 1 of Ref. 7) are 0.97 ps, 0.67 ps and 0.60 ps, respectively. The relaxation intersubband time we calculated is about 2 times larger than that of Ref. 7, but we believe that our calculations consider more accurately such processes as tunnelling between the wells, acoustic phonon interactions, electron degeneracy and includes also the applied bias. The population inversion conditions $\tau_S - \tau_2 > 0$ and $\tau_S - \tau_1 > 0$ are even better satisfied in our case. We have also calculated a capture time of 1.8 ps for the structure in [7]. This time, which represents an efficiency of the electron capture from the injection region into the active region, is short enough to encourage the rebuilding of the electron population inversion in the upper level. The tunnelling time τ_{23} has also been calculated and found to have an unusually high value of 6.6 ps. This is because the energy difference between the levels 2 and 3 is less than the pop energy. In fact, if one wants to find the tunnelling time more exactly, the transitions into the following injection region should be also taken into account.

The results obtained here can be used, for example, in order to ascertain the direct-current modulation response of such lasers. Such work is in progress.

References

1. N. Mustafa, L. Pesquera, C. Y. L. Cheung and K. A. Shore, *IEEE Photonics Tech. Lett.*, vol. 11, to be published 1999.
2. N. Mustafa, L. Pesquera, C. Y. L. Cheung and K. A. Shore, *IEEE MTT, Special Issue on THz Electronics*, submitted for publication.
3. W. M. Yee, K. A. Shore and E. Schöll, *Appl. Phys. Lett.*, vol. 63, p.1089, 1993.
4. W. M. Yee and K. A. Shore, *Semicond. Sci. Technol.*, vol. 9, p.1190, 1994.
5. C. Y. L. Cheung, P. S. Spencer and K. A. Shore, *IEE Proc. Opto.*, vol. 144, p.44,1997.
6. C. Y. L. Cheung and K. A. Shore, *J. Mod. Optics*, vol. 45, no. 6, p.1219, 1998.
7. C. Sirtori, P. Kruck, *et al* *Appl. Phys. Lett.* vol. 73, p.3486, 1998.
8. K. Kalna, C. Y. L. Cheung, I. Pierce and K. A. Shore, *IEEE MTT, Special Issue on THz Electronics*, submitted for publication.
9. C. Y. L. Cheung, P. Rees and K. A. Shore, *IEE Proc. Opto.*, vol. 146, accepted for publication, 1999.
10. D. F. Nelson, R. C. Miller, and D. A. Kleinman, *Phys. Rev. B*, vol. 35,p.7770, 1987.
11. B. K. Ridley, *Quantum processes in semiconductors*. 3rd ed. Oxford, U.K.: Clarendon, 1993
12. S. M. Goodnick and P. Lugli, in *Hot Carriers in Semiconductor Nanostructures*, edited by J. Shah, New York: Academic, p. 191, 1992.

Modeling spatiotemporal dynamics of high power semiconductor lasers: microscopically computed gain and device simulation

R.A. Indik, J. Hader, J.V. Moloney
Arizona Center for Mathematical Sciences
University of Arizona, Tucson, AZ 85721
Tel: (520) 621-6755, Fax: (520) 621-1510
Email: indik@math.arizona.edu

S.W. Koch
Physics Department
Universität Marburg
35032 Marburg, Germany
email: stephan.w.koch@physik.uni-marburg.de

Wide aperture semiconductor lasers offer possibilities for space-based communications applications and as pump sources for fiber amplifiers. Broad area devices exhibit weakly turbulent outputs from the very onset of lasing, thereby degrading device performance. By weakly turbulent, we mean persistent random dynamical bursts of spatially coherent structures within the laser medium. These dynamical filamentation instabilities create local hot-spots and can lead to permanent facet damage. The MFA-MOPA device, for example, was designed to offset the tendency for filamentation instabilities and thereby ensure high brightness operation up to a few Watts CW. Our simulation model [1] discussed below, was instrumental in redesigning the shape of the flare with the prediction of a doubling of the single-mode output power over the conventional linearly expanding flare MFA-MOPA [2]. It has also been used to show that the current modulated MFA-MOPA shows severe degradation of the output due to very weak but finite reflectivity of the output facet of the power amplifier [3].

Important issues which influence the onset of filamentation instability in these devices will be discussed. In particular, recent microscopic many-body calculations of the semiconductor optical response have yielded quantitative agreement with experimental gain, index and linewidth enhancement factor spectral measurements for different QW gain media over the past year [4]. An important conclusion of this phase of our effort is that femtosecond timescale multi-band carrier-carrier and carrier-phonon scattering events, profoundly affect the shape and magnitude of the CW optical gain. Barrier state filling at high current pump levels has little effect on the optical gain but modifies the refractive index, and hence, the magnitude of the effective Linewidth Enhancement factor, significantly. Large values of the latter lead to increased tendency for dynamic filamentation and beam degradation.

The semiconductor optical response depends on frequency, total carrier density and temperature (plasma and lattice). The very large gain bandwidth of the semiconductor material means that multiple longitudinal modes can compete effectively for gain. Coupled with transverse filamentation instabilities, this leads to extremely complicated spatio-temporal behavior. Beam propagation methods which can only resolve steady state behavior are simply inapplicable. Our approach has been to incorporate the microscopically computed

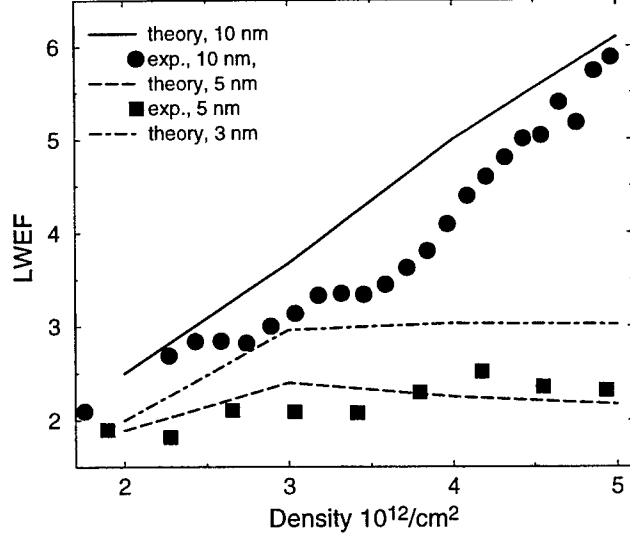


Figure 1: Linewidth enhancement factor (LWEF) as a function of carrier density

semiconductor optical response into a laser simulation model which resolves the full space time behavior of the counterpropagating optical fields and carrier density distributions throughout an arbitrary laser or amplifier structure[1]. This modular approach allows us to consider multi-section devices with very general geometries.

We will report on recent progress on the microscopic many-body calculations of the semiconductor optical response and on recent simulations of high power gain-switched pulsed broad area lasers. We will show that conduction band non-parabolicity and Coulomb-induced intersubband coupling strongly modify the gain/absorption and refractive index spectra of QW materials with GRINSCH and SCH confinement barriers. Inclusion of these effects in a multi-band microscopic calculation gives quantitative agreement with experimental measurements for different laser structures [5]. Quantitative agreement with experimentally measured Linewidth Enhancement factors (LWEF) provides the most stringent test of the many-body theory as we are comparing the ratio of differential quantities. As an illustration, we will show an example of structures for which the LWEF increases strongly with increasing carrier density and for which the LWEF clamps with increasing density [Figure 1]. For the first time, we have the capability to start at the same level of the materials grower (i.e input to the calculation includes bulk bandgaps, Luttinger parameters, strain constants, dipole matrix elements and band offsets between different materials in a heterostructure configuration) and a priori design and optimize a semiconductor amplifier/laser from the ground up. The semiconductor optical response, so computed, is input as a look-up table to the nonlinear partial differential equations that resolve the full space-time development of the counterpropagating optical fields and total carrier density within a general amplifier or laser structure.

As an illustration of a full scale simulation, we present results in Figure 2 of high peak power pulsed generation in a gain-switched twin-section flared semiconductor laser. The device has a narrow section, part of which is reverse biased. The remainder is forward biased with a single contact covering the remaining narrow section and the expanding flare. The experimental pulsed output generated at Sandia National Laboratories agrees remarkably well with this simulation result [6]. The generated optical pulse is highly multi-moded but detector averaging yields a smooth temporal profile. The fully resolved multi-mode and time-averaged output power is shown in the figure. In the simulation, we include the detector averaging

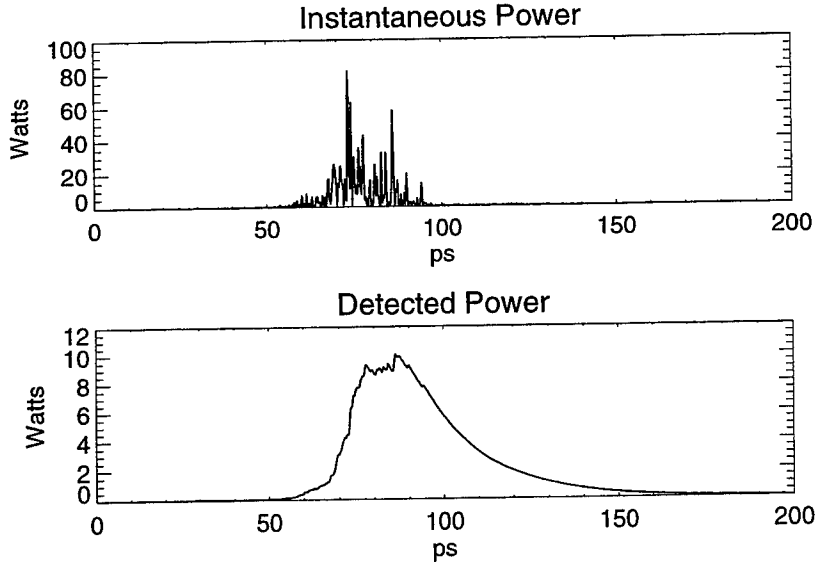


Figure 2: Instantaneous power output, and power that a detector with a 17ps response time would measure for a simulation of a gain switched twin section flared laser with an applied reverse bias, note the difference in scales

using a response time of 17 ps as supplied by the experimentalists. Using the simulation, we have been able to optimize the structure by adjusting the lengths of the absorbing and amplifying region's narrow sections as a function of reverse bias. We will also discuss how the LWEF clamping shown in Figure 1 influences the degree of filamentation in high power broad area devices and hence the time-averaged far-field broadening of multi Watt devices. At the high carrier densities reached in such devices, a combination of carrier leakage into the barrier confinement layers and strong blue-shifting of the gain peak, are key players in influencing the magnitude of the LWEF.

1. J.V. Moloney, R.A. Indik and C.Z. Ning, *Full Space-Time Simulation of High Brightness Semiconductor Lasers*, IEEE Phot. Tech. Lett., **9**, 731 (1997).
2. P.M.W. Skovgaard, J.G. McInerney, J.V. Moloney, R.A. Indik and C.Z. Ning, *Enhanced Stability of MFA-MOPA Semiconductor Lasers using a Nonlinear Trumpet Flare*, IEEE Phot. Tech. Lett., **9**, 1220 (1997).
3. J.V. Moloney, A.E. Egan, C.Z. Ning and R.A. Indik, *Spontaneous Spatiotemporal Instabilities in Current Modulated Master Oscillator Power Amplifier Lasers*, IEEE Phot. Tech. Letts., **10**, 1229 (1998).
4. A. Girndt, F. Jahnke, A. Knorr, and W.W. Chow, *Multi-Band Bloch Equations and Gain Spectra of Highly Excited II-VI Semiconductor Quantum Wells*, Phys. Stat. Sol., **202**, 725, (1997).
5. J. Hader, D. Bossert, J. Stohs, W.W. Chow, S.W. Koch and J.V. Moloney, *Clamping of the Linewidth Enhancement α -Factor in Narrow Quantum Well GRINSCH Semiconductor Lasers*, Applied Phys. Letts (in press) (1999).
6. A. Mar, G.A. Vawter, F.J. Zutavern, S.W. Koch, W.W. Chow, R. Indik and J.V. Moloney, *High Peak Power Gain Switched Flared Waveguide Lasers*, Submitted to CLEO'99.

Microwave and Frequency-Conversion Devices

Faraday-configured mode-locked p-Ge laser and p-Ge far-infrared amplifier

R. E. Peale, A. V. Muravjov, S. H. Withers, R. C. Strijbos

Department of Physics, University of Central Florida, Orlando, FL 32816

rep@physics.ucf.edu

S. G. Pavlov, V. N. Shastin

Institute for Physics of Microstructures, Russian Academy of Sciences, GSP-105, Nizhny Novgorod 603600, Russia

Abstract: A solid-state broad-band amplifier of far-infrared radiation (1.5 – 4.2 THz) based on intersubband transitions of hot holes in p-Ge is demonstrated using two p-Ge active crystals, when one operates as an oscillator and one as an amplifier. A peak gain higher than usual for p-Ge lasers has been achieved using time separated excitation of the oscillator and amplifier. Active mode locking of the p-Ge laser has been achieved in the Faraday configuration of electric and magnetic fields with distinct advantages over Voigt geometry. The 200 ps pulses of $80\text{-}110\text{ cm}^{-1}$ radiation were achieved by local gain modulation from an applied rf electric field at the 454 MHz round trip frequency of the laser cavity.

OCIS codes: (140.3070) Infrared and far-infrared lasers; (140.3280) Laser amplifiers; (140.4050) Mode-locked lasers

Far-infrared p-Ge lasers operate in the wavelength range 70 to 200 μm [1]. The mechanism of amplification of terahertz emission in bulk p-Ge is based on direct optical transitions between light and heavy hole valence subbands (Fig. 1) in strong crossed electric and magnetic fields, when the crystal is cooled to liquid helium temperatures. Population inversion is built up via light hole accumulation at certain values of electric E and magnetic B fields. At the optimal ratio E/B , heavy holes repeatedly emit an optical phonon after being accelerated beyond the threshold energy 37 meV while light holes move on closed cyclotron orbits below this threshold and have a much longer lifetime. A large gain

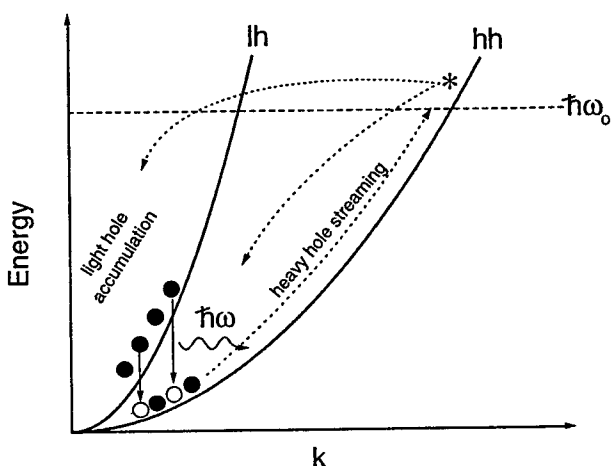


Fig. 1. Mechanism of THz amplification by intersubband transitions. Solid parabolas represent the light- (lh) and heavy-hole (hh) bands. The dotted-lines represent heavy holes accelerated beyond the optical phonon energy ($\hbar\omega_0$), then scattered back to the heavy- or light-hole band. Accumulation of hot light-holes is indicated together with downward transitions and THz photon emission.

bandwidth ($\Delta\omega/\omega \sim 1$) and low dispersion make this active medium promising for wide range tunability and for propagation, amplification and generation of short pulses of far-infrared radiation with picosecond duration $\tau \sim 1/\Delta\omega$.

Usual p-Ge lasers span the frequency range 1.5 - 4.2 THz, deliver 1-10 W peak output power for 1 cm³ typical active volume, and have 1-5 μ s laser pulse duration. The saturation intensity inside the active crystal can reach kW/cm², but this intensity cannot be extracted because the typical gain of only $\sim 10^{-2}$ cm⁻¹ requires small out-coupling losses for development of stimulated emission. An oscillator-amplifier p-Ge laser system has the potential to increase the useable p-Ge laser power since a single-pass amplifier does not require feedback from an out-coupling mirror.

Generation of 200 ps far-infrared pulses by the p-Ge laser has been obtained by active mode locking in Voigt geometry of applied fields with gain modulation at one end of the laser crystal[2-5]. The modulation field E_{rf} is applied at a frequency v_{rf} equal to the half of the cavity roundtrip frequency v_r and parallel to the magnetic field. E_{rf} periodically accelerates light holes beyond the optical phonon threshold, upon which they are predominantly scattered to the heavy hole band. As a consequence, the gain is modulated at the roundtrip frequency, inducing mode locking. This proposed mechanism[6] required Voigt geometry of applied fields, where the main electric E and magnetic B fields are both perpendicular to the optical axis of the active crystal (direction of light propagation) and perpendicular to each other. Here we demonstrate the first achievement of active mode locking in Faraday geometry where the magnetic field is applied along the long optical axis of the sample and the orientation of the applied modulating field E_{rf} is perpendicular to B.

Experiment

The oscillator-amplifier scheme is shown in Fig. 2. Rectangular rods were cut from single crystal Ge, doped by Ga with a concentration $N_A = 7 \times 10^{13}$ cm⁻³. The crystal ends were polished parallel within 30 arc-seconds. Si spacers between the crystals prevented electrical breakdown. The out-coupling mirror for the laser was an evaporated Al film on one of the Si spacers with a centered 1.5 mm hole. The back copper mirror was attached via 20 μ m teflon film. Electric field pulses E_1 and E_2 were applied to the laser and amplifier crystals from separate pulsers via ohmic Al contacts evaporated on the crystal sides. The system was inserted in a superconducting solenoid, putting both crystals in the same magnetic field B, and cooled by liquid helium. The radiation was detected by a whisker-contacted Schottky diode outside the cryostat or with a cooled Ge:Ga photoconductor inside the cryostat.

For the mode-locking experiment, the crystal dimensions were 5 x 7 x 84.2 mm³. Two external copper mirrors were attached to them via 20 μ m teflon film. The field orientations were $E_{HV} \parallel [1-10]$ and $B \parallel [111]$. For gain control and modulation the active sample had a few pairs of small additional contacts with a length of 4 mm and 1 mm separation on the sides of the crystal perpendicular to the main contacts (Fig. 2). In these experiments, the external rf electric field was applied only to the contact pair nearest the back mirror. The remaining additional contacts serve as equipotential surfaces, which are important for the mechanism of gain modulation discussed below. Fig. 2 shows the electronic set up [5] for application of E_{rf} and E_{HV} , as well as the scheme for controlling independent bias voltages to the rf contacts on each side. The bias voltages U_1 and U_2 are obtained from the main-contact pulse, U_0 , using potentiometers. The obtainable U_1 and U_2 vary from zero to U_0 .

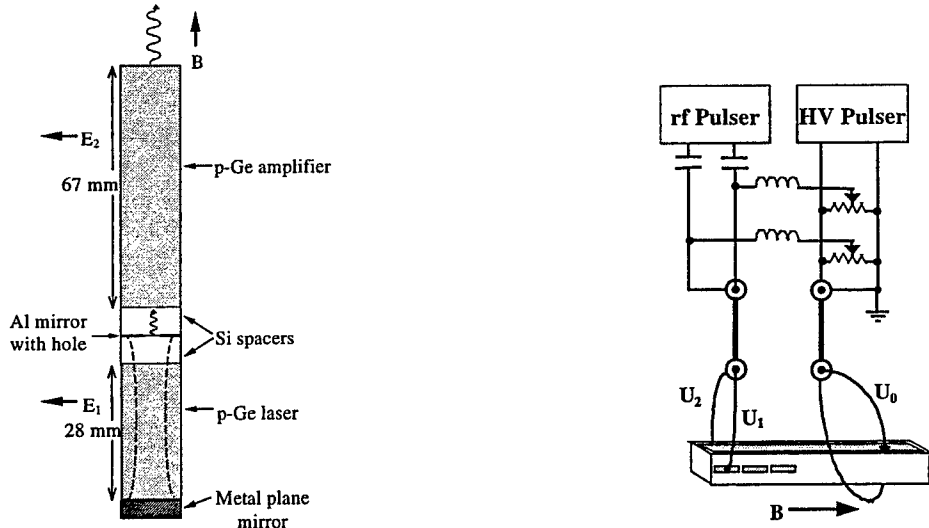


Fig. 2. Left: Oscillator-amplifier p-Ge laser construction. Right: Contact configuration with excitation and modulation electronics for mode-locked p-Ge laser. Thick lines denote coaxial cables.

Amplifier results

The amplifier experiment is performed in the high-frequency region of p-Ge emission [1], where the laser generates a broad multimode spectrum from 70 to 140 cm^{-1} . The transmission T of oscillator radiation by the amplifier is presented in Fig. 3. For low excitation of the amplifier ($E_2 < 20-50 \text{ V/cm}$), there is no transmission of oscillator radiation, but for higher fields, transmission appears. For electric field values E_2 in the range 800 to 1200 V/cm the amplifier enters the active zone of amplification on l-h transitions due to light-hole accumulation. To define the amplifier zero-gain level ($T=1$) in Fig. 3, the threshold electric fields of self-excitation were independently determined for the amplifier crystal with external mirrors applied to its ends (i.e. when it starts to lase). Because the threshold might depend on the mode structure, maximum and minimum estimated threshold levels for that sample, giving the range δE_2 , are marked on Fig. 3. These levels define the range of values for transmission δT (dashed curves) and for gain $\delta \alpha$. Accounting for multiple reflections inside the amplifier crystal (considering 100% reflection from the back Al mirror and $R = (n-1)/(n+1) = 0.35$ from the output end, $n_{\text{Ge}} = 3.925$), the absolute value of the gain is found from the expression $T = g(1-R)/(1-Rg^2)$, where $g = \exp(\alpha L)$ and L is length of the crystal. The gain α obtained from the peak in Fig. 3a has the value $0.028 (+/- 0.008) \text{ cm}^{-1}$. The measurement of the absolute gain from the rise time of the stimulated emission pulse when external mirrors are applied to the crystal gives the lower value 0.010 to 0.015 cm^{-1} .

The enhanced amplifier gain is achieved by delaying E_2 with respect to the E_1 pulse (Fig. 4). The amplifier is switched on near the oscillator-output peak. (Note that the laser emission shown in Fig. 4 is detected with a Ge:Ga photoconductor inside the cryostat in close proximity to the cavity construction, allowing detection of oscillator emission from rays that leak *around* the amplifier.) The 400 ns delay in Fig. 4 between the onset of oscillator excitation E_1 and the oscillator emission pulse (solid curve) is the typical p-Ge laser build-up time. The solid curve shows the usual decay caused by crystal heating. If the amplifier is excited when oscillator signal is present, the signal output from the combined system rises with essentially no delay (dashed curve).

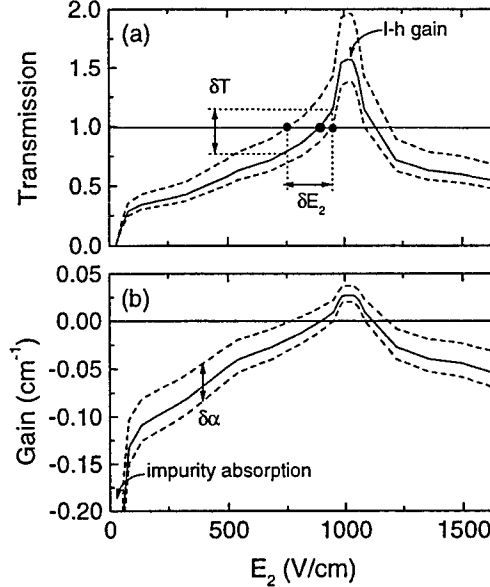


Fig. 3. (a) Transmission of high-frequency-domain p-Ge laser radiation by the p-Ge amplifier vs. excitation field E_2 . (b) Gain in the amplifier crystal determined from transmission data. The bounding dashed data curves indicate the uncertainty range. The spectral range of the emission is 80 to 100 cm^{-1} . $E_1 = 800$ V/cm and $B = 0.69$ T.

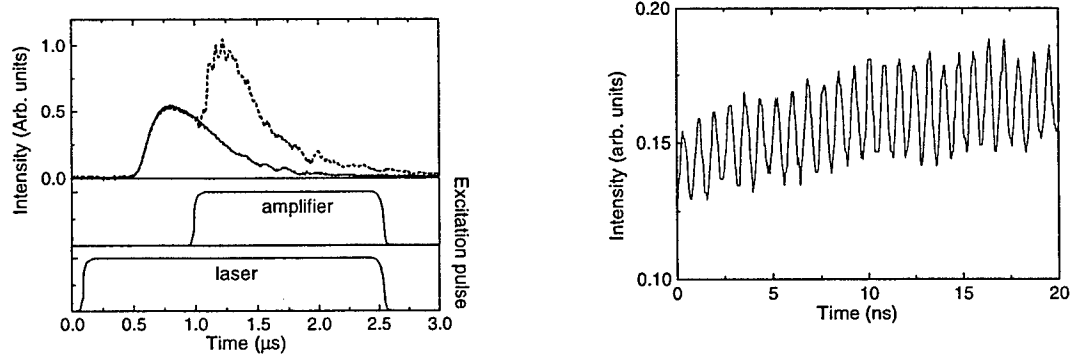


Fig. 4 (left). Timing diagram of oscillator excitation pulse E_1 , amplifier excitation pulse E_2 , oscillator output pulse (solid data) and amplifier output pulse (dashed data).

Fig. 5 (right). Fast dynamics of the p-Ge amplifier output. Sub-nanosecond round trip intensity oscillations of the p-Ge laser oscillator are preserved by passage through the amplifier.

Outside the cryostat, the room temperature fast whisker-contacted Schottky diode detects only the second peak of the dashed curve in Fig. 4, which corresponds to a highly collimated beam transmitted by the amplifier only while it is active. If $E_2 = 0$, the amplifier crystal is opaque, and the scattered oscillator signal is strongly attenuated by reflections within the light pipe. A fragment of Schottky signal (Fig. 5) shows fast periodic structure with 800 ps period corresponding to round trip oscillations of the oscillator cavity (28 mm Ge plus Si spacer). No distortion by dispersion or multiple reflections inside the amplifier appears, which demonstrates that the second active crystal works similarly to a single pass amplifier and that this amplifier reproduces the sub-nanosecond dynamics of

the laser intensity. This observation, and the known broad gain spectrum, suggests that the p-Ge amplifier is suitable for propagation and amplification of pulses of THz radiation even as short as 1 ps.

Mode-locking results

A strong dependence of the p-Ge laser operation on the potentials U_1 and U_2 applied to the additional contacts (Fig. 2) was found. This observation is similar to that found in Voigt geometry[5], but in Faraday geometry the laser is more sensitive to a change of the average potential $(U_1 + U_2)/2$ than to the voltage drop $U_2 - U_1$. This is displayed in Fig. 6, where intensity contours are plotted vs U_1/U_0 and U_2/U_0 . The laser does not operate outside the outer contour in the unshaded region. Without applying external bias, U_1 and U_2 have values determined by the Hall effect. These values are optimal for the gain due to maximal homogeneity of the electric field along the magnetic field direction. The dashed line in Fig. 2 indicates the condition $U_1 - U_2 = U_{\text{Hall}}$, and a symbol indicates the optimal lasing point.

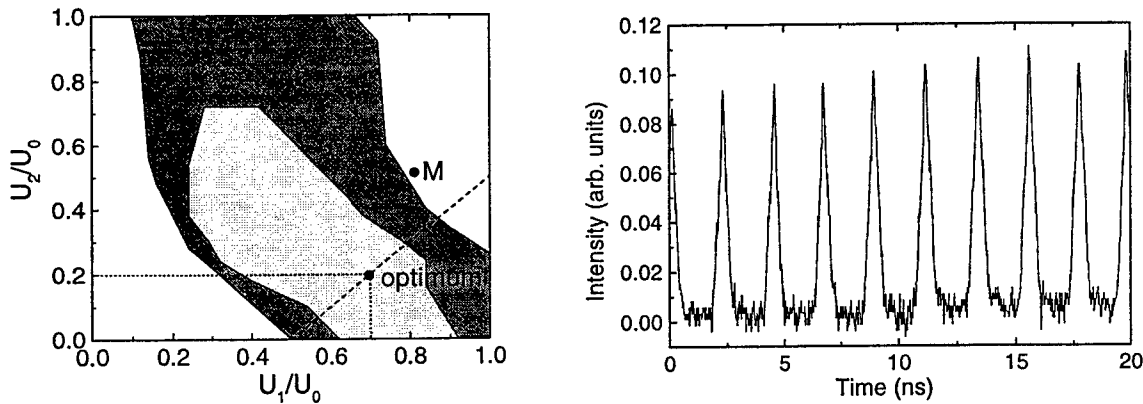


Fig. 6 (left). Intensity contours vs. normalized bias potentials at the additional contacts. The diagonal dashed line indicates the condition $U_1 - U_2 = U_{\text{Hall}}$. The optimum point indicates the bias values for best lasing. Point M indicates the bias values for the best mode locking effect.

Fig. 7 (right). Mode-locked output of Faraday-configured p-Ge laser. The peak widths are bandwidth limited by the transient digitizer.

Active mode locking is achieved via local modulation of the gain inside the active crystal by applying an rf electric field. The best active mode locking was found at the bias conditions labeled M in Fig. 6. At point M, the laser starts to operate only when the additional rf field is applied exactly at the laser-cavity round-trip frequency. The laser is then mode-locked, and the output appears as a train of 200 ps pulses (Fig. 7). The rf resonance is about 1 MHz wide, as defined by the build-up time for stimulated emission of a several hundred nanoseconds. During this time, the gain should be modulated precisely at the round trip frequency of the cavity.

The local gain modulation is induced by the appearance of a longitudinal E-field component along B in the center of the sample when external voltages U_1 and U_2 are applied to the additional contacts. This is explained schematically in Fig. 8. Equipotential contours in steps of $0.1 U_0$ are shown over two cross sections of the laser crystal, as indicated. Supposing that bias potentials U_1 and U_2 corresponding to point M are applied to the first pair of additional contacts (Fig. 8a), the potential distribution between the second pair of additional contacts (Fig. 8b) assumes values given by the optimum point in Fig. 6. A schematic of the resulting potential distribution in the center of the crystal

cross section along the long axis z is then shown in Fig 8c, where the positions of the additional contacts are indicated along the upper horizontal axis. The curve representing the electrostatic potential has two solid symbols, which give the

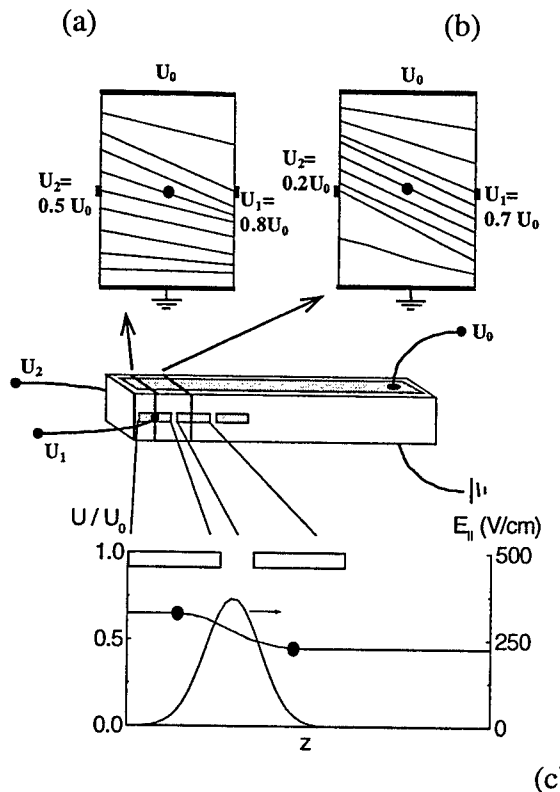


Fig. 8. Schematic of electric potential distributions inside the p-Ge laser crystal. (a) Cross sectional slice under the first pair of additional contacts with equipotential contours in units of $0.1 U_0$. The U_1 and U_2 bias values correspond to point M in Fig. 2. (b) Cross sectional slice under the second pair of additional contacts without external bias. U_1 and U_2 assume values close to the optimum point in Fig. 2. (c) Potential vs. distance along the main crystal axis and the corresponding electric field E_{\parallel} .

potential values at the points with the same symbols in Figs. 8a and 8b. The potential gradient along z corresponds to the appearance of a local electric field E_{\parallel} along the magnetic field. The rf electric field on the additional contacts modulates the potential at the center of the local crystal cross-section, thus modulating the potential gradients along B , and finally the local gain.

Discussion and conclusions

The small signal gain determined from amplifier transmission exceeds the value obtained from the lasing rise time. The reason is that the typical build-up time of the radiation intensity from spontaneous level to the measurable level is several hundred nanoseconds. Meanwhile, the sample is Joule heated to about 10 K, where the absolute gain is reduced by light-hole lifetime quenching and increased multiphonon lattice absorption. The oscillator/amplifier system avoids this problem by delaying the amplifier excitation until the oscillator output peaks. Thus, the amplifier crystal is still cold when the injected radiation reaches its peak intensity, allowing this radiation to be amplified with higher gain than usual. This method will in principle allow higher than usual output intensities for the same excited

crystal volume. The broad-band nature of the p-Ge amplification holds promise for amplification of femtosecond THz pulses created using ultrafast lasers and photoconductive antennas.

Short pulse generation by active mode locking of the p-Ge laser in Faraday geometry is new, but this successful demonstration reveals a number of advantages over Voigt geometry. The magnetic fields are conveniently applied by compact, low-current superconducting solenoids. The train of 200 ps output pulses is more repeatable and stable than in Voigt geometry. The impedance between additional contacts is comparatively high, permitting low rf current, so that the required rf modulating-field power is lower. In Faraday geometry, magnetoresistance increases the impedance to ~ 50 ohm (as compared to less than 5 ohm in Voigt[2-5]), which is ideal for most commercial electronics. The measured level of reflected rf power was less than 20% without special impedance matching tricks.

Acknowledgments

Funding at UCF was provided by NSF and BMDO. IPM colleagues thank the Russian Foundation for Basic Research.

References

1. Special Issue on Far-infrared Semiconductor Lasers, edited by E. Gornik and A. A. Andronov, *Opt. Quantum Electron.* **23** (1991).
2. J. N. Hovenier, A. V. Muravjov, S. G. Pavlov, V. N. Shastin, R. C. Strijbos, and W. Th. Wenckebach, "Active mode locking of a p-Ge hot hole laser," *Appl. Phys. Lett.* **71**, 443 (1997).
3. J. N. Hovenier, T. O. Klaassen, W. Th. Wenckebach, A. V. Muravjov, S. G. Pavlov, and V. N. Shastin, "Gain of the mode locked p-Ge laser in the low field region," *Appl. Phys. Lett.* **72**, 1140 (1998).
4. A.V. Muravjov, R. C. Strijbos, C. J. Fredricksen, H. Weidner, W. Trimble, A. Jamison, S. G. Pavlov, V. N. Shastin, and R. E. Peale, "Mode-locked far-infrared p-Ge laser using an offset rf electric field for gain modulation," in *Radiative Processes and Dephasing in Semiconductors*, OSA-TOPS, Vol. **18**, edited by D. Citron (OSA, Washington DC, 1998), pp. 102-107.
5. V. Muravjov, R. C. Strijbos, C. J. Fredricksen, S. H. Withers, W. Trimble, S. G. Pavlov, V. N. Shastin, and R. E. Peale, "Pulse separation control for mode-locked far-infrared p-Ge lasers," *Appl. Phys. Lett.* **74**, 167 (1999).
6. R. C. Strijbos, J. G. S. Lok, and W. Th. Wenckebach, "A Monte Carlo simulation of mode-locked hot-hole laser operation," *J. Phys. Condens. Matter* **6**, 7461 (1994).

A three-diode-laser, terahertz-difference-frequency synthesizer and its applications toward far-infrared spectroscopy of ammonia and water

Pin Chen

Time and Frequency Division, 847.10

National Institute of Standards and Technology, 325 Broadway, Boulder, CO 80303

Tel: 303- 497-7884, Fax: 303-497-7845, Email: chenpin@boulder.nist.gov

John C. Pearson and Herbert M. Pickett

Jet Propulsion Laboratory, 183-301

California Institute of Technology, 4800 Oak Grove Drive, Pasadena, CA 91109

Tel: 818-354-6861, Fax: 818-354-8460, Email: jcp@spec.jpl.nasa.gov, hmp@spec.jpl.nasa.gov

Shuji Matsuura and Geoffrey A. Blake

Division of Geological and Planetary Sciences, 150-21

California Institute of Technology, Pasadena, CA 91125

Tel: 626-395-6296, Fax: 626-368-0935, matsuura@gps.caltech.edu, gab@gps.caltech.edu

Upcoming astrophysical and atmospheric investigations using space/air-borne submillimeter remote sensing demand robust, compact, power-efficient, narrow- linewidth, and tunable THz local oscillators; moreover, such a source is highly desirable for laboratory far-infrared spectroscopy as well. The advent of THz optical heterodyne conversion (TOHC) in low-temperature-grown (LTG) GaAs—when using semiconductor lasers as pump sources—promises such a source; detectable output power up to 5 THz has been reported [1]. However, the enhanced linewidth and frequency jitter of free-running diode lasers must be overcome for high-resolution applications since, for example, Doppler linewidths at 1 THz for small molecules are only $\sim 1\text{--}3$ MHz. Moreover, absolute calibration of the THz frequency is essential. Although narrow-linewidth spectrometers have been achieved using TOHC with diode lasers [2], frequency calibration of the THz output was not generally available. This paper presents an all-solid-state, high-resolution, frequency-calibrated, THz spectrometer based on TOHC in LTG-GaAs with DBR (distributed-Bragg-reflector) lasers [3].

Figure 1 depicts the experimental setup. A fully fiber-coupled optical pumping system consisting of three DBR lasers was developed to synthesize completely tunable and accurate THz frequency-differences for heterodyne conversion in an LTG-GaAs photomixer. Each DBR laser's linewidth is narrowed by forming an external cavity with a 4% beamsplitter and a rooftop reflector mounted on a piezoelectric translator (PZT) to enable fine frequency tuning. The laser output is coupled into fiber in a compact ($25 \times 5 \times 5$ cm) and rigid optical rail to demonstrate potential for space/air-borne, remote-sensing applications. The THz linewidth (measured by the heterodyne beatnote between two of the lasers) has a full- width-at-half-maximum of 0.7 – 2 MHz. Figure 2 shows a typical beatnote spectrum. Lasers #1 and #2 are locked to different longitudinal modes of a ultra-low-expansion (ULE), Fabry-Perot etalon via the Pound-Drever-Hall method [4]. The etalon is hermetically sealed inside an aluminum enclosure that is pumped and back filled with dry nitrogen. The loop bandwidth is approximately 2 kHz, limited by the PZT resonance. Laser #3 is offset-locked to laser #2, and the offset frequency is set by a 2 – 6 GHz microwave synthesizer. The primary outputs of lasers #1 and #3 are injected into a master-oscillator power amplifier (MOPA). The two simultaneously amplified beams are focused onto the LTG-GaAs photomixer to generate

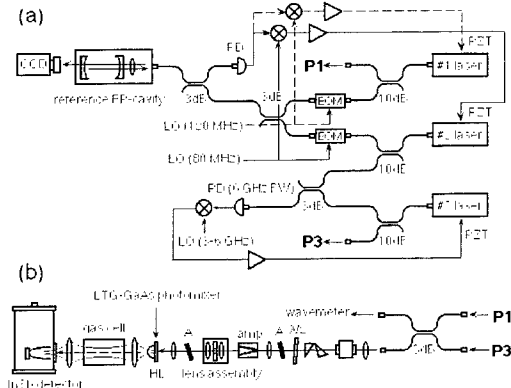


Figure 1: Schematic diagram of (a) the three DBR laser system that synthesizes a precise difference frequency, and (b) the MOPA system and the setup for spectroscopy.

THz radiation. We have found that the simultaneous amplification does not add any significant spectral noise so long as the frequency separation between the seed lasers is greater than 10 GHz [5].

The free-spectral-range (FSR) of the ULE (expansion coefficient at room temperature = -2×10^{-10} C^{-1}), Fabry-Perot etalon was calibrated to 50 ppb by measuring the 10 rotational transitions of CO in the 0.230 – 1.611 THz region. On the average, the stability of the calibration was ~ 250 ppb over one-month. Figure 3 shows the time series of the FSR value over a two-month period. Small leaks in the enclosure of the ULE etalon, leading to changes in the moisture content inside the etalon, can cause such drifts in the FSR. This potential cause can be greatly mitigated by maintaining a good vacuum (instead of back filling) in the enclosure.

This spectrometer has been employed to carry out spectroscopic investigations of ammonia ($^{14}\text{NH}_3$) in the $\nu_2 = 1$ state and water (H_2^{16}O) in the ground and $\nu_2 = 1$ states. Absorption measurements of NH_3 and H_2O gas samples were made in a single-pass, 1.6-m cell under flow conditions. For water measurements, cell pressure was maintained at approximately 100 mtorr. For ammonia, each transition was measured at a number of different pressures ranging from 50 – 200 mtorr in order to extract the frequency value that is free of pressure shifts. Spectral linewidths were pressure limited (~ 5 MHz at 100 mtorr). Spectra were acquired with a Si-composite bolometer operating at 2 K, with the source radiation chopped at 100 Hz. Lock-in detection was employed with a time constant of 1 s. The overall spectrometer NEP was ~ 2 pW, probably limited by $1/f$ noise. Signal-to-noise of the observed lines ranged from 10 to 10^3 . The estimated frequency accuracy is 250 kHz for a one-sigma measurement. Currently, the frequency accuracy is limited by residual FM noise in the Pound-Drever-Hall loops, resulting in a frequency jitter of ~ 200 kHz.

Twenty-six ν_2 -ammonia pure inversion and inversion-rotation transitions have been measured at an accuracy significantly higher (by a factor of 20 in most cases) than previously published values. Six rotational transitions of water in the ground state and 11 rotational transitions in the ν_2 state have been measured. Measured frequency values of these 17 transitions have not been previously pub-

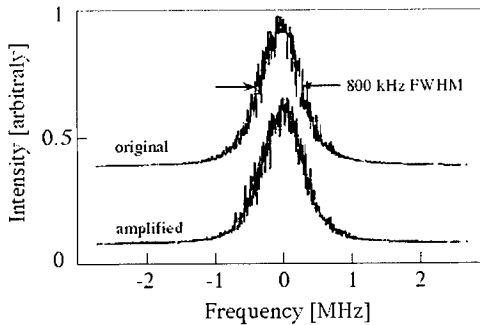


Figure 2: Spectrum of the beatnote signal between the #1 and #3 lasers before (upper) and after (lower) amplification with the MOPA.

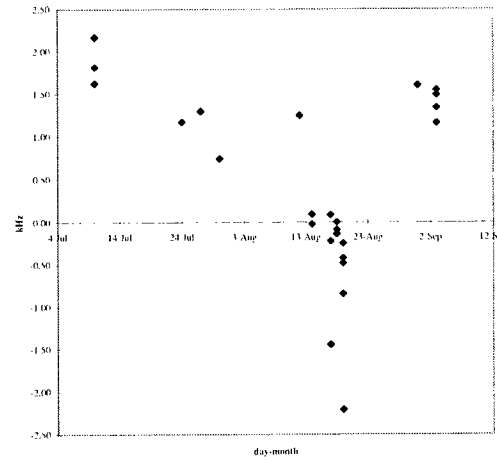


Figure 3: Deviation of the FSR value from an average value of 2.9967607 GHz vs. time.

lished. Preliminary analysis of the effective rotation-inversion Hamiltonian of ν_2 -NH₃ determined additional sextic and octic centrifugal-distortion constants. Frequency values and descriptions of the analysis can be found in reference [6]. Forthcoming papers will present comprehensive analyses of the water and ammonia spectra in conjunction with other existing high-resolution data.

References

- [1] K. A. McIntosh, E. R. Brown, K. B. Nichols, O. B. McMahon, W. F. DiNatale, and T. M. Lyszczarz. *Applied Physics Letters* 67 (1995): 3844.
- [2] P. Chen, G. A. Blake, M. C. Gaidis, E. R. Brown, K. A. McIntosh, S. Y. Chou, M. I. Nathan, and F. Williamson. *Applied Physics Letters* 71 (1997): 1601.
- [3] S. Matsuura, P. Chen, G. A. Blake, J. C. Pearson, and H. M. Pickett. *IEEE MTT* 1999, in press.
- [4] R. W. P. Drever, J. L. Hall, F. V. Kowalski, J. Hough, G. M. Ford, A. J. Munley, and H. Ward. *Applied Physics B* 31 (1983): 97.
- [5] S. Matsuura, P. Chen, G. A. Blake, J. C. Pearson, and H. M. Pickett. *Int. J. of Infrared and Millimeter Waves* 19 (1998): 849.
- [6] P. Chen. "Terahertz Generation via Optical-Heterodyne Conversion: Development of a New Far-Infrared Spectrometer and Its Applications toward a Better Understanding of Nonrigid, Astronomically Important Molecules." Diss. California Institute of Technology, Pasadena, 1999.

A compact microwave frequency reference using diode lasers¹

N. Vukičević, A. S. Zibrov, L. Hollberg, F. Walls and J. Kitching

Time and Frequency Division, National Institute of Standards and Technology

M.S. 847.10, 325 Broadway, Boulder CO 80303

Tel: (303)-497-6353, Fax: (303)-497-7845, E-mail: natasa@boulder.nist.gov

A compact microwave frequency reference that uses a diode laser to excite stimulated Raman transitions in a small Rb vapor cell is being developed. The system's simplicity and use of advanced semiconductor laser and photodetector technology allows it to be compact and power-efficient, while maintaining a reasonable degree of long-term stability and a potentially high degree of insensitivity to environmental perturbations. Baseline design goals are a volume of $3 \times 3 \times 9 \text{ cm}^3$, power consumption of less than 1 W and a fractional frequency instability of 10^{-11} at one day.

Compact microwave frequency references have a number of important potential applications in the areas of telecommunications, global navigation and instrumentation. For example, such devices might be installed in cellular telephone networks in order to maintain timing synchronization without the need for a reference timing signal common to all nodes. A fractional frequency inaccuracy of 10^{-10} at one day would likely be adequate for this application, but insensitivity to large temperature changes, humidity and vibrations is essential. Compact, power-efficient, vibration-insensitive frequency references could also be used in global positioning system receivers in order to acquire a GPS signal lock more quickly and maintain the lock in adverse environments. Finally, many common laboratory instruments, such as frequency synthesizers, counters and spectrum analyzers might benefit from compact, inexpensive atomic frequency references to replace or enhance commonly used quartz reference oscillators.

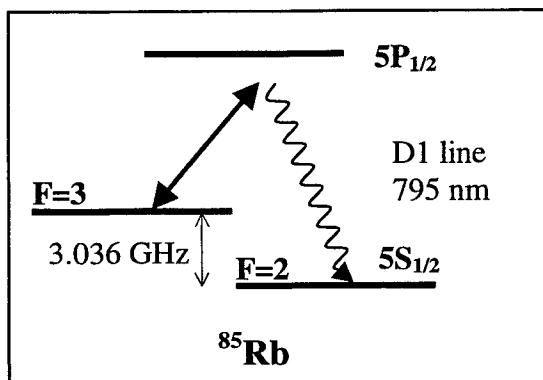


Figure 1: Basic optical field configuration.

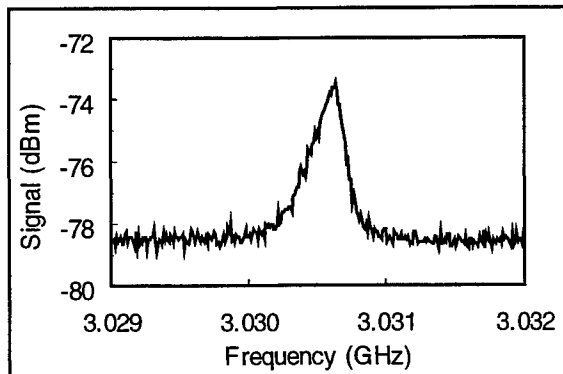


Figure 2: Ramam beatnote for unmodulated laser.

The compact Rb oscillator described here is based on atomic coherence-induced gain observed in a previous simple experiment². The basic optical field configuration and the relevant atomic energy levels are shown in Figure 1. Light from a distributed Bragg reflector (DBR) diode laser at 795 nm is focussed through a miniature, heated ^{85}Rb vapor cell. Within the cell, stimulated Raman scattering (SRS) generates a second optical field, co-propagating with the first, but shifted by the hyperfine frequency of the atom. These two optical fields are focussed onto a high-speed

photodetector resulting in a beat note at the 3.036 GHz hyperfine splitting. In one initial design implementation, this signal, shown in Figure 2, is simply amplified and used as the frequency reference output. While this configuration has the advantage of simplicity, could fit into an extremely small package, and is expected to be acceleration insensitive, the output frequency is fairly broad (FWHM \sim a few hundred kilohertz) and troubled by laser light-induced shifts that will need to be controlled. Nevertheless, a fractional frequency instability of 1×10^{-9} between 0.01 s and 1 s was obtained.

In a refinement of the basic design, shown in Figure 3, the laser injection current is directly modulated at the hyperfine frequency with a voltage-controlled oscillator (VCO). In the laboratory experiments described here, a crystal oscillator is used but will be replaced eventually by a VCO. This modulation provides an additional optical frequency to the Rb cell that is then amplified by SRS. The width of the resulting resonance at 3.036 GHz is narrowed to \sim 800 Hz. The photodetector output is then mixed with the original modulating signal and the resulting error signal is fed back to the VCO stabilizing it to the atomic resonance (Figure 3, RF servo). In order to reduce laser frequency-induced fluctuations in the beat note frequency, a laser frequency servo is also implemented using the detector DC photocurrent (Figure 3, DC servo). The locked VCO frequency is monitored in time; Figure 4 shows a typical Allan deviation, with fractional frequency fluctuations $< 1 \times 10^{-10}$ for averaging times $1 \leq \tau \leq 300$ s. The small remaining frequency excursions are due to uncontrolled thermally-induced frequency drifts.

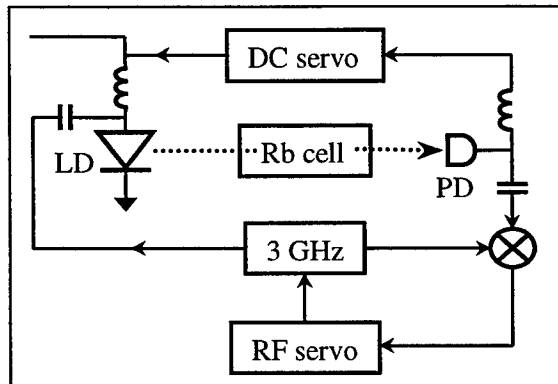


Figure 3: Refined experimental setup showing RF lock and laser frequency lock. LD: Laser Diode, PD: Photodiode.

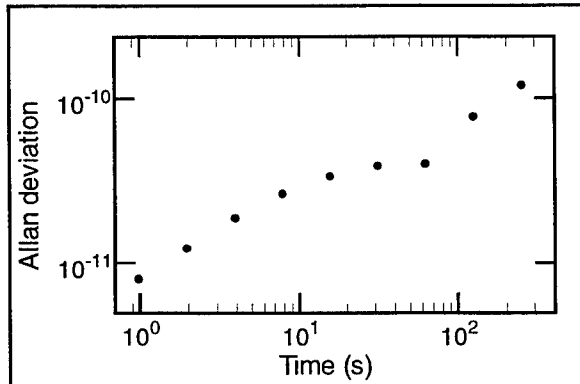


Figure 4: Allan deviation of compact Rb frequency reference.

The two-section DBR laser³ used here was chosen because of its reasonably narrow spectral linewidth (\sim 1 MHz) and its tunability combined with a compact, monolithic design. While this laser has a reasonably low electrical power consumption (<200 mW), a considerable advantage could be gained by replacing it with a vertical cavity surface-emitting laser (VCSEL)⁴. A typical operating current of several milliamperes for these devices results in a power consumption value about an order of magnitude smaller than that for edge-emitting lasers. Their high modulation bandwidth would also be a significant advantage in this application, since a lower power RF amplifier would then suffice to put modulation sidebands on the laser. Preliminary evaluations of VCSELs show two possible drawbacks, larger linewidth (several tens of MHz) and high sensitivity of wavelength to current variations (\sim 100 times higher than edge-emitting Fabry-Perot lasers).

In summary, preliminary table-top experiments have demonstrated the feasibility of a compact, low power, atomic frequency reference with a fractional frequency instability of $< 1 \times 10^{-10}$. While sensitivity to environmental perturbations continues to be a problem with the current unoptimized system, improved RF and structural design and modest temperature control are expected to reduce these difficulties substantially. Re-engineering of the system into a small package is currently underway.

¹ Contribution of NIST. Not subject to copyright.

² A. S. Zibrov, et al., Proc. 5th Symposium on Frequency Standards and Metrology, J. C. Bergquist, ed., World Scientific, 1996.

³ T. Hirata, M. Maeda, M. Suehiro and H. Hosomatsu, IEEE J. Quantum Electron. **27**, 1609, 1991.

⁴ High wallplug efficiency lasers at 850 nm have recently been reported in R. Jager, et al., Electron. Lett., **33**, 330, 1997; also see C. Affolderbach, et al., submitted to Appl. Phys. B, 1999 for spectroscopic applications of VCSELs.

Frequency Shifting of Four-Wave Mixing of Picosecond Optical Pulses in Semiconductor Optical Amplifiers

J.M.Tang and K.A.Shore

University of Wales, Bangor,

School of Electronic Engineering and Computer Systems,
BANGOR, LL57 1UT, UK.

Tel: +44(1248)382618; Fax: +44(1248)361429;

e-mail: alan@sees.bangor.ac.uk

1. Introduction

Four-Wave Mixing (FWM) has been considered as a useful technique for investigating the physical origin of ultrafast nonlinearities in semiconductor waveguides, and as a phenomenon having applications in high-capacity optical communication systems. For practical applications, FWM among ultrashort optical pulses is of great importance [1], which has been extensively studied in Semiconductor Optical Amplifiers (SOAs) [2-4] and passive semiconductor waveguides [5]. To isolate the generated conjugate wave from the probe and pump waves, several methods have been demonstrated. First, use is made of spectrally and spatially resolved mixing waves directly [6], this technique is valid only for FWM in broad-area semiconductor devices. For conventional FWM configurations, the mixing waves are collinear, optical frequency filters are, therefore, widely employed to separate the frequency shifted conjugate wave from other mixing waves [2,3]. In addition, to automatically provide isolation of the destination wavelength from the background amplified spontaneous emission, polarization beam splitter followed by an optical frequency filter can also be utilised in polarization sensitive FWM schemes [7]. It is desirable to fix the width of the band-pass filter and the filter position in FWM spectrum, to simplify the FWM configuration. This arrangement is successful for the cases of FWM among CW waves since the frequency deviation between output conjugate and pump waves always equals to that between input probe and pump waves. However, the equal frequency detuning condition does not hold for the cases of FWM of short optical pulses in SOAs, resulting from pulse spectral peak shift. This would cause that after passing through the position-fixed filter the measured conjugate power is smaller than its real value, and in some cases, the filter would completely block the conjugate power. Therefore, the investigation of frequency shift is of great importance, especially for simultaneous wavelength conversion on multi-channels in WDM networks [1].

In this paper, frequency shifting of FWM of picosecond optical pulses in SOAs is analysed for the first time, based on an improved FWM theoretical model [4]. It is shown that larger frequency detuning, shorter optical pulse width and higher optical pulse energy considerably enhance conjugate frequency shift to lower frequency side of FWM spectrum. Frequency detuning asymmetry of conjugate and probe pulses with respect to pump pulses is also reported.

2. Theoretical Model

An improved theoretical model [4] for investigating FWM of picosecond optical pulses has been reported, taking into account inter- and intra-band carrier processes, Two-Photon Absorption (TPA), Ultrafast Nonlinear Refraction (UNR), Cross-Gain Modulation (XGM), Probe Depletion (PD) and gain dispersion. The detailed description of the model can be found in Ref.4, which can be successfully applied not only in active semiconductor devices but also in passive semiconductor waveguides [5] after some essential modification. The main parameters used in the calculations are representative for InGaAsP semiconductor material operating at wavelengths around $\sim 1.55\mu\text{m}$ [4]. The input unchirped Gaussian zero time-delay pump and probe pulses are taken to have identical polarization states and widths, and the input pulse energy ratio between them is assumed to be

10:1. To account for the gain dispersion effect, a gain model presented in Ref.8 is adopted here. The central frequency of the pump pulse is assumed to be located at the peak of the gain spectrum of the SOA.

3. Results and Discussions

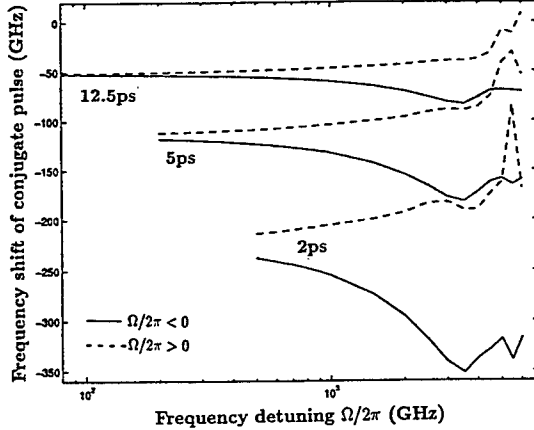


Fig.1 Frequency shift of conjugate pulse from $(-\Omega + \omega_0)/2\pi$. The input pulse energy is fixed at 100fJ.

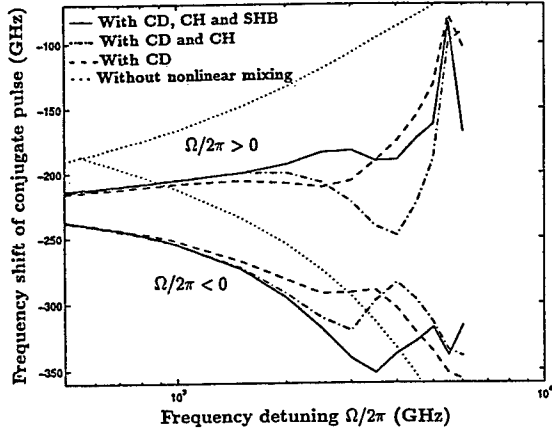


Fig.2 Investigation of various contributions to conjugate frequency shift. The properties of input pump pulses are 2ps of width and 100fJ of energy. The CD, CH and SHB account for the nonlinear mixing processes induced by carrier depletion, carrier heating and spectral holeburning, respectively.

The frequency detuning between the input probe (ω_1) and pump (ω_0) pulses is defined as $\Omega = \omega_1 - \omega_0$. $\Omega > 0 (< 0)$ is called as positive (negative) frequency detuning. The frequency shift of conjugate pulse from $(-\Omega + \omega_0)/2\pi$ is illustrated in Fig.1 for different input pulse widths. The frequency shift is only computed for detunings considerably larger than the pulse spectral width. Fig.1 shows that central frequency of conjugate pulses moving towards red frequency side, which agrees with the experimental measurements [2]. Fig.1 also demonstrates that frequency shifts are significantly dependent on pulse width and frequency detuning $\Omega/2\pi$. Shorter pulse width and larger detuning $|\Omega/2\pi|$ increase the frequency shift significantly. When the value of $|\Omega/2\pi|$ is of several hundred GHz, in which cases, most of FWM experiments are performed, the magnitude of frequency shift would be comparable with the input pulse spectral width.

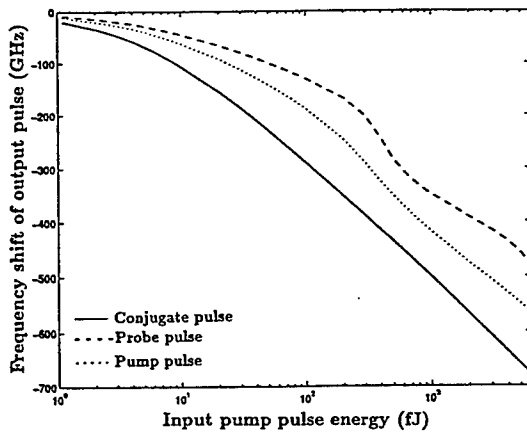


Fig.3 Frequency shifts of mixing pulses versus input pump pulse energy. The input pump pulse width is 2ps and input frequency detuning is -2THz .

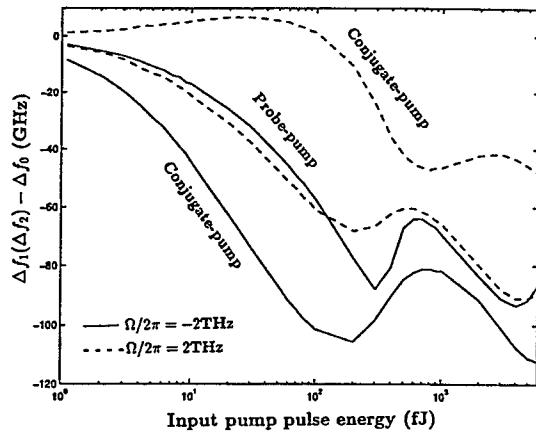


Fig.4 Difference between frequency deviations of mixing pulses and $|\Omega/2\pi|$. Other parameters are the same as that in Fig.3.

The frequency shift behaviours are mainly contributed by the gain dispersion effect and interband and intraband nonlinear mixing processes, as shown in Fig.2, where the output probe

pulse frequency shift (corresponding to $\Omega/2\pi$) calculated without including PD and XGM effects, is treated as the conjugate frequency shift (corresponding to $-\Omega/2\pi$) for the case without considering all the nonlinear mixing processes. The gain dispersion effect is responsible for the behaviours demonstrated by the dotted lines: a smaller central frequency is related to a larger saturation energy, which reduces the effect of the gain saturation induced by the pump pulses, the decreased gain saturation leads to a smaller frequency shift. The nonlinear mixing processes shift considerably the conjugate pulse frequency to low frequency side, especially for the case of $\Omega/2\pi > 0$, and also cause sharp frequency shift evolution in larger frequency detuning region. The contribution from the interband mixing processes (CD) to the frequency shift is dominant for frequency detuning less than several hundreds of GHz. Beyond that detuning region, intraband mixing processes become important. Furthermore, it can be also seen from Fig.2 that the nonlinear mixing processes lead to unequal frequency shift between conjugate and probe pulses. The unequal frequency shift will bring about a frequency detuning asymmetry of conjugate and probe pulses with respect to the pump pulses. The magnitude of frequency detuning asymmetry is a function of pulse width and frequency detuning.

The frequency shift and detuning asymmetry behaviours are greatly strengthened for input larger pump pulse energy, as shown in Fig.3. All the central frequencies of the mixing pulses are significantly decreased with increased input pump pulse energy. Step-like frequency shift lineshapes for probe and pump pulses occur in the pulse energy region from several hundreds fJ to ~ 1 pJ due to the TPA and UNR effects starting to play important roles. The step-like structure disappears for the conjugate frequency shift, resulting from the TPA and UNR based nonlinear mixing. The difference between the frequency deviation for all mixing pulses and the input frequency detuning is plotted in Fig.4. At the output facet of the SOA, the frequency deviation between conjugate (probe) and pump pulses is smaller than $|\Omega/2\pi|$. The frequency asymmetry behaviours can also be clearly identified from Fig.4. The frequency shift evolution features corresponding to the pump pulse energy of ~ 1 pJ can be understood by considering the step-like lineshapes in Fig.3.

4. Conclusions

Frequency shifting of FWM of short optical pulses in SOAs has been investigated. It is shown that frequency shifting of mixing pulses from the frequency value determined by the input frequency detuning is significant for shorter pulse width, larger frequency detuning and higher pulse energy. Frequency detuning asymmetry of probe and conjugate pulses with respect to pump pulses is also identified, which arises due to the nonlinear mixing processes.

Acknowledgements

This work was supported by EPSRC under grant GR/L03262. J.M.Tang is supported by the Professor Wynn Humphrey Davies Scholarship and the School of Electronic Engineering and Computer Systems, University of Wales, Bangor, UK.

References

- 1 D.Nesbet, D.D.Marcenac, P.L.Mason, et al., *Electron. Lett.*, Vol.34, p.107, 1998.
- 2 S.Diez, C.Schmidt, R.Ludwig, et al., *IEEE J. Sel. Top. Quantum Electron.*, Vol.3, pp.1131-1145, 1997.
- 3 J.Inoue and H.Kawaguchi, *IEEE Photon. Technol. Lett.*, Vol.10, p.1566, 1998.
- 4 J.M.Tang and K.A.Shore, *IEEE Photon. Technol. Lett.*, Vol.10, pp.1563-1565, 1998.
- 5 J.M.Tang and K.A.Shore, *Appl. Phys. Lett.*, Vol.74, 1999 (accepted for publication)
- 6 D.X.Zhu, D.Tishinin, K.Uppal, et al., *Electron. Lett.*, Vol.34, p.87, 1998.
- 7 A.Corchia, C.Antonini, A.D'Ottavi, et al., *IEEE Photon. Technol. Lett.*, Vol.11, p.275, 1999.
- 8 K.Obermann, S.Kindt, D.Breuer, et al., *IEEE J. Lightwave Technol.*, Vol.16, p.78, 1998.

Single and Multiple Wavelength Conversion Using Double Pump Four-Wave-Mixing in a Semiconductor Optical Amplifier

Abhik Ghosh , Guang-Hua Duan*, Guoxi Sun and Mario Dagenais

Dept. of Electrical Engineering, University of Maryland

College Park, MD 20742, USA

Phone: (301) 405-36 84, Fax: (301) 314-92 81, Email: dage@eng.umd.edu

* *On leave from Departement Communications et Electronique*

Ecole Nationale Supérieure des Télécommunications

46, rue Barrault, 75634 Paris cedex 13, France

Abstract

Bit error rate measurement at 2.5Gbit/s on single and multiple input wavelength converted signals using double pump four wave mixing in a semiconductor optical amplifier has been performed. It is found that the wavelength converted signal can be made wavelength insensitive for single input for detuning from -30nm to 15nm. Multiple-input wavelength conversion using low pump powers has also been demonstrated for the first time with a low penalty of about 1.5 dB.

Keywords-- Nonlinear optics, Four-wave mixing, frequency conversion, semiconductor optical amplifier

I. INTRODUCTION

Wavelength conversion is a key function that will be essential for future optical telecommunication networks using dense wavelength-division-multiplexing (DWDM). Wavelength conversion can be realized all optically by using nonlinear optical phenomena such as cross-gain modulation, cross-phase modulation and four-wave-mixing (FWM) in a semiconductor optical amplifier (SOA) [1]. The FWM is particularly interesting as it offers advantages such as being applicable at high bit rate and as being independent of the input data format. However, the wavelength conversion range using a single pump is limited as the efficiency decreases rapidly with the wavelength shift. To improve the wavelength conversion range, a double-pump scheme was first proposed in 1988 [2]. The principle of operation of such a scheme is based on the fact that the second pump experiences the gain and index modulation created by both the input data and the first pump wavelength. Side-modulation bands around the second pump are thus created, and carry the same information as the input probe. More recently several groups have studied the conversion efficiency of this scheme using CW beams, and have found a nearly flat variation with the wavelength separation between the two pump signals [3,4]. BER results have also been reported at a fixed wavelength detuning (~80nm) [5]. Additionally, the double-pump scheme has been demonstrated to obtain polarization insensitive wavelength conversion [6].

Simultaneous conversion of multiple input channels is very useful in converting a group of wavelengths from C-band to L-band or vice versa. It is also desirable in order to scale the wavelength conversion capability in a modular fashion as the network evolves. Until this date

researchers have used difference-frequency-generation in AlGaAs waveguides [7] and in quasi-phase matched LiNbO₃ [8] and FWM in SOA [9] to demonstrate multiple channel wavelength conversion. However, in the first two of these approaches passive waveguides were used which meant that large pump powers (65mW and 110mW respectively) were required to get the wavelength converted signals. In the scheme involving FWM in an SOA, the beating of the pumps were used to create the sidebands around the modulated signal which puts a limit on the range over which wavelength conversion is possible. In this paper, double pump FWM in an active medium (SOA) is proposed to achieve multiple wavelength conversion with a large conversion range and using much lower pump power levels. We report for the first time the bit-error-rate (BER) performance of single and multiple wavelength conversion using the new double pump scheme. The BER performance for different wavelength shifts, both positive as well as negative, will also be given for a single-input wavelength.

II EXPERIMENTAL SETUP

Figure 1 shows the experimental setup. One or two Ortel DFB lasers mounted in a WDM transmitter rack are used as the probe [11]. These lasers with a wavelength separation of 1.6 nm are modulated with a pseudo-random sequence of length $2^{23}-1$ at 2.5 Gbit/s. A third Ortel DFB laser is used as the first pump. A tunable external cavity laser is used as the second pump. Both pump lasers are operated CW. The polarization of each signal is controlled to ensure maximum FWM efficiency. These three or four lasers are connected to an arrayed-waveguide grating (AWG). The AWG has a wavelength spacing of 1.6 nm, a FWHM of about 0.48 nm and an insertion loss of 3 dB. The AWG's output is connected to the input of the SOA. The output of the SOA is analyzed by an Optical Spectrum Analyzer (OSA), or filtered by a similar arrayed-waveguide grating. The filtered signal is sent to a 2.5 Gbit/s SONET receiver.

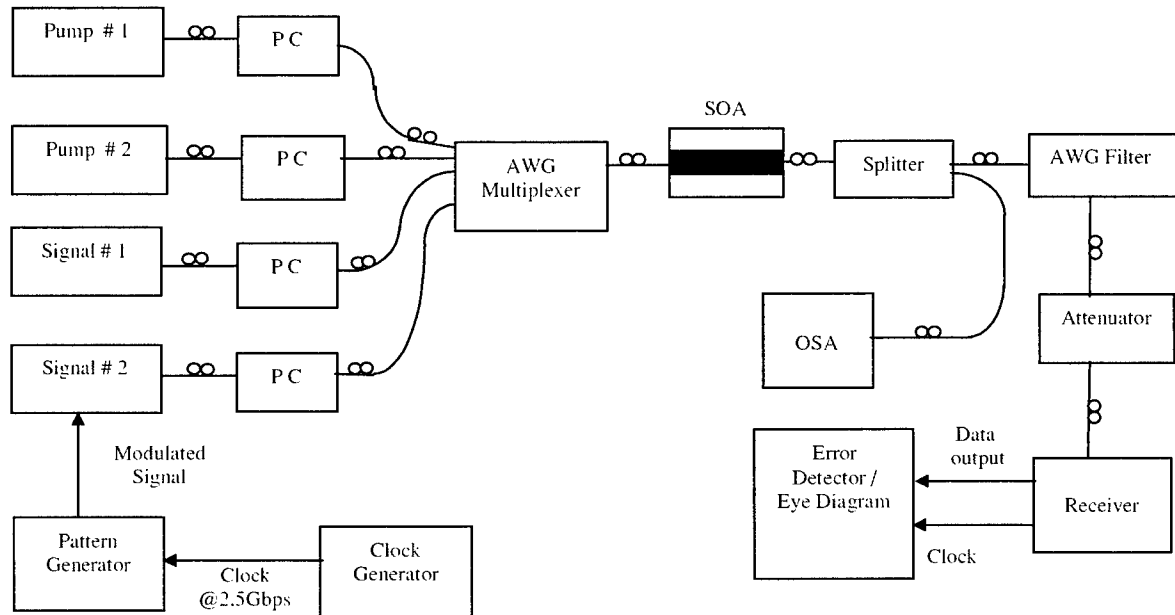


Figure 1: Experimental setup of the double-pumped FWM. PC: polarization controller, SOA: semiconductor optical amplifier, OSA: optical spectrum analyzer, AWG : arrayed waveguide grating

The SOA used for this experiment is a polarization insensitive multiple-quantum-well device with buried ridge structure, incorporating lateral spot-size converters and windows. The length of the device is 940 μm . A 6° angle tilted waveguide was used, in combination with a 10 μm long InP window, to reduce the back reflection from the facet. The maximum small-signal internal gain is about 30 dB. Fiber-to-fiber gain of 23dB has been obtained at 1.55 μm using lensed fibers. The saturation power at 150 mA is about 7 dbm. Other characteristics can be found in [10].

III. RESULTS and DISCUSSION

Figure 2 shows a typical optical spectrum after the SOA for (a) single and (b) double input signal wavelengths for an injection current of 175 mA to the SOA. The power level is about -5 dbm, 3

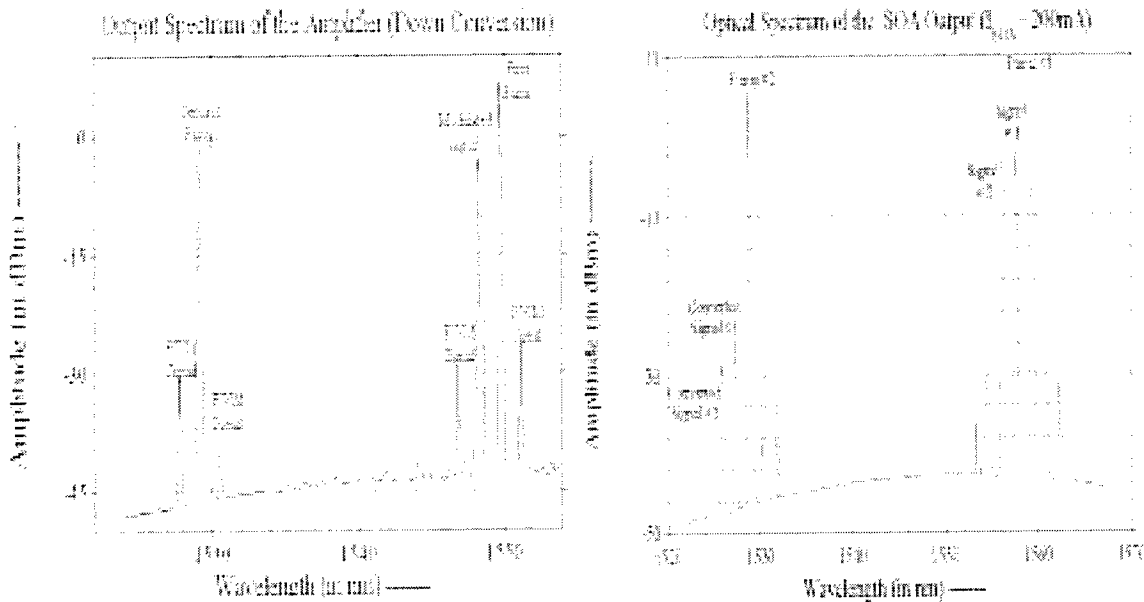


Figure 2: The optical spectrum at the output of the SOA for (a) one and (b) two input signals

dbm and 5 dbm, for the input modulated signal, the first pump and the second pump, respectively. One can clearly identify the newly generated conjugate wavelengths around the first and the second pump. The stronger conjugated signal around the second pump is used as the converted signal. For the double input wavelengths, one can observe a slightly decreased conjugate signal power for the signal #2 due to the reduced FWM efficiency with the increased wavelength spacing. The chosen converted signal is filtered using another arrayed waveguide grating filter which has similar characteristics as the one used to combine the signals. It has been verified from the filtered signal that there is at least a 10 dB discrimination between the filtered and the input modulated signal. This discrimination ratio ensures that there is a negligible influence of the input wavelength on the BER measurement of the wavelength converted signal. It is also worth noting that in our experiment, the polarization of the first pump is controlled to be the same as that of the probe. As the SOA used is a polarization insensitive device, the polarization of the second pump does not affect the FWM efficiency. The FWM phenomenon due to the beating between the two pumps is nearly invisible as long as the detuning wavelength between them is larger than 5 nm.

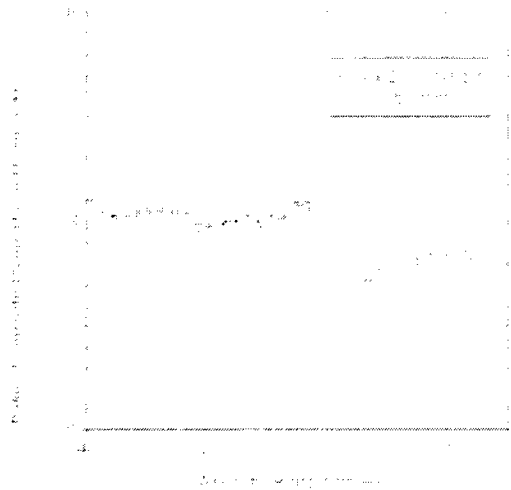


Figure 3: Power ratio between the converted signal and the second pump versus wavelength separation between the two pumps.

Figure 3 shows the ratio between the converted signal power and the second pump power for an injection current of 175 mA to the SOA. We can see that for a wavelength shift from -40 nm to 25 nm between the two pumps, this ratio does not change more than 4 dB. It is worth noting that the ratio is with respect to the second pump output power, instead of the input signal power. Such a definition allows us to compensate for the variation of the amplifier gain of the second pump signal over the large wavelength range. In this measurement, the input power level for all wavelengths is kept fixed. The result shown in figure 3 implies that for a given input signal wavelength, the conversion ratio shows a much smoother variation compared to the single pump scheme for which a 20 dB variation has been observed for the same wavelength conversion range (from -40 nm to 25 nm) [12].

Figure 4 shows the eye diagrams for the input data and the converted signal with the double-pump scheme. The converted signal has a different waveform than the input data as it has been regenerated by the receiver. One can observe here an open eye diagram for both the signals indicating a low bit-error-rate.

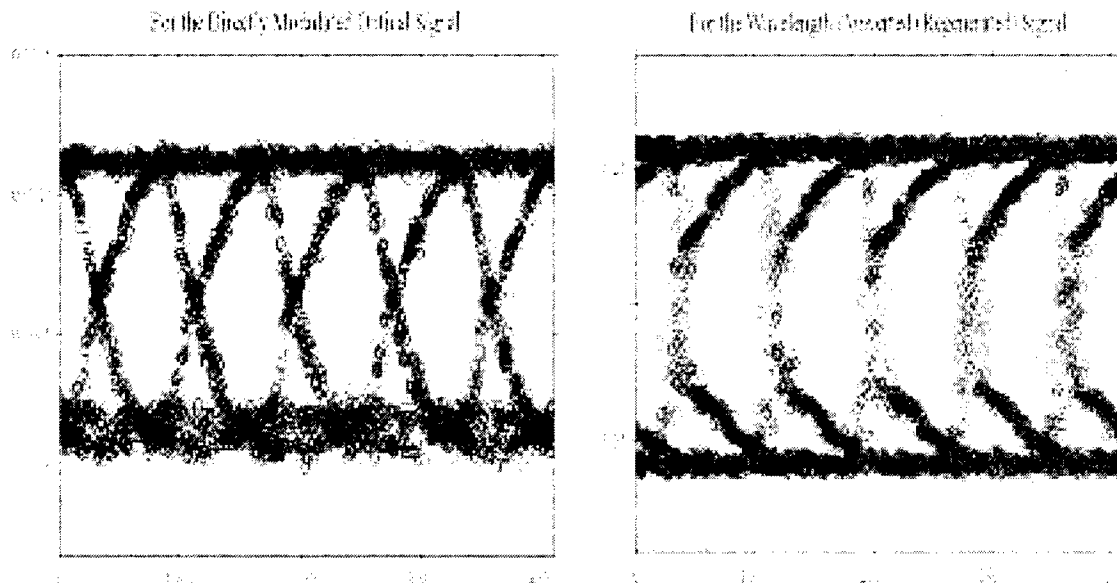


Figure 4: Eye diagrams of (a) the input data, and (b) the regenerated converted signal

Figure 5 shows the BER as a function of the input power to the receiver for different configurations (1) back-to-back, (2) single pump and (3) double pump with up conversion of 10nm(x) and 5nm(o), and down conversion of 21nm(*). One can see that there is a 3 dB penalty between the wavelength converted signal and the back-to-back configuration. It is important to note

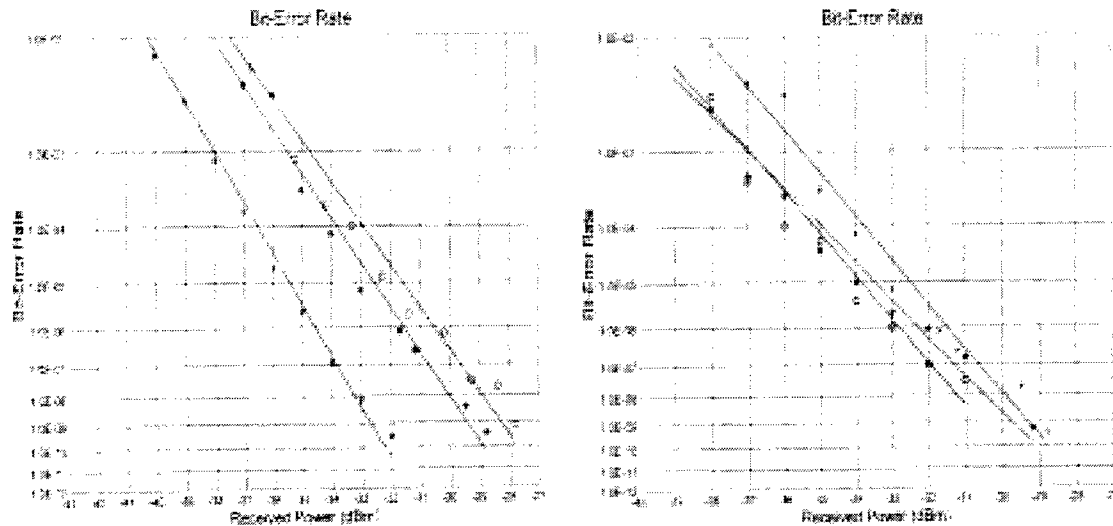


Figure 5: BER performance for different configurations. (a) BER for the directly modulated signal(x), single pump(o) and double pump(*), b) BER of double pump scheme with up conversion of 10nm(x) and 5nm(o), and down conversion of 21nm(*)

that there is no extra penalty between the single pump and double pump scheme (for equal intensity pump), and the penalty for different wavelength shifts does not change if we take into account the measurement accuracy and stability.

Figure 6 shows the BER against the received power for the scheme with two input signals. One can see that the penalty for the converted signal is about 1.5 dB for the first wavelength 6(a) and 3 dB for the second wavelength 6(b). That difference of penalty comes from the fact that the

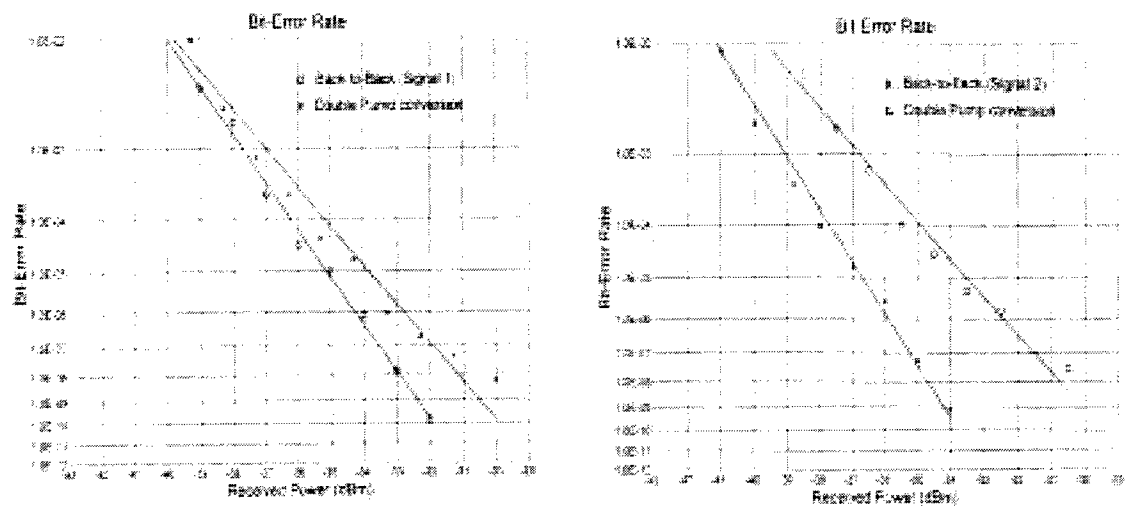


Figure 6: BER plots for the back-to-back and converted signals (a) first and (b) second wavelengths

signal-to-background ratio for the second converted signal is about 3 dB less than that of the first one (due to the difference in the conversion efficiencies).

IV. CONCLUSION

In conclusion, BER measurements at 2.5Gbit/s on wavelength converted signals using double pump FWM in a semiconductor optical amplifier have been performed experimentally for both single- and multiple-input wavelengths. It is found that the wavelength-converted signal can be made wavelength insensitive for detuning from -30nm to 15nm. We have also seen that the double pump scheme enables us to perform multiple-input wavelength conversion with very low penalty. These results demonstrate the potential system application of double pump FWM scheme in future optical networks.

Acknowledgments:

The authors acknowledge receiving two NEL arrayed waveguide gratings from the Joint Optoelectronic Project (JOP) between Japan and the USA. They also acknowledge receiving partial financial support from AFOSR and NSF.

References :

- [1] G-H. Duan, "Semiconductor lasers and amplifiers for optical switching", Chapter 10 in *Semiconductor lasers: past, present, and future*, edited by G. P. Agrawal, AIP Press, 1994.
- [2] G. Grosskopf, R. Ludwig and H. G. Weber, "140Mbit/s DPSK transmission using an all-optical frequency converter with a 40000 GHz conversion range", Electron. Lett., vol. 24, pp. 1106-1107, 1988.
- [3] I. Tomkos, I. Zacharopoulos, D. Syvridis, T. Sphicopoulos, C. Caroubalos, and E. Roditi, "Improved performance of a wavelength converter based on dual pump four-wave mixing in a bulk semiconductor optical amplifier", Appl. Phys. Lett. 72, 2499 (1998)
- [4] G. Contestabile, F. Martelli, A. Mecozzi, L. Graziani, A. D'Ottavi, P. Spano, G. Guekos, R. Dall'Ara and J. Eckner, "Efficiency Flattening and equalization of frequency up- and down-conversion using four wave mixing in semiconductor optical amplifiers", IEEE Photonics Technology Lett., vol. 10, pp. 1398-1400, 1998.
- [5] Trefor J. Morgan, Rodney S. Tucker and Jonathan P.R. Lacey, "C-band to L-band shift of 80 nm (10THz) using four-wave mixing in a semiconductor optical amplifier", Proc. Of Optical Fiber Communication Conference, San Diego, February 1999.
- [6] I.Brenner, M.H.Chou, M.M.Fejer, "Efficient wideband wavelength conversion using cascaded second-order nonlinearities in LiNbO₃ waveguides", Proc. Of Optical Fiber Communication Conference, San Diego, February 1999.

[7] C.M.Greco, F.Martelli, A.D'Ottavi, A.Mecozzi, P. Spano, R.Dall'Ara, "Frequency-Conversion Efficiency Independent of Signal-Polarization and Conversion-Interval Using Four-Wave Mixing in Semiconductor Optical Amplifiers", IEEE Photonics Technology Lett., vol. 11, no 6, pp. 656-658, June 1999.

[8] S.J.B.Yoo, G.K.Chang, Wei Xin, M.A.Koza, "Simultaneous multi-channel conversion of analog and digital signals by polarization independent-difference-frequency generation", Proc. Of Optical Fiber Communication Conference, San Diego, February 1999.

[9] R.Schnabel, et al, " Polarization Insensitive Frequency Conversion of a 10-Channel OFDM Signal Using Four-Wave-Mixing in a Semiconductor Laser Amplifier", IEEE Photonics Technology Lett., vol 6, no 1, pp 56-58, 1994.

[10] D. Sigogne, A. Ougazzaden, D. Meichenin, B. Mersali, A. Carenco, J. C. Simon, I. Valente, C. Vassallo, and L. Billes, "1.55mm polarization insensitive InGaAsP strained MQW optical amplifier integrated with short spot-size converters", Electron. Lett., vol. 32, pp. 1403-1405, 1996.

[11] Ortel WDM transmitter (model 10348A) data sheet.

[12] J.Zhou, N.Park, K.J.Vahala, M.Newkirk, B.I.Miller, "Four-wave mixing wavelength conversion efficiency in semiconductor travelling-wave amplifiers measured to 65 nm of wavelength shift", IEEE Photonics Technology Lett., vol. 6, p. 984, 1994.

Efficient generation of tunable mid-infrared radiation in a channel waveguide

Douglas J. Bamford, Konstantin P. Petrov, Arti P. Roth, Thomas L. Patterson

Gemfire Corporation

2471 East Bayshore Road, Suite 600, Palo Alto, CA 94303 U.S.A.

tel.: 650-849-6800, fax: 650-849-6900

e-mail: djbamford@aol.com

Development of highly efficient, low-loss integrated channel waveguides has enabled the efficient frequency conversion of continuous-wave lasers operating in the milliwatt power regime. Tight containment of laser beams in a waveguide eliminates tradeoff between mode size and interaction length, characteristic of beam interaction in bulk crystals. For the process of difference-frequency generation (DFG), in which a much longer (idler) wavelength is produced by mixing two relatively short (pump and signal) wavelengths, the use of a tapered periodically-segmented coupling region has been shown to facilitate single-mode excitation [1]. However, the periodically segmented structure is more difficult to design and fabricate, and has higher optical losses, than a solid waveguide. In this work we report the first use of a solid tapered waveguide structure in the production of mid-infrared radiation by DFG.

We designed and fabricated a three-stage integrated channel waveguide array in periodically poled lithium niobate (PPLN) using the process of annealed proton exchange (APE). Our choice of fabrication conditions, as well as theoretical predictions of waveguide performance, were based on a prior systematic study of refractive index profiles and dispersion of planar APE waveguides. The channel waveguide array was used to produce a continuous-wave, single-frequency tunable 3.6- μ m radiation by difference-frequency mixing of diode lasers at 787 nm and 1008 nm, each operated at 150 mW output power.

The waveguide channel mask had a 2-mm-long, 2- μm -wide mode filter followed by a 2-mm-long, 2 \rightarrow 20 μm linear width taper and a 17-mm-long, 20- μm -wide mixing channel. The width taper was designed to change the size of the TM_{00} mode adiabatically and with low loss according to the criteria presented by Milton and Burns [2]. Waveguides were fabricated by proton exchange in pure benzoic acid for 34 hours at 160°C, followed by annealing in air for 75 hours at 326°C.

Figure 1 shows the waveguide quasi-phase-matching (QPM) curve at room temperature for one of the waveguide structures. An output power of 80 μW was generated in this experiment with 42 mW pump power and 48 mW signal power coupled into the waveguide. The corresponding device efficiency is 4% $\cdot\text{W}^{-1}$. Based on physical length of the DFG section (17 mm), we compute a normalized DFG efficiency of 1.4% $\cdot\text{W}^{-1}\cdot\text{cm}^{-2}$. This is the highest reported normalized DFG efficiency for production of such a long wavelength in a guided-wave DFG device [3]. Calculations show that waveguide structures prepared using this mask design and fabrication recipe are capable of generating wavelengths as long as 4.3 μm with a properly chosen QPM period. Efficient production of radiation at these longer wavelengths would make possible highly sensitive spectroscopic detection of carbon dioxide.

A second device was optimized for the production of tunable radiation at 2.8 μm . The waveguide channel mask had a 2-mm-long, 3- μm -wide mode filter followed by a 2-mm-long, 3 \rightarrow 20 μm linear width taper, and a 17-mm-long, 20- μm -wide mixing channel. Waveguides were fabricated by proton exchange in pure benzoic acid for 8 hours at 160°C, followed by annealing in air for 24 hours at 326°C. An output power of 136 μW was generated in this experiment with 120 mW pump power (at 791 nm) and 68 mW signal power (at 1096 nm) coupled into the waveguide. The corresponding device efficiency is 1.7% $\cdot\text{W}^{-1}$. Based on the effective length of the DFG section (13 mm), we compute a normalized DFG efficiency of 1.0% $\cdot\text{W}^{-1}\cdot\text{cm}^{-2}$. The tunable radiation generated in this structure has been used to perform spectroscopic detection of atmospheric water vapor.

We anticipate that integration of similar channel waveguides with diode lasers will create a very compact, room-temperature, low-power source of tunable mid-infrared light for spectroscopic and trace gas sensing applications. Improvements in uniformity (over 3 cm) and in design of the mixing channel are expected to yield devices with DFG conversion efficiency of over 20%·W⁻¹.

- [1] M.H. Chou, M.A. Arbore, and M.M. Fejer, Opt. Lett. **21**, 794 (1996).
- [2] A.F. Milton and W.K. Burns, IEEE J. Quant. Elect. **QE-13**, 828 (1977).
- [3] M.A. Arbore, M.H. Chou, and M.M. Fejer, CLEO'96 Technical Digest **10**, 120 (1996).

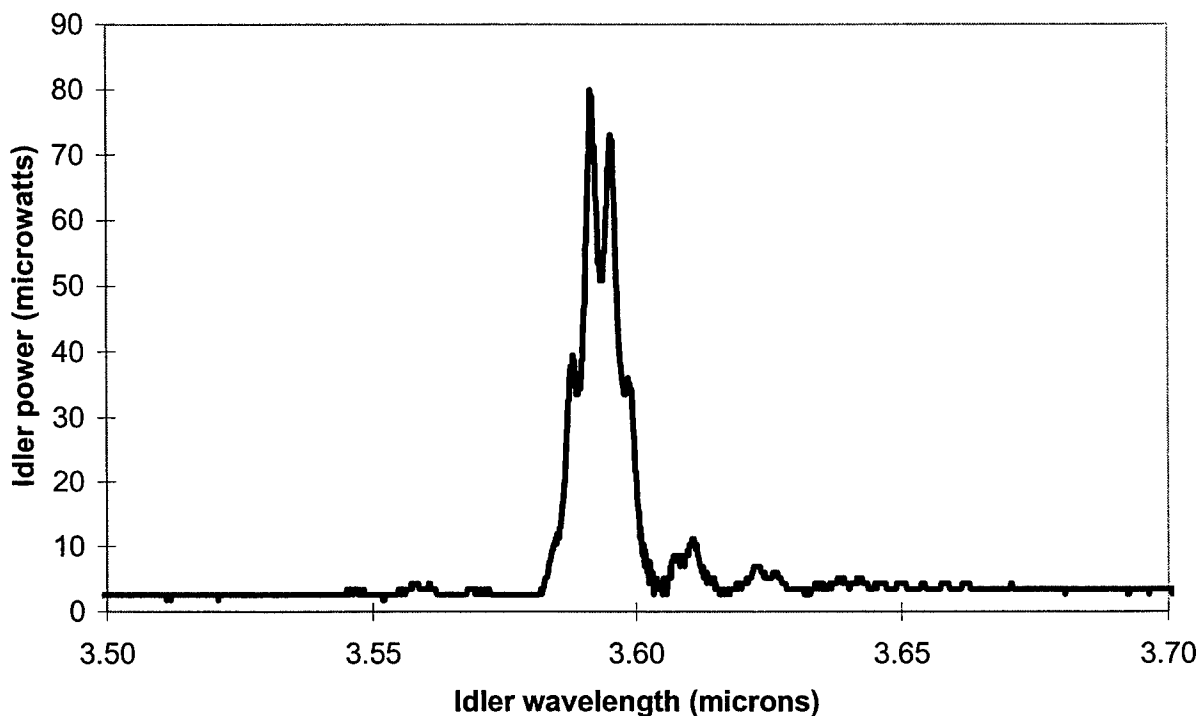


Figure 1. Guided-wave DFG output power as a function of idler wavelength, for mixing of a tunable pump laser near 780 nm with a fixed-frequency signal laser at 1008 nm.

Difference-frequency radiation around $4.3\text{ }\mu\text{m}$ for high sensitivity and sub-Doppler spectroscopy of CO_2

D. Mazzotti, G. Giusfredi, and P. De Natale

Istituto Nazionale di Ottica (INO), Largo Fermi, 6 I-50125 Firenze, Italy

mazzotti@generale.lens.unifi.it, giusfredi@fox.ino.it, denatale@fox.ino.it

J. Mitchell and L. Hollberg

National Institute for Standards and Technology (NIST), Boulder, Colorado 80303, USA

mitchej@ucsu.colorado.edu, hollberg@boulder.nist.gov

Abstract: We report on difference-frequency-generation (DFG) in periodically-poled lithium niobate (PPLN) around $4.3\text{ }\mu\text{m}$, using as pumping sources an injection-locked diode laser, tunable around 852 nm, and a diode-pumped Nd-YAG laser at 1064 nm. Peculiar features of the infrared generated radiation are a linewidth of about 100 kHz, amplitude fluctuations close to the quantum limit and a high conversion efficiency. Details of such a source configuration are given and potential applications to high sensitivity spectroscopy are discussed. With this set-up we were able to observe sub-Doppler lineshapes in the fundamental vibro-rotational band of CO_2 . A characterization of these derivative profiles is reported.

OCIS codes: (190.2620) Frequency conversion; (300.6460) Spectroscopy, saturation; (300.6340) Spectroscopy, infrared; (300.6390) Spectroscopy, molecular.

Introduction

Periodically poled non-linear crystals and diode lasers represent a breakthrough in convenience for spectroscopic applications throughout the spectrum and particularly in the infrared. Indeed, they allow full spectral coverage of the mid-infrared region at wavelengths up to about $5\text{ }\mu\text{m}$, encompassing the fundamental vibro-rotational bands of many molecules. Although Doppler-limited spectroscopy has already been demonstrated with difference-frequency-generation (DFG) in such crystals [1-6], present devices have not yet reached the performance of semiconductor or solid-state lasers for the highest resolution in high sensitivity spectroscopic applications. Desired improvements are narrower linewidth, quantum noise limited operation and a simultaneous increase of the IR output power.

Source characterization

We have developed a new experimental set-up that allows to produce an infrared beam (at $4.3\text{ }\mu\text{m}$) with a linewidth of about one hundred kilohertz, while preserving broad IR tunability, reducing the amplitude noise down to near the quantum limit and generating IR powers many times higher than the saturation limit of existing detectors. In this system the pump and signal sources are, respectively, a non-planar ring Nd-YAG CW laser at 1064 nm (InnoLight, maximum output power 800 mW) and a diode laser (slave laser, SDL 5422, maximum output power 150 mW). The latter is injection-locked by a low power diode (master laser, SDL 5401) mounted in an external-cavity Littrow-configuration (maximum power out of the cavity 23 mW). [7]

This master-slave configuration allows to use the broad tunability of external cavity diode lasers, as well as its narrow linewidth, while being able to take advantage of the full output power of the slave laser. Fig. 1 shows the measured fluctuations in the center frequency of the injected laser as compared to the same slave laser without any injection. As anticipated, for all time scales, there is a significant reduction in the injected laser's frequency fluctuations.

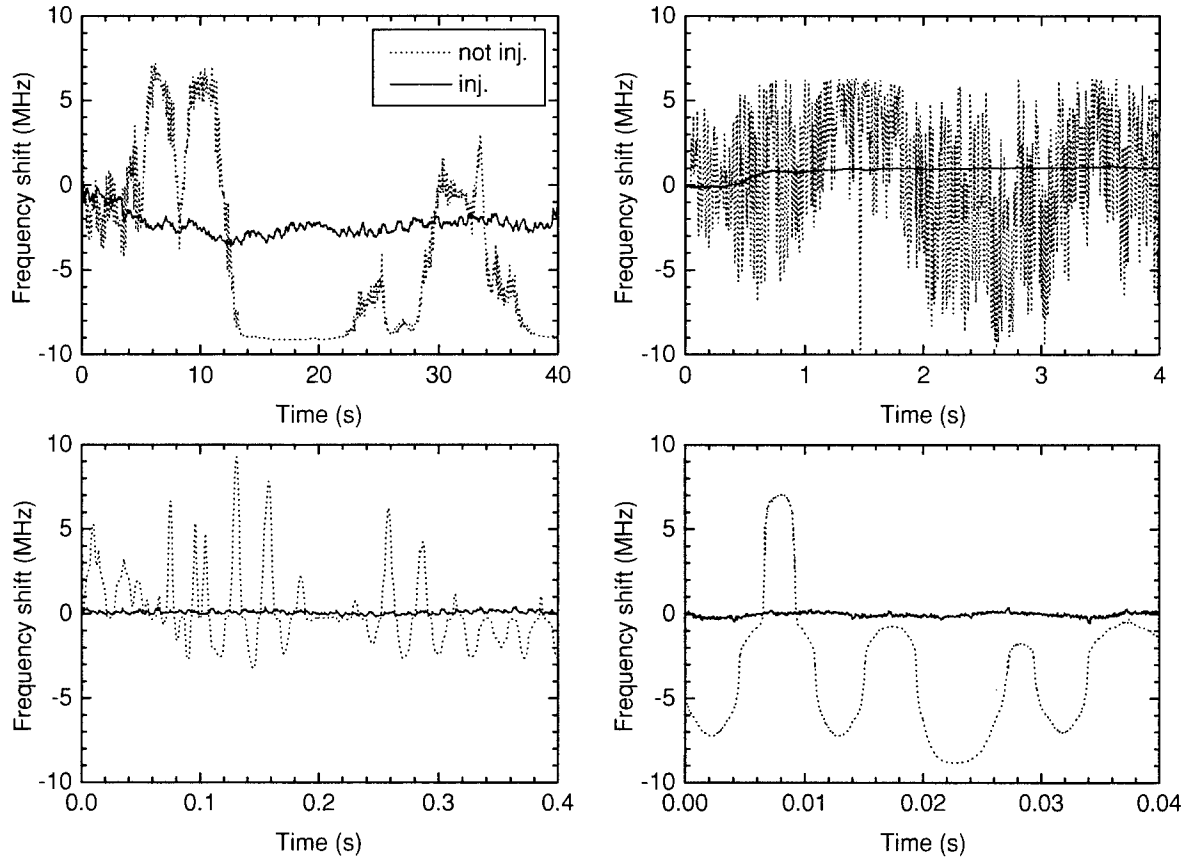


Fig. 1. Fluctuations in the center frequency of the high-power diode laser under conditions of injection lock and not injection locked. Measurements were taken by using a side of a Fabry-Perot fringe as frequency discriminator.

Most importantly, when the slave was injection locked, we measured the spectral distribution of the amplitude noise on the $4.3\text{ }\mu\text{m}$ beam and observed a noise reduction of up to 30 dB for Fourier frequencies between 1 and 4 kHz. We also investigated the composition of amplitude noise affecting the IR detector. Fig. 2 shows the spectral density of the noise from the InSb liquid- N_2 cooled detector.

The three traces shown were taken with the detector looking at: a mirror in front of it (which means the detector is looking at a background close to 77 K); a 25° C background; the same background except with the crystal oven heated at the operating temperature of 284° C and occupying part of the field of view. From such measurements, we determined that about 60 % of the noise floor above quantum noise is due to background fluctuations and the remaining 40 % depends on internal detector noise. The former contribution can be reduced close to zero with use of appropriate optical cold filtering on the detector. The higher temperature trace corresponds to the case of the detector viewing the hot oven, which controls the periodically poled LiNbO_3 ($17.5 \times 10 \times 0.5\text{ mm}$) to the appropriate temperature to quasi-phase-match incoming radiation for $4.3\text{ }\mu\text{m}$ generation.

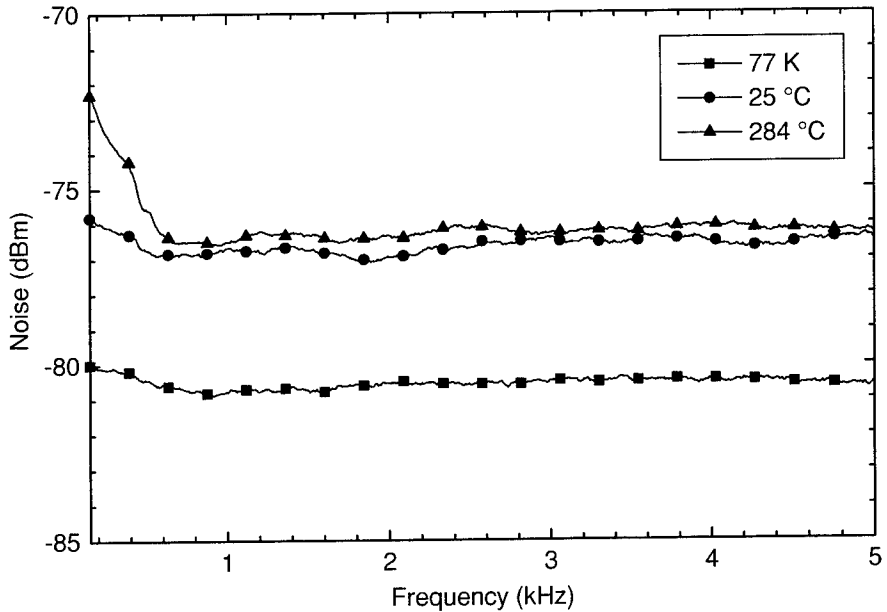


Fig. 2. Detector amplitude noise dependence on background temperature. Intrinsic detector noise coincides with the trace recorded at 77 K.

CO₂ detection sensitivity

After careful calibration of the detector responsivity with a reference black-body, we measured a maximum efficiency to the IR at 4.3 μ m of 0.012 % $W^{-1} cm^{-1}$, corresponding to a maximum IR power of 12 μ W. This result enables to perform sub-Doppler spectroscopy on CO₂ transitions (saturation intensity $I_s \approx 1$ mW/mm², for the strongest lines), taking advantage of the narrow IR linewidth. From amplitude noise measurements on the 4.3 μ m beam and considering a signal of 2 μ W (which saturates our InSb detector) we estimate a sensitivity of 0.01 ppb m Hz^{-1/2} (air-broadened lines) for this spectrometer. In table 1 we compare this value with those obtained with semiconductor lasers operating on the weaker CO₂ overtone bands near 1.6 and 2.0 μ m wavelengths.

Table 1. Comparison of sensitivity for CO₂ detection using different absorption lines and methods.

CO ₂ IR transition	2v ₁ +2v ₂ +v ₃ P(8)	v ₁ +2v ₂ +v ₃ R(24)	v ₃ R(16)
λ (μ m)	1.577	2.002	4.235
S (cm/molecule)	$1.2 \cdot 10^{-23}$	$1.0 \cdot 10^{-21}$	$3.5 \cdot 10^{-18}$
Sensitivity (Hz ^{-1/2})	$7 \cdot 10^{-8}$	$7 \cdot 10^{-7}$	$4 \cdot 10^{-7}$
Sensitivity (ppb m Hz ^{-1/2})	1000	100	0.01
Reference	[6]	[6]	This work and [8]

Sub-Doppler spectroscopy

Very recently, we were able to record saturated-absorption Lamb-dips, with our DFG source [9]. Fig. 3 shows a recording of the v₃ R(14) CO₂ transition. We show the Doppler profile (trace a), and the corresponding Lamb-dip (trace b). The saturation Lamb-dip was not visible in the Doppler trace, recorded by

modulating the Nd-YAG amplitude using a chopper, but wavelength modulation of the Nd-YAG laser was required, giving a first derivative lineshape.

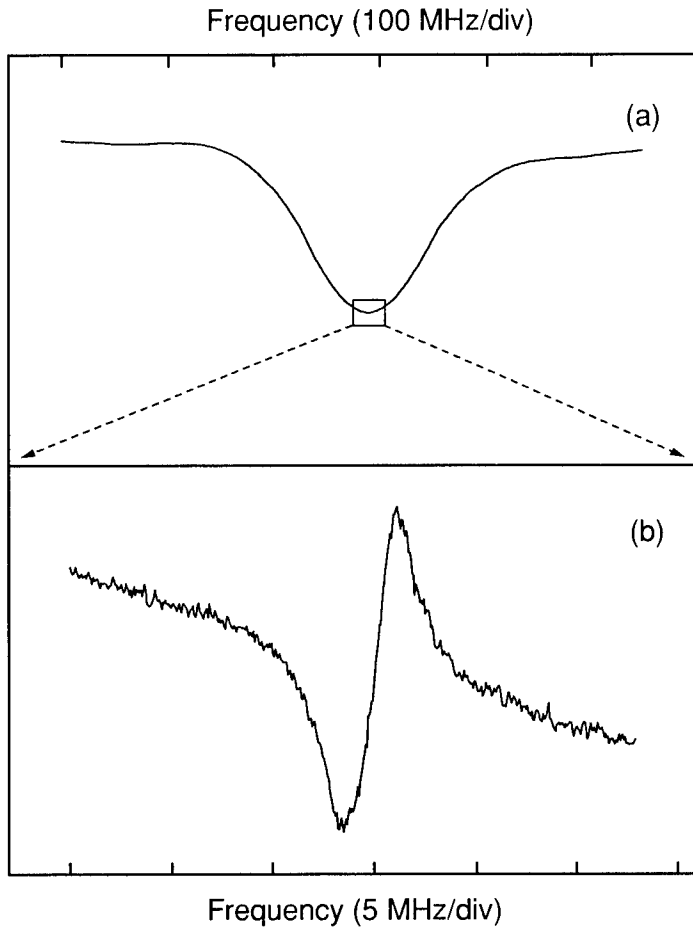


Fig. 3. (a) Direct absorption recording of n_3 R(14) CO_2 Doppler profile. (b) Wavelength modulation recording of the Lamb-dip, shown in a magnified frequency scale. The modulation frequency was 2 kHz.

about 100 kHz. We chose, for our set-up, a cell length of 0.5 mm, a beam-waist w_0 of 35 μm and a CO_2 pressure of 10 Pa, therefore pressure broadening only contributed about 160 kHz (assuming a self-broadening coefficient of 15.7 kHz/Pa [10]) to the halfwidth at half maximum (HWHM), while the transit-time/wavefront-curvature broadening amounted to about 1.3 MHz. The expression for this contribution is [11]:

$$\gamma = \frac{\sqrt{2 \ln 2}}{2\pi} \frac{v}{w(z)} \sqrt{1 + \left[\frac{\pi w(z)^2}{R(z)\lambda} \right]^2} = \frac{\sqrt{2 \ln 2}}{2\pi} \sqrt{\frac{k_B T}{m}} \frac{1}{w_0} \quad (1)$$

From data in Tab.1 it comes out that, if the very strong absorption of the v_3 R(14) and neighbouring lines lowers the saturation intensity, it also severely limits propagation in atmospheric air of peak-resonant IR radiation. Indeed, 1/e absorption is experienced in a distance as short as 5.8 cm by a beam propagating in air, considering a line strength of $3.5 \cdot 10^{-18}$ cm/molecule and a 0.3 ‰ (33 Pa) CO_2 concentration in air. Therefore, atmospheric absorption is of main concern to perform spectroscopic experiments using radiation resonant with such lines. To overcome this problem, we enclosed our saturated-absorption set-up in a box and purged it with a slow flux of pure N_2 , thus reducing to about 30 % the total absorption, mainly due to the 2 cm air-pathlength that separated the PPLN crystal from the box entrance.

To observe the saturated absorption lineshape, a proper combination of cell length, beam waist, modulation depth and gas pressure had to be chosen. Considering the very long natural lifetimes of the upper levels of these IR transitions, corresponding to a few tens of Hz, the observed linewidth is mainly determined by pressure and transit-time/wavefront-curvature broadening, IR linewidth contributing only

where $w(z)$ and $R(z)$ are, respectively, waist and radius of curvature at position z , v is the radial mean velocity (rms) of the molecules, m is the molecular mass and T the absolute temperature. It is notable that the dependence on the position z , for a Gaussian beam, completely disappears.

The cell length was chosen equal to the Rayleigh range of the $4.3\text{ }\mu\text{m}$ beam, to have an homogeneous field along the cell. As a consequence, the cell was filled with a gas pressure around 10 Pa , to maximize the S/N ratio. Fig. 4 shows how the Lamb-dip signal varies, changing the CO_2 pressure in the cell.

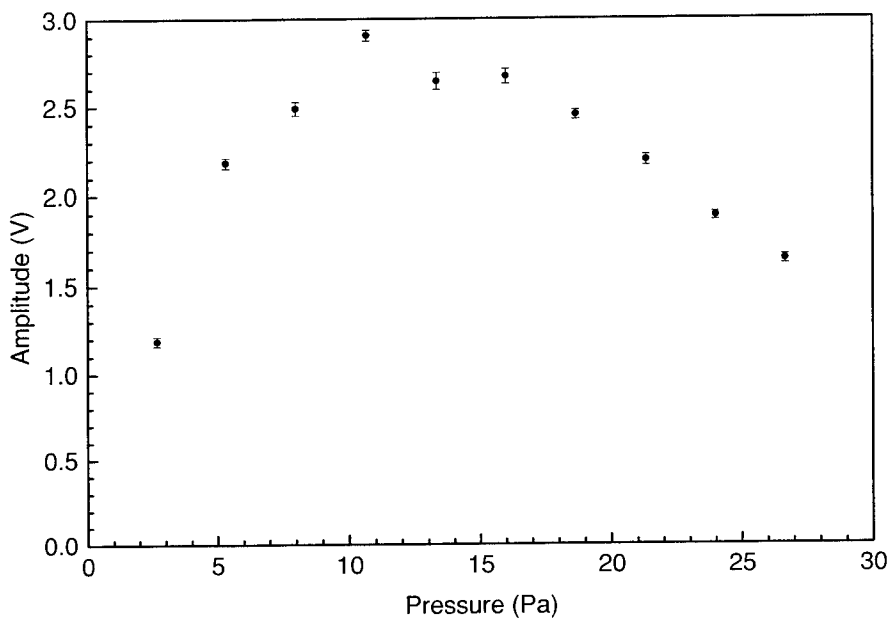


Fig. 4. Dependence of the Lamb-dip amplitude as a function of the gas pressure. Saturated lineshapes were recorded using wavelength modulation technique. Signal was demodulated at the third harmonic frequency (obtaining a third derivative lineshape).

The waist size determines, through the transit-time/wavefront-curvature broadening, the observed linewidth γ and, hence, the saturation intensity I_S , that quadratically depends on γ :

$$I_S = \frac{\epsilon_0 c}{2} \left(\frac{h\gamma}{\mu} \right)^2 \quad (2)$$

Obviously, also the beam intensity I increases quadratically with the beam waist so that the ratio I/I_S , determining the contrast, i.e. the ratio between Lamb-dip depth and the Gaussian profile amplitude, is about independent on the waist size, until the linewidth is due to transit-time broadening.

Summary

This novel diode-laser based DFG spectrometer, resonant with the strong ν_3 absorption band, proved to be a useful tool for high sensitivity measurements of CO_2 concentrations. Sub-Doppler resolution was also demonstrated with a simple saturation set-up. Considering the broad tunability of this spectrometer

and the strong absorption bands of many other molecules, in this wavelength region, it may find application in atmospheric chemistry (global warming etc), biological systems, process monitoring and fundamental physics experiments.

Acknowledgements

It is a pleasure to acknowledge Chiara Fort (LENS-Firenze) for constructing the diode-lasers system and Massimo Inguscio (LENS-Firenze) for useful discussions and suggestions.

References

1. K. P. Petrov, L. Goldberg, W. K. Burns, R. F. Curl, and F. K. Tittel, "Detection of CO in air by diode-pumped 4.6 μm difference-frequency generation in quasi-phase-matched LiNbO₃", Opt. Lett. 21 86-88 (1996).
2. A. Balakrishnan, S. Sanders, S. DeMars, J. Webjorn, D. W. Nam, R. J. Lang, D. G. Mehuis, R. G. Waarts, and D. F. Welch, "Broadly tunable laser-diode-based mid-infrared source with up to 31 μW of power at 4.3 μm wavelength", Opt. Lett. 21 952-954 (1996).
3. K. P. Petrov, S. Waltman, E. J. Dlugokencky, M. Arbore, M. M. Fejer, F. K. Tittel, and L. W. Hollberg, "Precise measurement of methane in air using 3.4 μm difference-frequency generation in PPLN", Appl. Phys. B 64 567-572 (1997).
4. K. P. Petrov, R. F. Curl, and F. K. Tittel, "Compact laser difference-frequency spectrometer for multicomponent trace gas detection", Appl. Phys. B 66 531-538 (1998).
5. K. Fradkin, A. Arie, A. Skliar, and G. Rosenman, "Tunable midinfrared source by difference frequency generation in bulk periodically poled KTiOPO₄", Appl. Phys. Lett. 74 914-916 (1999).
6. G. Modugno, C. Corsi, M. Gabrys, F. Marin, and M. Inguscio, "Fundamental noise sources in a high-sensitivity two-tone frequency modulation spectrometer and detection of CO₂ at 1.6 μm and 2 μm ", Appl. Phys. B 67 289-296 (1998).
7. Mention of specific products is for technical clarity only and is not a recommendation.
8. D. Mazzotti, P. De Natale, G. Giusfredi, C. Fort, J. Mitchell, L. Hollberg, "Difference frequency generation in PPLN at 4.3 μm : an analysis of sensitivity limits for DFG spectrometers", to be published.
9. D. Mazzotti, P. De Natale, G. Giusfredi, C. Fort, J. Mitchell, L. Hollberg, "Saturated-absorption spectroscopy using low power difference-frequency radiation", to be published.
10. L. S. Rothman, R. R. Gamache, R. H. Tipping, C. P. Rinsland, M. A. H. Smith, D. Chris Benner, V. Malathy Devi, J.-M. Flaud, C. Camy-Peyret, A. Perrin, A. Goldman, S. T. Massie, L. R. Brown, R. A. Toth, "The HITRAN molecular database: editions of 1991 and 1992", J. Quant. Spectrosc. Radiat. Transfer 48 469- (1992).
11. W. Demtröder, *Laser Spectroscopy* (Springer, Berlin, 1996), pp. 85-88.

VCSELs and Applications

Micromachined tunable optoelectronic devices for spectroscopic applications

James S. Harris, Jr., Chien-chung Lin, Wayne Martin

Solid State and Photonic Laboratory, Stanford University, CA 94305

harris@snow.stanford.edu, cclin@snow.stanford.edu

Fred Sugihwo

Hewlett-Packard Microwave Technology Center, Santa Rosa, California, USA

FRED_SUGIHWO@HP-Sonoma-om3.om.hp.com

Michael Larson

Lawrence Livermore National Laboratory, Livermore, California, USA

larson@snowmass.stanford.edu

Barbara Paldus

Informed Diagnostics, Sunnyvale, California, USA

barbara@infodiag.batnet.com

Abstract: Micromachined tunable optoelectronic devices can be used to improve spectroscopic measurements. The standing wave enhancement effect in Fabry-Perot cavities can be used to increase sensitivity. The size and cost of semiconductor micromachined devices make them an attractive alternative to conventional tabletop spectroscopy setups. Recent advances in micromachined tunable optoelectronic devices and their application to spectroscopy are described. **OCIS codes:** (300.6260) Spectroscopy, diode laser; (140.3600) Lasers, tunable.

Absorption spectroscopy a commonly used technique for detecting the presence or concentration of a chemical species. It is as simple as shining a light through the material and measuring the reduction in its intensity. Strong, incoherent light sources and abundant target material is needed to achieve high sensitivity in absorption spectroscopy. Lasers and resonant cavities have enabled new spectroscopic techniques including laser spectroscopy and multipass cell absorption spectroscopy. Because of their higher sensitivity, they play important roles in measuring weak transitions and low concentrations in the chemical species. These advances have enabled a wide range of applications in the fields of air pollution control and hazardous gas detection.

Micromachined tunable optoelectronic devices are now promising components in communications systems. Due to their wavelength tunability, these devices can also be used in spectroscopy with reasonable sensitivity and narrow linewidth. Compared to other tunable coherent sources, micromachined tunable vertical cavity devices are tiny in volume and are inexpensive to fabricate in large arrays. They also have much lower power requirements and higher efficiencies. These features make tunable semiconductor devices suitable for low-cost spectroscopy equipment and wide area, low power distributed gas-detection systems.

Figure 1 shows a schematic diagram of the typical structure for micromachined tunable devices. The main structure (optoelectronic active regions and mirrors) is grown by using molecular beam epitaxy (MBE) technology. The membrane structure is deposited by PECVD and e-beam evaporation. The membrane structure of the devices is released by selective etching and is identical for all of the device types discussed in this paper while the active region is designed according to the particular application: vertical cavity laser [1], resonant cavity photodetector [2], resonant cavity phototransistor [2], and interferometer [3]. The micromachined structure consists of a deformable membrane made of

$\text{Si}_3\text{N}_4/\text{SiO}_2$ and gold metalization to form a distributed Bragg reflector (DBR) and an electrical contact. The sacrificial layer is selectively etched to release the membrane and is supported by four Si_3N_4 legs stretching from the posts. When a voltage is applied on the membrane, the membrane will be pulled downward due to electrostatic attraction. The top membrane and bottom DBR form a Fabry-Perot cavity and the decreasing cavity length changes the resonant wavelength of the devices. In Figure 2, we demonstrate the tuning spectrum of the tunable interferometer which is composed of 12.5 pairs of bottom AlAs/GaAs DBR and a silicon nitride/gold top mirror. The tuning range is 31nm. [3]

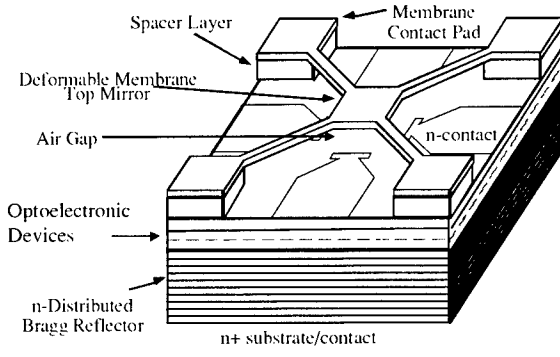


Fig. 1: Schematic diagram of micromachined tunable optoelectronic devices

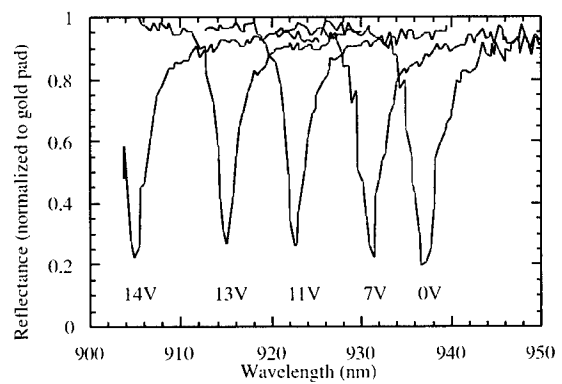


Fig. 2 The tuning spectrum of micromachined interferometer [3]

Figure 3 demonstrates a micromachined tunable vertical cavity laser with 30.4 nm of tuning range [4]. Figure 4 shows a narrow linewidth (<2nm) tunable PIN photodiode. The structure of these devices is basically the same: 25.5 pairs of AlAs/GaAs bottom DBR, 2λ cavity, and 2.5 pairs of $\text{Si}_3\text{N}_4/\text{SiO}_2$ DBR. If the optical signal is weak and high electrical gain is required for the system, a phototransistor rather than a p-i-n diode can be used to meet this requirement[5]. All of the devices that we have fabricated use InGaAs quantum wells as the active layer and operate in the 0.9 to 1.0 μm region.

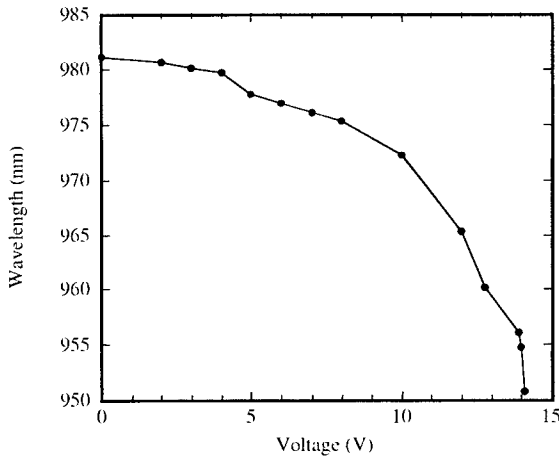


Fig. 3: Lasing wavelength of a micromachined tunable laser versus the tuning membrane bias

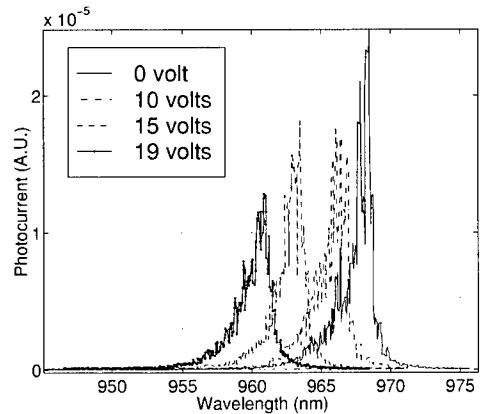


Fig. 4: Spectrum of narrow-linewidth PIN tunable photodiode

However, in some cases it is desirable for the detector to have gain to overcome amplifier thermal noise when the signal is weak and a simple PIN structure won't work. We have proposed and fabricated tunable phototransistors which can provide electronic amplification[5]. Figure 5 shows the preliminary results from a first generation device. The tuning range is 25.5 nm and the linewidth is a wide (6 to 8 nm) due to a low finesse cavity caused the low bottom mirror reflectance (9.5 AlAs / GaAs DBR pairs). With a higher finesse cavity design, a narrower linewidth is expected. The current gain of the phototransistor is around 100.

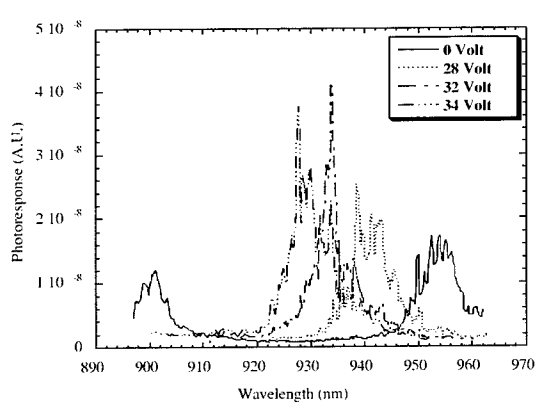


Fig. 5: The spectrum of the micromachined tunable phototransistor

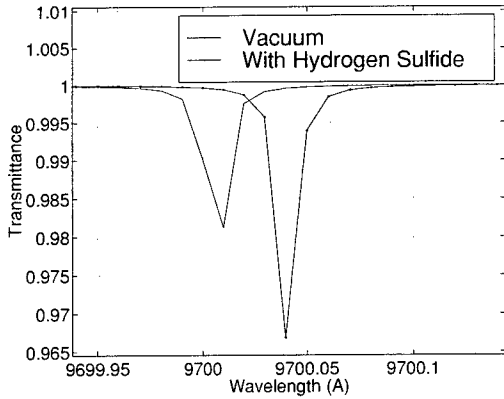


Fig. 6: Resonant spectrum change due to the presence of hydrogen sulfide

Detection of the presence of gases is a relatively simple operation with such devices. In a very high finesse cavity, only minute optical absorption and hence quantity of a gas is needed to alter the resonance condition of the cavity due to the strong circulating optical field. For example, in Figure 6, the transmittance change of a F-P filter due to the presence of hydrogen sulfide in the air gap is simulated. The tunable filter is made of a fixed bottom DBR mirror and top tunable membrane DBR and the air gap serves as the real cavity. When there is vacuum in the gap incident light at 970nm will be transmitted through the filter. Once there is a tiny amount of hydrogen sulfide in the air gap, the change in index of refraction and absorption will move the resonant wavelength away from 970 nm and greatly reduce the transmission of light at 970 nm. The present design for an interferometer based spectroscopic system shows a 2 percent change in transmission for a refractive index change of 10^{-5} or absorption in the order of 1 cm^{-1} .

Intracavity laser absorption spectroscopy has been demonstrated by V.M. Baev, et. al. [6] The target species was placed inside the laser cavity. Once the lasing wavelength matches the absorption peak, the laser output intensity will be lowered or even turned off. Because of the resonant cavity enhancement, we expect the sensitivity to be greatly improved. In our tunable devices, the intracavity region is formed by the air-gap plus the semiconductor active regions. If there are spectral peaks in the tuning range of the laser, as the membrane continuously tunes the laser, the laser spectrum will significantly decrease or even disappear at those wavelengths because of the absorption by the gas in the air-gap. Because of the coupling between the semiconductor and air cavities, a number of design tradeoffs are possible to optimize the device for different operating regimes. The Semiconductor Coupled Cavity (SCC) structure [7] is a better design for this type of gas detection device. The SCC design confines the high optical field largely in the semiconductor instead of the air-gap as in the filter case. With reduced coupling, the device will continue to lase with weak absorption, but a strong absorption line will turn the laser off. Recording the continuous tuning spectrum with and without the

presence of the chemical species and taking the difference between two data will reveal the absorbing spectrum of the species (Fig. 7).

Combining the active and passive devices, we can implement Continuous-Wave Cavity Ring-Down Spectroscopy (CW-CRDS). CW-CRDS has demonstrated significant enhancement of the sensitivity of such measurements. A detectable absorbance as low as 10^{-10} to 10^{-12} cm^{-1} can be detected in CW-CRDS[8]. As shown in Figure 8, aligning a tunable laser with a tunable filter and measuring the time variation in transmitted light intensity provides a measure of the absorbance. Using the exponential time decay of the laser and the following relationship [8]:

$$I_{\text{out}}(t) = K \times \exp(-2(\alpha_{\text{abs}} + \alpha_{\text{cav}})t/t_{\text{rt}}) \quad (1)$$

Where K is a constant, $(\alpha_{\text{abs}}$ is the absorbance of the material and α_{cav} is the cavity loss of the tunable filter and t_{rt} is the round trip time.

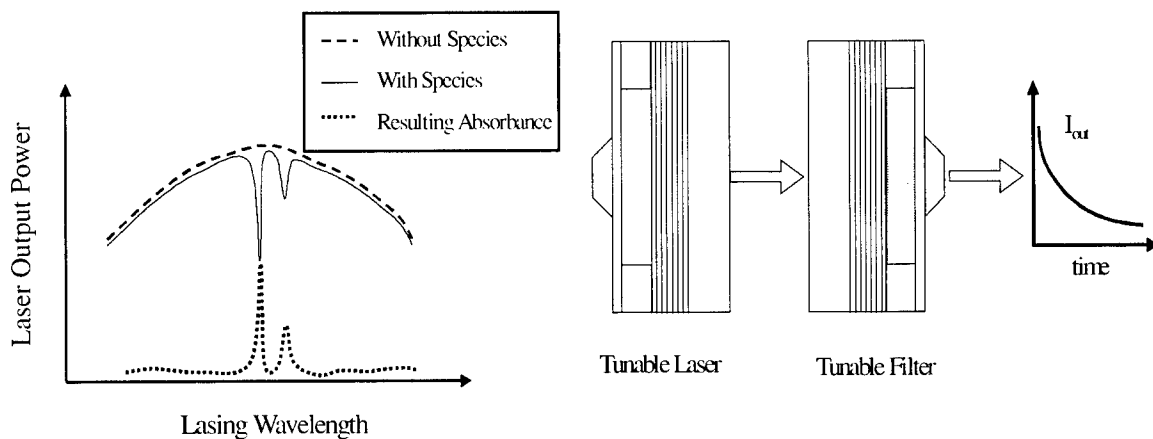


Fig. 7: Extraction of absorbance from the output power of a tunable vertical cavity laser

Fig. 8: Schematic Diagram for CW-CRDS using tunable optoelectronic devices

In CRDS it is more important to have a low optical cavity loss than it is to have long cavities. With CRDS micromachined tunable optoelectronic devices are capable of implementing high resolution, high sensitivity spectroscopy. Using semiconductor device fabrication methods enables the development of much smaller spectroscopy setups with a lower cost. The large and expensive laser and complicated tabletop optics will no longer be necessary.

In conclusion, monolithic micromachined tunable optoelectronic devices may enable a dramatic increase of spectroscopic applications. This paper describes progress in realizing monolithic micromachined tunable optoelectronic devices and discusses their application to spectroscopy and gas detection. Simulation shows that the detection sensitivity of such systems can be extremely high when high finesse F-P cavities are utilized.

References

1. M. C. Larson and J. S. Harris, Jr., *Appl. Phys. Lett.* 68, p. 893-3, February 12, 1996.
2. F. Sugihwo, et. al. *Proceedings of IEDM*, San Francisco, p. 665-668, Dec. 1998.
3. M. C. Larson, B. Pezeshki, and J. S. Harris, Jr., *IEEE Photon. Technol. Lett.*, vol. 7, pp. 382-384, Apr. 1995.
4. F. Sugihwo, M. C. Larson, and J. S. Harris, Jr., *Appl. Phys. Lett.*, Vol 72, no. 1, pp. 10-12, Jan. 5, 1998.
5. F. Sugihwo, C.C. Lin, W. Martin, J. S. Harris, Jr. (Submitted to *IEEE Photon. Technol. Lett.*, 1999)

6. V. M. Baev, J. Eschner, E. Paeth, R. Schuler, and P.E. Toschek. "Intracavity spectroscopy with laser diodes", *Appl. Phys. B*, B55, no.6, pp. 463, 1992
7. F. Sugihwo, Ph.D. Thesis, Stanford University, CA, August, 1998.
8. B.A. Paldus, Ph.D. Thesis, Stanford University, CA, May, 1998.

Nonlinear spectroscopy using a current-modulated VCSEL

C. Affolderbach, W. Kemp, S. Knappe, A. Nagel, R. Wynands

Institute for Applied Physics, Bonn University

Wegelerstraße 8, D-53115 Bonn, Germany

Phone +49-228-733483; Fax +49-228-733474

E-mail: wynands@iap.uni-bonn.de

Abstract: We have performed a series of experiments demonstrating the use of a vertical-cavity surface-emitting laser for nonlinear spectroscopy on the cesium D_2 transition at 852 nm wavelength. Due to the high modulation efficiency of the VCSEL sufficiently strong modulation sidebands at 9.2 GHz frequency can be produced by direct modulation of the laser injection current. Using the carrier and one of the modulation sidebands coherent population trapping (CPT) resonances in a buffered cesium vapor can be prepared with linewidths of only 60 Hz. For application of these narrow resonances to precision magnetometry we find a sensitivity of 10 pT in 0.3 s integration time. For the use of our setup as a frequency reference a relative stability of $1 \cdot 10^{-11}/\sqrt{\tau}$ is predicted. In both applications of CPT resonances the use of VCSELs as light sources helps to build compact and reliable devices.

OCIS codes: (140.2020) Diode lasers; (300.6420) Spectroscopy, nonlinear; (270.1670) Coherent optical effects; (120.3940) Metrology.

Recently vertical-cavity surface-emitting lasers (VCSEL), which hold great promise for telecommunications, are also available in the near infrared [1–3] where cesium and rubidium, some of the well-studied model systems in atomic spectroscopy, have their strongest resonance lines (894 nm, 852 nm, 794 nm, 780 nm). The benefits arising from a VCSEL’s characteristic properties like intrinsic single mode operation and large modulation bandwidth are also desirable for laser spectroscopy and in special applications might compensate for some disadvantages compared to conventional edge-emitting laser diodes. Here we report that in spite of their inherently larger linewidth (several 10 MHz) and rather low output power (typically not more than a few milliwatts) VCSELs are well suited for coherent population trapping spectroscopy [4,5] on a thermal cesium vapor, mainly due to their high modulation bandwidth exceeding 10 GHz [6]. The optical setup is greatly simplified and its reliability improved because no external mode-selection optics is needed.

Coherent population trapping (CPT) can occur in a so-called Λ system like, e.g., in cesium atoms where the two hyperfine components of the $S_{1/2}$ ground state are coupled to a common excited state via two light fields (Fig. 1). If the difference frequency of these light fields exactly matches the ground state splitting $\Delta_{\text{hfs}} = 9.2$ GHz the atoms are optically pumped into a coherent superposition of the ground states which no longer absorbs the light. Since this leads to a reduction of fluorescence intensity from the vapor the resonance is called a “dark resonance”. The essential physical process is the creation of ground state coherence and the resonance width is fundamentally limited by the ground state relaxation rate. In the case of cesium vapor discussed here the two lower states are part of the same hyperfine multiplet so that electric dipole transitions between them are forbidden and radiative damping is negligible. Hence careful control of experimental parameters

such as difference frequency stability, time-of-flight and collisional broadening results in very narrow experimental linewidths [7].

In previous CPT experiments large experimental effort had to be spent to provide phase-stable light fields at the 9.2 GHz frequency difference required for cesium by electronically phase-locking two extended-cavity diode lasers onto each other [7]. When a VCSEL is used the production of phase-coupled light fields becomes very simple and can be achieved by direct modulation of the laser injection current. The VCSEL employed here provides a modulation bandwidth of about 10 GHz and thus allows the creation of sufficiently strong sidebands at 9.2 GHz so that the carrier and one of the first-order sidebands can be used to prepare CPT resonances. For conventional edge-emitting lasers this is impossible because the modulation efficiency drops dramatically at frequencies exceeding their relaxation oscillation frequency of about 3 GHz (Fig. 2).

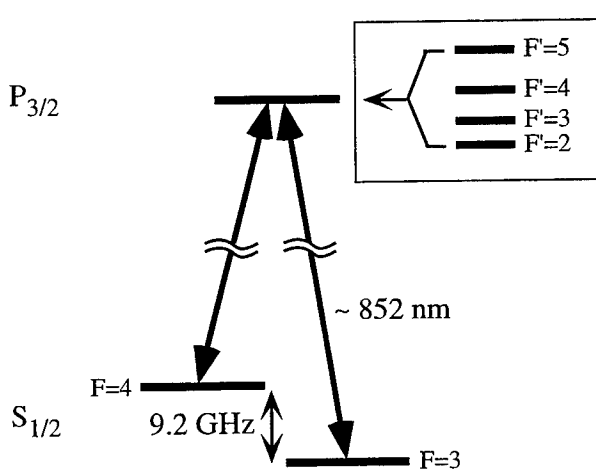


Fig. 1. Level scheme for coherent population trapping on the cesium D_2 line. The hyperfine structure of the $P_{3/2}$ excited state is given in the inset.

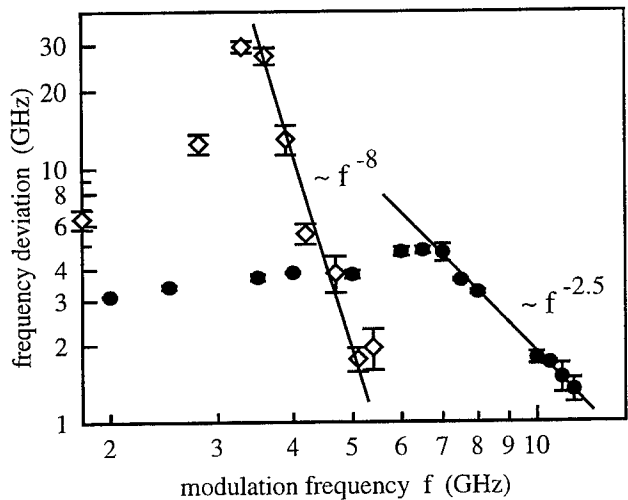


Fig. 2. Measured modulation efficiency in terms of the resulting frequency deviation for the VCSEL (circles) and an edge-emitting diode laser (diamonds). The data was obtained from the relative strengths of the carrier and the modulation sidebands.

In principle the dark resonance can be prepared by current modulation at both 4.6 and 9.2 GHz. At first glance, employment of the 4.6 GHz modulation (Fig. 3a) seems favorable because of the large relative sideband intensity of about 17 % that can be obtained. However, this method has the disadvantage that the strong carrier does not contribute to the preparation of coherent population trapping but only increases the overall noise level on the photo detector. Furthermore, when a buffer gas is added to the cesium vapor in order to reduce time-of-flight broadening [7] the excited state is strongly homogeneously broadened. As a consequence, the strong carrier – detuned from resonance by only a few homogeneous linewidths – can partially destroy coherent couplings and serve as a loss mechanism via one-photon absorption into hyperfine components of the excited state not involved in the CPT process ($F' = 2$ and $F' = 5$ on the cesium D_2 line). Therefore, after having demonstrated CPT preparation with the help of 4.6 GHz sidebands in a first experiment, 9.2 GHz modulation was chosen for the experiments presented below (Fig. 3b and c). Because of

the high modulation bandwidth of the VCSEL this is much easier than using a cavity to filter out the carrier in the 4.6 GHz case. In this configuration it is even possible to choose different relative intensities of the two light fields by selecting the radio frequency power used for modulation – an important optimization parameter for the trade-off between signal amplitude and power broadening. However, the obtainable sideband intensities at 9.2 GHz were restricted to about 1.6 % by the limited modulation efficiency in the experiments reported here.

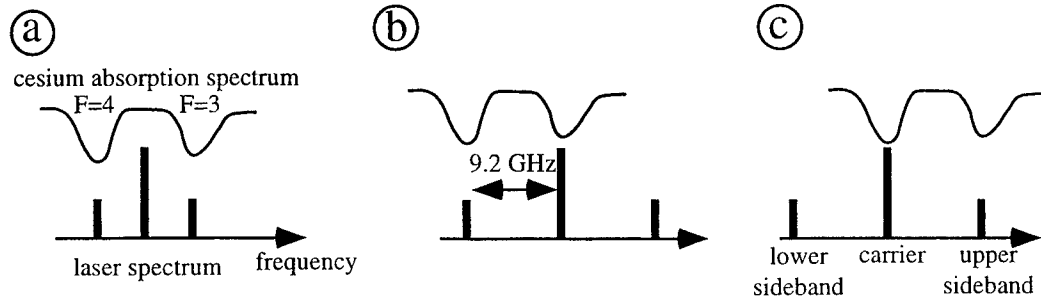


Fig. 3. Three ways to prepare the coherent population trapping resonance using a frequency-modulated light field. (a) Modulation at half the hyperfine frequency (i.e., 4.6 GHz for cesium) and use of both modulation sidebands. (b) and (c): Modulation at the full hyperfine frequency (9.2 GHz) and use of the carrier with either the lower or the upper sideband. The schematic Doppler-broadened absorption spectrum consists of two components, one starting from the $F = 4$ ground state (left) and one from the $F = 3$ ground state (right).

Using one single current-modulated VCSEL not only guarantees the phase stability of the two light fields which now is basically limited by the stability of the radio frequency source only, but also automatically delivers a perfect beam overlap and thus avoids residual Doppler broadening [8]. Furthermore, no external optics are needed for mode selection because of the intrinsic single-mode operation of the VCSEL. As a consequence, the experimental setup for the observation of coherent population trapping becomes very simple, compact, and robust (Fig. 4). The laser beam impinges on a cesium vapor cell at room temperature and the intensity transmitted through the cell is detected on a photodiode. If necessary, an optional fiber link can be implemented to filter the transverse mode profile. The optical carrier frequency of the VCSEL is stabilized to a Doppler-broadened absorption spectrum in an auxiliary cesium cell via the laser diode injection current. This D.C. bias current is combined with the GHz signal for the current modulation in a bias-tee directly coupled to the laser diode housing. The wide, mode hop-free tuning range of the VCSEL allows to choose different carrier detunings from the optical resonance for optimized performance.

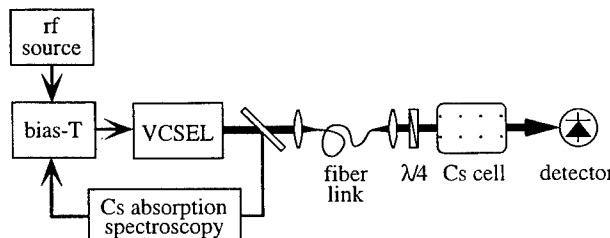


Fig. 4. Setup for the observation of narrow coherent population trapping resonances in a cesium vapor cell using a current-modulated VCSEL. In some experiments the vapor cell is protected from magnetic noise by a μ -metal shielding. A coil arrangement allows to apply well-defined magnetic fields.

Because the bandwidth of the light itself is irrelevant for the resonance width [9] the broad linewidth of the VCSEL (about 50 MHz) should be of only minor concern for the observation of narrow CPT resonances. However, a rather low contrast of the dark resonance line was observed for pure cesium vapor. This is because the VCSEL light fields cannot interact efficiently with the optical transitions of about 5 MHz homogeneous width. However, in practice buffered vapor cells are used in order to obtain narrow resonances so that the width of the pressure broadened optical transitions exceeds the laser linewidth and signal contrast is strongly increased [10].

While inconvenient, the rather low output power of the VCSEL of less than 1 mW does not really restrict dark resonance spectroscopy because the light intensity has to be reduced to below $100 \mu\text{W}/\text{cm}^2$ anyway in order to avoid power broadening. A more severe problem is given by the large tuning rate of the output frequency of $320 \text{ MHz}/\mu\text{A}$ with respect to the VCSEL injection current. At typical drive currents of about 2 mA ($\approx 2 I_{\text{threshold}}$) some residual noise due to 50 Hz power line interference is always present and causes frequency fluctuations of the laser output of about 20 MHz amplitude. These fluctuations are considerably smaller than the fast linewidth of the VCSEL itself but of course they add some additional amplitude noise to the signal. Finally, the modulation technique implies equal polarizations for both frequency components. However, as the investigations reported in [11] show, this is a very favorable configuration. In conclusion, the VCSEL setup is a well suited and reliable tool for the preparation of CPT resonances. Linewidths of only 60 Hz are routinely obtained.

In a magnetic field the dark resonance splits into up to 21 Zeeman components due to the sublevel structure of the ground state hyperfine components (Fig. 5). There have been theoretical proposals [12,13] and a first experimental realization [14] of dark resonances as a sensitive magnetometer based on this effect. In this approach, the strength of the magnetic field is determined through a precise measurement of the Zeeman-shifted positions of the dark resonance components. For optimized sensitivity it is favorable to use the outermost Zeeman component corresponding to the Λ system coupling the $|F = 3, m = 3\rangle$ and $|F = 4, m = 4\rangle$ states because this resonance line exhibits the largest shift rate of $24.5 \text{ Hz}/\mu\text{T}$. Of course, this large shift rate causes the outermost resonance to be more sensitive to inhomogeneities of the magnetic field, as well. In a lock-in spectrum of the outermost Zeeman component the noise level outside the resonance line was compared to the steepest slope at the center of the resonance. From this data and the shift rate a sensitivity limit of 9.9 pT in 0.3 s integration time was derived, which is already close to the noise levels of the best commercially available flux-gate magnetometers.

As a second application of dark resonance spectroscopy one can think about compact primary frequency references [15]. In this case, an intuitive approach would be to stabilize the frequency of the rf oscillator providing the modulation signal to the central resonance component of Fig. 5, corresponding to the Λ system coupling the $|F = 3, m = 0\rangle$ and $|F = 4, m = 0\rangle$ states. These ground states also form the so-called “clock transition” in microwave spectroscopy and are shifted by a magnetic field in second order only so that drifts due to changing magnetic fields are rather small. For our preliminary setup the uncertainty in frequency position of this central dark resonance component could be determined as 0.3 Hz in 0.1 s integration time. This corresponds to a relative frequency uncertainty of $1 \cdot 10^{-11}/\sqrt{\tau}$ for $1 \text{ ms} \leq \tau \leq 0.3 \text{ s}$. However, at longer integration times frequency resolution is degraded due to drifts which still have to be eliminated with an improved setup. We expect interesting applications for such a frequency standard because of the low power consumption of less than 1 W that is conceivable for an optimized device.

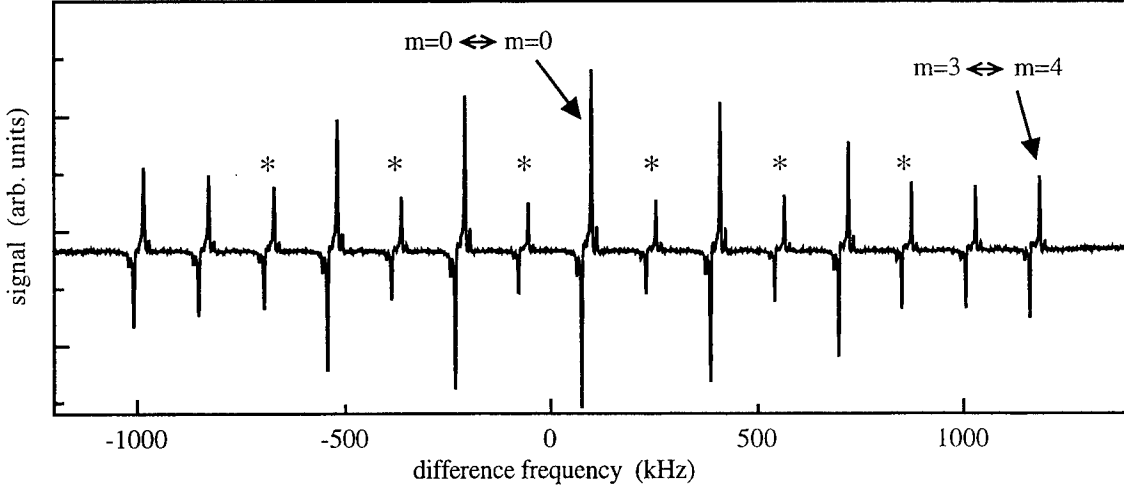


Fig. 5. Zeeman splitting of the dark resonance in a magnetic flux density of $44.4 \mu\text{T}$ (about the strength of the geomagnetic field). The central component corresponds to the $m = 0 \leftrightarrow m = 0$ “clock transition” while the outermost $m = 3 \leftrightarrow m = 4$ components exhibiting the largest shift rate are well suited for magnetometry. The dispersive lineshapes of the resonances are due to lock-in detection of the transmission signal. At even higher resolution the six components marked with a * are resolved into a doublet each due to the influence of the nuclear magnetic moment [16].

The results presented here clearly show that coherent population trapping spectroscopy using VCSELs has promising applications in sensitive magnetometry and for the realization of compact and robust frequency references. Further improvements can be expected from the implementation of VCSELs emitting at the D_1 wavelengths of cesium (894 nm) or rubidium (794 nm). On the D_2 line the hyperfine components $F' = 2$ and $F' = 5$ in the $P_{3/2}$ excited state cannot form Λ systems due to electric dipole selection rules but cause a broadening of the dark resonance by inducing additional dark state relaxation via one-photon losses [17]. This broadening can be avoided when coherent dark states are prepared on the D_1 line because here the excited state ($P_{1/2}$) has only hyperfine components $F' = 3$ and $F' = 4$. A further improvement in sensitivity can be expected from an increase of the dark resonance amplitude, for instance through the optimization of the intrinsic VCSEL modulation efficiency at the relevant radio frequencies of 9.2 and 6.8 GHz, respectively, as well as through improved impedance matching of the laser housing.

Acknowledgments

This work has been supported by the Land Nordrhein-Westfalen through the Bennigsen-Foerder-Prize and by the Deutsche Forschungsgemeinschaft. We thank the group of K. J. Ebeling for providing us with a prototype of their VCSELs.

References

- [1] B. Weigl, G. Reiner, M. Grabherr, K. J. Ebeling, “Oxidised GaAs QW vertical-cavity lasers with 40 % power conversion efficiency,” *Electron. Lett.* **32**, 1784 (1996).
- [2] R. Jäger, M. Grabherr, C. Jung, R. Michalzik, G. Reiner, B. Weigl, K. J. Ebeling, “57% wallplug efficiency oxide-confined 850nm wavelength GaAs VCSELs,” *Electron. Lett.* **33**, 330 (1997).

- [3] J. L. Jewell, A. Scherer, S. L. McCall, Y. H. Lee, S. Walker, J. P. Harbison, L. T. Florez, "Low-threshold electrically pumped vertical cavity surface-emitting microlasers," *Electron. Lett.* **17**, 1123 (1989).
- [4] G. Alzetta, A. Gozzini, L. Moi, G. Orriols, "An experimental method for the observation of r. f. transitions and laser beat resonances in oriented Na vapor," *Il Nuovo Cim.* **36B**, 5 (1976).
- [5] E. Arimondo, "Coherent population trapping in laser spectroscopy," *Progress in Optics* **35**, 257 (1996).
- [6] R. King, R. Michalzik, C. Jung, M. Grabherr, F. Eberhard, R. Jäger, P. Schnitzer, K. J. Ebeling, "Oxide confined 2D VCSEL arrays for high-density inter/intra-chip interconnects," in *Vertical-cavity Surface-Emitting Lasers II*, R. A. Morgan and K. D. Choquette (eds.), *Proc. SPIE* 3286 (1998).
- [7] S. Brandt, A. Nagel, R. Wynands, D. Meschede, "Buffer-gas-induced linewidth reduction of coherent dark resonances to below 50 Hz," *Phys. Rev. A* **56**, R1063 (1997).
- [8] A. M. Akulshin, A. A. Celikov, V. L. Velichansky, "Sub-natural absorption resonances on the D_1 line of rubidium induced by coherent population trapping," *Opt. Commun.* **84**, 139 (1991).
- [9] B. J. Dalton, P. L. Knight, "The effects of laser field fluctuations on coherent population trapping," *J. Phys. B* **15**, 3997 (1982).
- [10] C. Affolderbach, A. Nagel, S. Knappe, C. Jung, D. Wiedenmann, R. Wynands, "Nonlinear spectroscopy with a vertical-cavity surface-emitting laser (VCSEL)", *Appl. Phys. B*, in print.
- [11] R. Wynands, A. Nagel, S. Brandt, D. Meschede, A. Weis, "Selection rules and line strengths of Zeeman-split dark resonances," *Phys. Rev. A* **58**, 196 (1998).
- [12] M. O. Scully, M. Fleischhauer, "High-sensitivity magnetometer based on index-enhanced media," *Phys. Rev. Lett.* **69**, 1360 (1992).
- [13] M. Fleischhauer, M. O. Scully, "Magnetometer based on atomic coherence and possible application to the search for P and T violating permanent electric dipole moments of atoms," *Quantum Semiclass. Opt.* **7**, 297 (1995).
- [14] A. Nagel, L. Graf, A. Naumov, E. Mariotti, V. Biancalana, D. Meschede, R. Wynands, "Experimental realization of coherent dark-state magnetometers," *Europhys. Lett.* **44**, 31 (1998).
- [15] N. Vukičević, A. S. Zibrov, L. Hollberg, F. Walls, J. Kitching, "A compact microwave frequency reference using diode lasers", *Annual Frequency Control Symposium Besançon*, April 1999.
- [16] S. Knappe, W. Kemp, C. Affolderbach, A. Nagel, R. Wynands, "Splitting of coherent population trapping resonances by the nuclear magnetic moment", submitted for publication.
- [17] A. Nagel, C. Affolderbach, S. Knappe, R. Wynands, "Influence of excited state hyperfine structure on ground state coherence", submitted for publication.

Commercial Gas Sensing with Vertical Cavity Lasers

Mark E. Paige

Southwest Sciences, Inc., 1570 Pacheco St, Suite E-11, Santa Fe NM 87505
(505)984-1322, Fax 988-9230, mpaige@swsciences.com

Vertical cavity lasers (VCSELs) have many characteristics that make them potentially superior to edge emitting lasers for gas sensing applications. These characteristics include a wider single mode current tuning range, a less divergent and round beam profile, less susceptibility to optical feedback, lower operating current and lower production costs. The single mode current tuning range of a VCSEL is typically 5 to 10 cm^{-1} . In comparison, DFB lasers currently being used in commercial gas sensors typically only current tune over a range of 1 cm^{-1} . Only relatively expensive external cavity lasers can match the single mode tuning range of a VCSEL. And while VCSELs can be current modulated at high MHz frequencies over their wide tuning range, external cavity lasers are limited to low kHz modulation frequencies over their wide tuning range because the modulation is performed mechanically. The advantages of a wide single mode tuning range for sensing are that multiple line detection becomes possible, as well as the ability to look at broader spectral features such as in condensed phase species or in congested spectral regions. The superior beam profile of VCSELs makes beam handling easier since astigmatic effects are not inherent. Thus, commonly available and less costly optics can be used with VCSELs. In addition, since the VCSEL output typically only diverges by 10 to 15 degrees, fiber coupling is more easily and efficiently performed. In our work, we have noted that the spectral quality of VCSELs is not effected by optical feedback from back reflections. In contrast, the spectral quality of edge emitting lasers is severely degraded by back reflections. This lack of sensitivity to optical feedback is very important for fiber coupling applications. Unlike the situation with fiber coupled edge emitting lasers, an optical isolator is not needed with VCSELs. Optical isolators are not only expensive, but they tend to induce etalons into the optical system that reduce the obtainable sensitivity. VCSELs have substantially lower production costs than edge emitting lasers because ten times more lasers can be prepared on a single wafer using MBE and the devices can be tested on the wafer. Hence, commonly available 850 nm VCSELs sell for \$10 to \$30/device. In comparison, commonly available telecommunication DFB lasers sell for \$500 and custom wavelength DFB lasers useful for spectroscopic monitoring applications cost several thousand dollars each.

Despite these advantageous qualities, VCSELs have not yet been utilized for sensing applications. The reasons that VCSELs have not been used in this capacity include a very limited availability of wavelengths, the lack of single mode versus multimode devices being produced by VCSEL manufacturers and some literature reports claiming detection with VCSELs is less sensitive than that obtained with DFB lasers. The wavelength range of VCSELs currently available from commercial manufacturers covers the 750 to 960 nm region. In this region, few species of commercial interest have absorption features. In addition, most VCSELs commercially available are multimode devices being produced for local area network communications. The spectral qualities of these devices are not suitable for detecting narrow spectral features. In addition, Weldon *et al* report that the obtainable absorption sensitivity using VCSELs is twenty times worse than that obtained with DFB lasers.

However, our work over the past few years has indicated that VCSELs can be employed for commercial gas sensing applications. In the 750 to 960 nm region, two species of commercial interest have absorption features. These species are oxygen at 760 nm and water vapor at 945 nm. Monitoring of these species is of interest to the chemical, pharmaceutical, food, semiconductor, meteorological and aeronautical industries. Using wavelength modulation spectroscopy, we have established that absorbances in the low 10^{-5} range are obtainable using VCSELs. These experiments have involved measurements of both oxygen and water vapor. VCSELs from a variety of manufacturers have been used in this work including BandGap Technology,

VIXEL Corp. and MicroOptical Devices, Inc. A sample wavelength modulation oxygen spectrum taken with a vertical cavity laser is shown in Fig. 1. We have noted that there are wide variations in the single mode qualities of these devices and thus, the measurable absorbance level can vary from the low 10^{-5} range to the low 10^{-3} level. In comparison, 1×10^{-6} absorbances are often observed in laboratory measurements with DFB lasers and an absorbance level of 1×10^{-5} is routinely measured with DFB laser based field instrumentation. The principal feature that limits measuring smaller absorbances with VCSELs is the presence of small nonlinear features in their I-L curves. These nonlinearities appear as background signals in the wavelength modulation spectra. These background signals become indistinguishable from the molecular absorption at small absorbance levels. These background effects with VCSELs are an order of magnitude worse than with DFB lasers. An example of the achievable sensitivity with a VCSEL and of the laser induced background effect is shown in Fig. 2, a 947 nm water vapor spectrum. The slight nonlinear I-L behavior manifested in the wavelength modulation spectrum is most likely due to the presence of multiple transverse modes in the laser. VCSELs are known to become multimode a few mA above their lasing threshold. With the more single mode devices, the obtainable sensitivity in units of concentration-optical pathlength is 100 ppm-m for oxygen and 2 ppm-m for water vapor at standard atmospheric conditions. At these sensitivity levels, VCSEL based oxygen and water vapor monitoring is useful for determining chemical process stream contamination. In addition, water vapor monitoring at this sensitivity level is of interest for meteorological measurements of atmospheric water vapor to altitudes of 20 km.

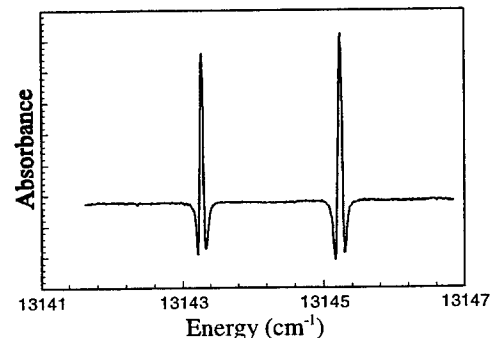


Figure 1 — Second harmonic wavelength modulation oxygen spectrum taken in room air over a 1 m path. The absorbance levels of these lines is ~ 0.02 .

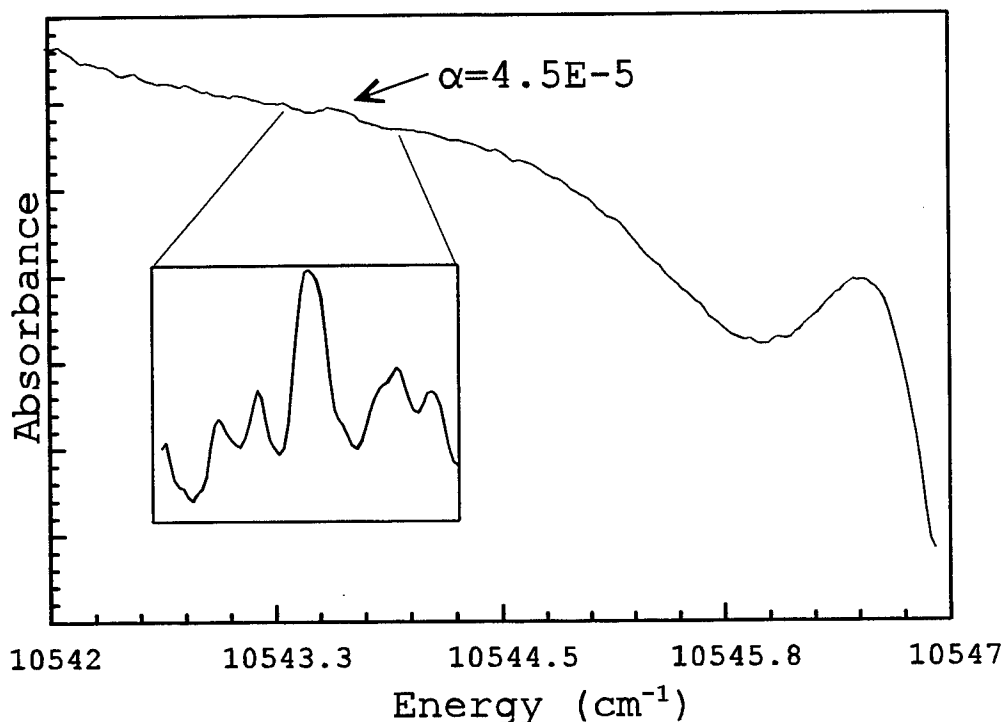


Figure 2 Second harmonic water vapor spectrum taken with a 947 nm VCSEL. The absorbance of the peak is 4.5×10^{-5} .

Because of the great cost savings possible with a VCSEL relative to DFB lasers, the market potential for VCSEL sensors is much greater for DFB based instruments. A VCSEL sensor with a market price under \$10,000 is possible. To demonstrate this possibility, we developed a stand alone prototype VCSEL based water sensor that has single quantity component costs of \$1,500 (excluding the laser). This instrument, which has a 1.5 m optical path, has measured water vapor concentrations as low as 4 ppm.

However, in order for VCSELs to be useful as the laser source in commercial sensors a number of issues need to be addressed. First, improvements in the uniformity of the single mode current tuning characteristics are required. Less variation in device performance will reduce cost incurred in characterizing the lasers and increase yield. Second, tighter wavelength specification is needed in producing these devices for spectroscopic applications. Currently, a VCSEL wafer can only be prepared to within a few nm of the desired wavelength. In addition, the lasers from a given wafer will vary over a few nm. Since an atmospheric gas line is typically 0.01 nm wide and the current tuning range is usually 0.5 nm, the wavelength spread is too large to be compensated with modest temperature tuning. Third, the number of species that can be detected that are of commercial interest will dramatically increase when VCSELs become available in the 1.3 to 2 μ m range. Such species include the halide acid gases, methane and ammonia. Furthermore, this spectral region includes water vapor absorptions that are forty times stronger than the 945 nm band. Lastly, increases in the single mode tuning range will permit the monitoring of broader spectral features and multiple spectral lines.

References:

W. Weldon, J. O'Gormann, J.J. Perez-Camacho and J. Hegarty, *Electronic Letters* 32(3), **1996**, 219.

Transverse mode selection in index-guided VCSELs

A. Valle , L.Pesquera

Instituto de Fisica de Cantabria, CSIC-UC ,
Facultad de Ciencias, E-39005 Santander, Spain

P. Rees and K. A. Shore

University of Wales, Bangor

School of Electronic Engineering & Computer Systems
Bangor LL57 1UT, Wales, United Kingdom

email: alan@sees.bangor.ac.uk; tel: +44 1248 382618; fax :+44 1248 361429

1 Introduction

The recent rapid advances in the performance of vertical cavity surface emitting lasers (VCSELs) give significant impetus to identifying practical applications of these devices in, for example, optical data links and two-dimensional optical switching. In looking towards such applications serious consideration must be given to basic device performance characteristics and specifically to their operating efficiencies, threshold currents and transverse mode structures [1]. Recent work has indicated the role of spatial hole-burning effects in determining both the transverse mode structure and the wall-plug efficiencies of gain-guided VCSELs. Here we show that the strength of the in-built transverse mode waveguide in index-guided VCSELs exerts a dramatic influence on the excitation of transverse modes. The influence is, in particular, revealed by calculated light-current characteristics of index guided VCSELs.

2 Model and Structures

The general features of the analysis technique which is utilised here are described in [2]. Noteworthy features of the model are its capability for treating the competition between transverse modes in nominally circularly symmetry VCSEL structures. The analysis is thus able to take into account transverse modes having azimuthally varying profiles. Attention here is focussed on the outcomes of calculations performed to determine how transverse mode competition affects the light current characteristics of weak and strong index-guided VCSELs. It is taken that the VCSELs are fabricated in the GaAs/ AlGaAs material system with core and cladding refractive indices are of order 3.5 and have lasing wavelengths in the vicinity of 850 nm. Other material and device parameters appropriate to this class of devices are utilised [2]. The weak index-guided structure is defined by a core-cladding layer refractive index step of 0.01 and the strong index-guided structure is taken to have a core-cladding layer refractive index step of 0.1. The basic approach taken is to follow the dynamical evolution of transverse modes when the laser is driven by a specified bias current. The static characteristics are obtained by using short current which are slow enough to ensure that the results are obtained in a quasi-steady situation whilst being fast enough to avoid the effects of self-heating. In this way the active region temperature is kept constant (and equal to the substrate temperature) during the current scan. The injected current profile is generally taken as being uniform current injection over the active region (disc contact) but attention has also been given to contact geometries designed to preferentially excite a specified transverse mode.

3 Light Current Characteristics

Results from calculations performed for weak and strong index-guided VCSELs are shown in Figures 1 and 2 respectively. It is apparent that the power partition between transverse modes depends dramatically on the strength of the index waveguide as defined by the core-cladding index step . Competition between modes is much stronger for the case of higher index step since then modes are better confined in the waveguide with a corresponding increase of the spatial overlapping between them. Then differences in

modal gain between modes are then much smaller in the case of high index step, as it is seen at the lower part of Fig. 2.

The present analysis has also been utilised to examine how spectral gain effects [3] and current profiling influence transverse mode competition in such devices. It is found that the light-current characteristics do not vary greatly when changing the operation wavelength for the case of small index step. This is due to the weak confinement of the modes induced by the small waveguide index step. In this way variations of the carrier density over the mode profiles are significant and then differences in modal gain between transverse modes dominate over differences in material gain.

However, for higher index steps material gain effects can be important in determining the power partition. This happens for instance in the case of 870 nm operation where power is mostly delivered in the high order LP12 and LP31 modes. This is because they have the shortest wavelengths and therefore their material gain is significantly higher than the material gain of the other modes. This follows because the gradient of the material gain at that wavelength and for typical carrier densities is high and then material gain effects clearly dominate over modal gain effects. Power partition in the case of 830 nm and 850 nm operation is rather similar since for typical carrier densities the material gain has a plateau at those wavelengths and then modal gain effects are dominant.

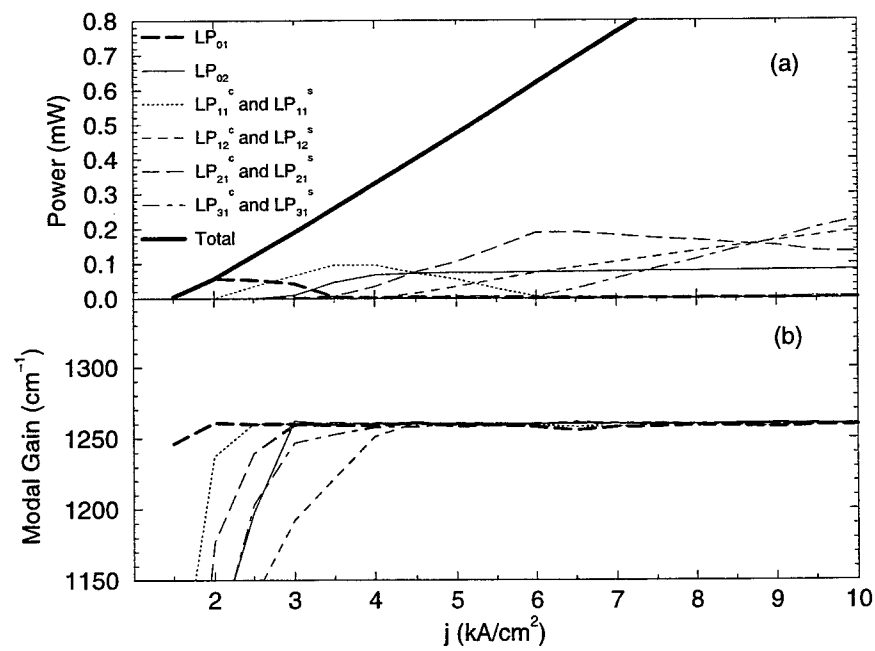
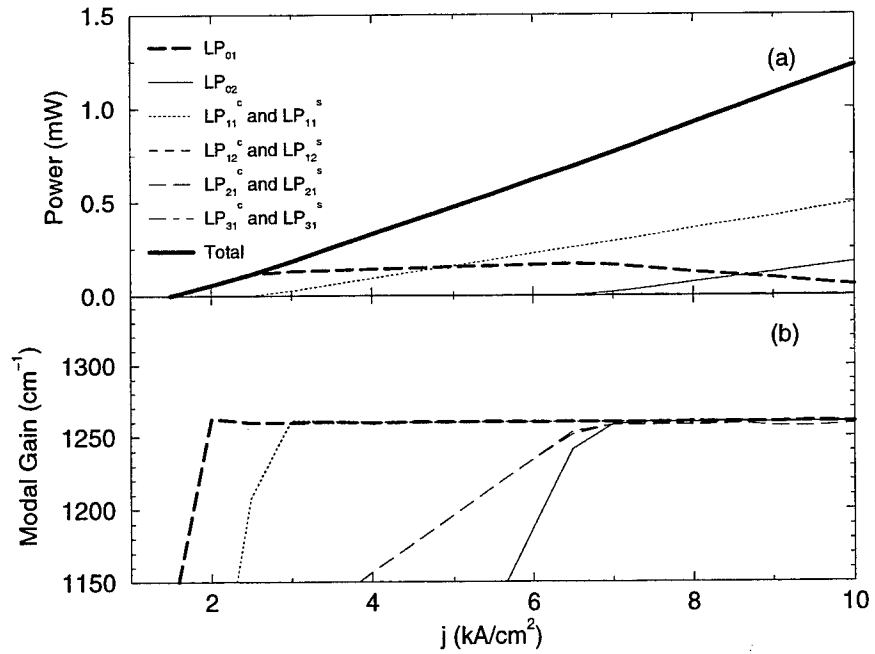
In both cases of modal confinement, for currents slightly above threshold, the fundamental transverse mode appears since its modal gain is the highest. The intensity profile overlaps in an optimal way with the carrier density because this is concentrated near the centre of the laser due to the assumed disc contact geometry. At higher currents the increasing stimulated recombination of carriers produces a hole in the carrier profile near the center of the device and LP12 and LP11 modes reach threshold. These modes are excited with similar power since the symmetry of the injected current does not favour any mode in particular. Further increase of the injected current also leads to the appearance of other higher modes in such a way that several modes are able to coexist. The competition is much more involved as the modal confinement is increased. The lowest threshold current and the highest total optical power are obtained for the 850 nm wavelength since that corresponds to operation near the material gain peak. These results can be compared with those obtained by using a simpler model where the material gain depends in a linear way on the carrier density and where all the transverse modes have the same material gain [2]. The simple model describes very well the small index step results obtained with the model used in this paper. It also describes qualitatively the results with higher index step when material gain effects are not relevant (830 nm and 850 nm). However, when these effects are important (870 nm) it fails to describe the power partition between modes.

4 Mode Control

The paper will also address the use of current profiles designed to excite a particular high order transverse mode. For example, excitation of the LP11 mode over a wide current range can be obtained in a weakly guiding VCSEL using a single contact placed where the mode has appreciable power. In that case it is also found that none of the other modes is able to reach the threshold gain. The impact of current spreading effects on the efficiency of this transverse mode selection mechanism has been ascertained by considering changes in light-current characteristics when the current injection area is changed. It will be shown in this way that there is an appreciable range of injection areas in which the transverse mode selection mechanism can be effective. However, this mode selection mechanism is found to be less effective for stronger index guided transverse modes.

References

- 1) C.J.Chang-Hasnain,et al IEEE J.Quantum Electron. QE-27, 1402-1409, 1991
- 2) A. Valle, al IEEE J.Quantum Electron. QE-34, 1924-1932, 1998.
- 3) F. P. Logue, P. Rees et al, J.Opt. Soc America B15, 1295-1303, 1998.



Injection locking of shear-strained photonic lattices based on VCSEL arrays

T. Fishman, A. Hardy

Department of Physical Electronics, Faculty of Engineering, Tel Aviv University, Tel Aviv 69978, Israel.

Fax: 972-36423508

E-mail: talf@eng.tau.ac.il, hardy@eng.tau.ac.il

E. Kapon and H. Pier

Department of Physics, Swiss Federal Institute of Technology (EPFL), 1015 Lausanne, Switzerland

E-mail: kapon@dpmail.epfl.ch, pier@epfl.ch

Abstract: Mode switching in critically strained and other tailored VCSEL based photonic lattices is demonstrated by means of injection locking. For strained lattices, switching between four-lobed and six-lobed far field modes is examined and it is shown that near the critical strain, relatively low injection power is needed to switch between these modes. For lattices tailored to have their modes localized, switching between localized modes is examined. Both the critically strained and the tailored lattices may be used in an all optical switching device.

OCIS codes: (140.3290) Laser arrays; (140.3520) Lasers, injection-locked; (230.1150) All-optical devices; (250.7260) Vertical cavity surface emitting lasers.

Introduction

Photonic lattices, i.e., structures that incorporate 2D or 3D periodical variation of their optical properties, are of interest lately due to their ability to control the propagation of light and the interaction of light with matter [1,2]. A somewhat different but also important aspect of photonic lattices is the confined photonic states. Recently, coherent vertical cavity surface emitting laser arrays (VCSEL's) were used both experimentally and theoretically [2-7] to explore the physics of these confined photonic states. Each VCSEL is capable of trapping photons and therefore plays the role of an "optical atom". Inter-cavity coupling among the closely spaced VCSELs via diffraction induces the formation of photonic bands whereas the array eigenmodes correspond to confine photonic states. Operating the VCSEL lattices above lasing threshold permits the selection of one or several photonic states within the photonic band, depending on their optical gain/loss characteristics. Alternatively, injection of light at certain frequencies may be used, by means of injection locking to switch between the photonic states.

These photonic lattices are defined by metal-patterning highly uniform VCSEL wafers. The resulting patterned mirror $\rho(x)$ consists of a high reflectivity square pixel (taken as unity) surrounded by a lower amplitude reflectivity r_b . Lasing only occurs at the location of high reflectivity pixels and the coupling between the lasers is achieved by diffraction (see Fig. 1).

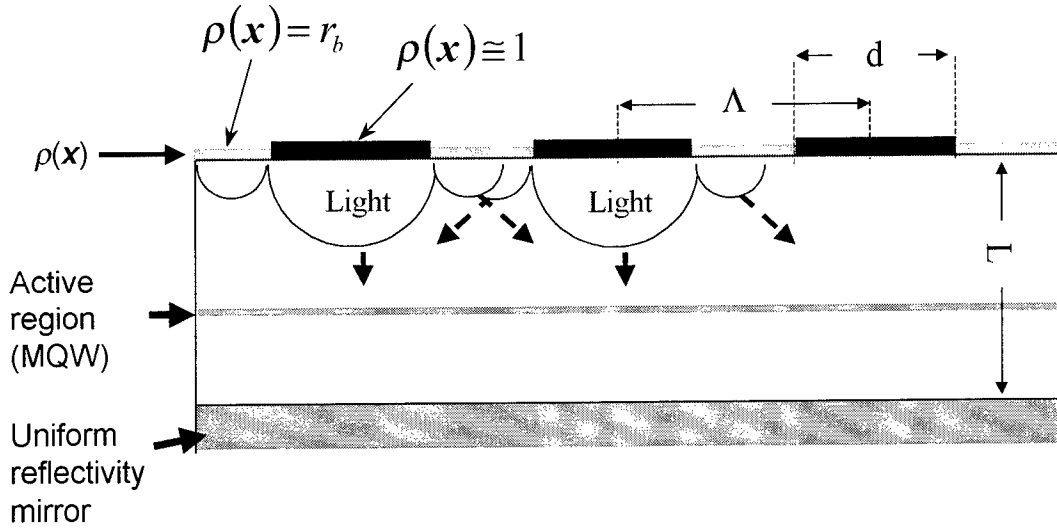


Fig. 1. Schematic illustration of a VCSEL based photonic lattice.

The uniform lattice structure is represented by a square $N \times N$ array with a lattice parameter Λ and pixel size d . Alternate shear strain is introduced by shifting every other row parallel to itself by δ ; For $\delta = \Lambda/2$, a quasi-hexagonal lattice structure is obtained (see Fig. 2). These lattices are of interest due to an abrupt switching, which is experimentally observed, for a critical value of strain δ_c , between a square-matrix lattice mode and a quasi-hexagonal mode [3-5]. Close to δ_c the two modes are almost degenerate, thus injection locking can easily be applied in order to induce switching between these modes. The square lattice mode produces a four lobed far field whereas the quasi-hexagonal mode produces a six lobed far field, thus we can use this scheme as a fast all optical switching device. Alternatively, an all-optical switching device may be obtain by switching between localized lattice modes of lattices, tailored to have their modes localized.

The proposes of this work is to propose and theoretically demonstrate mode switching in critically strained VCSEL lattices and in tailored lattices by means of injection locking.

Injection locking formalism

We used the analysis of [8] to examine injection locking of VCSEL arrays. The array is subjected to an externally injected field $\mathbf{E}_{inj}(y)$ at a frequency ω_{inj} . Consequently, in addition to the free running field $\mathbf{E}_f(y)$ at frequency ω_f , a driven field $\mathbf{E}_c(x)$ at frequency ω_{inj} is generated which obeys

$$\mathbf{E}_c(y) = \mathbf{E}_{inj}(y) + \gamma p(y) \iint K_{\omega_0}(y, x) \mathbf{E}_c(x) dx \quad (1)$$

where $K_{\omega_0}(y, x)$ is the free space propagation kernel at some arbitrary frequency ω_0 near ω_{inj} and near ω_f , γ is a complex parameter which contains the net round trip gain in its absolute value $|\gamma|$ and the argument of γ determines the injection frequency ω_{inj} (see Ref. [8]). We assume that the free running field is identical in its shape to the lowest order cold cavity mode, namely $\mathbf{E}_f(x) \propto \mathbf{u}_1(x)$. The cold cavity eigenmodes $\mathbf{u}_m(x)$ are obtained via

$$\mathbf{u}_m(y) = \gamma_m \rho(y) \iint K_{\omega_0}(y, x) \mathbf{u}_m(x) dx \quad (2)$$

where γ_m is the eigenvalue, $|\gamma_m|$ represents the round trip modal losses and $\text{Phase}\{\gamma_m\}$ determines the modal eigenfrequencies ω_m (i.e., the cold cavity resonance frequencies). In addition, the gain is simultaneously saturated by both $\mathbf{E}_f(\mathbf{x})$ and $\mathbf{E}_c(\mathbf{x})$, namely

$$g = \frac{g_0}{1 + (P_c + P_f)/P_{sat}} \quad (3)$$

where P_{sat} is the saturation average power density, $P_c = \frac{1}{A} \iint |E_c|^2 d\mathbf{x}$, and $P_f = \frac{1}{A} \iint |E_f|^2 d\mathbf{x}$ are respectively the driven and free running average power densities, A is the area of the lattice, and g_0 is the small signal gain which depends on the pumping rate.

Without injection (i.e., with an injection power density $P_{inj} = \frac{1}{A} \iint |E_{inj}|^2 d\mathbf{x} = 0$) the laser is free running with $P_c = 0$ and $P_f = P_f^{(0)}$. If P_{inj} is increased P_c also increases on the expense of P_f . Eventually for $P_{inj} > P_{inj}^{lock}$, $P_f = 0$ since the gain can no longer support free running oscillations. Thus, the free running mode is switched off while the driven field prevails.

Results and discussion

Let us first examine switching between the square matrix and the quasi-hexagonal modes of a shear strained lattice. If the array is free running with a square matrix lattice mode at $\omega_f = \omega_{sq}$ the injected power will be at $\omega_{inj} = \omega_{hx}$ and vice versa if the array is free running with a quasi-hexagonal mode at $\omega_f = \omega_{hx}$ the injected power will be at $\omega_{inj} = \omega_{sq}$.

The results discussed in what follows correspond to a 10×10-element lattice with $r_b = 0.98$, $d = 4\mu\text{m}$, $\Lambda = 5\mu\text{m}$ and an effective cavity length $L = 5\lambda_0/n_r$ [see Fig. 1] where $\lambda_0 = 940\text{nm}$ is the free space wavelength and $n_r = 3.5$ is the refractive index inside the cavity. Using the formalism of [9], we find that the critical strain value is $\delta_c \approx 1.45\mu\text{m}$ and the resonance frequencies of the square and the quasi-hexagonal lattice modes are respectively $\Delta\omega_{sq} = 7.08 \times 10^{-4}\omega_0$ and $\Delta\omega_{hx} = 5.67 \times 10^{-4}\omega_0$, where $\Delta\omega$ is defined as $\omega - \omega_0$ (e.g., $\Delta\omega_{hx} = \omega_{hx} - \omega_0$). In order to maximize the degree of overlap between the injection and the quasi-hexagonal desirable mode, the (gaussian) injected field is selected to be aimed at the center of one of the lattice elements (see Fig. 2), i.e., the gaussian is centered at $\mathbf{x}_0 = [3.2\mu\text{m}, 2.5\mu\text{m}]$.

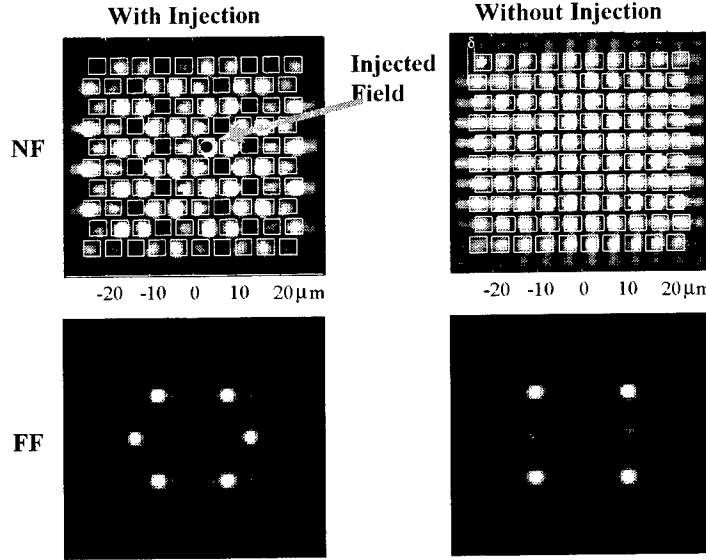


Fig. 2. The near field (NF) and the far field (FF) intensity patterns of a critically strained 10x10 element lattice without (right side) and with (left side) injection. The lattice pattern is in dashed lines and the injected gaussian field with a spot size $\sigma=1\mu\text{m}$ is illustrated by a black spot.

Fig. 2 shows the calculated near-field (NF) and far-field (FF) intensity patterns that are obtained in the switching of a lattice with $\delta=1.4\mu\text{m}$. Without injection the array is free running in the square matrix mode at $\omega_f=\omega_{sq}$ with a four-lobed far field. If an external field with $P_{inj} = P_{inj}^{lock}$ at a frequency $\omega_{inj}=\omega_{hx}$ is injected, the array switches to the quasi-hexagonal mode with a six-lobed far field.

Fig. 3 examines the switching properties of the above lattice. Fig. 3a draws $P_{inj}^{lock} / P_f^{(0)}$ as a function of $\Delta\omega_{inj}/\omega_0 \equiv \text{Phase}\{\gamma\}/20\pi$ for three different strain values of the lattice. As expected, in all of the cases $P_{inj}^{lock}=0$ for $\omega_{inj}=\omega_f$ (e.g., for $\delta=1.1\mu\text{m}$ $P_{inj}^{lock}=0$ at $\omega_{inj}=\omega_{sq}$). Both for the sub-critical strain $\delta=1.1\mu\text{m}$ (free running in the square lattice mode) and for the super-critical strain $\delta=1.6\mu\text{m}$ (free running in the quasi-hexagonal lattice mode) relatively large injection powers are needed in order to lock (switch) the array to the other mode. Whereas for $\delta=1.4\mu\text{m}$, which is only slightly below δ_c , relatively low injection power at $\omega_{inj}=\omega_{hx}$ is sufficient to switch the array from the free running square-matrix mode to the quasi-hexagonal mode. Note that the switching bandwidth (marked on the graph as BW) is depended on the injection power available and the degree of overlap between the injected power and the desirable mode.

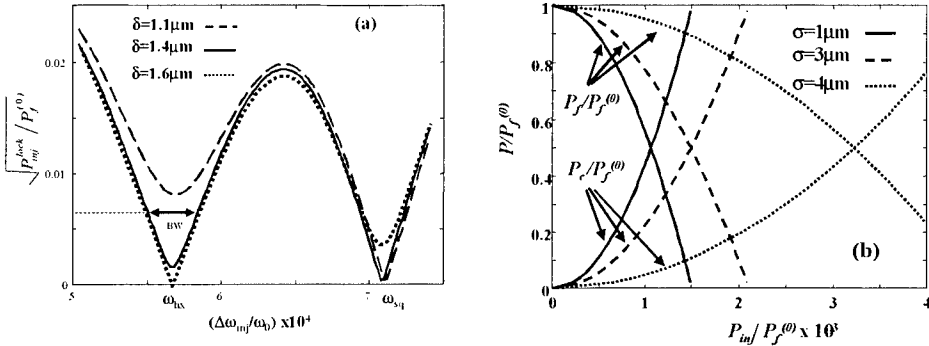


Fig. 3. Switching properties of the 10×10 strained lattice of Fig. 2. (a) Square root of the normalized switching average power density $P_{inj}^{lock}/P_f^{(0)}$ as a function of $\Delta\omega_{inj}/\omega_0$ for three different strain values of the lattice; and (b) The normalized free running $P_f/P_f^{(0)}$ and driven $P_d/P_f^{(0)}$ average power densities as a function of the normalized injected power density $P_{inj}/P_f^{(0)} \times 10^3$ for three values of σ .

In Fig. 3b we examine the switching sensitivity to variations in the injected gaussian spot size σ . The normalized free running power $P_f/P_f^{(0)}$, and normalized driven power $P_d/P_f^{(0)}$, are presented for three values of σ as a function of the normalized injected power $P_{inj}/P_f^{(0)}$. As P_{inj} increases P_f increases and P_d decreases, thus the quasi-hexagonal mode is switch on whereas the square-matrix mode vanishes. However, as the injected beamwidth increases the overlap between the injected power and the quasi-hexagonal mode decreases thus, higher switching power is needed.

Injection locking is, in practice, very hard to achieve since it requires a very accurate and stable master laser. Fig. 4 presents a future practical all optical switching device, on a single wafer, with an inherently stable master laser. Here, both the master and the slave lasers are VCSEL lattices, and thus they can be highly identical and can be driven by the same current source. The master laser is without strain (i.e., with $\delta=0$) and thus it operates steadily in the square-matrix lattice mode. Whereas the slave laser is configured slightly above the critical strain (e.g., with $\delta=1.5\mu\text{m}$) so that without injection it operates in the quasi-hexagonal (six-lobed FF) lattice mode. Once light from the master laser is directed at the slave laser, the master laser will be switched to the square-matrix (four-lobed FF) lattice mode. And thus an all-optical switching device is obtained.

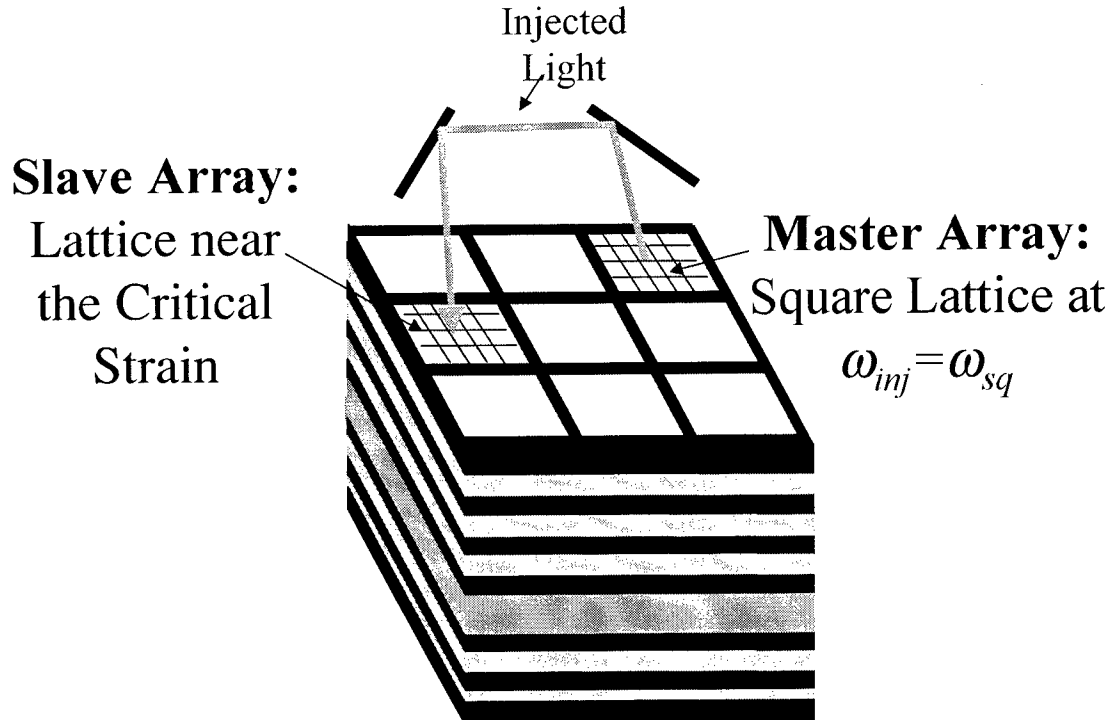


Fig. 4. A practical all optical switch configuration on a single wafer. Both the master and the slave lasers are VCSEL lattices. The master array may be a square matrix lattice ($\delta=0$) that operates steadily at the square matrix mode and the slave array is configured slightly above the critical strain. If light from the master lattice is directed to the slave lattice, it will be switched from the quasi-hexagonal free running mode to the square-matrix mode.

Finally, as an example of switching between localized modes of tailored lattices, Fig. 5 presents the NF (intensity) patterns of an 'H' shaped lattice with and without injection. The lattice is formed by a sub-lattice of larger size elements ($d=3\mu\text{m}$) within a background lattice of smaller elements ($d=2\mu\text{m}$). Other lattice parameters are $\Lambda=3.4\mu\text{m}$, $r_b=0.95$, and $D=55\mu\text{m}$. The free running mode $u_1(x)$ has the expected 'H' shape of the sub-lattice with the corresponding free running frequency $\omega_f=\omega_1$. If an externally injected field is applied at $\omega_{inj}=\omega_3$, the lattice is switched to the localized mode $u_3(x)$. Thus, we may use this scheme as an all optical switch as well. Note however, that it is very important, in this context, that $\omega_1 \neq \omega_3$ otherwise switching will not be possible by means of variation of the injection frequency.

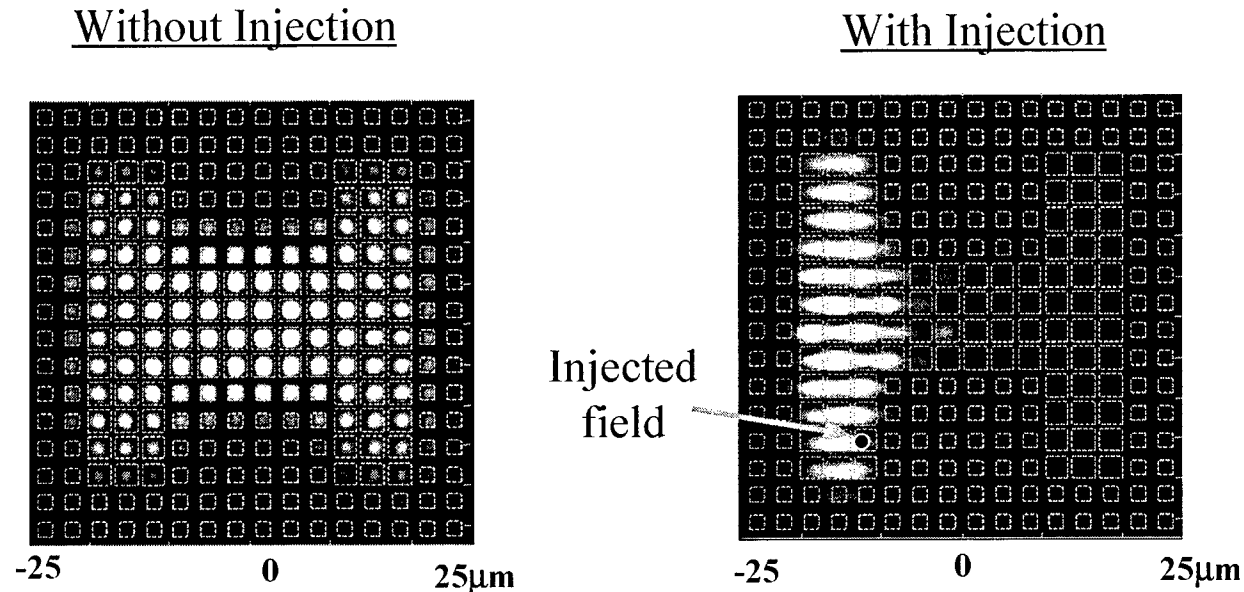


Fig. 5. NF intensity patterns of an 'H' shaped sub-lattice without (left) and with injection (right).

Summary

We demonstrated theoretically that switching between the modes of critically strained and tailored VCSEL based photonic lattices may be achieved by means of injection locking. For strained lattices, switching between four-lobed and six-lobed far field modes is examined and it is shown that near the critical strain, relatively low injection is needed to switch between these modes. An 'H' shaped lattice is examined, as an example for switching between localized lattice modes of lattices tailored to have their modes localized. Both the critically strained and the tailored lattices may be used as an all optical switching device.

References

1. E. Yablonovitch. Phys. Rev. Lett., 58, 2059-2062. (1987).
2. See, e.g., J. D. Joannopoulos, R. D. Meade, and J. N. Winn. *Photonic Crystals* (Princeton University Press, Princeton, 1995).
3. H. Pier, E. Kapon and M. Moser. Invited presentation at the *Conference on Lasers and Electro-Optics* (CLEO-Europe), September 13-18 1998, Glasgow, Scotland.
4. H. Pier, E. Kapon and M. Moser, T. Fishman and A. Hardy, *CLEO* (Conference on Lasers and Electro-Optics) in Baltimore, May 1999.
5. T. Fishman, E. Kapon, H. Pier and A. Hardy, App. Phys. Lett. 74, 3595-3597 (1999).
6. H. Pier and E. Kapon, Optics. Lett. 22 (8), 546-548 (1997)
7. A. Golshani, H. Pier, E. Kapon and M. Moser, J. Appl. Phys. 85 (4), 2454-2456 (1999)
8. T. Fishman and A. Hardy, J. Opt. Society of America B: Optical Physics, Vol.16 pp. 2-198, Jan. 1999.
9. T. Fishman, A. Hardy and E. Kapon, IEEE J. Quantum Electron. 33 (10), 1756 - 1762 (1997).

Quantum Cascade and Interband IR Lasers

High Performance Quantum Cascade Lasers for Trace Gas Analysis

**Federico Capasso and Claire Gmachl, Bell Labs, Lucent Technologies, Murray Hill
NJ 07974**

Quantum cascade (QC) lasers are fundamentally new semiconductor light sources in that: (1) their wavelength can be tailored over a wide range (from 3 to 17 microns) using the same combination of materials by a suitable choice of the active layer thickness, (2) their optical power is greatly enhanced by the cascade effect (one injected electron creates 25-30 photons in traversing the active region).¹ They are a textbook case of materials by design since all key microscopic properties (energy levels, radiative and non-radiative matrix elements and their corresponding lifetimes, etc) are engineered "bottom-up" to optimize material and device performance. QC Fabry Perot Lasers have demonstrated peak pulsed powers as high as 0.5 W at room temperature at 8 micron wavelength and corresponding average powers of 15 mW with a few % duty factor. QC distributed feedback lasers have large single mode continuous tuning range that makes them ideal for spectroscopy applications.² Dynamic linewidths in pulsed mode at room temperature of a few hundred MHz and of a few MHz in cw operation, limited by technical noise, have been demonstrated. In this talk the physics, operation and applications of QC DFB lasers will be discussed in detail.

QC DFB lasers with loss gratings were used to demonstrate for the first time wavelength modulation spectroscopy of trace gases using mid-infrared semiconductor lasers operating at room temperature.³ The devices were cooled slightly below room temperature to position the laser wavelength on the short wavelength side of a molecular resonance in N₂O. Tuning across the resonance was obtained with a slow (seconds) current sweep which heats the device, thus reducing the refractive index and redshifting the Bragg wavelength. The derivative of the absorption spectrum was measured with lock-in techniques by dithering the laser current and therefore the wavelength with a ~ kHz modulation.

In another experiment⁴ high resolution spectra of NH₃ and NO were obtained with index-coupled grating DFB lasers, and with DFB lasers emitting at ~ 5.2 μ m, all operating cw at 80 K in order to achieve narrow linewidth. Direct absorption spectroscopy was performed by ramping the laser current with a ~ 10 kHz saw-tooth waveforms and averaging many sweeps. From these data a laser linewidth, limited by technical noise, of tens of MHz over a few milliseconds was obtained. The instantaneous linewidth was estimated to be a few MHz. The latter estimate was obtained without a superimposed ramp by driving the laser in cw at 80 K. More recently Richard Williams, Jim Kelly, Stephen Sharpe and John Hartman of Pacific Northwest National Labs (private communication) have made similar measurements on DFB QC lasers with very low noise current drivers on two of our 8 μ m index coupled DFBs cooled at 80 K. They have found that the average linewidth is a few MHz over a few ms and that the instantaneous one is ~ a few hundred kHz. More over the width of the recorded high resolution molecular absorption of N₂O is found to be independent of the number m of sawtooth current sweeps as m is varied from 2 to 1000. This important result shows that QC lasers are

much more immune to wavelength drifts and jitters, compared to lead salt lasers and therefore better suited for high-resolution spectroscopy.

The fundamental linewidth of QC lasers should be Schawlow-Townes limited as, for example in gas lasers, because the linewidth enhancement factor or α parameter for QC lasers is expected to be zero if the DFB Bragg wavelength is positioned at the peak of the gain spectrum. In QC lasers the gain spectrum has basically the same shape of the absorption spectrum unlike interband diode lasers. Thus at the peak of the gain spectrum the fluctuations of the refractive index, caused by electron density fluctuations, are zero because of the Kramers-Krönig relationships, leading to $\alpha=0$.

Finally in a recent experiment ⁵ the first photoacoustic spectroscopy with QC lasers has been reported, demonstrating ~ 10 parts per billion sensitivity in the detection of NH_3 diluted in Nitrogen.

Collaborations with J. Kelly, R. Williams, J. Hartman, Ed Whittaker, B. Paldus, R. Zare, D. L. Sivco and A. Y. Cho are gratefully acknowledged

References.

1. F Capasso, J. Faist, C. Sirtori and A Y Cho, "Infrared (4-11 μm) quantum cascade lasers" *Solid State Comm.* 102 pp 231-236, 1997
2. C. Gmachl et al. "Continuous wave and high power pulsed operation of index-coupled distributed-feedback quantum cascade lasers at $\lambda \sim 8.5 \mu\text{m}$ " *Appl. Phys. Lett.* 72 pp 1430-1433, 1998
3. K Namjou et al. "Sensitive absorption spectroscopy with a room temperature distributed -feedback quantum cascade laser", *Opt. Lett.* 23 pp 219-221, 1998
4. S W Sharpe et al. "High-resolution (Doppler limited) spectroscopy using quantum-cascade distributed-feedback lasers" *Opt. Lett.* 23 pp 1396-1398, 1998
5. B A Paldus et al. "Photoacoustic spectroscopy using quantum-cascade lasers" *Opt. Lett.* 24 pp 178-180, 1999

High-temperature continuous-wave operation of optically-pumped W lasers with $\lambda = 3\text{--}7.1\text{ }\mu\text{m}$

W. W. Bewley, I. Vurgaftman, C. L. Felix, D. W. Stokes, L. J. Olafsen, E. H. Aifer, and J. R. Meyer

Naval Research Laboratory, Code 5613, 4555 Overlook Ave. SW, Washington, DC 20375

vurgaftm@aphrodite.nrl.navy.mil

M. J. Yang and B. V. Shanabrook

Naval Research Laboratory, Code 6870, 4555 Overlook Ave. SW, Washington, DC 20375

H. Lee, R. U. Martinelli, and J. C. Connolly

Sarnoff Corporation, CN 5300, Princeton, NJ 08543-5300

A. R. Sugg

Sensors Unlimited, Inc., Princeton, NJ 08540-5914

The development of semiconductor lasers emitting at wavelengths longer than 3 μm at high cw operating temperatures has proven to be quite challenging. To our knowledge, the best result reported previously was $T_{\text{max}} = 225\text{ K}$ for a lead-salt device ($\lambda = 4.2\text{ }\mu\text{m}$).¹ One promising approach is the W laser,² named for the shape of the conduction-band profile in its four-constituent type-II active region (e.g., InAs/GaInSb/InAs/AlSb). In this work, we report the cw operation of optically pumped W lasers nearly to room temperature. The maximum wavelength for an interband III-V device has also been extended by 2 μm , to 7.1 μm .

TABLE I. DESIGN AND OPERATING CHARACTERISTICS OF 10 OPTICALLY PUMPED W LASERS

Sample	Periods	Active Region Design		$\lambda(\mu\text{m})$ (78 K)	$\lambda(\mu\text{m})$ (T_{max})	$T_0\text{ (K)}$ (cw)	$\text{cw } P_{\text{max}}$ (mW) (78 K)	$\text{cw } \eta_{\text{ext}}$ (%/facet) (78 K)	$\text{cw } T_{\text{max}}$ (K)
		Structure							
S1	50	InAs/GaSb/InAs/AlSb 18 Å/25 Å/18 Å/35 Å		2.72	2.98	70	142	1.52	290
S2	80	InAs/Ga _{0.7} In _{0.3} Sb/InAs/AlAs _{0.17} Sb _{0.83} 16 Å/25 Å/16 Å/40 Å		3.14	3.47	63	229	3.31	275
N1	50	InAs/Ga _{0.74} In _{0.26} Sb/InAs/AlSb 17 Å/26 Å/17 Å/43 Å		3.59	3.86	65	110	1.53	265
N2	50	InAs/Ga _{0.72} In _{0.28} Sb/InAs/AlSb 17 Å/26 Å/17 Å/43 Å		3.66	3.92	55	112	1.19	250
N3	50	InAs/Ga _{0.8} In _{0.2} Sb/InAs/AlSb 18 Å/40 Å/18 Å/43 Å		3.75	4.05	46	161	1.92	240
N4	50	InAs/Ga _{0.8} In _{0.2} Sb/InAs/AlSb 21 Å/40 Å/21 Å/43 Å		4.19	4.45	52	73	0.79	230
N5	70	InAs/Ga _{0.7} In _{0.3} Sb/InAs/AlSb 23 Å/22 Å/23 Å/40 Å		5.41	5.87	43	48	0.60	210
N7	50	InAs/Ga _{0.7} In _{0.3} Sb/InAs/AlSb 24 Å/22 Å/24 Å/40 Å		6.05	6.26	—	31	0.40	170
N8	70	InAs/Ga _{0.64} In _{0.36} Sb/InAs/AlSb 28 Å/22 Å/28 Å/40 Å		6.95	7.13	—	3.3	0.094	130

The samples were grown by molecular beam epitaxy on GaSb and had $\text{Al}_{0.9}\text{Ga}_{0.1}\text{As}_{0.07}\text{Sb}_{0.93}$ or AlSb optical cladding layers. The lasers were mounted on a diamond heat sink using the diamond-pressure-bonding (DPB) technique³ and were optically pumped with a cw 1.064 μm Nd:YAG laser. The active region designs and cw results are given in Table I along with the emission wavelengths at 78 K and the maximum cw operating temperature. The values at 78 K are for a pump stripe width of 40 μm (FWHM), while the final column is for a width of 17 μm .

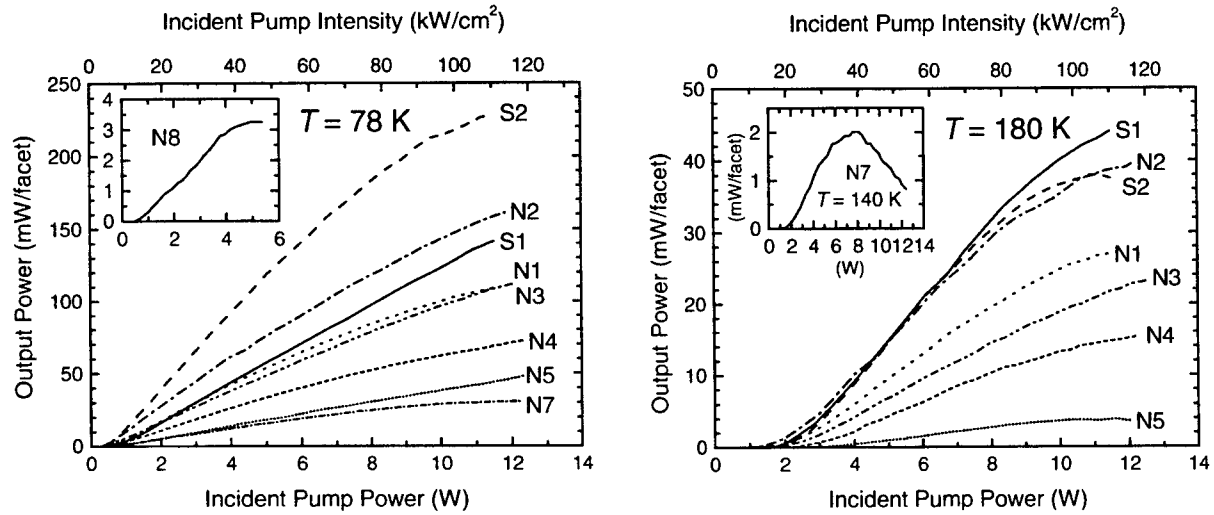


Figure 1: Continuous-wave output power per facet vs. incident pump power at heat sink temperatures of 78 K and 180 K. Cavity lengths were $\approx 520 \mu\text{m}$ and pump-stripe widths were 40 μm .

The left panel of Fig. 1 shows cw output powers per facet as a function of incident pump power (bottom scale) and intensity (top scale) for the nine laser samples at a heat sink temperature of 78 K. In the right panel, the cw output power is shown at $T = 180$ K for all of the lasers still operating at that temperature, while the behavior of N7 at 140 K is shown in the inset. At 78 K, S2 ($\lambda = 3.1 \mu\text{m}$) had the highest output power (230 mW) and differential conversion efficiency (3.3%). However, its performance becomes more comparable to other devices at 180 K, probably due to the greater difficulty of extracting heat from its thicker 80-period active region. Encouraging cw powers have been obtained at 180 K (40 mW at $\lambda = 3.8 \mu\text{m}$). The stripe widths used for the data shown in Figure 1 were 40 μm (FWHM), although the maximum output powers far above threshold at 78 K were nearly constant for all stripe widths ranging from 17 μm to 100 μm . This behavior is in stark contrast to that observed in a previous study of sample S2, in which it was mounted epitaxial-side-up (50- μm -thick substrate) on a copper heat sink using a conventional In-Sn solder bond.⁴ Note that in most cases the output powers had not saturated at the maximum available pump power of 12 W, especially for the low heat sink temperature.

Figure 2 shows the cw threshold intensity, I_{th} , as a function of heat sink temperature for four of the lasers. In all cases, I_{th} at T_{max} was between 35 and 60 kW/cm^2 for the stripe width of 17 μm . For a wider stripe of 40 μm , T_{max} averaged more than 20 K lower, and the threshold intensity was in the 18–31 kW/cm^2 range, indicating the importance of lateral heat flow. The characteristic temperatures, T_0 , indicated in Fig. 2 and listed in Table I decreased nearly monotonically with increasing wavelength, from 70 K for $\lambda(T_{\text{max}}) = 3.02 \mu\text{m}$ to 35 K for $\lambda(T_{\text{max}}) = 7.1 \mu\text{m}$ (not pictured).

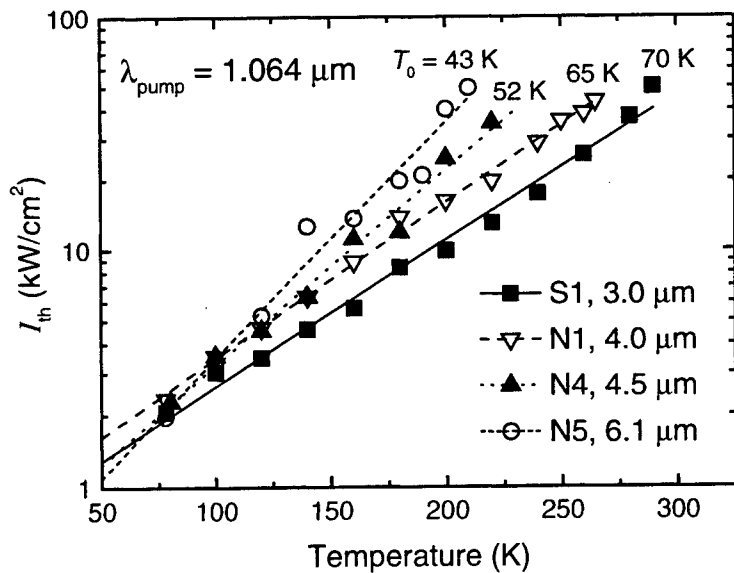


Figure 2: Continuous-wave optical pumping intensity thresholds vs. temperature for four of the eight samples, identified by $\lambda(T_{max})$. All pump-stripe widths were 17 μm .

The maximum cw operating temperatures listed in Table I are higher than any reported previously for semiconductor lasers in the wavelength range covered by these structures. Sample S1 demonstrated near-room-temperature operation (290 K) at $\lambda = 3.0 \mu\text{m}$. Another sample lased cw up to 130 K at $\lambda = 7.1 \mu\text{m}$, which represents the longest wavelength for any III-V interband laser (the previous best was 5.3 μm for pulsed operation^{5,6}). This may be attributed both to the suppression of Auger recombination in type-II InAs/GaInSb-based quantum wells⁷ and to the efficiency of the DPB heat sinking.

These results demonstrate the promise of the W geometry as a potential basis for high-temperature cw semiconductor lasers emitting in the mid-IR. Significant further improvements are expected following optimization of the active-region designs and the use of 2- μm pump lasers. Long-wavelength type-II W diodes are also expected to have attractive properties.

¹ Z. Feit, M. McDonald, R. J. Woods, V. Archambault, and P. Mak, *Appl. Phys. Lett.* **68**, 738 (1996).

² J. R. Meyer, C. A. Hoffman, F. J. Bartoli, and L. R. Ram-Mohan, *Appl. Phys. Lett.* **67**, 757 (1995).

³ W. W. Bewley, C. L. Felix, I. Vurgaftman, D. W. Stokes, E. H. Aifer, L. J. Olafsen, J. R. Meyer, M. J. Yang, B. V. Shanabrook, H. Lee, R. U. Martinelli, and A. R. Sugg, *Appl. Phys. Lett.* **74**, 1075 (1999).

⁴ E. H. Aifer, W. W. Bewley, C. L. Felix, I. Vurgaftman, L. J. Olafsen, J. R. Meyer, H. Lee, R. U. Martinelli, J. C. Connolly, and A. R. Sugg, *Electron Lett.* **34**, 1587 (1998).

⁵ M. E. Flatte, T. C. Hasenberg, J. T. Olesberg, S. A. Anson, T. F. Boggess, C. Yan, and D. L. McDaniel, Jr., *Appl. Phys. Lett.* **71**, 3764 (1997).

⁶ T. Ashley, C. T. Elliott, R. Jeffries, A. D. Johnson, G. J. Pryce, A. M. White, and M. Carroll, *Appl. Phys. Lett.* **70**, 391 (1997).

⁷ J. R. Meyer, C. L. Felix, W. W. Bewley, I. Vurgaftman, E. H. Aifer, L. J. Olafsen, J. R. Lindle, C. A. Hoffman, M. J. Yang, B. R. Bennett, B. V. Shanabrook, H. Lee, C.-H. Lin, S. S. Pei, and R. H. Miles, *Appl. Phys. Lett.* **73**, 2857 (1998).

Optical Gain Calculations for 1.55 μ m Unipolar Intersubband Semiconductor Lasers

C. Y. L. Cheung, I. Pierce, P. Rees and K. A. Shore

University of Wales, Bangor

School of Electronic Engineering & Computer Systems

Bangor LL57 1UT, Wales, United Kingdom

email: alan@sees.bangor.ac.uk; tel: +44 1248 382618; fax :+44 1248 361429

1 Introduction

The very considerable progress which has been made in improving the characteristics of unipolar semiconductor lasers has prompted the present authors to undertake work aimed at assessing the expected performance characteristics of intersubband lasers devices including their waveguiding properties [1], and in particular, their anticipated direct current modulation capabilities. In earlier work, use was made of the rate equation model to describe the dynamical properties and direct current modulation capability of intersubband lasers. It was observed [2] that since electron lifetimes in intersubband lasers are typically of the same order as the photon lifetime, there is a fine balance between the contributions of the resonance frequency and damping factor in the determination of the maximum modulation frequency in these devices. That work, in particular, indicated that THz modulation bandwidths of intersubband lasers are quite feasible on the basis of the carrier dynamics [3].

In that initial analysis, representative values for carrier lifetimes and interwell tunneling times were utilised. In subsequent work, a self-consistent analysis of the modulation response was performed through a direct calculation of the relevant carrier and tunneling times for a prototype triple quantum well structure suitable for incorporation in near-infrared intersubband lasers [4].

2 Optical gain spectra

Our starting point is the following expression for the gain:

$$g(\hbar\Omega) = \frac{e^2 |z_{12}|^2 m_r \Omega}{\hbar^2 c n \epsilon_0 L} \int_0^\infty d\epsilon \frac{\hbar\gamma(\epsilon) \cdot [f_2(\epsilon) - f_1(\epsilon)]}{\pi [\hbar\Omega - \hbar\Omega_\epsilon]^2 + [\hbar\gamma(\epsilon)]^2} \quad (1)$$

which is similar to that given in [5] except that equation (1) above is in mks units and has the reduced effective subband mass, m_r , where $|z_{12}|^2$ is the dipole moment matrix element, Ω_ϵ the optical transition frequency for the in-plane electron momentum $\hbar k = \sqrt{2m_2\epsilon}$, namely $\hbar\Omega_\epsilon \equiv \hbar\Omega_0 + \epsilon_2 - \epsilon_1$, where $\epsilon_2 \equiv \epsilon$ and $\epsilon_1 = \hbar^2 k^2 / 2m_1$ are kinetic energies in the upper and lower subbands respectively, characterized by the effective masses m_1 and m_2 , and the Fermi distribution functions f_1 and f_2 . Hence the reduced mass, $m_r = m_1 m_2 / (m_1 + m_2)$. The function $\gamma(\epsilon)$ describes the transverse phase relaxation due to intrasubband scattering.

3 Carrier temperature dynamics

The carrier temperature dynamics can be modelled using the intersubband energy density equations developed here for a four-level structure such as that shown in Figure 1, following the nomenclature of Willatzen's model for interband lasers [6]:

$$\frac{dU_1}{dt} = \frac{N_2^{(2)} \langle E_{21} \rangle}{L_1 \tau_{12}} - \frac{N_1 \langle E_{12} \rangle}{\tau_{12}} + \frac{J \langle E_{p,2} \rangle}{eL_1} - \frac{U_1 - U_{L,1}}{\tau_{heat}}, \quad (2)$$

$$\begin{aligned} \frac{dU_2^{(2)}}{dt} = & -aP(N_2^{(2)} - N_2^{(1)})E_{lase} - \frac{U_2^{(2)}}{\tau_S} + \frac{L_1 N_1 \langle E_{12} \rangle}{L_2 \tau_{12}} \\ & - \frac{N_2^{(2)} \langle E_{21} \rangle}{\tau_{12}} - \frac{U_2^{(2)} - U_{L,2}^{(2)}}{\tau_{heat}}, \end{aligned} \quad (3)$$

$$\begin{aligned} \frac{dU_2^{(1)}}{dt} = & aP(N_2^{(2)} - N_2^{(1)})E_{lase} + \frac{U_2^{(2)}}{\tau_S} + \frac{L_3 N_3 \langle E_{43} \rangle}{L_2 \tau_{23}} \\ & - \frac{N_2^{(1)} \langle E_{34} \rangle}{\tau_{23}} - \frac{U_2^{(1)} - U_{L,2}^{(1)}}{\tau_{heat}}, \end{aligned} \quad (4)$$

$$\frac{dU_3}{dt} = \frac{N_2^{(1)} \langle E_{34} \rangle}{L_3 \tau_{23}} - \frac{N_3 \langle E_{43} \rangle}{\tau_{23}} + \frac{J \langle E_{p,1} \rangle}{eL_3} - \frac{U_3 - U_{L,3}}{\tau_{heat}}, \quad (5)$$

where τ_{heat} is the thermalisation time towards the equilibrium energy density $U_{L,i} = U_i(N_i, T_L)$ and is assumed to be the same for all subbands. $E_{p,2}$ is the difference in energy between the electrons coming into the structure and the energy level in W1, while $E_{p,1}$ is the difference in energy between the electrons leaving the structure and the energy level in W3. E_{ij} denotes the energy difference in electrons coming from subband i to subband j . Only electrons coming in from a higher subband are assumed to contribute to the energy of a subband. Finally, $U_i = \int dE E \rho(E) f_i(E)$ gives the energy density in the i th subband, $\rho(E)$ is the density of states function in a quantum well and $f_i(E)$ is the Fermi distribution function for the i th subband. In the above model, free carrier absorption has been neglected.

4 NIR structure and gain

A NIR triple quantum well (TQW) structure suitable for intersubband lasing is shown in Figure 1, where the relevant energy levels are indicated with subscripts denoting the quantum well and the superscripts denoting the subband (there is only one subband in W1 and W3 and hence the superscripts are omitted). The structure is designed so that at an appropriate bias, its four energy levels are aligned in a manner that causes a transition wavelength of $1.55 \mu\text{m}$ to be achieved. At this bias voltage, there also exists an inversion of state lifetimes. An intrawell lasing transition scheme is chosen since, in addition to the larger dipole matrix elements achievable, the threshold current for intrawell is lower than that for interwell transitions [7].

Calculations of optical gain at NIR wavelengths, shown in Figure 2, are seen to have significantly lower threshold currents than at MIR wavelengths. Taken together with the lower optical losses expected in the NIR this strongly suggests that NIR intersubband lasing can be sustained using very few coupled quantum well structures and hence the prospect of THz bandwidth in direct current modulation would appear to be available in such devices.

References

1. P. S. Spencer, C. Y. L. Cheung and K. A. Shore, *IEE Proc. Opto.* **144** p.323, 1997.
2. C. Y. L. Cheung, P. S. Spencer and K. A. Shore, *IEE Proc. Opto.* **144**, p.44, 1997.
3. N. Mustafa, L. Pesquera, C. Y. L. Cheung and K. A. Shore, *IEEE Photon. Tech. Letts.* to be published May 1999.
4. C. Y. L. Cheung and K. A. Shore, *J. Mod. Optics* **45**, p.1219, 1998.
5. V. B. Gofinkel, B. Gelmont and S. Luryi, *IEEE J. Quant. Electron.* **32**, p. 1995, 1996.
6. M. Willatzen *et al* *IEEE Photon. Technol. Lett.* **3**, p.606, 1991.
7. J. H. Smet, C. G. Fonstad and Q. Hu, *J. Appl. Phys.* **79**, p.9305, 1996.

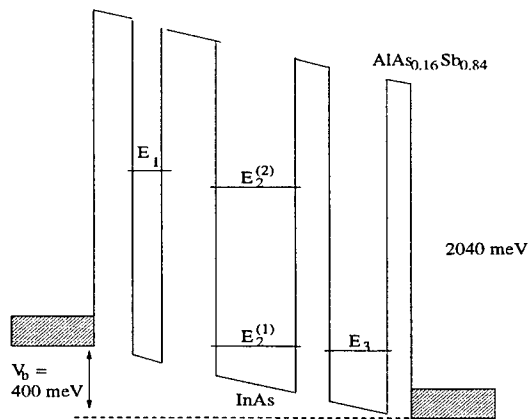


Fig. 1 Schematic conduction band diagram of the TQW structure for near-infrared (NIR) lasing, biased to an appropriate operating voltage. Structure composition and parameters: barriers - AlAs_{0.16}Sb_{0.84}, 2.0, 1.6, 1.2, 1.2 nm respectively; wells - InAs, 5.7, 4.8, 4.0 nm respectively.

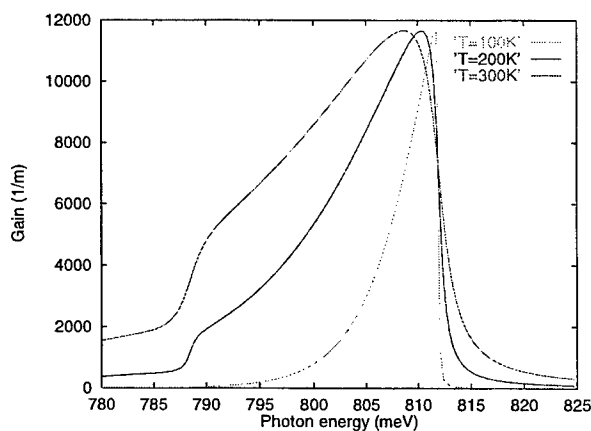


Fig. 2 Optical gain of the structure at various lattice temperatures ($T_L = 100-300$ K). The threshold currents are $J_{th} = 40$ A/cm² (100 K), $J_{th} = 107$ A/cm² (200 K) and $J_{th} = 180$ A/cm² (300 K).

Relative intensity noise of unipolar intersubband semiconductor lasers

N. Mustafa^{1,2}, L. Pesquera¹, and K. A. Shore³

¹ Instituto de Física de Cantabria (CSIC-UC), E-39005 Santander, Spain.

² Departamento de Física Moderna, Univ. de Cantabria, E-39005 Santander, Spain.

³ University of Wales, Bangor, School of Electronic Engineering and Computer Systems, BANGOR, LL 57 1 UT, Wales, UK

Phone: 44 (0)1248 38 2618 Fax: 44 (0)1248 361429 E-mail: alan@sees.bangor.ac.uk

Intersubband lasers have become a topic of active research particularly following the development of mid-infrared quantum cascade lasers [1]. Subsequent research has given rise to significant developments in the performance of these lasers. In this context it is of considerable interest to consider noise characteristics of unipolar lasers. In this work we perform a theoretical study of the relative intensity noise (RIN) of intersubband semiconductor lasers.

The generic structure which is assumed to form the building block of the active layer of the electrically pumped intersubband laser of interest here is a coupled triple quantum well element with an injector well(QW1), a central laser well (QW2) and an extractor well (QW3). The carrier transport between QW1 and QW2 (QW2 and QW3) is characterised by a tunnelling time τ_{12} (τ_{23}). As shown in previous work [2, 3] by using the rate equation model introduced in [2], the laser dynamics is further determined by the carrier transit time through the structure, τ_T , and intersubband radiative relaxation time τ_s . It has been shown that THz modulation bandwidth can be achieved in the chosen structure [4]. The threshold current is given by [2] $J_{th} = (2eL_2)/[a\tau_p(4\tau_s - \tau_T + \tau_{12} - \tau_{23})]$, where e is the electron charge, L_2 the lasing well width, τ_p the photon lifetime, and a the gain coefficient. It is appropriate here to take into account the following relations which define the relative magnitudes of the carrier lifetimes in the structure: $\tau_T \geq 2\tau_s + \tau_{12} + \tau_{23}$ and $\tau_{23} < \tau_s$ to get a positive carrier density in the extractor well [4], and $4\tau_s > \tau_T - \tau_{12} + \tau_{23}$ (population inversion condition [2, 3]). It is known from these previous works [2-4] that considerable simplifications of the analysis can be obtained when the triple-quantum well is designed to have equalised tunnelling times, i.e. $\tau_{12} = \tau_{23} = \tau_w$. That assumption will initially be made here to derive expressions for the RIN of intersubband lasers as a function of carrier lifetimes. The rate equation model introduced in [2] will be supplemented with spontaneous emission noise to calculate the RIN. Concerning the carrier lifetimes we take $\tau_T = 2\tau_s + \tau_{12} + \tau_{23} = 2\tau_s + 2\tau_w$, that corresponds to the minimum possible value for τ_T and to a lower bound for J_{th} . The intersubband relaxation time $\tau_s = 1.2$ ps is mainly due to optical phonon scattering (wavelength emission around 10 μ m [3]).

When tunnelling times are equal the following result is obtained

$$RIN = \frac{2\beta\bar{N}_2^{(2)}}{P_o\tau_s} \times \frac{\left[(2aP_o + \tau_s^{-1} - \omega^2\tau_w)^2 + \omega^2(2 + 2aP_o\tau_w + \tau_s^{-1}\tau_w)^2\right]}{\left[2aP_o\tau_p^{-1} - \omega^2(2 + 2aP_o\tau_w + \tau_s^{-1}\tau_w)\right]^2 + \omega^2\left[2aP_o\tau_w\tau_p^{-1} + 2aP_o + \tau_s^{-1} - \omega^2\tau_w\right]^2}, \quad (1)$$

where $\beta = 10^{-5}$ is the spontaneous emission factor, $a = 10^{-5} \text{ s}^{-1} \text{ cm}^3$ the gain coefficient, $P_o = [(J/J_{th}) - 1]/(2a\tau_s)$ the output optical power for an injected current J , and $\bar{N}_2^{(2)} = [1 + (J/J_{th})(\tau_T/4\tau_s - \tau_T)]/(2a\tau_p)$ is the carrier density in the upper level of the lasing well.

The RIN of intersubband lasers with symmetric structure (equal tunnelling times) is shown in Fig. 1 for different injection currents, $\tau_w = 0.5 \text{ ps}$, and two different values of the photon lifetime. It is seen that the RIN is constant for frequencies smaller than 10 GHz. This constant is given by

$$RIN = 2\beta\tau_p \frac{J^2}{J_{th}^2} \frac{\left[1 + \frac{J}{J_{th}} \frac{\tau_T}{4\tau_s - \tau_T}\right]}{\left[\frac{J}{J_{th}} - 1\right]^3}. \quad (2)$$

It is clear that the RIN increases with τ_p and decreases with the injection current. A nonzero limit is obtained for large values of J . This is due to the fact that the carrier density increases in the upper level of the lasing well. It is also apparent from (2) that the RIN increases with τ_T , that is when the tunnelling time increases (see Fig. 2). At frequencies greater than 10 GHz and low injected current the RIN shows a peak that disappears when J and/or the photon lifetime are increased. In the limit of large frequencies the RIN decreases as ω^{-2} .

Attention is now turned to the case of asymmetric structures with unequal tunnelling times. The RIN for different values of τ_{12} and τ_{23} is shown in Fig. 2 for a current $J = 1.8J_{th}$ and $\tau_p = 1 \text{ ps}$. It is clear that the noise level is mainly determined by the tunnelling time from the lasing well to the extractor well. The RIN level decreases when τ_{23} decreases, and the value at the peak increases slightly when τ_{12} increases. The threshold current also decreases when τ_{23} decreases. However, the modulation bandwidth decreases [4] for small values of τ_{23} .

In conclusion it has been found that the RIN decreases with the injected current towards a nonzero value for large values of J . The noise level is also found to increase with the photon lifetime. Finally, the RIN decreases when the tunnelling time τ_{23} decreases.

- [1] J. Faist et al, *Science*, **264**, 553-556, (1994).
- [2] W. M. Yee, K. A. Shore and E. Schoell, *Appl. Phys. Lett.*, **63**, 1089-1091, (1993).
- [3] C. Y. L. Cheung and K. A. Shore, *J. Mod Optics*, **45**, 1219-1229, (1998).
- [4] N. Mustafa, L. Pesquera, C. Y. L. Cheung, and K. A. Shore, *IEEE Photonics Tech. Letts.*, (May 1999).



Novel Semiconductor Lasers

Blue Nitride Lasers : Physics of Operation and Opportunities in Vertical-Cavity Devices

Arto V. Nurmikko and Y.-K. Song
*Brown University, Division of Engineering
Providence RI 02912*

Abstract

The blue nitride laser presents a fascinating case for the study of the microscopics of optical gain. For InGaN quantum wells, these are highlighted by the competition between localized and extended electronic states in this unusual, heterogeneous active laser medium. The InGaN QW gain medium present specific opportunities and challenges for the vertical cavity emitters whose contemporary progress is illustrated in this article.

1. Introduction

Progress with edge emitting InGaN blue/violet MQW diode lasers has crossed the threshold of commercial availability at the Nichia Company in Japan (1). In the U.S., there have been demonstrations of the continuous-wave operation (2,3) of the blue/violet laser. Other advances suggest a further broadening of the base of this emerging technology, for which potential applications abound. Thus, in spite of several technical, device-related challenges, optimism is warranted.

A notable feature of the present InGaN QW lasers is their high threshold current density, implying an unusually high electron-hole pair density for a semiconductor laser, typically in excess of 10^{19} cm^{-3} . The closest comparison that can be readily made (within the effective mass approximation to the electronic bandstructure) is with the blue-green II-VI QW diode lasers. These have achieved room temperature threshold current densities below 200 A/cm^2 (4), a value approximately one order of magnitude smaller than so far accomplished in the best InGaN QW lasers. Furthermore, and in notable contrast to the ZnCdSe active QW medium in the green II-VI lasers, the InGaN QW shows strong departures from a usual random alloy. Finite indium clustering in the InGaN system affect the bandedge electronic states which form the “electronic power supply” for optical emission, both for light emitting diodes and diode lasers. These compositional anomalies in InGaN QWs lead to a veritable competition of electronic excitations between localized and extended electronic states. This translates to a requirement for a high injection level for optical gain of sufficient magnitude to form in a real device. The overall picture is still not fully understood, given the added complications created by large piezoelectric and spontaneous dielectric polarization fields which typify the wurtzite nitrides in general. Thus, for example, no clear evidence has been seen of the types of many-body (excitonic) enhancements to optical gain spectra that are striking in their presence in the widegap II-VI lasers [Ding, 1994].

On the other hand, the nitride laser material is exceptionally robust and the large current densities applied to the edge emitting lasers create substantial peak optical gains, with typical gain coefficients in the active InGaN MQW medium on the order of $3000\text{-}5000\text{ cm}^{-1}$. This fact raises the prospect of vertical cavity surface emitting diode lasers (VCSEL) in the nitrides. Blue and violet VCSELs would have attractive potential technological applications ranging from optical storage to biomedical applications. The implementation of a nitride VCSEL does, however, have its own special challenges which derive from the physical properties of the underlying materials. Below, we examine current efforts at the basic research level, aimed at exploring the blue/violet VCSEL. Reasonably robust optically pumped InGaN MQW VCSELs with moderate thresholds have now been realized, and rudimentary resonance cavity LEDs (RCLED) have been demonstrated. Such initial steps point to the emerging likelihood of a blue/violet VCSEL in the future.

2. Gain Spectroscopy of InGaN QW Diode laser

A key issue is the nature of those band edge electronic states that supply the requisite optical gain, given the demonstrably large departure of InGaN from a random alloy in terms of the In-concentration fluctuations (x_{In}) on a microscopic (atomic) scale. Typically, the mean values of x_{In} in the laser devices are in the range of $x_{In} \sim 0.1\text{-}0.2$; ad hoc arguments can be made for the probable partial cation segregation due to the differences in the bond energies and lattice constants for the InN and GaN binary endpoints. The question that arises when this type of nanoscale heterogeneous semiconductor forms the active laser material concerns the competition between localization and many electron correlations within the available electron-hole pair states, given the very high pair densities required in present devices to reach lasing threshold ($> 10^{19}\text{ cm}^{-3}$).

Useful insight to the optical gain spectra of the InGaN blue diode laser active medium has been recently acquired, based on the analysis of the spontaneous emission spectra of the diode laser, in conjunction with its threshold characteristics. A gain/absorption spectrum for a blue InGaN MQW diode laser is shown in **Fig. 1**, for ridge waveguide device emitting at $\lambda\sim425\text{ nm}$, with an indium concentration $x_{In}=0.15$ in the active region (5). The values for the current range from low injection in the LED regime ($I = 20\text{ mA}$) to the lasing threshold and somewhat beyond. The spectral position of lasing slightly above threshold is indicated by an arrow as is the location of the quasi-Fermi level difference ΔE_F at approximately 2.995 eV at this injection level. The experiment and analysis, correlating spontaneous/stimulated emission spectra with absorption (6), also yield a self-consistent determination for the position of ΔE_F as a function of the injection current, graphed in **Fig. 2**. The vertical axis in Fig. 1 was calibrated from the threshold modal gain, measured for devices of different cavity reflectivities. Assuming a modal overlap

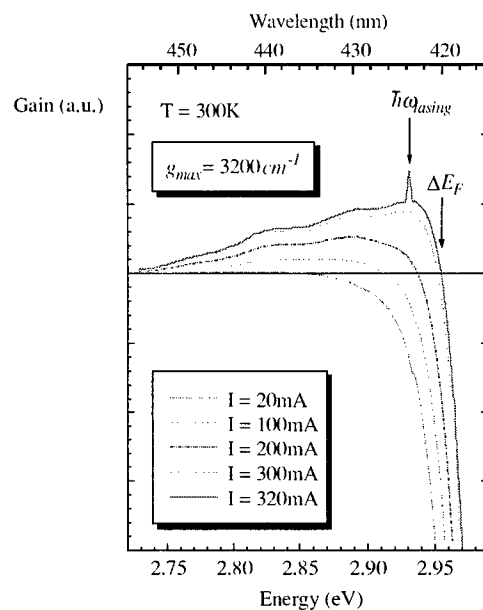


Figure 1: Gain/absorption spectrum of an InGaN MQW diode laser at different injection levels. Spectral position of laser emission and the quasi-Fermi level separation at threshold are shown.

Figure 1 shows the gain/absorption spectrum of an InGaN MQW diode laser. The x-axis is labeled 'Wavelength (nm)' at the top and 'Energy (eV)' at the bottom. The y-axis is labeled 'Gain (a.u.)'. The plot shows five curves for different injection currents: $I = 20\text{ mA}$ (dotted), $I = 100\text{ mA}$ (dashed), $I = 200\text{ mA}$ (dash-dot), $I = 300\text{ mA}$ (dash-dot-dot), and $I = 320\text{ mA}$ (solid). A peak at approximately 425 nm is labeled $\hbar\omega_{lasing}$. A vertical arrow at approximately 2.995 eV is labeled ΔE_F . A box indicates $g_{max} = 3200\text{ cm}^{-1}$ at $T = 300\text{ K}$.

factor of $\Gamma = 0.025$, based on the analysis of the passive waveguide performance, we obtain the peak gain at threshold of approximately 3200 cm^{-1} for the QW material.

The main result of Fig. 1 is the pronounced extension of the gain spectra associated with the $n = 1$ QW transition into the low energy region. At threshold, finite gain is found as much as 200 meV below its peak position, indicating a degree of broadening which is uncharacteristic of common semiconductor lasers. Note however, that the system reaches the transparency condition relatively easily, at levels of injection which are not very different from that of the conventional LED regime. With increasing current, gain builds up over the large spectral range, indicative of the participation of a corresponding range of electronic states. The position of the peak gain blue shifts somewhat at higher injection levels, but considerably less than anticipated from a one electron state-filling picture, possibly due to many-body bandgap renormalization effects. Qualitatively, we may now understand one reason for the high e-h pair density required for laser operation, apart from extrinsic reasons such as unwanted optical losses. That is, while the spectrally integrated gain is, in fact, quite large, its peak value (determining the lasing threshold) is much diluted at the expense of the excess broadening.

These observations provide an extension to earlier arguments (7) that the radiative recombination processes at the lowest interband transition in the InGaN QW are profoundly influenced by localized e-h pair states at room temperature, within an energy range which is up to an order of magnitude larger than estimated for a simple random alloy. That is, the description of the system in terms of weak disorder, as usually applied to ternary and quaternary compounds in the III-V and II-VI semiconductors, is probably inapplicable. Available optical data on InGaN QWs and thin films to date display the striking ‘softening’ of the bandedge states so that, for example, excitonic features in absorption at the $n=1$ QW states have not been unambiguously identified. By contrast, gain spectroscopy performed on widegap ZnCdSe QW diode lasers shows very clearly the characteristic influence of the strong excitonic enhancement of the peak gain and an overall optical response at the $n = 1$ HH exciton with the pronounced Coulomb correlations in evidence. Such effects are clearly masked by the disorder contributions in the InGaN QW, making it difficult to isolate predicted many-body interactions (8) in the dense e-h system within the active region of the blue diode laser.

From Figs 1 and 2, one sees how filling of the localized states is a necessary prerequisite prior to the buildup of a sufficient population inversion for threshold gain in the present devices. On the other hand, since transparency is reached at a rather low injection level ($n = p \sim 10^{18} \text{ cm}^{-3}$) it may be possible to reduce the threshold current by designing a laser resonator with very low optical losses. The near ‘clamping’ of E_F at higher injection may be due to a significant increase in the effective density of states. *We wish to emphasize that the issue of the In compositional anomalies increases in severity very*

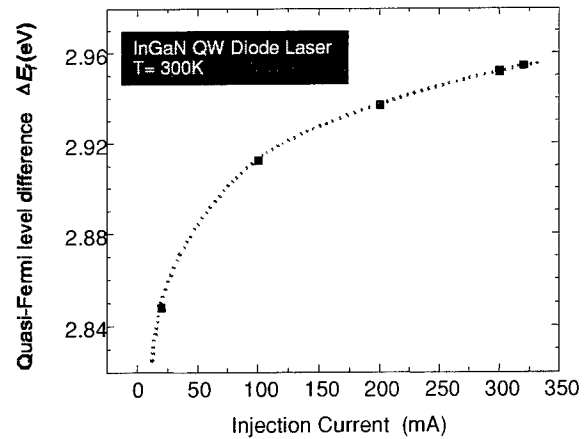


Figure 2: Quasi-Fermi level as a function of injection in an InGaN MQW laser at room temperature

rapidly as the In concentration reached about $x_{In} = 0.1$ and beyond; in fact for $x_{In} < 0.1$, the nearly random alloy behavior of InGaN appears to be approximated. Very recent work at Xerox PARC laboratories (9) and in our group has shown how the gain spectra does indeed significantly narrow as the In concentration is reduced, for lasers operating in the violet (~395-405 nm). On the other had, to maintain adequate electronic/optical confinement, one then needs to increase the Al-concentration in the cladding layers, adding different type of materials science challenge. This combination of features appears to point to a fairly narrow wavelength range ~395-405 nm as the presently optimal choice for the InGaN MQW diode laser, insofar as the lowest threshold current density is concerned. As one corollary, it may be difficult to extend the practical operation of the laser to the green.

3. Vertical Cavity Nitride Devices

Work on blue, green, and near ultraviolet VCSELs and RCLEDs is at very early research stages. For instance, at this writing it is unclear what combination of epitaxial growth and device design/processing schemes might result in a technologically viable VCSEL. At the same time, there are ample fundamental physical reasons to suggest that microcavity emitters based on widegap semiconductors have special properties that offer opportunities both in terms of basic physics and device performance. These features derive in part from the strong light-matter coupling, fundamental to lower dimensional nitride (and II-VI) heterostructures due to the strong excitonic enhancements to optical gain.

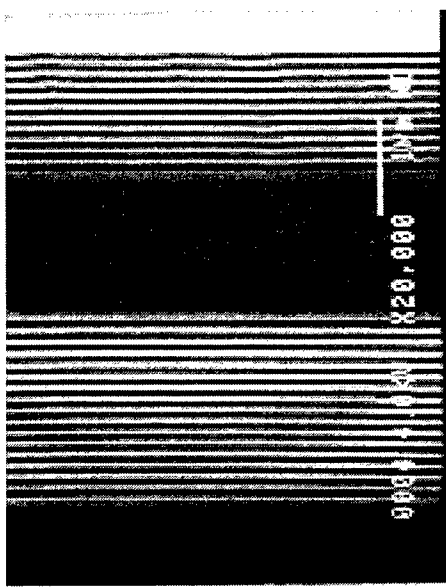


Fig.3: SEM cross sectional image of a InGaN MQW vertical cavity structure, equipped with two dielectric DBRs

The current challenges facing efforts to realize blue and violet RCLEDs and VCSELs in the AlGaN material system have many parallels with those encountered in somewhat earlier II-VI semiconductor work (10). On one hand, the nitride pn-junction heterostructures have produced both excellent LEDs and strikingly robust diode lasers. On the other hand, the realization of a reasonably high quality vertical cavity is a sizeable challenge. Two techniques are presently used in microcavity fabrication, employing in-situ, as-grown distributed GaN/AlGaN multilayer Bragg reflectors (DBRs) and dielectric DBRs, respectively. We note that the low index of refraction contrast within the AlGaN alloy system makes it at first sight a tour de force to create low loss, high reflectivity DBR mirrors by direct MOCVD growth on a sapphire substrate. Nonetheless, Arakawa and co-workers (11) have incorporated a 43 period MOCVD grown GaN/Al_{0.34}Ga_{0.66}N DBR mirror (R~0.98) on sapphire into a hybrid vertical cavity structure, in which the second mirror comprises a 15 period ZrO₂/SiO₂ dielectric DBR (R=0.995). The ‘active’ medium in the resonator was a 2.5 λ thick InGaN MQW composed of 26 wells. Upon high excitation, pulsed pumping by a low repetition rate nitrogen laser, the authors observe stimulated emission from the structure and attribute this to vertical cavity lasing (12). The threshold for the onset of stimulated emission was very high, ~10 mJ/cm² in terms of the incident pulse energy density. Similarly high excitation threshold for “surface lasing” have been reported by Krestinov et al (13) in structures

emission from the structure and attribute this to vertical cavity lasing (12). The threshold for the onset of stimulated emission was very high, ~10 mJ/cm² in terms of the incident pulse energy density. Similarly high excitation threshold for “surface lasing” have been reported by Krestinov et al (13) in structures

where the vertical cavity is formed by one as-grown GaN/AlGaN high reflectance DBR and the nitride-air surface acting as another mirror.

A different approach to the fabrication of high quality vertical cavity has been demonstrated by Song et al (14,15), the objective being to create an all-dielectric DBR resonator. The idea involves the separation of a quantum well heterostructure from its sapphire substrate and its integration with high reflectivity, low loss dielectric mirrors. The process begins with the initial flip-chip mounting of the nitride substrate on an artificial host substrate (by various wafer bonding and related approaches) and the subsequent release of the sapphire substrate by the exposure of the structure to a single pulse of excimer laser radiation ($\lambda=308$ nm) (16). The UV laser radiation is absorbed selectively near the GaN/sapphire interface and, once a critical pulse energy density is exceeded, physical separation of the sapphire over a macroscopic area occurs, presumably due to rapid thermal decomposition of the GaN. This allows the deposition of a second $\text{HfO}_2/\text{SiO}_2$ multilayer dielectric stacks to complete a vertical cavity structures, as shown in the cross sectional electron micrograph of **Fig. 3**. Song and co-workers have demonstrated a vertical cavity blue light emitting diode and observed stimulated emission in optically pumped structures that show a cavity Q-factor approaching 1000 in initial experiments. The spectrum of **Fig. 4** (top) shows the emission spectrum at $T=258$ K from one such structure, under quasi-continuous wave optical pumping (15). The modes are well defined and exhibit a linewidth of approximately 0.5 nm under high resolution. Under optical pumping at relatively modest levels of quasi-cw excitation (average power ~ 30 mW), strong stimulated emission has been measured from these structures (Figure 4, bottom), at frequencies corresponding to the modal positions, including a well defined threshold and the clear observation of linearly polarized far field emission, in the form of a beam strikingly visible to the naked eye in the laboratory (15). In our experience, it has been very difficult to reach this type of “true vertical cavity lasing”, the primary reason being that such true VCSEL operation has to severely compete with in-plane lasing, the latter aided by the formation of “accidental” optical resonators defined by cracks induced by strained AlGaN layers.

The competition between in-plane and true perpendicular vertical cavity lasing is a serious obstacle to further development of the nitride VCSELs. The nitride heterostructures contain extended defects such as the cracks that develop along principal crystalline axis in the case of AlGaN, once the composition of Al exceeds, say about 10%. In their recent work on surface mode lasing from stacked InGaN insertions within a GaN matrix, Krestnikov et al et al have noted that optical pumping conditions

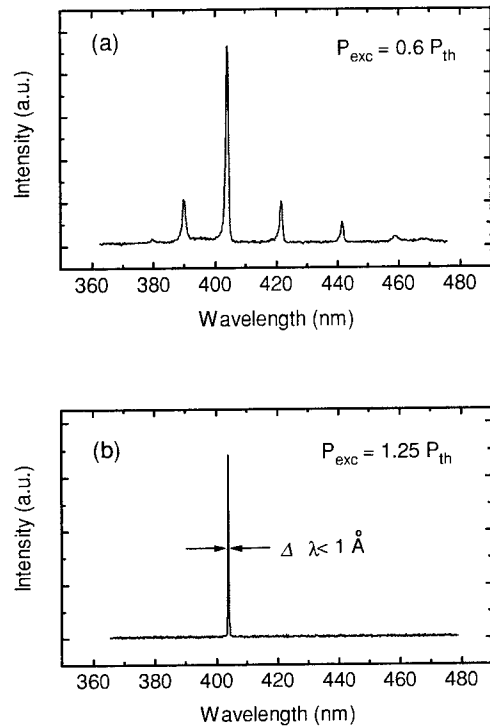


Fig. 4: Upper Trace: Spontaneous emission spectra of the InGaN MQW VCSEL below threshold. Lower trace: Stimulated emission spectra above threshold under quasi-cw pumping conditions at $T=258$ K

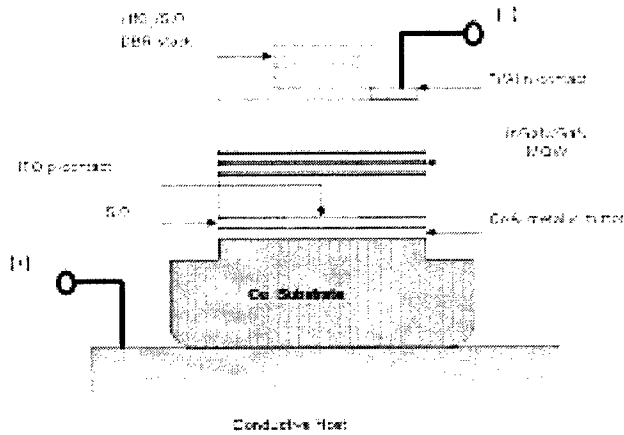


Fig. 5: Schematic of a simple vertical cavity blue LED

the sapphire substrate from the InGaN/GaN/AlGaN QW nitride heterostructure by excimer laser irradiation and the deposition of a high reflectivity dielectric DBR on the n-side of the device. The p-side uses the natural reflectivity of the contact metals (typically up to $R \sim 0.6$) to define the vertical cavity. The typical optical aperture defined by this construction was about 20 μm in diameter. A schematic of a device is shown in **Fig. 5**. The devices have been operated in a continuous mode up to a current density of 1 kA/cm^2 , demonstrating both well defined vertical cavity modal structure as well as their robustness as rudimentary RCLEDs. Example of device performance is shown in **Fig. 6**.

The current-voltage characteristics of such devices highlight a specific, difficult challenge for RCLEDs and, especially, blue VCSELs. The ‘turn-on’ voltage at which significant forward bias current (and LED emission) occurs is up to two volts higher than that for a device fabricated by conventional means. This issue is associated with the rather low resistivity of p-GaN and its alloys. The hole mobility in p-GaN is on the order of $1 \text{ cm}^2/\text{Vsec}$ while the maximum reported free hole concentrations are $p < 1 \times 10^{18} \text{ cm}^{-3}$. Thus in case of vertical cavity structures that employ dielectric DBRs or other low conductivity mirrors, the injection of holes requires some enhancement scheme which will allow the holes to reach the optically active region (below the DBR). In the case of a standard p-type GaN “current spreading layer”, the lateral conductivity is insufficient to compete with vertical transport, until the device area approaches approximately 1 μm . Such a small optical aperture, in turn, implies prohibitive (transverse) modal losses for a VCSEL.

need to be sufficiently extreme so that the in-plane lasing saturates (13). In these circumstances the lasing threshold for a true VCSEL might be prohibitively high. Hence considerable further effort is required for improving the material homogeneity for a realistic VCSEL in the blue and near ultraviolet.

Finally, we mention rudimentary first efforts that have shown some promise but also highlighted the challenges for the realization of a electrical injection vertical cavity device in the nitride semiconductors. Song et al have fabricated a demonstration device that may form one approach for creating a resonant cavity LED (16). The method is again based on the separation of

the sapphire substrate from the InGaN/GaN/AlGaN QW nitride heterostructure by excimer laser irradiation and the deposition of a high reflectivity dielectric DBR on the n-side of the device. The p-side uses the natural reflectivity of the contact metals (typically up to $R \sim 0.6$) to define the vertical cavity. The typical optical aperture defined by this construction was about 20 μm in diameter. A schematic of a device is shown in **Fig. 5**. The devices have been operated in a continuous mode up to a current density of 1 kA/cm^2 , demonstrating both well defined vertical cavity modal structure as well as their robustness as rudimentary RCLEDs. Example of device performance is shown in **Fig. 6**.

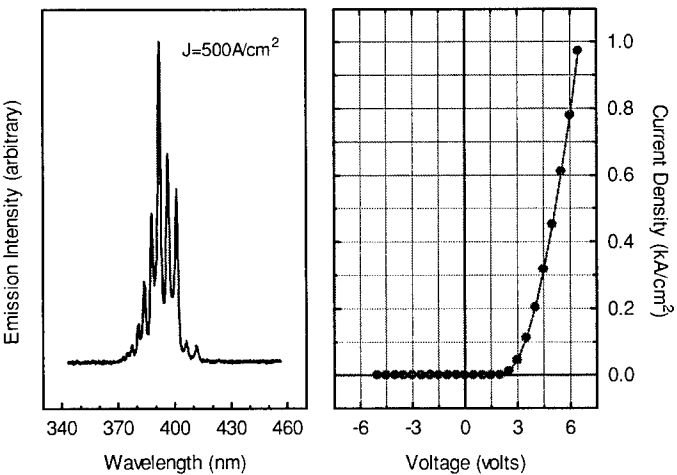


Fig. 6: Spectrum and I-V characteristics of a vertical cavity InGaN MQW blue LED

Some progress has been made recently for reducing the lateral resistivity in GaN by employing concept which is related to modulation doping in conventional III-V semiconductors. Kozodoy et al have achieved high p-type conductivity in Mg-doped AlGaN/GaN superlattices. Effective hole concentrations exceeding $2.5 \times 10^{18} \text{ cm}^{-3}$ have been achieved and a lateral resistivity as low as $0.2 \Omega \text{cm}$ is realized (17). In case of the nitride heterostructures, dielectric polarization and piezoelectric contributions significantly modulate the bandedge energies that can be exploited in these types of modulation doped schemes. While the value of the lateral resistivity reached by these authors is still about one order of magnitude less than required for a practical VCSEL, the approach suggests that further improvements maybe possible by optimizing the superlattice structure with specific nitride compounds. Other “bandstructure engineered” schemes for enhancing lateral current injection are also under way.

This work was supported by the National Science Foundation. We acknowledge with gratitude H. Zhou and M. Diagne at Brown University, and R.P. Schneider Jr. and other collaborators at Agilent Technologies, whose work has been featured in this article and in the reference list.

References:

1. S. Nakamura, *Semicond. Sci. Technol.* **14**, R27 (1999)
2. J. Edmond et al, *Proc. Int. Conference on Nitride Semiconductors ICSNS'97*, Oct. 27-31, 1997, Tokushima, Japan, pp. 448-449; M. Kneissl, D. P. Bour, C. G. Van de Walle, L.T. Romano, J. E. Northrup, R.M. Wood, M. Teepe, and N. M. Johnson, *Appl. Phys. Lett.* **75**, 581 (1999)
3. K. Katayama et al, *Appl. Phys. Lett.* **73**, 102 (1998)
4. J. Ding, M. Hagerott, P. Kelkar, A.V. Nurmikko, D.C. Grillo, Li He, J. Han, and R.L. Gunshor, *Phys. Rev.* **50**, 5787 (1994)
5. Y.-K. Song, M. Kuball, A. V. Nurmikko, G. E. Bulman, K. Doverspike, S. T. Sheppard, T. W. Weeks, M. Leonard, H. S. Kong, H. Dieringer, and J. Edmond, *Appl. Phys. Lett.* **72**, 1418 (1998)
6. C.H. Henry, R.A. Logan, and F.R. Merritt, *J. Appl. Phys.* **51**, 3042 (1980)
7. S. Chichibu, T. Azuhata, T. Sota, and S. Nakamura, *Appl. Phys. Lett.* **70**, 2822 (1997); **69**, 4188(1996); Y. Narukawa, Y. Kawakami, Sz. Fujita, Sg. Fujita, and S. Nakamura, *Phys. Rev.* **B55**, R1938 (1997); S. Chichibu, K. Wada, and S. Nakamura, *Appl. Phys. Lett.* **71**, 2346 (1997)
8. W.W. Chow, A. Knorr, and S.W. Koch, *Appl. Phys. Lett.* **67**, 754 (1995)
9. M.A. Kneissl et al, *Int. Conference of Luminescence*, Osaka, Japan, Sept. (1999); *J. Lumin.* (in press)
10. H. Jeon, V. Kozlov, P. Kelkar, A. V. Nurmikko, C.-C. Chu, D. C. Grillo, J. Han, G. C. Hua, and R. L. Gunshor, *Appl. Phys. Lett.* **67**, 1668 (1995)
11. T. Someya, K. Tachibana, J. Lee, T. Kamiya, and Y. Arakawa, *Jpn. J. Appl. Phys.* **37**, L1424 (1998).
12. T. Someya, Y. Arakawa, R. Werner, and A. Forchel, *CLEO*, Baltimore, May, 1998
13. I. L. Krestnikov, W. V. Lundin, A. V. Sakharov, V. A. Semenov, A. S. Usikov, A. F. Tsatsul'nikov, *Zh. I. Alferov*, N. N. Ledentsov, A. Hoffmann, and D. Bimberg, *Appl. Phys. Lett.* **75**, 1192 (1999)
14. Y.-K. Song, H. Zhou, M. Diagne, I. Ozden, A. Vertikov, A. V. Nurmikko, C. Carter-Coman, R. S. Kern, F. A. Kish, and M. R. Krames, *Appl. Phys. Lett.* **74**, 3441 (1999)
15. Y.-K. Song, H. Zhou, M. Diagne, I. Ozden, A. Vertikov, A. V. Nurmikko, R.P. Schneider, C. Carter-Coman, R. S. Kern, F. A. Kish, and M. R. Krames, *Appl. Phys. Lett.* (in press)
16. M. K. Kelly, O. Ambacher, R. Dimitrov, R. Handschuh, and M. Stutzmann, *Phys. Status Solidi A* **159**, R3 (1997); W. S. Wong, T. Sands, and N. W. Cheung, *Appl. Phys. Lett.* **72**, 599 (1998).
17. Y.-K. Song, H. Zhou, M. Diagne, A. V. Nurmikko, R.P. Schneider, C. Carter-Coman, R. S. Kern, F. A. Kish, and M. R. Krames, *Appl. Phys. Lett.* **74**, 3720 (1999)
18. P Kozodoy, M. Hansen, S. DenBaars, and U. Mishra, *Appl. Phys. Lett.* **74**, 3681 (1999)

Quantum dot laser diodes

S. Fafard, C. Ni. Allen, K. Hinzer, Z.R. Wasilewski

Institute for Microstructural Sciences, National Research Council, Ottawa, Ontario, Canada, K1A 0R6
Tel. :(613) 993-6018/ Fax.: (613) 952-8701/ E-mail: simon.fafard@nrc.ca

Recently, semiconductor quantum dot (QD) laser diodes have been successfully demonstrated. The emphasis in this paper is on the recent progresses at our institute, towards the understanding the physics of such zero-dimensional heterostructures and pointing out the benefits and challenges associated with incorporating these nanostructures in the active layers of practical devices such as laser diodes. The uniform self-assembled quantum dots are obtained using the spontaneous islanding of highly strained III-V semiconductors grown with standard epitaxy. For example, visible stimulated emission has been obtained with red-emitting self-assembled quantum dots (QDs) of highly strained InAlAs grown by molecular beam epitaxy (MBE) on a GaAs substrate [1]. The carriers injected electrically from the doped regions of a separate confinement heterostructure thermalized efficiently into the zero-dimensional QD states, and continuous (CW) threshold current densities well below $100\text{A}/\text{cm}^2$ have been measured at low temperatures. External efficiencies of $\sim 8.5\%$ at low temperature and peak powers greater than 200 mW demonstrated the good size distribution and high gain of the QDs. Room temperature lasing has also been observed for higher threshold current densities in such short-wavelength QD laser diodes [2]. For longer wavelengths where the thermionic emission problem is less important, InAs/GaAs QD lasers can lase at room temperature for current densities below $\sim 100\text{A}/\text{cm}^2$. For eg. see fig. 1 which demonstrate QD laser diodes with very low current threshold densities of $13\text{ A}/\text{cm}^2$ at 77K and $82\text{ A}/\text{cm}^2$ at 15 °C.

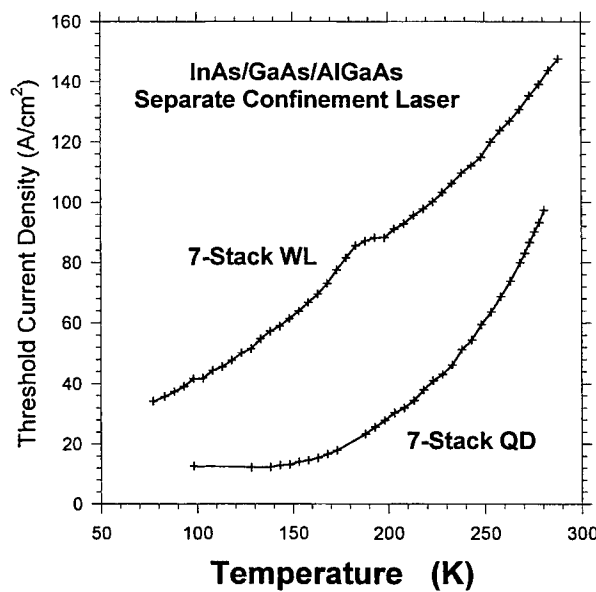


Fig. 1: Temperature dependence of the threshold current density for a InAs/GaAs/AlGaAs QD laser diode, compared with the equivalent laser with wetting-layers (WL) only.

From a recent systematic study of the growth and the optical properties of QDs, we demonstrated that artificial atoms with up to five well-defined electronic shells can be fabricated with good control using self-assembled quantum dots (QDs) grown by molecular beam epitaxy [3]. Size and shape engineering of the QDs during growth permits the tailoring of their intersublevel energy spacings. We demonstrate a

much improved uniformity of the macroscopic ensembles of QDs, with well-resolved electronic shells (see fig. 2).

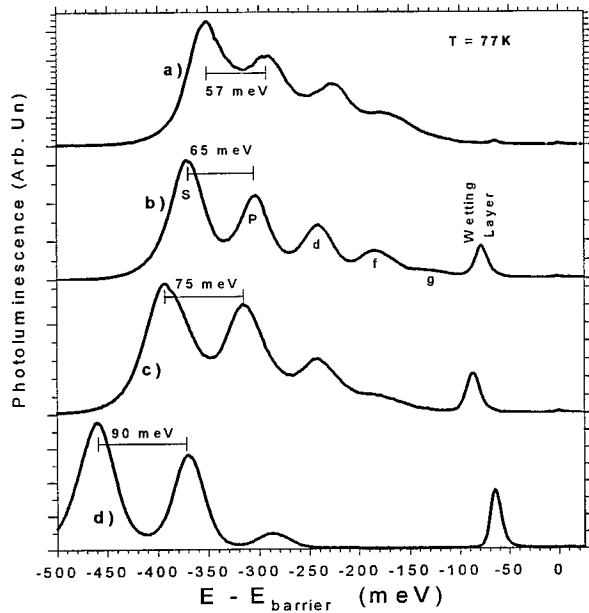


Fig. 2: State-filling spectroscopy of single layers of InAs/GaAs QDs demonstrating tunability during growth. The PL spectra from a) to d) are for $T_{\text{growth}} = 535^{\circ}\text{C}$, 515°C , 500°C , and $\sim 480^{\circ}\text{C}$ respectively.

In addition to size and shape engineering of the QDs in the case of single-layer samples, we demonstrate significant improvements in the uniformity of the vertically self-assembled stacked QDs [4]. These studies are important to increase the density of QDs in the active region of laser diodes, and clearly identify the key parameters to be controlled: a precise amount of strain material deposited with an appropriate in-plane coverage of QDs, an anneal time which together with the deposition rate allows the QDs to evolve to the desired size and uniformity, a growth temperature which yields QDs with the desired intersublevel energy spacing, and an indium-flush technique which cycles the temperature during the overgrowth of InAs/GaAs QDs. State-filling spectroscopy of the zero-dimensional transitions between confined electrons and holes demonstrates that the energy levels are readily tunable. One to five confined levels, with an inter-level energy spacing between 25 and 90 meV, are obtained by adjusting the growth temperature or with post-growth annealings [5]. Such QDs having well-defined excited-states have been grown in the active region of devices such as laser diodes. For example, fig. 3 shows the electroluminescence (EL), photoluminescence (PL), and lasing in a broad area laser having bare cleaved facets and an injection gate width of 100 microns at $T = 77\text{K}$, and fig. 4 show similar results obtained at room temperature. The results show that by increasing the gain using larger QD densities or with longer cavity lengths the lasing is obtained in the lower states, but for higher temperatures or for short cavities, the lasing can clearly be associated to the well-defined excited-states.

- [1] S. Fafard, *Photonics Spectra* 31, 160 (1997). S. Fafard, K. Hinzer, S. Raymond, M. Dion, J. McCaffrey, Y. Feng, and S. Charbonneau, *Science* 274, 1350 (1996).
- [2] S. Fafard, K. Hinzer, A. J. SpringThorpe, Y. Feng, J. McCaffrey, S. Charbonneau, and E. M. Griswold, *Material Science and Engineering* 51, 114 (1998).

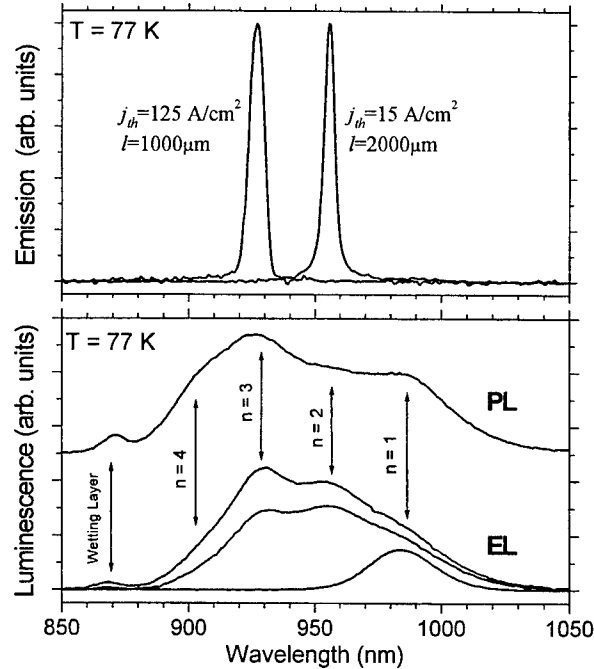


Fig. 3: QD laser diodes with well resolved-excited states.

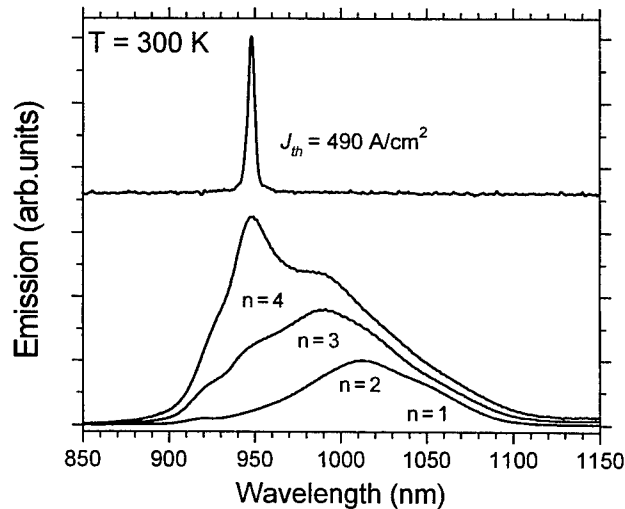


Fig. 4: QD laser diodes with well resolved-excited states at room temperature. Broad-area lasers with bare cleaved facets with a $60 \times 500 \text{ micron}^2$ gate.

- [3] S. Fafard, Z. R. Wasilewski, C. Ni Allen, D. Picard, P. G. Piva, J. P. McCaffrey, *Superlattices and Microstructures* 25, pp. 87-96, (1999).
- [4] Z. R. Wasilewski, S. Fafard, and J.P. McCaffrey, *in-press, J. Crystal Growth*.
- [5] R. Leon, S. Fafard, P. G. Piva, S. Ruvimov, Z. Liliental-Weber, *Phys. Rev. B* 58, R4262 (1998).

Narrow-linewidth complex-coupled DFB lasers with gain coupling induced by vertical emission

Nguyen Hong Ky, J. Robadey, J. -D. Ganière, C. Gourgon,
D. Martin, B. Deveaud, and F. K. Reinhart

Department of Physics, Institute of Micro- and Optoelectronics,
Swiss Federal Institute of Technology - EPFL, CH-1015 Lausanne, Switzerland
Ky.Nguyen@epfl.ch

Abstract: InGaAs quantum-well complex-coupled DFB lasers with gain coupling induced by vertical emission are demonstrated. Continuous-wave operation of these lasers at room temperature provides single-mode emission at a wavelength around 980 nm. A spectral linewidth as narrow as 15 MHz and a side-mode suppression ratio larger than 40 dB are obtained. The use of this gain coupling mechanism permits to reduce the influence of the regrown interface quality on the laser performance.

OCIS codes: (140.3490) Lasers, distributed-feedback; (140.3570) Lasers, single-mode; (140.5960) Semiconductor lasers; (140.3070) Infrared and far-infrared lasers.

Introduction

Complex-coupled (CC) distributed feedback (DFB) laser diodes are one of the most suitable light sources for advanced optical sensor and high-speed optical communication systems because they have many advantages such as narrow linewidth, high mode stability, improved immunity to feedback, high side mode suppression ratio, and low chirp [1]. In addition, a quarter-wave shifted region or antireflective coatings are not required for single-mode operation of CC DFB lasers [2]. The complex coupling can be achieved by a periodic modulation of both the refractive index and the gain along the laser cavity. The index modulation is usually realized by forming a periodic grating in the laser waveguide. As far as the gain coupling is concerned, different mechanisms have been proposed: direct patterning of the active layer by molecular-beam epitaxial (MBE) regrowth over V-groove gratings [1, 3]; use of saturable absorptive [4, 5] or non-saturable metallic gratings [6]. In particular, the gain coupling mechanism based on the radiation loss induced by a second-order grating [7] has received considerable attention. Using this gain coupling mechanism, the fabrication difficulties that hinder the direct patterning of the active layer [1, 3], and the instabilities due to the absorber saturation at high-power operation [4, 5] can be avoided. Since the m -th order grating along the laser waveguide couples two oppositely propagating waves with propagation vectors β_m and $-\beta_m$, the one-dimensional wave field $E(z)$ of the fundamental lasing mode in the longitudinal z -direction can be written as [6]:

$$E(z) = A^+(z)\exp(i\beta_m z) + A^-(z)\exp(-i\beta_m z) , \quad (1)$$

where the amplitudes $A^+(z)$ and $A^-(z)$ are slowly varying functions of z . When a second-order grating having reflection symmetry is present, first-order radiation modes occur in

the direction perpendicular to the grating plane [8]. In this case, the coupled-wave equations for $A^+(z)$ and $A^-(z)$ has the form [7]:

$$-\frac{\partial}{\partial z} A^+(z) + \left(\frac{g}{2} - \kappa_{1rad} + i \frac{\Delta\omega}{v_g} \right) A^+(z) = -i(\kappa_2 + i\kappa_{1rad}) A^-(z) , \quad (2a)$$

$$\frac{\partial}{\partial z} A^-(z) + \left(\frac{g}{2} - \kappa_{1rad} + i \frac{\Delta\omega}{v_g} \right) A^-(z) = -i(\kappa_2 + i\kappa_{1rad}) A^+(z) , \quad (2b)$$

where $\Delta\omega$, g and v_g denote the angular frequency deviation from the angular Bragg frequency, the net gain, and the group velocity, respectively. κ_2 is the coupling coefficient related to the second-order grating whereas κ_{1rad} is the coupling coefficient related to the first-order vertical radiation. Hence, the radiation loss acts as an additional gain coupling mechanism. On the basis of this theoretical result, we have realized CC DFB laser structures with non-saturable gain coupling induced by the vertical emission.

Laser structure

The laser structure (Fig. 1) is fabricated in three steps: i) MBE growth of the n -type $\text{Al}_{0.33}\text{Ga}_{0.67}\text{As}$ cladding and GaAs waveguide, the undoped GaAs active region with three

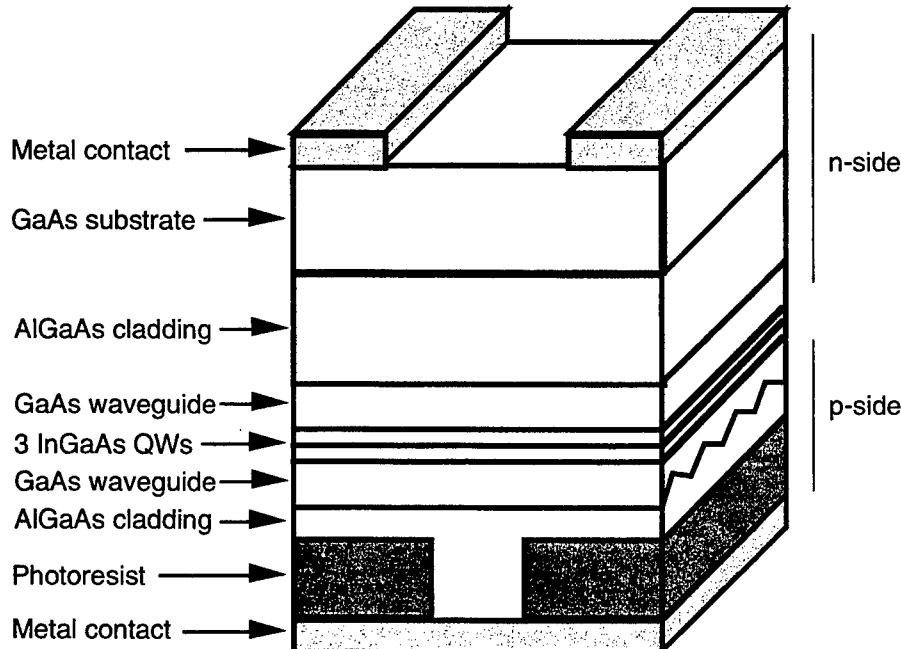


Fig. 1. Schematic structure of CC DFB laser with gain coupling induced by vertical radiation.

strained $\text{In}_{0.18}\text{Ga}_{0.82}\text{As}$ quantum wells, and the *p*-type GaAs waveguide; ii) Formation of the second-order V-groove grating in the waveguide by using UV-holography and wet chemical etching; iii) MBE regrowth of the remaining *p* side of the structure including the $\text{Al}_{0.33}\text{Ga}_{0.67}\text{As}$ cladding and a thin p^+ -GaAs cap layer. For this structure, the fabrication of high-quality active layers is not difficult. The active layers are fabricated during the first growth and are relatively far from the regrown interface. Therefore, the interface quality barely affects the laser performance. A ridge waveguide is formed on the *p* side by reactive ion etching of the AlGaAs cladding. A hardbaked photoresist is used as an insulating layer between the *p*-side metal contact and the etched cladding. A window is opened in the *n*-side metal contact. The CC DFB lasers with a nominal ridge width of 4 μm have been mounted *p*-side-down on sample holders to simultaneously characterize the emissions from two cleaved facets and the vertical emission from the opening in the *n*-contact.

Experimental results

The CC DFB lasers have been characterized by current-voltage (I-V) and light-current (L-I) measurements. A series resistance as low as 1×10^{-6} ohm.cm² is deduced from the I-V curves. Reproducible and low threshold currents, I_{th} , are obtained for these lasers. The lowest threshold current density is about 200 A/cm². Single-mode DFB lasing emission has been achieved in continuous-wave operation at room temperature. The side-mode suppression ratio, SMSR, of the DFB emission at 972 nm is larger than 40 dB for 85 % of the lasers on a wafer. The highest SMSR value is 47 dB. Figure 2 shows the L-I curves of a CC DFB laser. The differential external quantum efficiency, QE, of the emission from each as-cleaved facet is approximately 10 %, whereas that of the vertical emission from the *n*-side surface is 15 %. At the injection current, I , of 110 mA corresponding to 2.25 I_{th} , the output power emitted from the *n*-side surface and one as-cleaved facet is 12.6 mW and 7.5 mW, respectively.

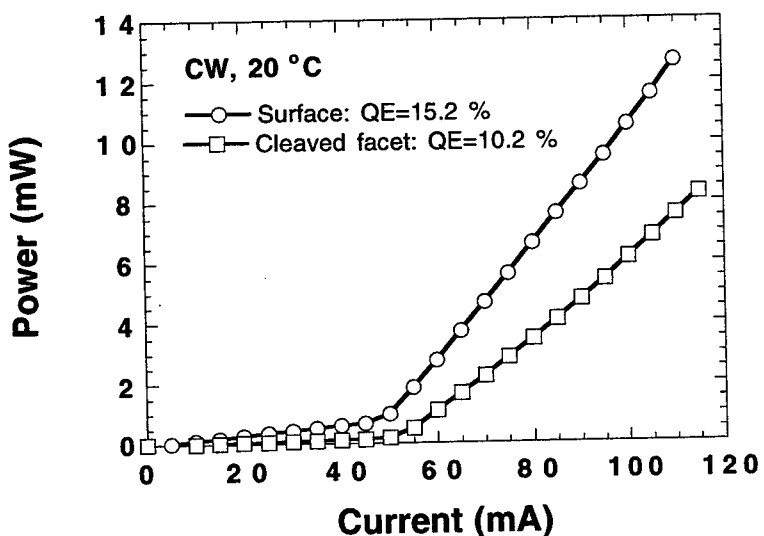


Fig. 2. Light-current characteristics of a CC DFB laser diode.

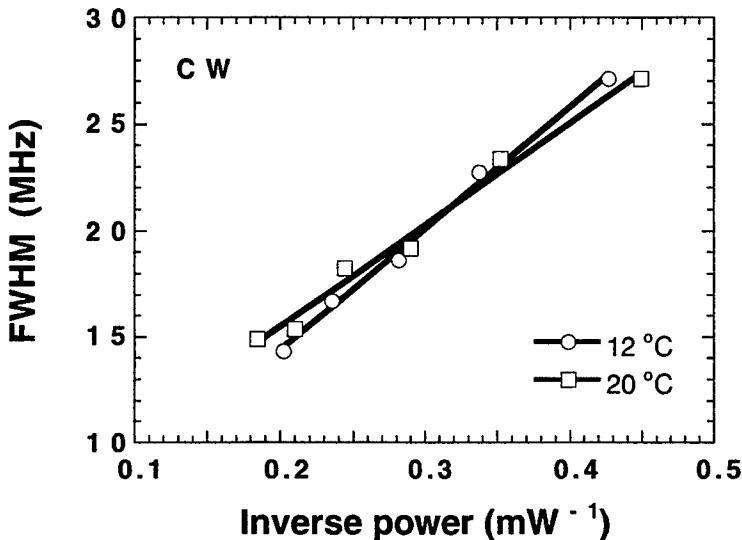


Fig. 3. Spectral linewidth of the DFB emission from an as-cleaved facet as a function of the facet output power.

The spectral linewidth of the DFB emission has been measured as a function of I at different temperatures by using a confocal interferometer with a free spectral range of 2 GHz and a finesse of 400 at 980 nm. In the $1.5I_{\text{th}} < I < 2I_{\text{th}}$ region where the single-mode emission is stable, the power spectrum fits well a Lorentzian curve and the linewidth is proportional to reciprocal output power (Fig. 3). The linewidth-power product depends on the temperature. It is about 57 and 48 MHz.mW at 12 and 20 °C, respectively. The extrapolated residual spectral linewidth is 3 MHz at 12 °C, whereas it is 6 MHz at 20 °C. We obtain the full width at half maximum, FWHM, value as low as 15 MHz at 20 °C and 5.4 mW. This FWHM value is close to the resolution limit of the interferometer.

In summary, InGaAs quantum-well CC DFB lasers with gain coupling induced by vertical emission have been fabricated and characterized. The advantages of this laser structure include a reduction of the influence of the regrown interface quality on the laser performance. Single-mode DFB lasing emission with a FWHM as narrow as 15 MHz and a SMSR larger than 40 dB is obtained for these lasers in continuous-wave operation at room temperature. The use of both vertical and longitudinal emissions provided by this CC DFB laser structure should be of interest for a variety of applications.

Acknowledgments

This work is supported by the European Project ESPRIT-NANOLASE and the Swiss Priority Program on Optics.

References

1. J. Robadey, U. Marti, R. O. Miles, M. Glick, F. Filipowicz, M. Achtenhagen, D. Martin, F. Morier-Genoud, P. C. Silva, Y. Magnenat, P. H. Jouneau, F. Bobard, and F. K. Reinhart, "Distributed

feedback gain-coupled lasers based on InGaAs quantum-wire arrays", IEEE Photon. Technol. Lett. 9 5-7 (1997).

- 2. H. Kogelnik and C. V. Shank, "Coupled-wave theory of distributed feedback lasers", J. Appl. Phys. 43 2327-2335 (1972).
- 3. J. Robadey, D. Martin, M. Glick, P. C. Silva, P.-H. Journeau, U. Marti, and F. K. Reinhardt, "Gain-coupled DFB lasers with active layer grown on a corrugated substrate by molecular beam epitaxy", Electron. Lett. 33 297-298 (1997).
- 4. B. Borchert, K. David, B. Stegmüller, R. Gesner, M. Beschorner, D. Sacher, and G. Frauz, "1.55 μ m gain-coupled quantum-well distributed feedback lasers with high single-mode yield and narrow linewidth", IEEE Photon. Technol. Lett. 3 955-957 (1991).
- 5. Y. Luo, H. -L. Cao, M. Dobashi, H. Hosomatsu, Y. Nakano, and K. Tada, "Gain-coupled distributed feedback semiconductor lasers with an absorptive conduction-type inverted grating", IEEE Photon. Technol. Lett. 3 955-957 (1991).
- 6. M. L. Osowski, R. Panepucci, I. Adesida, and J. J. Coleman, "A strained-layer InGaAs-GaAs asymmetric cladding gain-coupled DFB laser with titanium surface gratings by metalorganic chemical vapor deposition" IEEE Photon. Technol. Lett. 9 422-424 (1997).
- 7. R. F. Kazarinov, and C. H. Henry, "Second-order distributed feedback lasers with mode selection provided by first-order radiation losses", IEEE J. Quantum Electron. 21 144-150 (1985).
- 8. W. Streifer, D. R. Scifres, and R. D. Burnham, "Analysis of grating-coupled radiation in GaAs:GaAlAs lasers and waveguides" IEEE J. Quantum Electron. 12 422-428 (1976).

Quantum Dot Semiconductor Optical Amplifiers

Richard P. Mirin
NIST/MS 815.04
325 Broadway
Boulder, CO 80304
Telephone: (303) 497-7955
FAX: (303) 497-3387
e-mail: mirin@boulder.nist.gov

Daniel J. Blumenthal
Optical Communications and Photonic Networks Laboratory
Department of Electrical and Computer Engineering
University of California, Santa Barbara
Santa Barbara, CA 93106
Telephone: (805) 893-4168
FAX: (805) 893-5705
e-mail: danb@ece.ucsb.edu

Introduction

Semiconductor optical amplifiers (SOAs) are important components for future generations of wavelength division multiplexed (WDM) lightwave systems. The traveling-wave semiconductor optical amplifier (TW-SOA), in which both facets of the semiconductor chip are anti-reflection (AR) coated, is the most heavily studied type of SOA because of its favorable properties as compared to Fabry-Perot type SOAs. One problem facing TW-SOAs in multiwavelength optical systems is interchannel crosstalk due to cross-gain modulation (XGM). Current SOAs have a bulk (three-dimensional) or quantum well (QW) (two-dimensional) gain medium with carriers (electrons and holes) that are in thermal equilibrium (Fermi-Dirac distribution). Thus, when a signal photon at frequency ω_n generates a stimulated photon and simultaneously reduces the net excited carrier population, the carriers redistribute themselves to maintain equilibrium. Therefore, the number of carriers at any given energy, and thus the gain at any given energy, is affected by photons at all wavelengths, leading to XGM.

In this paper, we propose the use of self-assembled semiconductor quantum dots (QDs) as the gain medium of a SOA. By using electronically-uncoupled QDs in place of a QW or bulk gain medium, the XGM can be greatly reduced or eliminated, and the saturated gain can be increased.

Quantum Dots

The study of self-assembled QDs has been increasingly popular in the last few years[1-3], particularly for use as the active region of semiconductor lasers. Performance improvements in QD lasers (as compared to bulk or QW lasers) have been predicted[4, 5], but fabrication of undamaged, high-density arrays of QDs that are suitable for laser active regions[6-8] have only been achievable in recent years. During growth, nucleation of the QDs does not happen simultaneously, which leads to a size distribution of the QDs. The emission from the array of QDs is inhomogeneously broadened due to the size distribution of the QDs.

The most important property that QDs have for SOA applications is that carriers in each individual QD can be electronically uncoupled, i.e., the carriers in each individual QD are not in thermal equilibrium with the carriers in any other QD. The strong evidence for this is demonstrated by photoluminescence excitation (PLE) experiments[9]. Note that it is also possible to have coupled or partially-coupled QDs, but we will not consider those systems in this paper. The nonequilibrium properties of carriers in QDs allows us to examine a new type of SOA, the

quantum dot semiconductor optical amplifier (QD-SOA). We shall analyze XGM and gain saturation in a QD-SOA.

Quantum Dot Semiconductor Optical Amplifiers

The main advantage of using a QD-SOA instead of a QW or bulk active region SOA is that the gain medium is inhomogeneously broadened in a QDSOA. The reason for this inhomogeneous broadening is that the QDs are electronically uncoupled. Thus, when a signal at some frequency ω_n is the input to the QDSOA, it will create stimulated photons only from those QDs whose emission is also at ω_n ; all carriers in other QDs are unaffected.

This is illustrated by examining the carrier rate equation that describes a TWSOA in a multichannel system:

$$\frac{dN}{dt} = \frac{\eta_i I}{qV} - \frac{N}{\tau_c} - \sum_{\omega} \frac{g(N, \omega)}{\hbar\omega} \langle |E_{sig}(\omega) + E_{SE}(\omega)|^2 \rangle, \quad (1)$$

where N is the net carrier concentration, η_i is the injection efficiency, I is the injected current, V is the volume of the active region, τ_c is the carrier lifetime, $g(N, \omega)$ is the gain at frequency ω and net carrier concentration N , $E_{sig}(\omega)$ is the electric field amplitude of the injected optical signal at frequency ω , and $E_{SE}(\omega)$ is the spontaneous emission. The summation is over all channels that are inputs to the amplifier. In order to describe the QD gain medium, with its electronically uncoupled QDs, the following modifications are needed:

$$\rho(E) = (\rho_D D)(2\pi(\Delta E)^2)^{-1/4} \exp\left[-\left(\frac{E - E_Q}{2\Delta E}\right)^2\right], \quad (2)$$

describes the density of states distribution in the array of QDs, where $\rho(E)$ is the areal density of states at some energy E , ρ_D is the areal density of QDs, D is the degeneracy of the quantum state at energy E_Q , and ΔE is the linewidth of the optical transition at centered at E_Q . The overall carrier concentration N is replaced by N_{ω} , where N_{ω} represents the carrier concentration in the QDs with emission energy $\hbar\omega$. $g(N, \omega)$ is replaced by $g(N_{\omega})$, where the gain is now explicitly only a function of the carrier density in the QDs with transition energy $\hbar\omega$. Note that in the previous equation the gain was simply a function of net carrier concentration, at a particular wavelength. So we can now replace equation (1) by a series of *independent* equations at each input frequency:

$$\frac{dN_{\omega}}{dt} = \frac{\eta_i I_{\omega}}{qV} - \frac{N_{\omega}}{\tau_c} - \frac{g(N_{\omega})}{\hbar\omega} \langle |E_{sig}(\omega) + E_{SE}(\omega)|^2 \rangle. \quad (3)$$

Equation (3) describes a situation in which an input channel at frequency ω only induces radiative transitions in those QDs that have emission energies at the same frequency as the input channel. The uncoupled carriers at other frequencies are unaffected by the input signal.

Another advantage of using a QD-SOA is the saturated gain can be higher than a SOA with a homogeneously broadened gain medium. Furthermore, the saturated gain is reached at a slower rate in the QDSOA. These two points are illustrated in Figure 1. It can be shown[10] that in a homogeneously broadened gain medium the expression for saturated gain is $g=g_0/(1+I/I_{sat})$. It can also be shown that for an inhomogeneously broadened gain medium $g=g_0/(1+I/I_{sat})^{1/2}$. This measurement should provide evidence on the broadening mechanism for the QD-SOA.

Conclusions

We have examined some properties of a proposed new SOA, the QD-SOA. The QD-SOA has some important advantages over conventional TW-SOAs, particularly the elimination of XGM. Furthermore, the QD-SOA is expected to be linear over a wider range of input powers than a conventional TW-SOA since the QD-SOA has an inhomogeneously broadened gain medium. Further examination of properties such as polarization sensitivity and time response are needed to determine what types of networks will be suitable for QDSOAs.

References

- [1] Goldstein, L., Glas, F., Marzin, J., Charasse, M., and LeRoux, G., *Appl. Phys. Lett.*, V.47 (10), p.1099-1101.
- [2] Leonard, D., Krishnamurthy, M., Reaves, C.R., DenBaars, S.P., and Petroff, P.M., *Appl. Phys. Lett.*, V.63 (23), p.3203-3205.
- [3] Moison, J. M., Houzay, F., Barthe, F., Leprince, L., Andre, E., and Vatet, O., *Appl. Phys. Lett.*, V.64 (2), p.196-198.
- [4] Arakawa, Y., and Sakaki, H., *Appl. Phys. Lett.*, V.40 (11), p.939-941.
- [5] Asada, M., Miyamoto, Y., and Suematsu, Y., *IEEE J. Quantum Electron.*, V.QE-22 (9), p.1915-1921.
- [6] Bimberg, D., Ledentsov, N., Grundmann, M., Kirstaedter, N., Schmidt, O., Mao, M., Ustinov, V., Egorov, A., Zhukov, A., Kopev, P., Alferov, Zh., Ruvimov, S., Gosele, U., and Heydenreich, J., *Jpn. J. Appl. Phys.*, V.35 p.1311-1319.
- [7] Kamath, K., Bhattacharya, P., and Phillips, J., *Journal Crys. Grow.*, V.175/176 p.720-724.
- [8] Mirin, R., Gossard, A., and Bowers, J., *Electron. Lett.*, V.32 (18), p.1732-1733.
- [9] Fafard, S., Leonard, D., Merz, J.L., and Petroff, P.M., *Appl. Phys. Lett.*, V.65 (11), p.1388-1390.
- [10] Yariv, A., *Optical Electronics*, 3rd ed. (Holt, Rinehart, and Winston, New York, 1985).

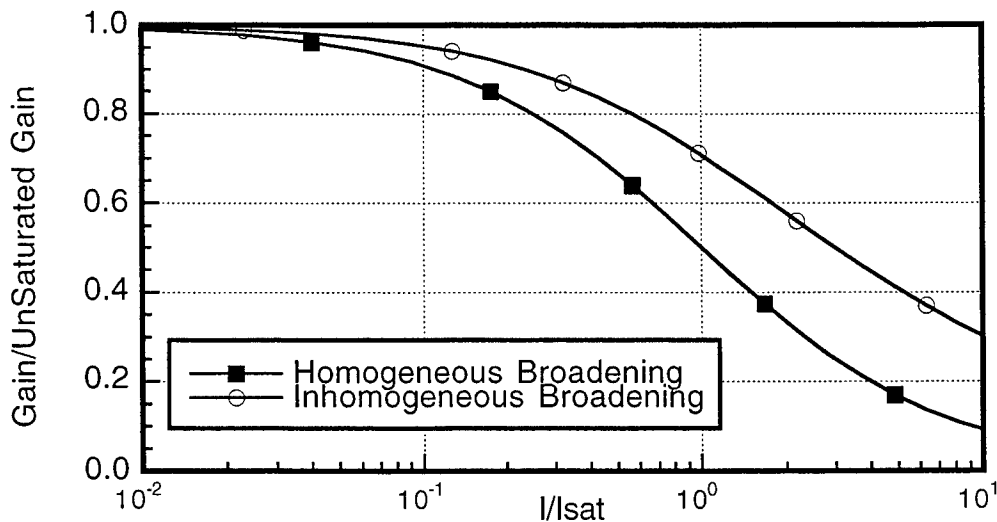


Figure 1 The inhomogeneously broadened gain medium has a higher saturated gain and approaches the saturation value more slowly than the homogeneously broadened gain medium.

100 GHz frequency step-tunable hybrid laser based on a vernier effect between a Fabry-Perot cavity and a sampled fiber Bragg grating

Jean-François Lemieux, Antoine Bellemare, Christine Latrasse, and Michel Têtu

Abstract— Frequency step-tunability is demonstrated in a hybrid fiber grating external cavity laser for the first time. This new configuration uses an in-fiber sampled Bragg grating (SBG) as the frequency selective element allowing the laser to be tuned by 100 GHz frequency steps from 1551.09 to 1556.66 nm. In this demonstration, the wavelength can be set to the eight strongest SBG reflection peaks giving a laser SMSR better than 25 dB and a linewidth of about 130 kHz.

Keywords— External cavity laser, fiber gratings, wavelength division multiplexing, ITU-grid, step-tunable laser, semiconductor lasers.

I. INTRODUCTION

TO achieve DWDM systems requirements, reliable, frequency stabilized single-frequency laser sources at precisely specified wavelengths are needed. Previous work has shown that hybrid fiber grating external cavity lasers [1]–[8] have the capability to meet DWDM requirements. These devices offer good frequency stability, easy wavelength selection during grating fabrication process, narrow linewidth, continuous accordability by stretching or compressing the fiber Bragg grating and, recently, the possibility of low chirp direct modulation at high bit rates [7], [8]. In this paper, step-tunability is achieved for the first time in a hybrid fiber grating external cavity laser by using a vernier effect between a Fabry-Perot (FP) cavity (gain medium) and an in-fiber sampled Bragg grating (SBG) [9]. We call this hybrid laser a sampled fiber Bragg grating external cavity laser (SBG-ECL). This narrow linewidth single-mode laser is 100 GHz step-tunable and the wavelength can be set to eight different reflection peaks of the SBG.

II. EXPERIMENTS

A schematic diagram of the SBG-ECL is given in Fig. 1. The device's simple design is similar to many fiber Bragg grating external cavity lasers except that the frequency selective element is an SBG. The gain medium is a Fabry-Perot (FP) semiconductor laser with a rear facet having a reflectivity of 31% and an AR coated ($R \sim 5 \times 10^{-3}$) front facet. To optimize coupling between the gain medium and the single-mode fiber, light is collected by an AR coated spherical lensed fiber. The SBG is written in hydrogen loaded B:Ge-codoped fiber. The sampled structure

All authors are with the Centre d'optique, photonique et laser (COPL), Département de génie électrique et de génie informatique, Université Laval, Québec (Québec), Canada, G1K 7P4. E-mail: mtetu@gel.ulaval.ca

is achieved by overlaying an amplitude mask on the phase mask used in the scanning beam technique [10]. The grating is 5 cm long (ℓ) with a sampling period of 1.03 mm and a duty cycle of $\sim 19\%$. The writing UV source is a frequency quadrupled Nd:YAG laser emitting at 266 nm. The induced refractive index change is $\sim 2.5 \times 10^{-4}$. Fig. 2 shows the high resolution (0.005 nm) reflection spectrum of the SBG centered at ~ 1554 nm. The FWHM of the reflection peaks is ~ 14 GHz, the strongest peak reflectivity is $\sim 99.7\%$ and the SBG is designed to have a 100 GHz channel frequency spacing (P). The sampled fiber Bragg grating is spliced to the spherical lensed fiber giving an external cavity length of ~ 13 cm (FSR ~ 800 MHz).

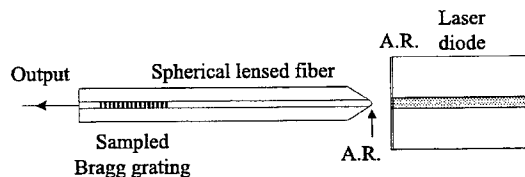


Fig. 1. Schematic diagram of the sampled fiber Bragg grating external cavity laser (SBG-ECL).

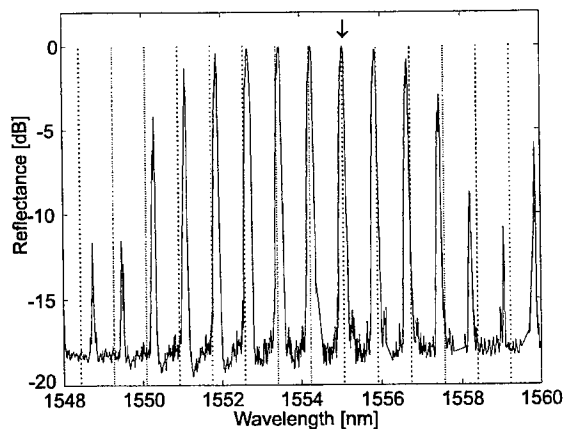


Fig. 2. SBG reflection spectrum (—) and FP cavity mode positions (···). The lasing mode is indicated by an arrow. By increasing (decreasing) the injection current, the FP modes are shifted to longer (shorter) wavelengths while the lasing mode steps to a shorter (longer) wavelength through the vernier effect.

III. RESULTS

The laser wavelength can be step-tuned by increment of 100 GHz from 1551.09 nm to 1556.66 nm by tuning the gain medium residual FP modes with the injection current. Fig. 3 displays the eight single-mode spectra obtained for the various current settings (44 mA to 87 mA) at 25°C. These eight wavelengths correspond to the eight strongest SBG reflection peaks shown in Fig. 2. The single-frequency spectrum observed is explained by the semiconductor chip imperfect AR coating leading to a residual FP cavity having an FSR of \sim 103 GHz. Giving this coupled-cavity scheme, the lasing mode is determined when a gain medium residual FP mode (FSR \sim 103 GHz) is in coincidence with one SBG reflection peak (FSR \sim 100 GHz). By a vernier effect, the laser wavelength gets higher (lower) as the current is decreased (increased) contrary to the usual semiconductor laser behavior. In fact, by diminishing (increasing) the current, the residual gain medium FP modes move to shorter (longer) wavelengths, and by a vernier effect, higher (lower) wavelength residual FP modes are in coincidence with higher (lower) wavelength SBG reflection peaks. This is a consequence of the gain medium residual FP cavity FSR (103 GHz) being slightly larger than the SBG FSR (100 GHz). The tuning mechanism is comparable to the one used in some super-structure grating DBR lasers [11] or SBG fiber lasers [12] which also use a vernier effect for step-tunability. However, the SBG-ECL configuration certainly has more similarities with hybrid fiber grating external cavity lasers [1]-[8].

The SMSR varies from 25.1 dB to 38.0 dB and as expected, higher SMSR is observed for higher injection current. The SMSR and the wavelength were measured for every current setting and the results are plotted in the top inset of Fig. 3. The maximum output power is \sim 100 μ W. This low output power is mainly due to the SBG high peak reflectivity giving low output coupling. Output coupler (SBG) reflection coefficient optimization could lead to higher output power. High reflectivity (HR) coating of the rear facet could also increase output power. Alternatively, the rear facet ($R=31\%$) could also be used as the output but with a lower SMSR.

The laser wavelength is locked to the same SBG reflection peak even if the injection current is changed by a few mA. This can be seen by monitoring the heterodyne beat spectrum between the SBG-ECL and a reference laser with a microwave spectrum analyzer. As the current is changed, the beat spectrum frequency does not vary, meaning that the laser frequency is fixed. The heterodyne spectrum for the SBG-ECL at 1552.69 nm is plotted in the bottom inset of Fig. 3. It clearly shows that there are no other lasing modes associated to the external cavity (FSR \sim 800 MHz). A self-heterodyne measurement (200 ms, 4 samples) with a resolution of 16 kHz showed a 130 kHz linewidth, a value limited by acoustic vibrations (see Fig. 4). Packaging and temperature control of the whole device would surely improve performance [2], [3].

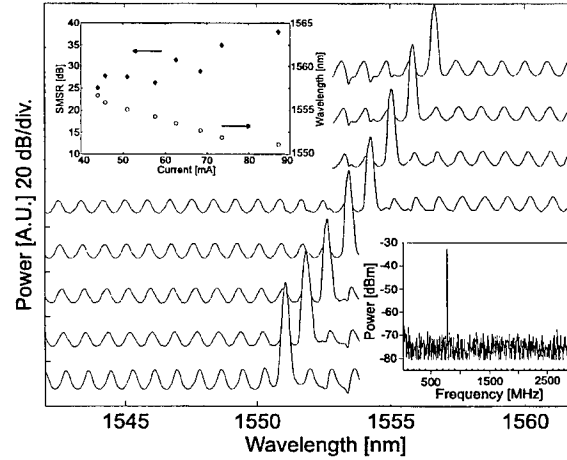


Fig. 3. SBG-ECL single-mode spectra. Top inset: SMSR and wavelength as a function of injection current. Bottom inset: Heterodyne beat spectrum between a reference laser and the SBG-ECL at 1552.69 nm.

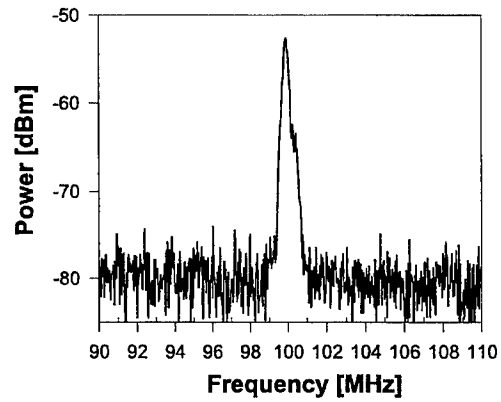


Fig. 4. Self-heterodyne spectrum of the SBG-ECL at 1552.69 nm. The measured linewidth is 130 kHz.

IV. DISCUSSION

It has already been shown that an SBG can be used as a referencing optical frequency scale for WDM [13]. As it is possible to tune the SBG reflection peaks at exact multiples of 100 GHz [14], the laser wavelengths could be set to the ITU grid. Fig. 5 shows eight reflection peak frequency values of an SBG against relative strain. We have found that the tuning coefficient, $(\Delta\lambda/\lambda)/(\Delta\ell/\ell)$, is \sim 0.79 for every peak in agreement with previous measurements for uniform Bragg gratings [15]. It can be seen that for three different relative strain values, the SBG reflection peak maxima are at exact multiples of 100 GHz. Compressing or stretching the fiber SBG sets the reflection peaks at exact multiples of 100 GHz and step-tunability of the device could then provide wavelengths at exact multiples of 100 GHz.

Since wavelength sensitivity with temperature is reduced by an order of magnitude with selective elements being fiber Bragg gratings instead of gratings in semiconductor material [2], [6], [7], a SBG-ECL could be used to calibrate and characterize DWDM components or as a unique frequency selectable transmitter within DWDM systems.

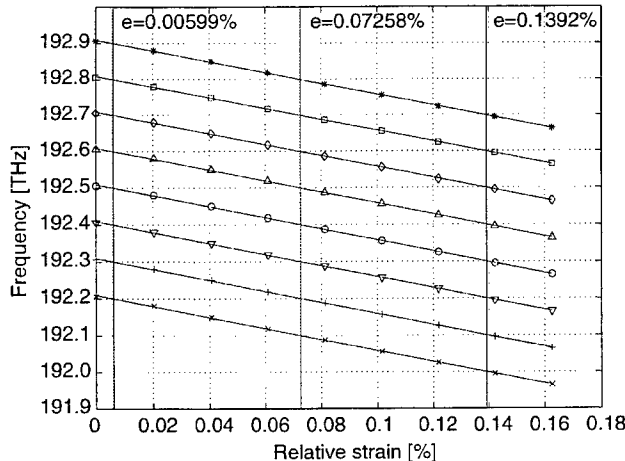


Fig. 5. Eight SBG reflection peaks position against relative strain

V. CONCLUSION

We have realized a single-frequency SBG-ECL tuned by steps of 100 GHz from 1551.09 nm to 1556.66 nm. To our knowledge, this is the first demonstration of frequency step-tunability in an hybrid fiber grating external cavity laser. Wavelength step-tunability is achieved by varying the gain medium injection current. The SMSR varies from 25.1 dB to 38.0 dB and the laser linewidth is \sim 130 kHz. Precise frequency positioning on the ITU frequency grid is possible with SBG fiber traction/compression. A promising feature of this device is that step-tunability on a broader wavelength range can be obtained with a SBG having a flatter response [16] and more reflection peaks. Finally, we believe that the SBG-ECL can be used for DWDM components characterization or as a frequency selectable transmitter.

VI. ACKNOWLEDGEMENTS

We would like to thank Dr. Mikelis Svilans and André Fekcs from Nortel (Ottawa) for providing us the semiconductor laser chip and the spherical lensed fiber and Dr. Jean Martin now with Innovative Fibers for his help in the fabrication of the SBGs.

REFERENCES

- [1] D. M. Bird, J. R. Armitage, R. Kashyap, R. M. A. Fatah and K. H. Cameron, "Narrow line semiconductor laser using fibre grating," *Electron. Lett.*, vol. 27, pp. 1115-1116, 1991.
- [2] P. A. Morton, V. Mizrahi, T. Tanbun-Ek, R. A. Logan, P. J. Lemaire, H. M. Presby, T. Erdogan, S. L. Woodward, J. E. Sipe, M. R. Phillips, A. M. Sergent, and K. W. Wecht, "Stable single mode hybrid laser with high power and narrow linewidth," *Appl. Phys. Lett.*, vol. 64, pp. 2634-2636, 1994.
- [3] J. J. Pan, X. L. Jing, and Y. Shi, "Fiber grating stabilized laser source for dense WDM systems," *Technical Digest of OFC'97*, paper WL48, p. 213, 1997.
- [4] F. Le Gall, S. Mottet, N. Devoldere, and J. Landreau, "External cavity laser for DWDM access network," *Technical Digest of ECOC'98*, paper TuC14, pp.285-286, 1998.
- [5] A. Hamakawa, T. Kato, G. Sasaki, and M. Shigehara, "A four channel multiwavelength fiber-grating external-cavity-laser array," *Technical Digest of OFC'97*, paper ThM3, pp. 297-298, 1997.
- [6] R. J. Campbell, J. R. Armitage, G. Sherlock, D. L. Williams, R. Payne, M. Robertson, and R. Wyatt, "Wavelength stable uncooled fibre grating semiconductor laser for use in an all optical WDM access network," *Electron. Lett.*, vol. 32, pp. 119-120, 1996.
- [7] F. N. Timofeev, P. Bayvel, V. Mikhailov, O. A. Lavrova, R. Wyatt, R. Kashyap, M. Robertson, and J. E. Midwinter, "2.5 Gbit/s directly-modulated fibre grating laser for WDM networks," *Electron. Lett.*, vol. 33, pp. 1406-1407, 1997.
- [8] Z. F. Fan, P. J. S. Heim, J. H. Song, Y. Hu, F. G. Johnson, D. R. Stone, and M. Dagenais, "Detuned loading effect and high-speed modulation of fiber grating semiconductor lasers," *IEEE Photon. Technol. Lett.*, vol. 10, no.12, pp. 1784-1786, 1998.
- [9] B. J. Eggleton, P. A. Krug, L. Poladian, and F. Ouellette, "Long periodic superstructure Bragg gratings in optical fibres," *Electron. Lett.*, vol. 30, pp. 1620-1622, 1994.
- [10] J. Martin and F. Ouellette, "Novel writing technique of long and highly reflective in-fibre Bragg gratings," *Electron. Lett.*, vol. 30, pp. 811-812, 1994.
- [11] Y. Tohmori, Y. Yoshikuni, H. Ishii, F. Kano, T. Tamamura, Y. Kondo, and M. Yamamoto, "Broad-range wavelength-tunable superstructure grating (SSG) DBR lasers," *IEEE J. of Quantum Electronics*, vol. 29, no. 6, pp. 1817-1823, 1993.
- [12] M. Ibsen, B. J. Eggleton, M. G. Sceats, and F. Ouellette, "Broadly tunable DBR fibre laser using sampled fibre Bragg gratings," *Electron. Lett.*, vol. 31, pp. 37-38, 1995.
- [13] J. Martin, M. Tétu, C. Latrasse, A. Bellemare, and M. Duguay, "Use of a sampled Bragg grating as an in-fiber optical resonator for the realization of a referencing optical frequency scale for WDM communications," *Technical Digest of OFC'97*, paper ThJ5, pp. 284-285, 1997.
- [14] A. Bellemare, J.-F. Lemieux, M. Tétu, and S. LaRochelle, "Erbium-doped fiber ring lasers step-tunable to exact multiples of 100 GHz (ITU-grid) using periodic filters," *Technical Digest of ECOC'98*, paper TuA13, pp. 153-154, 1998.
- [15] G. A. Ball and W. W. Morey, "Continuously tunable single-mode erbium fiber laser," *Opt. Lett.*, vol. 17, pp. 420-422, 1992.
- [16] M. Ibsen, M. K. Durkin, M. J. Cole, and R. I. Laming, "Sinc-sampled fiber Bragg gratings for identical multiple wavelength operation," *IEEE Photon. Technol. Lett.*, vol.10, no.6, pp. 842-844, 1998.

Characterization and coupling of diode lasers by photorefractive wave mixing

Peter Pogany, Hans J. Eichler

Optisches Institut, Technische Universität Berlin, Strasse des 17. Juni 135, 10623 Berlin, Germany
Pogany@physik.tu-berlin.de

The techniques to be discussed here are based on laser induced refractive index gratings in photorefractive crystals such as barium titanate or semi-insulating indium phosphide and cadmium telluride. These crystals belong to the highest-sensitivity nonlinear optical materials for operation at moderate power levels. The photorefractive effect [1] is a multistep process, in which first, two light beams are used to form an intensity interference pattern. The intensity gradients induce a space charge field in the crystal. The space charge field changes the local optical properties of the material due to the electro-optic effect to form a dynamic refractive index grating having the same spatial dependence as the intensity interference pattern of the two light beams. This process and the resulting index hologram are dynamic in that they follow any changes in the phases of the writing beams.

One important feature of the photorefractive effect is the 90° phase shift between the interference pattern and the induced index grating. This phase shift allows for energy transfer between the two beams writing the grating in a process called two-wave mixing [1]. One of the beams referred to as the signal beam is amplified at the expense of the other beam called pump or reference beam. We investigate the wave-mixing of co-directional light beams in bulk photorefractive crystals. We show how the temporal coherence function of cw diode lasers can be simply measured using the wave mixing technique. From the measured coherence function the most important spectral characteristics of the laser emission can be calculated. Multiple two-wave mixing can also be used to combine the outputs of several locked solitary lasers or elements of diode laser arrays [2, 3]. We demonstrate two diode laser oscillator-amplifier systems with photorefractive BaTiO₃ and InP:Fe crystals, respectively.

MEASUREMENT OF COHERENCE FUNCTIONS OF DIODE LASERS

The temporal coherence function of a light wave is defined as the autocorrelation function of the complex field amplitude. For equal input intensities of the signal and reference beams and for moderate coupling strength the energy transfer between the beams due to the photorefractive two-wave mixing is proportional to the square of the input coherence degree [4]. This provides a simple determination of the squared coherence function by measurement of the signal intensity enhancement as function of the time delay between the beams. The experimental setup is shown in Fig. 1.

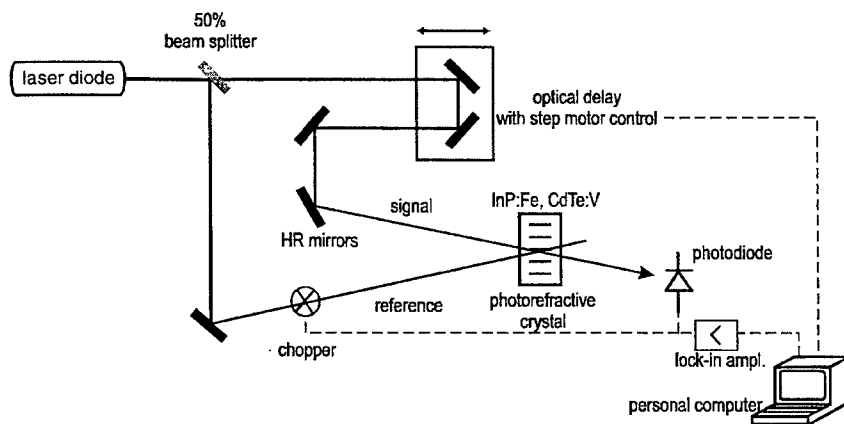


Fig. 1. Experimental setup for measurement of the coherence function, HR, highly reflecting

The coherence properties of multimode and monomode 5mW diode lasers emitting in the 1.3-1.5μm spectral region were characterized by the method to be explained here making use of induced photorefractive grating. The beam from the laser is split by a 50% beam splitter into a signal and a reference beam. After the signal beam is delayed by a delay line in which two mirrors are moved by a stepper motor, the beams intersect in the photorefractive crystal at an angle of 9°. Photorefractive InP:Fe and CdTe:V samples were applied to record the

interference fringes. All crystals were cut along the $\langle 1\bar{1}0 \rangle$, $\langle 111 \rangle$ and $\langle 11\bar{2} \rangle$ crystallographic directions. The polarization of the writing beams lay within the plane of incidence, and these beams formed a grating along the $\langle 111 \rangle$ direction in the photorefractive crystal. The power of the signal beam was detected by a Ge-photodiode using a lock-in amplifying technique. A personal computer was used for data acquisition and to control the stepper motor. Without an external applied field the photorefractive semiconductors provide moderate coupling gain, and the assumption of weak coupling is valid. With our crystals the coupling coefficients were always smaller than 0.4cm^{-1} for crystal lengths of 0.3cm , providing 6% maximum intensity changes of the signal beam.

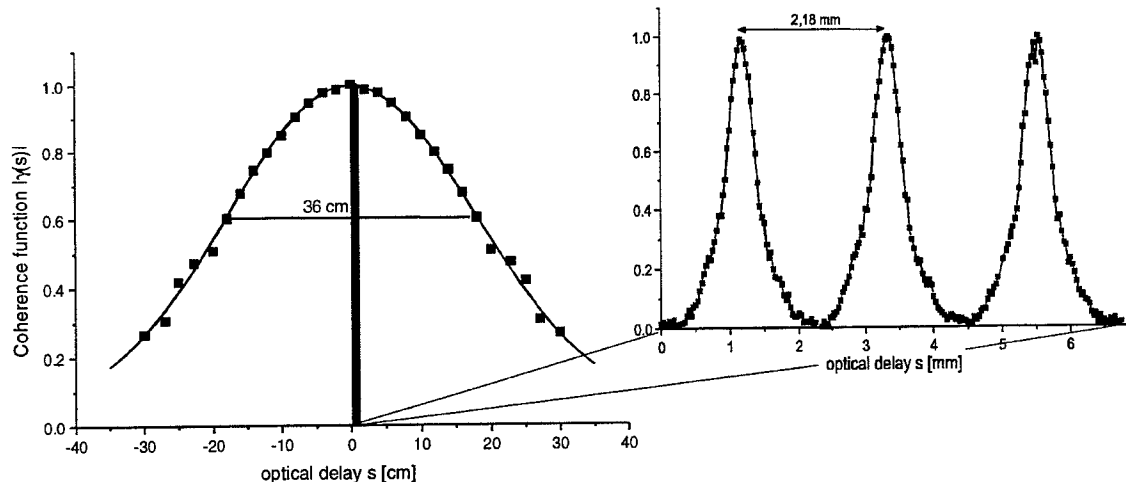


Fig. 2. Measured coherence function of a multimode laser diode

Fig. 2 shows the measured coherence function of a multimode $1.3\mu\text{m}$ laser diode. The coherence function is a periodical function under an approximately Gaussian envelope. The inset in Fig. 2 shows the periodic substructure in detail. The Wiener-Khintchine theorem [5] allows the power spectrum to be calculated by means of Fourier transformation of the coherence function. The envelope width of the coherence function is related to an average spectral linewidth of a single longitudinal mode of the laser diode. The calculated FWHM linewidth of 624MHz , or 3.5pm corresponds to a coherence length of 18cm .

The substructure of the coherence function in Fig. 2 is related to the spacing and power distribution of the modes. The measured spacing of the coherence peaks of $\Delta s = 2.18\text{mm}$ corresponds to the length of the microresonator $\Delta s/2n \approx 307\mu\text{m}$ with refractive index $n \approx 3.55$, yielding a mode spacing of $\Delta f = 137\text{GHz}$ or $\Delta\lambda = 0.77\text{nm}$. The emission spectra measured directly by an optical grating spectrometer shown the same mode spacing.

BEAM COMBINING BY MULTIPLE TWO-WAVE-MIXING

An important feature of two-wave-mixing is the fact that although energy is transferred from the pump beam to the signal beam, the wavefronts of both beams do not interact. This feature allows the possibility of converting a severely phase distorted high power beam into a clean beam [6]. In our experiments we amplify the output of a single mode diode laser by two parallel semiconductor laser amplifiers. The two amplified pump beams and a clean signal beam coming directly from the master oscillator are combined into a single diffraction-limited output beam in a photorefractive crystal.

The experimental setup used for our investigations is shown in Fig. 3. In the experiments with photorefractive $\text{BaTiO}_3:\text{Ce}$ a strained GaInP quantum-well diode laser emitting up to 10mW optical cw power at $\lambda = 678\text{nm}$ was applied as master oscillator. The signal beam is emitted from one face of the diode and the two pump beams from the opposite face. The three collimated beams with a diameter of about 1mm were combined in the barium titanate crystal with the following internal angles to the normal on the entrance facet: $\theta_S = 14^\circ$, $\theta_{P1} = 20^\circ$, $\theta_{P2} = 22^\circ$, where the subscripts S and P refer to the signal and the pump beams, respectively.

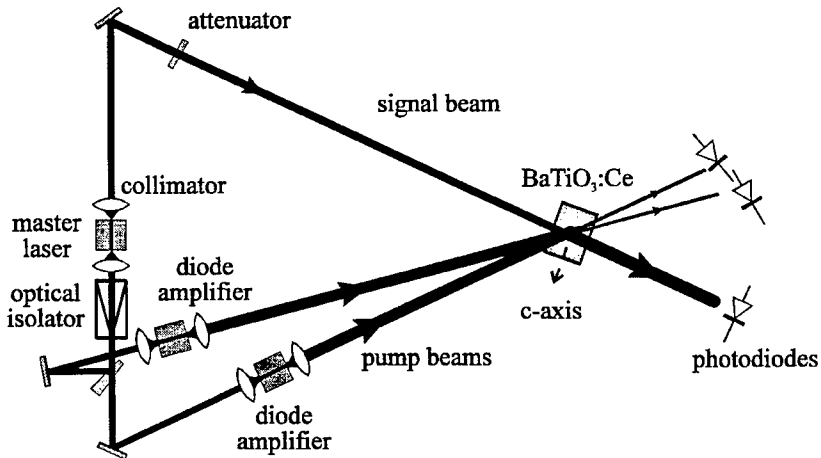


Fig. 3. Experimental setup for parallel operation of laser diode amplifiers. The energy from the pump beams is transferred to the signal beam in photorefractive $\text{BaTiO}_3:\text{Ce}$.

A similar diode laser system at $1.3\mu\text{m}$ optical wavelength was also investigated. We used a photorefractive InP:Fe crystal for beam combining. Such photorefractive semiconductors have the advantages of low cost and fast response time (about 0.1 s) relative to rather costly BaTiO_3 with response times by factor 10-100 higher for the same intensity level. Unfortunately, the induced refractive index change is smaller in InP:Fe, than in BaTiO_3 . Therefore we used an applied DC electric field of 6kV/cm on the InP:Fe crystal to enhance the photorefractive coupling [7].

In beam combining systems the energy transfer from the pump beams into the signal beam should be optimized. In both systems up to 50% of the input pump energy were transferred into the output signal beam. About 70% of the losses are due to incomplete depletion of the pump beams and 30% are due to absorption in the crystal. Our investigations indicate that a significant part of the undepleted pump beam is incoherent to the signal beam. This incoherent light results from the spontaneous emission of the amplifiers. Thus the photorefractive crystal also acts as a filter for incoherent radiation. Since absorption is responsible for the photorefractive effect, some absorption losses are unavoidable.

In conclusion, the dynamic nature of laser induced diffraction gratings formed in photorefractive crystals makes a simple self-adjusting realization of complex optical functions possible. We have presented an innovative technique to determine the coherence functions of cw lasers by using the photorefractive grating method. We have also demonstrated the coherent combining of three beams without any active control of the beam phases. This application of the photorefractive wave-mixing has great potential to achieve high brightness semiconductor laser sources.

REFERENCES

1. P. Günter, J.-P. Huignard, Photorefractive Materials and Their Applications I-II, Topics in Applied Physics, Vol. 61-62, Springer-Verlag Berlin (1988); P. Yeh, Introduction to Photorefractive Nonlinear Optics, John Wiley & Sons, Inc New York (1993); D. D. Nolte, Photorefractive Effects and Materials, Kluwer Academic Publishers Norwell (1995)
2. S. MacCormack and R. W. Eason, "Sequential power transfer between stripes of a diode laser array via photorefractive two-wave mixing in BaTiO_3 ", *J. Appl. Phys.* **67**, 7160 (1990)
3. S. MacCormack, G. D. Bacher, J. Feinberg, S. O'Brien, R. J. Lang, M. B. Klein, B. A. Wechsler, Powerfull diffraction-limited semiconductor laser using photorefractive beam coupling, *Opt. Lett.* **22**, 227, (1997)
4. P. Pogany, H. J. Eichler, J. Dziambor, V. Hagemann, B. Smandek, Measuring the coherence function of cw lasers by a photorefractive grating method. *Appl. Opt.* **38**, 516 (1999)
5. M. Born, E. Wolf, *Principles of Optics*, Pergamon Press, London (1970)
6. A.E.T. Chiou, P. Yeh, Beam clean-up using photorefractive two-wave mixing, *Appl. Phys. Lett.* **10**, 621 (1985)
7. G. Picoli, P. Gravey, C. Ozkul, V. Vieux, Theory of two-wave mixing gain enhancement in photorefractive InP:Fe: A new mechanism of resonance, *J. Appl. Phys.* **66**, 3798 (1989)

Comparison between performances of SG and BSG DBR semiconductor lasers

M. Gioannini, V. Guja, I. Montrosset

Politecnico di Torino, Dipartimento di Elettronica, C.so Duca degli Abruzzi 24, Torino, Italy

email: montrosset@polito.it

Abstract: We compare simulation results of statical characteristics of DBR lasers realized with Sampled Grating and Binary Superimposed Grating and demonstrate that for a laser of today practical interest the same performances can be obtained with both devices by a proper choice of the design parameters.

OCIS codes: (140.0140) Lasers and laser optics; (230.0230) Optical devices; (140.3600) Lasers, tunable; (230.1480) Bragg Reflectors.

Introduction

Multiwavelength transmission systems can work on over one hundred channels equally spaced in a wide spectral range [1] and appropriate wide tunable semiconductor lasers are emerging for this kind of application. There are three structures competing, all based on the Vernier effect applied to the multiple peaks reflectivity of their DBR mirrors [2]: Sampled Grating (SG) [3], Binary Superimposed Gratings (BSG) [4] and SuperStructure Grating (SSG) [5]. The last two cases are reported with better performances but are technologically more difficult to realize. The SG limitations are usually attributed to the non-uniform peak reflectivity of the mirrors. In order to stress the comparison between these structures we used as a reference a DBR laser for today practical applications with asymmetric mirrors power reflectivity ($R_{f,b}=0.6$ and 0.2), 40 nm tuning range, $SMSR > 35\text{ dB}$ for an output power greater than 2 mW . We found that by proper choice of the parameters characterizing the SG-DBR it is possible to obtain the same laser performances of BSG-DBR.

Mirrors design

The design of widely tunable semiconductor lasers is strongly dependent on the design of the DBR mirrors. The next steps define the general procedure that we have followed for their design:

- establish the number of reflectivity peaks necessary to cover the desired tuning range with the available refractive index variation produced by current injection;
- choose the reflectivity, flatness and bandwidth of the grating peaks to maximize the external quantum efficiency, the output power uniformity for all the channels and the prescribed SMSR by controlling the maximum acceptable reflectivity of the adjacent non lasing channels;
- design the grating structure for the particular case of BSG or SG.

A BSG with N reflection peaks can be designed starting from the digitalization of the function representing the superposition of N ordinary analog Bragg gratings:

$$F(z) = \sum_{i=1}^N a_i \sin\left(\frac{2\pi}{\Lambda_i} z + \varphi_i\right) \quad (1)$$

where $\Lambda_i = \lambda_i/n_{eff}$ is the grating period satisfying the Bragg condition for the wavelength i and the constants a_i , φ_i ($i=1, N$) have been considered as free parameters to be optimized in order to match the

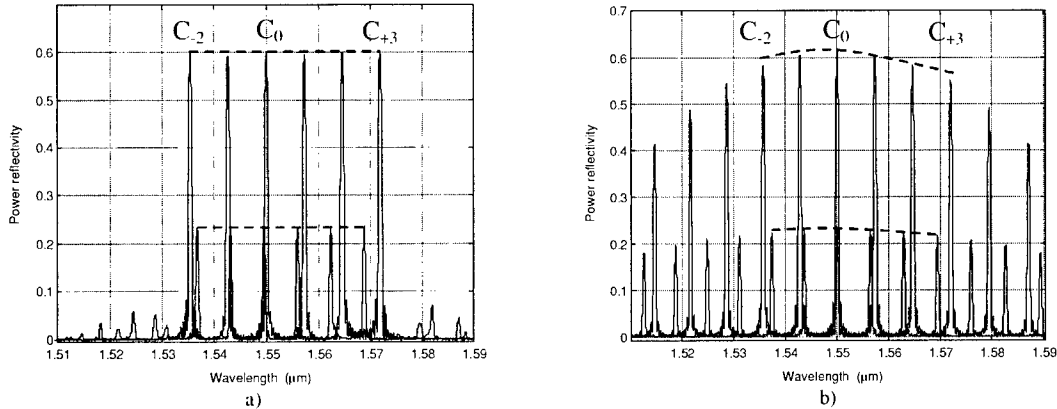


Fig. 1. Power reflectivity spectrum of the gratings, a) BSG b) SG; the dotted segments indicate the peaks that are used to tune the laser in the 40 nm range from $1.53\text{ }\mu\text{m}$ to $1.57\text{ }\mu\text{m}$;

prescribed reflectivity and spacing of the reflection peaks; to this purpose we used always successfully the Nedler-Mead Simplex method [6]. The design procedure we used differs just slightly with respect to the method presented by Avrutsky [4] and allows to obtain compact mirror structures with any reflectivity; the limited total waveguide losses obtainable with these gratings allows to use also low grating coupling coefficients. We have chosen a value of 97 cm^{-1} and a length of $600\text{ }\mu\text{m}$ for both gratings with the single reflectivity peak bandwidth of about 0.7 nm . In Fig. 1 a) are shown the reflectivity characteristics of the designed BSG gratings. The various values of the maximum reflectivity have been obtained by sampling with a different step the grating function; wider steps led to smaller equivalent coupling coefficients [4] and than to lower reflectivity and viceversa.

The SG reflectors have been designed to obtain with approximately the same length the reflectivity of the BSG mirrors in order to have comparable grating tuning currents and losses and the same external quantum efficiency of the BSG laser. A method to increase the reflectivity of the SG could be to make longer reflectors but, as shown in Fig. 2, this is limited by the waveguide losses. Another alternative could be to increase the value of the grating's length for each period but this would lead to a greater non-uniformity of the reflectivity values for the usable reflection peaks. The last possibility is to use high coupling coefficients. As shown in Fig. 2, the power reflectivity of 0.6 in a SG with 10 cm^{-1} waveguide losses can be obtained with a coupling coefficient of 260 cm^{-1} with 15 periods of a $6.3\text{ }\mu\text{m}$ long grating region for each period and a total grating length of $675\text{ }\mu\text{m}$.

The obtained reflectivity spectrum is shown in Fig. 1 b). The 0.23 value of the power reflectivity of the other SG has been obtained with a total grating length of $612\text{ }\mu\text{m}$, 12 periods and $2.7\text{ }\mu\text{m}$ of grating for each period; the use of smaller grating length in each grating period allows to reduce the reflectivity and permits to obtain a better flatness for the reflectivity of the usable peaks as shown in Fig. 1 b). The peaks of the SG are not equally spaced because of the refractive index dispersion while the BSG design allowed obtaining equally spaced peaks. In Fig. 3 a) and b) we present the power reflectivity product of the front and rear mirrors for BSG and SG respectively.

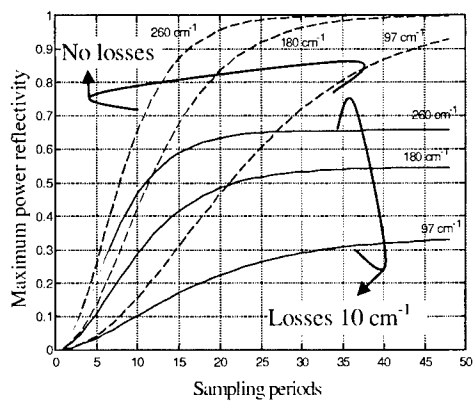


Fig. 2. SG maximum reflectivity vs the number of sampling periods for various coupling coefficient and grating propagation losses.

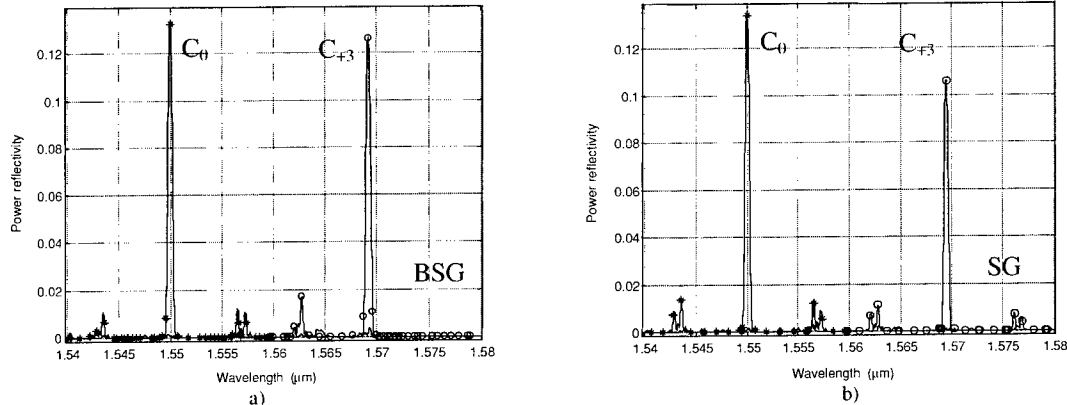


Fig. 3. Power reflectivity product of the laser gratings for a) BSG b) SG. Asterisk and circle are used to indicate the longitudinal mode positions when the laser is operating at $1.55 \mu\text{m}$ and $1.569 \mu\text{m}$ respectively.

The two peaks in each figure correspond to the cases when the device is working at the central wavelength of the tuning range (C_0 in Fig. 1) and for the grating current injection that overlap the peaks at the highest wavelength in the tuning range (C_{+3} in Fig. 1). In our design the peaks overlapping at $1.55 \mu\text{m}$, C_0 , is obtained without current injection in the grating while the C_{+3} peaks overlapping at $1.69 \mu\text{m}$ is obtained with current injection in the grating opposite to the facet where the power is extracted (9.57 mA for SG and 8.8 mA for BSG, different due to the slightly smaller BSG length). The reduction of the power reflectivity product value at high wavelength with respect to the central wavelength in the SG case is due to the reduced reflectivity of the lateral peaks (see C_{+3} in Fig. 1) combined with the plasma effect losses due to the injection in the gratings. In the BSG case we have just the plasma effect losses contribution and than the reflectivity product is more uniform.

Laser modeling

The laser we consider has four sections: two grating mirrors, an active region and a phase control region. The semiconductor-air interfaces of the gratings have been supposed covered with ideal antireflection coatings. The simulator that we have realized is based on the multi longitudinal modes mean field model [7] and calculates the static characteristics of the structure (facets optical output power for a given number of longitudinal modes around the wavelength of the mode with the highest power, SMSR, emission wavelength etc.) for any current injection configuration of the four section device; gain saturation effects have also been included in the model. The program is capable to adjust the current in the phase region such that always one longitudinal mode resonance is situated at the wavelength corresponding to the peak of the gratings reflectivity product (Fig. 3). The numerical code allows to simulate all the static characteristics of the device that are usually measured in the laboratory [8].

Performances comparison

In this section we compare the static characteristics of the designed SG and BSG lasers. In Fig. 4 the optical power output from the lower reflectivity facet and the SMSR versus active region current are reported for the two grating injection conditions shown in Fig. 3. For all the considered currents there is one mode on the reflectivity peak because we have always compensated, with the current injected in the phase section, the longitudinal mode displacement with respect to the peak reflectivity due to the tuning and gain saturation effects. The results shown in Fig. 4 are for three devices: SG with symmetrical

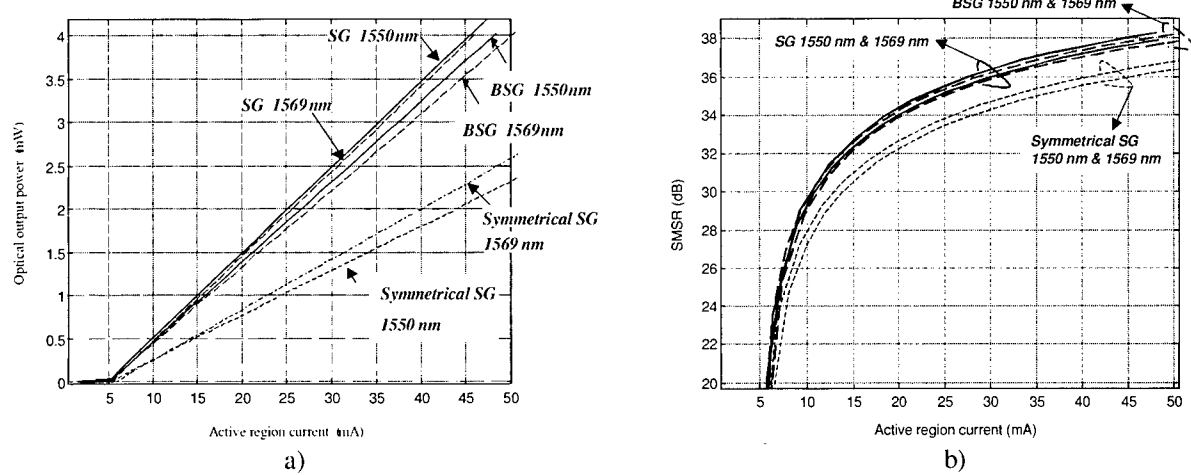


Fig. 4. a) Comparison between optical power versus active region current for SG and BSG at 1550 nm and 1569 nm for the structures with the reflectivity presented in Fig. 1 and for a SG with symmetrical reflectivity and the same cavity losses b) corresponding SMSR;

reflectivity, SG with asymmetrical reflectivity and its equivalent BSG. Fig. 4 a) clearly shows that the differences between the characteristics of the equivalent structures are very small. These differences can not be eliminated improving the design because the losses are different due to the slightly different lengths of the SG and BSG structures. In this particular case the power versus current characteristic variations due to the SG peaks non-uniformity is comparable with the loss variation due to plasma effect in the phase region. The symmetrical structure has a low external quantum efficiency and as expected can not compete with the other two.

The same conclusions are valid for the SMSR where the -30 dB value is obtained in both cases at twice the threshold current. The improvement with respect to the SG with symmetrical reflectivity is obvious from Fig. 4 b).

Our numerical program allows also to simulate the coarse and continuous tuning operations. In the first case the current injection is varied only in one grating section while the current in the phase region guarantees the position of the lasing mode on the maximum of the reflectivity product.

In Fig. 5 and Fig. 6 are reported the lasing emission characteristics, for a 50 mA active region current, versus the grating currents with the assumption that positive (negative) currents represent injection in the front (rear) mirror. In Fig. 5, the operating wavelength shows discontinuities due to the lasing mode jumps from one couple of grating peaks to the adjacent. The small differences between the BSG and the SG laser operation wavelengths are mainly due to different losses in the gratings because of the slightly different lengths of the gratings and to the non-uniform spacing of the reflectivity peaks in the SG structure.

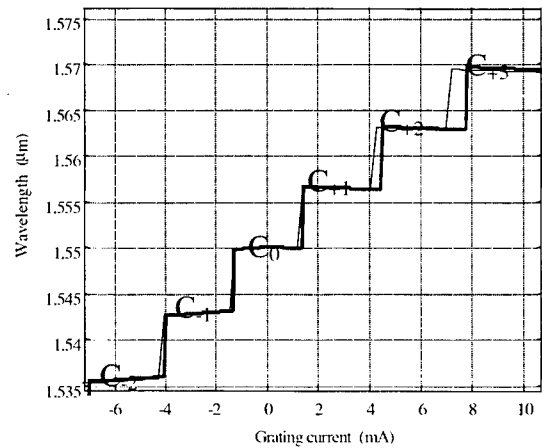


Fig. 5. Coarse tuning for BSG (thin) and equivalent SG (thick); current positive values correspond to injection in the high reflectivity grating while negative to injection in the low reflectivity grating

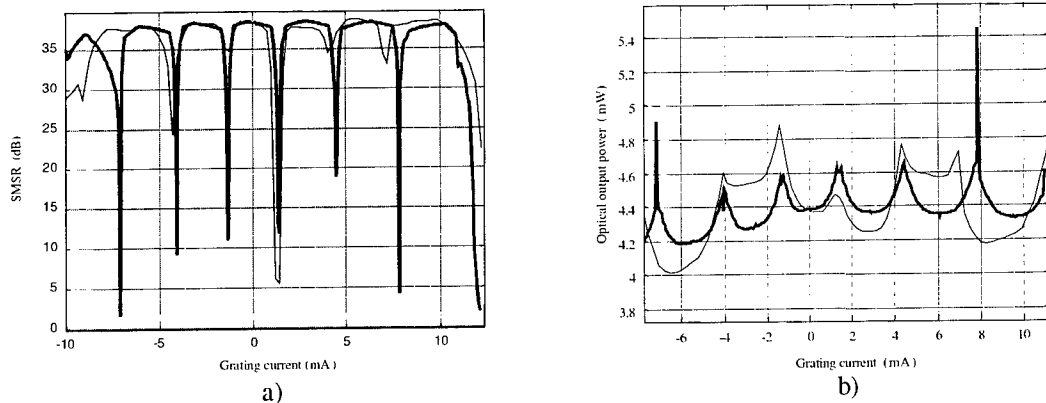


Fig. 6. Coarse tuning: SMSR a) and output power b) for the BSG (thin) and the SG (thick) structures

In Fig. 6 are shown the SMSR and the output optical power for the same operation conditions. The sharp variation in the characteristics occurs at the jump condition of Fig.5.

In Figs. 7-9 we report the laser emission characteristics for the SG (a) and the BSG (b) in the case of continuous tuning operation for 50 mA active region current. The simulator automatically proceeds for all the usable couples of reflectivity peaks, identified with C_i ($i = -2, +3$), to overlap them with a current injection in only one grating and than to move them synchronously with a proper current injection in both gratings; for each couple of grating currents a proper injection in the phase region allows to align the lasing mode to the maximum of the reflectivity product.

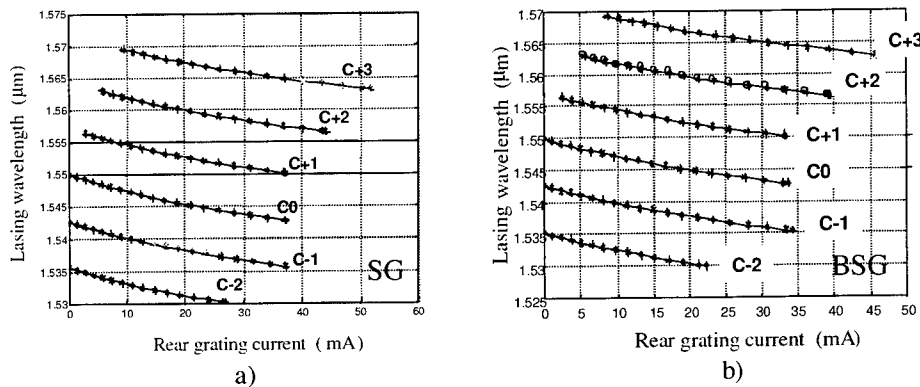


Fig. 7. Continuous tuning: operating wavelength for various peak alignments (C_i), a) SG, b) BSG laser

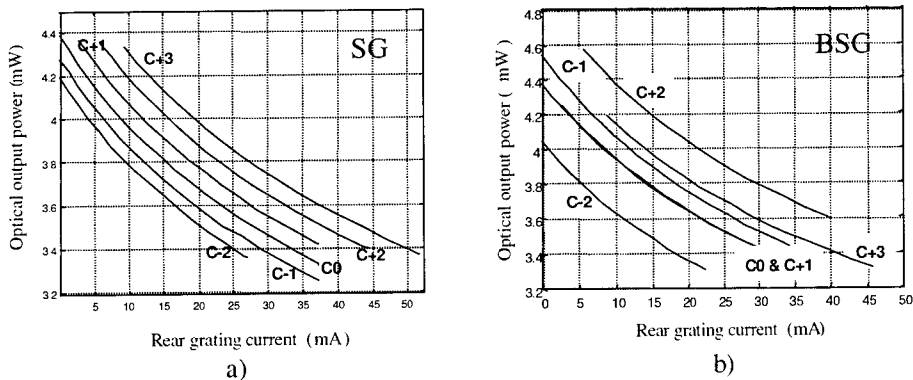


Fig. 8. Continuous tuning: output power for various peak alignments (C_i), a) SG, b) BSG laser

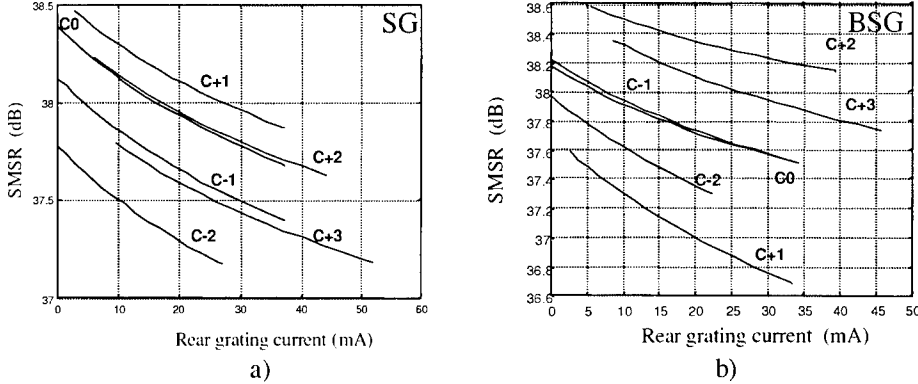


Fig. 9. Continuous tuning: SMSR for various peak alignments (C_i),- a) SG, b) BSG laser

The smooth variation of the lasing wavelength (Fig. 7), of the output power (Fig. 8) and of the SMSR (Fig. 9) is very similar to reported measured data [1,5] and confirm the correctness of the design procedure. The points in the wavelength operation characteristics in Fig. 7 are associated to the possible use of the designed structures in a WDM system with 100 channels spaced of 50 GHz. The maximum power variation of about ± 0.65 mW between the channels for an average power of 4 mW can be attributed to the grating loss changes due to the grating current variation. The SMSR is over 35 dB for all current configurations in both structures as by design specifications.

Finally in Figs. 10-11 the maps of the optical power and of the lasing wavelength are reported when the front and rear grating currents are simultaneously changed; as before the phase current aligns the lasing mode to the maximum of the product reflectivity peak and the active region current is 50 mA.

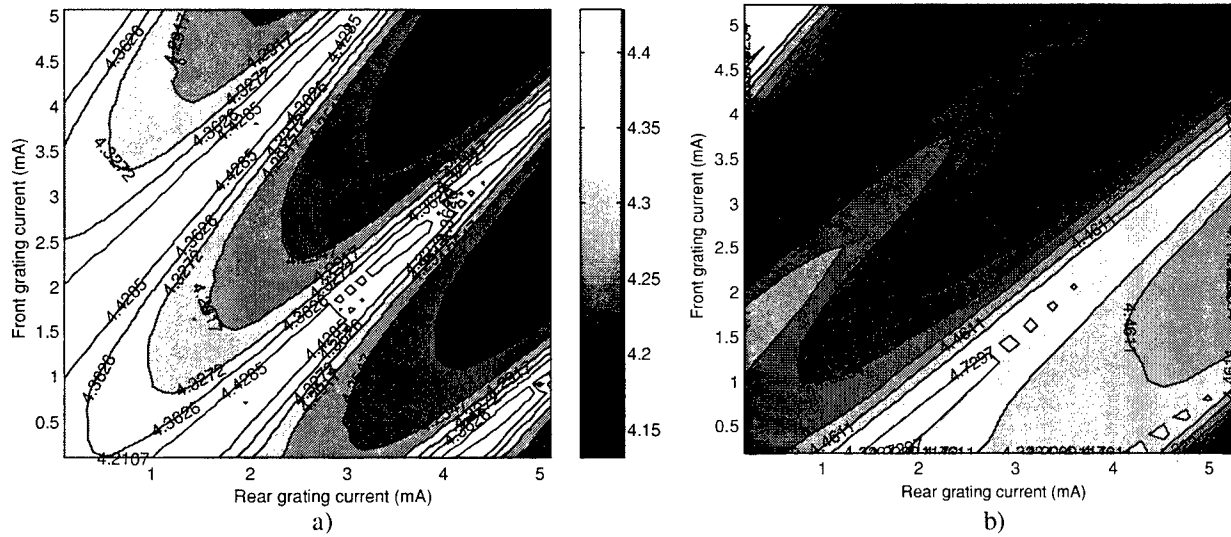


Fig. 10. Optical power maps (mW) vs. grating currents for a) SG and b) BSG laser.
The gray scale is the same for both maps.

The regions of fast variation on all the maps (white regions on the optical power maps) are associated to the mode hopping transition between adjacent peaks (C_i, C_{i+1}).

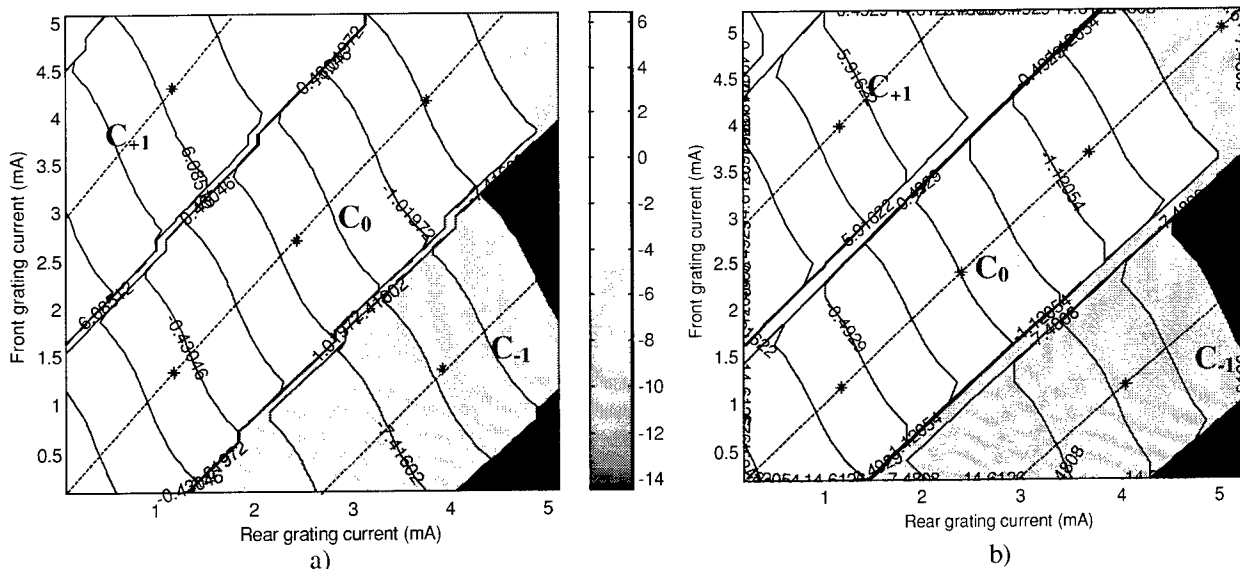


Fig. 11. Lasing wavelength maps (wavelength deviation with respect to 1550 nm) vs. grating currents for a) SG and b) BSG laser. The colour scale is the same for both maps.

The dashed lines in Fig. 11 indicate the maximum SMSR condition and the continuous tuning trajectory in the front-rear grating currents plane; the stars (*) indicate the operating points spaced of 50 GHz.

Conclusions

The goal of this paper was to compare the simulation results obtained for the static lasing characteristics of a BSG and a SG laser cavity designed to have comparable performances. The results reported in literature [4] seem to favor the BSG structure due to the possibility to obtain a flatter profile of the gratings reflection peaks. Our results clearly show that, in the case of a laser with 40 nm of tunability, by properly designing the SG's structure there is no net advantage for the BSG's with respect to the SG's structure. The manufacturing facility becomes than a key factor to make a decision for the structure to choose.

Acknowledgments

This work was done with the support of the CNR (Italian National Research Council) on the framework of “Progetto finalizzato MADESS II”.

References

1. F. Delorme, G. Alibert, C. Ougier, S. Slempkes and H. Nakajima, "Sampled-grating DBR lasers with 101 wavelengths over 44 nm and optimised power variation for WDM applications", *IEE Electronics Letters*, vol.34, nr.3, pp.279-281, 1998.
2. L. A. Coldren, "Multi-Section Tunable Laser with Differing Multi-Element Mirrors", *United States Patent*, Number 4,896,325, January 23, 1990.
3. V. Jayaraman, Z. M. Chuang and L. A. Coldren, "Theory, Design, and Performance of Extended Tuning Range Semiconductor Lasers with Sampled Gratings", *IEEE J.Quantum Electronics*, vol.29, nr.6, pp.1824-1834, 1993.

4. I. A. Avrutsky, D. S. Ellis, A. T. Tager, H. Anis, J. M. Xu, "Design of Widely Tunable Semiconductor Lasers and the Concept of Binary Superimposed Gratings (BSG's)", *IEEE J. Quantum Electronics*, vol.34, nr.4, pp.729-741, 1998.
5. H. Ishii, H. Tanobe, F. Kano, Y. Tohmori, Y. Kondo, Y. Yoshikuni, "Quasicontinuous Wavelength Tuning in-Superstructure-Grating (SSG) DBR Lasers", *IEEE J. Quantum Electronics*, vol.16, nr.3, pp.433-441, 1996.
6. J.C. Lagarias, J.A. Reeds, M.H. Wright, P.E. Wright, "Convergence Properties of the Nelder-Mead Simplex Algorithm in Low Dimensions", *SIAM Journal of Optimization*, vol.9, nr.1, pp.112-147, 1993.
7. K.J. Ebeling, *Integrated Optoelectronics*, Springer Verlag, 1992.
8. H. Ishii, F. Kano, Y. Yoshikuni, H. Yasaka, "Mode Stabilization Method for Superstructure-Grating DBR Lasers", *IEEE J. of Lightwave Technology*, vol.16, nr.3, pp.433-441, 1998.

A Simple Polarization Insensitive Scheme for Four-Wave Mixing Using One Semiconductor Optical Amplifier and Single Pump Source

J.M.Tang and K.A.Shore
University of Wales, Bangor,
School of Electronic Engineering and Computer Systems,
BANGOR, LL57 1UT, UK.
Tel: +44(1248)382618; Fax: +44(1248)361429;
e-mail: alan@sees.bangor.ac.uk

1. Introduction

The major challenges to the utilization of Four-Wave Mixing (FWM) in Semiconductor Optical Amplifiers (SOAs) in practical networks is the strong polarization sensitivity of the mixing processes. Since polarization states of a light wave at a certain position in a real transmission system cannot be readily controlled, polarization insensitive FWM schemes are required. To date, several such schemes have been demonstrated using FWM in SOAs. These include, for example, the polarization diversity technique which requires two SOA devices that independently process two orthogonal polarization states of pump beams [1]. The disadvantage of this technique is that any imbalance of optical gain and relative conversion efficiency of the two converters would cause polarization sensitivity. Another method is the utilization of one SOA device associated with two co- or orthogonally polarized pump waves at different wavelengths [2,3]. However, the wavelength spacing between the pump waves sets a minimum frequency shift, beyond that limit FWM operation also becomes seriously polarization sensitive [4]. All the above mentioned methods employ rather complex configurations involving several optical devices. Also a polarization independent configuration consisting of one SOA and one input pump source has been reported [5], the converter device is, however, a special band-tailored multiquantum-well SOA operating under specific conditions.

To compare the properties of the available polarization insensitive schemes, an analytical lumped model has been published [6]. Unfortunately, the model cannot be used to describe FWM processes involving counter propagating waves.

In this paper, we develop an improved space-averaged model, which is valid for the cases where FWM processes take place between both co- and counter propagating waves. In particular, based on the improved model, a proposal is made of a simple polarization insensitive FWM scheme which employs one conventional polarization insensitive SOA and one input pump source. The presented FWM structure is not only very simple compared with other configurations, but also completely eliminates the minimum frequency shift limitation.

2. Description of The Space-Averaged Model

The generation of a conjugate wave $\hat{E}_{\alpha\beta\gamma}$ at frequency $\omega_\alpha - \omega_\beta + \omega_\gamma$ through third-order nonlinearity of an SOA can be described as in [7]: the nonlinear coupling between the waves $\hat{E}_{\alpha n}$ and $\hat{E}_{\beta n}$ produces population pulsations at a beat frequency $\omega_\alpha - \omega_\beta$, which leads to temporal gain and index gratings. As a result of scattering the wave $\hat{E}_{\gamma n}$ by the gratings, the conjugate wave $\hat{E}_{\alpha\beta\gamma}$ is created. The generated conjugate wave can be written as

$$\hat{E}_{\alpha\beta\gamma} = (\hat{E}_{\alpha n} \cdot \hat{E}_{\beta n}^*) r(\omega_\alpha - \omega_\beta) \hat{E}_{\gamma n} T(\Delta k_{\alpha\beta\gamma} z) e^{i\Delta k_{\alpha\beta\gamma} z} \quad (1)$$

where the strength of the contribution from the nonlinear coupling to the conjugate wave is determined by the complex coupling coefficient $R(\omega_\alpha - \omega_\beta) = r^2(\omega_\alpha - \omega_\beta)$ [8]. The wave number mismatch

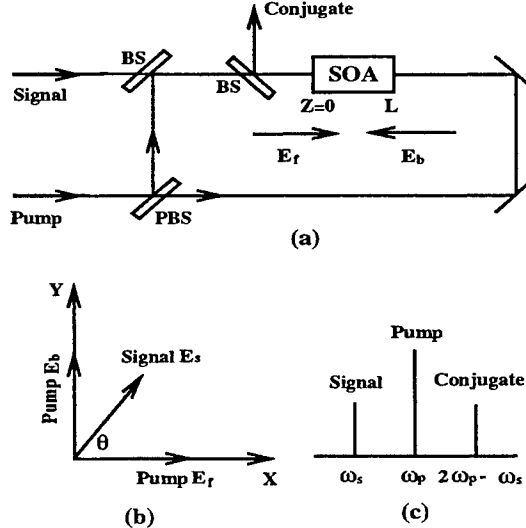


Figure 1: Polarization insensitive FWM scheme: (a) layout,, (b) input states of polarization and (c) output spectrum. PBS: Polarization beam splitter. BS: Beam splitter

$\Delta k_{\alpha\beta\gamma} (= k_{\alpha\beta\gamma} - (k_\alpha - k_\beta + k_\gamma))$ is taken into account in Eq.(1). $k_{\alpha\beta\gamma}$ is the wave number of the conjugate wave. The function, $T(\Delta k_{\alpha\beta\gamma} z)$, having the form of $|\sin(\Delta k_{\alpha\beta\gamma} z/2)/(\Delta k_{\alpha\beta\gamma} z/2)|$ accounts for the influence of wave number mismatch on the conjugate amplitude. The term $e^{i\Delta k_{\alpha\beta\gamma} z}$ associated with the phase terms of mixing waves governs the propagation direction of the conjugate wave. Note that if the group-index dispersion effect is neglected (which is a good approximation for frequency shift less than $\sim 15\text{THz}$ [8]), for a co-propagating wave mixing scheme we have $\Delta k_{\alpha\beta\gamma} = 0$, then $T(\Delta k_{\alpha\beta\gamma} z) = 1$, in which case, Eq.(1) reduces to the form of the previous analytical model [6].

3. The Simple Polarization Insensitive FWM Scheme And Operating Principle

The simple polarization insensitive FWM configuration, is illustrated in Fig.1, which employs only a polarization insensitive SOA and an input pump wave. The injected pump wave is split into two orthogonally polarized beams after passing through the polarizing beam splitter (PBS). The two pump fields are adjusted to collinearly counter-propagate in the SOA. The polarized states of the pump beams are aligned with the TE and TM modes of the SOA, respectively. A collinear signal wave with an arbitrary polarization direction is launched into the front facet of the SOA. Conjugate waves appear at both facets of the SOA. From the front facet, a polarization insensitive conjugate wave can be obtained.

The principle of polarization insensitive operation of the scheme can be analysed by considering the improved model. For simplicity, the forward $\hat{\mathbf{E}}_f$ and backward $\hat{\mathbf{E}}_b$ pump beams at frequency ω_p are assumed to be polarized in the $\hat{\mathbf{x}}$ and $\hat{\mathbf{y}}$ direction respectively, and the signal wave $\hat{\mathbf{E}}_s$ at frequency ω_s is polarized at an arbitrary direction, as shown in Fig.1. The pump and signal waves can thus be written as: $\hat{\mathbf{E}}_f = \hat{\mathbf{x}}\sqrt{P_f}e^{-i(\omega_p t - k_p z)}$, $\hat{\mathbf{E}}_b = \hat{\mathbf{y}}\sqrt{P_b}e^{-i(\omega_p t + k_p z)}$ and $\hat{\mathbf{E}}_s = \hat{\mathbf{e}}_s\sqrt{P_s}e^{-i(\omega_s t - k_s z)}$ ($k_p, k_s > 0$).

Conjugate waves at the frequency $2\omega_p - \omega_s$ can be obtained by using Eq.(1). The conjugate wave generated by co-propagating pump and signal waves is

$$\hat{\mathbf{E}}_{fsf} = \hat{\mathbf{x}}P_f\sqrt{P_s}G_x^{\frac{3}{2}}\cos\theta r(\omega_p - \omega_s)e^{-i[(2\omega_p - \omega_s)t - (2k_p - k_s)z]} \quad (2)$$

As expected, the conjugate wave $\hat{\mathbf{E}}_{fsf}$ is polarization sensitive and travels in $+z$ direction. Meanwhile,

the conjugate waves generated by the counter propagating pump and signal waves travel in both $-z$ and $+z$ directions. The $-z$ direction travelling conjugate waves are

$$\hat{\mathbf{E}}_{fsb} = \hat{\mathbf{y}} \sqrt{P_f P_s P_b} G_x \sqrt{G_y} \cos \theta r (\omega_p - \omega_s) T(\Delta k z) e^{-i[(2\omega_p - \omega_s)t + (k_s - \Delta k)z]} \quad (3)$$

$$\hat{\mathbf{E}}_{bsf} = \hat{\mathbf{x}} \sqrt{P_b P_s P_f} G_y \sqrt{G_x} \sin \theta r (\omega_p - \omega_s) T(\Delta k z) e^{-i[(2\omega_p - \omega_s)t + (k_s - \Delta k)z]} \quad (4)$$

$$\hat{\mathbf{E}}_{bsb} = \hat{\mathbf{y}} P_b \sqrt{P_s} G_y^{\frac{3}{2}} \sin \theta r (\omega_p - \omega_s) T(\Delta k_{bsb} z) e^{-i[(2\omega_p - \omega_s)t + (2k_p + k_s - \Delta k_{bsb})z]} \quad (5)$$

where $\Delta k = \Delta k_{fsb} = \Delta k_{bsf} = 2(k_s - k_p)$, and $\Delta k_{bsb} = 2k_s$. $\Delta k_{bsb} \gg \Delta k$ results in $T(\Delta k_{bsb} L) \ll T(\Delta k L)$, the conjugate wave $\hat{\mathbf{E}}_{bsb}$ can therefore be neglected. If the SOA's gain is polarization insensitive, $G_x = G_y = G$, then the output conjugate power at the front facet is

$$P_c = P_f P_s P_b G^3 R(\omega_p - \omega_s) T^2(\Delta k L) \quad (6)$$

Eq.(6) demonstrates that the output conjugate power from the front facet of the SOA in the present configuration is polarization independent. It can be clearly seen from Eq.(6) that if the condition $\Delta k L \ll 2\pi$ is fulfilled, the wave number mismatch effect would not seriously reduce the output conjugate power. For a conventional SOA based on InGaAsP material operating at a wavelength of $1.55\mu\text{m}$, an SOA of length $100\mu\text{m}$ would allow frequency shift as large as $\sim 1\text{THz}$. Note that the $+z$ direction travelling conjugate waves generated by counter propagating waves can be neglected due to larger mismatch effect. Such operating characteristics make the present scheme attractive for experimental evaluation.

4. Conclusions

The significant advantages of the polarization insensitive FWM scheme presented here is the use of an extremely simple structure. Furthermore, the FWM scheme involving two pump beams at the same wavelength would completely eliminate the minimum limitation to the frequency shift which exists in two non-zero wavelength spaced pump structures. In addition, the proposed polarization insensitive FWM scheme here would be also valid for FWM of optical pulses. By using optical pulses, in particular, FWM conversion efficiency can be significantly enhanced [9].

Acknowledgements

This work was supported by EPSRC under grant GR/L03262. J.M.Tang is supported by the Professor Wynn Humphrey Davies Scholarship and the School of Electronic Engineering and Computer Systems, University of Wales, Bangor, UK.

References

- 1 J.P.R.Lacey, et al., *IEEE Photon. Technol. Lett.*, Vol.9, p.1355, 1997.
- 2 R.Schnabel, U.Hilbk, et al., *IEEE Photon. Technol. Lett.*, Vol.6, p.56, 1994.
- 3 R.M.Jopson and R.E.Tench, *Electron. Lett.*, Vol.29, p.2216, 1993.
- 4 I.Zacharopoulos, I.Tomkos, et al., *IEEE Photon. Technol. Lett.*, Vol.10, p.352, 1998.
- 5 K.Ovsthus and V.Khalfin, et al., *IEEE Photon. Technol. Lett.*, Vol.8, p.527, 1996.
- 6 J.P.R.Lacey, et al., *IEEE J. Lightwave Technol.*, Vol.16, p.2419, 1998.
- 7 G.P.Agrawal, *J. Opt.Soc.Am.B*, Vol.5, p.147, 1988.
- 8 A.Uskov, J.Mørk, and J.Mark, *IEEE J. Quantum Electron.*, Vol.30, p.1769, 1994.
- 9 J.M.Tang and K.A.Shore, *IEEE Photon. Technol. Lett.*, Vol.10, p.1563, 1998.

How to Have Narrow-Stripe Semiconductor Lasers Self-Pulsate

Shahram M. Shahruz

Berkeley Engineering Research Institute, P. O. Box 9984, Berkeley, CA 94709

Abstract: The rate equations of narrow-stripe semiconductor lasers are considered. These equations represent the dynamics of the photon number and the electron densities in the active and absorbing regions. Having the rate equations, (i) it is shown that the laser is the bounded-input bounded-state (BIBS) and the bounded-input bounded-output (BIBO) stable; (ii) the amplitudes of step inputs are determined for which all equilibrium points of the laser are unstable. The boundedness of the laser output and the instability of its equilibrium points imply that the laser can have a periodic, a quasi-periodic, or a chaotic output. When the output is periodic, the laser is self-pulsating, which is the desirable behavior of the laser. Moreover, a procedure is given to determine the values of laser parameters for which the laser self-pulsates.

OCIS code: (140.5960) Semiconductor lasers

1. Introduction

Due to their short coherence length, self-pulsating lasers reduce the effect of the mode hopping noise and the optical feedback noise [5], [9-11], as well as the modal noise in multimode fiber links [6]. This property makes self-pulsating lasers useful light sources when optical coherence is undesirable; for instance, in compact disk and video disk players, multimode fiber communication networks, and optical interconnects. Due to their usefulness, different types of self-pulsating lasers have been studied by researchers; see, e.g., [3], [5-11], and the references therein.

From the point of view of dynamical systems, a laser is essentially a nonlinear system. From this point of view, a self-pulsating laser, whose output is a periodic train of pulses, is nothing but a nonlinear system with the limit-cycle behavior. The occurrence of self-pulsation depends on the values of laser parameters and the amplitudes of applied step inputs (biases). It is desirable to know for what values of parameters and input amplitudes a laser can self-pulsate, i.e., can have the limit-cycle behavior.

A novel, systematic, and easy-to-apply procedure for making lasers self-pulsate is given in [7]. The procedure in [7] is quite general and can be applied to different types of lasers. In order to apply this procedure, it is necessary to have the rate equations representing the laser dynamics. Having the rate equations, two steps should be taken: (i) the bounded-input bounded-state (BIBS) stability and the bounded-input bounded-output (BIBO) stability of the laser should be established; (ii) values of laser parameters and input amplitudes, which render all equilibrium points of the laser unstable, should be determined. The boundedness of the laser output and the instability of its equilibrium points imply that the laser can have a periodic, a quasi-periodic, or a chaotic output. When the output is periodic, the laser is self-pulsating.

In this paper, we use the procedure proposed in [7] to systematically determine the values of laser parameters and the amplitudes of step inputs which make narrow-stripe semiconductor lasers self-pulsate.

The organization of the paper is as follows. In Section 2, we briefly describe the rate equations (mathematical model) representing the dynamics of narrow-stripe semiconductor lasers. In Section 3, we present a preliminary result regarding the rate equations. In Section 4, we first establish the BIBS stability and the BIBO stability of the laser. Then, we describe how to choose the laser parameters and the input amplitudes that destabilize all equilibrium points of the laser with non-negative coordinates. In Section 5, we present a specific example to illustrate the procedure of making narrow-stripe semiconductor lasers self-pulsate.

2. Dynamics of Narrow-Stripe Semiconductor Lasers

Narrow-stripe semiconductor lasers are typically represented by the following set of nonlinear ordinary differential equations, known as the rate equations (see, e.g., [10]):

$$\dot{S}(t) = \left[a_1 \xi_1 [N_1(t) - N_{g_1}] + a_2 \xi_2 [N_2(t) - N_{g_2}] - G_{th} \right] S(t) + \left(\frac{C V_1}{T_s} \right) N_1(t),$$

$$S(0) =: S_0 > 0, \quad (1a)$$

$$\dot{N}_1(t) = - \left(\frac{a_1 \xi_1}{V_1} \right) [N_1(t) - N_{g_1}] S(t) - \left(\frac{1}{T_s} + \frac{1}{T_{12}} \right) N_1(t) + \frac{N_2(t)}{T_{12}} + \frac{I}{e V_1},$$

$$N_1(0) =: N_{10} > 0, \quad (1b)$$

$$\dot{N}_2(t) = - \left(\frac{a_2 \xi_2}{V_2} \right) [N_2(t) - N_{g_2}] S(t) + \frac{N_1(t)}{T_{21}} - \left(\frac{1}{T_s} + \frac{1}{T_{21}} \right) N_2(t),$$

$$N_2(0) =: N_{20} > 0, \quad (1c)$$

for all $t \geq 0$. In (1), the state $S(\cdot)$ denotes the photon numbers, and the states $N_1(\cdot)$ and $N_2(\cdot)$ denote, respectively, the electron densities in the active and absorbing regions; S_0 , N_{10} , and N_{20} are the initial conditions of the states; $a_1 > 0$ and $a_2 > 0$ are, respectively, the slopes of the linear approximations of the gain characteristic in the active and absorbing regions; $\xi_1 > 0$ and $\xi_2 > 0$ are, respectively, the distribution ratios of the optical power in the active and absorbing regions; $N_{g_1} > 0$ and $N_{g_2} > 0$ are, respectively, the transparent levels of the electron densities in the active and absorbing regions; $G_{th} > 0$ is the threshold gain level; $C > 0$ is the spontaneous emission coefficient which gives coupling rate between the spontaneous field and the lasing mode; $V_1 > 0$ and $V_2 > 0$ are, respectively, the volumes of the active and absorbing regions; $T_s > 0$ is the electron life time due to the spontaneous emission; $T_{12} > 0$ (respectively, $T_{21} > 0$) denotes the time constant that characterizes the electron diffusion from the active region (absorbing regions) to the absorbing regions (active region); $I > 0$ denotes the amplitude of the applied step input (constant current); $e = 1.602 \times 10^{-19}$ is the electronic charge.

The values of laser parameters are carefully evaluated in [10]. It turns out that some of the laser parameters satisfy certain relations; for instance,

$$T_{21} = \frac{V_2}{V_1} T_{12}, \quad (2)$$

which will be used in the paper.

The desired behavior of the laser is self-pulsation, i.e., when the output of the laser is a periodic train of pulses. The self-pulsation depends crucially on the values of laser parameters and the amplitudes of step inputs. Thus, an important problem of practical interest is the following:

Problem I: Determine the values of laser parameters and the amplitudes of applied step inputs for which the laser represented by the system (1) self-pulsates. \square

In this paper, we give a systematic solution to Problem I.

3. A Close Look at the Laser Dynamics

In this section, we present an important and useful result regarding the dynamics of the laser represented by the system (1). This result will be used repeatedly in the paper.

The state space of the system (1) is \mathbb{R}^3 . Let the state vector of the system (1) be denoted by $X(t) := [S(t) \ N_1(t) \ N_2(t)]^T \in \mathbb{R}^3$ for all $t \geq 0$. Let the solution of the system starting at $t = 0$ from the initial vector $X_0 := X(0) = [S_0 \ N_{10} \ N_{20}]^T$ be denoted by the vector $X(t, 0, X_0)$ for all

$t \geq 0$.

The important result to be established is that the nonnegative orthant \mathbb{R}_+^3 is an invariant set of the system (1). That is, if the system starts from *any* initial vector in \mathbb{R}_+^3 , then its solution vector will remain in \mathbb{R}_+^3 .

Lemma 3.1: The nonnegative orthant \mathbb{R}_+^3 is an invariant set of the system (1).

Proof: First, we consider the subspace

$$\Sigma_S := \{ (S, N_1, N_2) \in \mathbb{R}^3 \mid S = 0 \}. \quad (3)$$

From (1a), we conclude that for any point in this subspace, $\dot{S}(t) \geq 0$ for all $t \geq 0$ if $N_1(t) \geq 0$.

Next, we consider the subspace

$$\Sigma_{N_1} := \{ (S, N_1, N_2) \in \mathbb{R}^3 \mid N_1 = 0 \}. \quad (4)$$

From (1b), we conclude that for any point in this subspace, $\dot{N}_1(t) > 0$ for all $t \geq 0$ if $S(t) \geq 0$ and $N_2(t) \geq 0$.

Finally, we consider the subspace

$$\Sigma_{N_2} := \{ (S, N_1, N_2) \in \mathbb{R}^3 \mid N_2 = 0 \}. \quad (5)$$

From (1c), we conclude that for any point in this subspace, $\dot{N}_2(t) \geq 0$ for all $t \geq 0$ if $S(t) \geq 0$ and $N_1(t) \geq 0$.

Knowing these properties of Σ_S , Σ_{N_1} , and Σ_{N_2} , we conclude that any trajectory of the system (1) starting in \mathbb{R}_+^3 cannot traverse into regions of \mathbb{R}^3 for which $S < 0$ or $N_1 < 0$ or $N_2 < 0$. \square

Remark: The invariance of \mathbb{R}_+^3 confirms the validity of the system (1) as a mathematical model for narrow-stripe semiconductor lasers to the extent that it does not predict negative values for the states $S_1(\cdot)$, $N_1(\cdot)$, and $N_2(\cdot)$. Note that from the physical point of view, it is meaningless to have negative values for the photon number S and the electron densities N_1 and N_2 . \square

4. Self-Pulsation

In this section, we present a solution to Problem I by achieving the following:

(i) We show that the states $S(\cdot)$, $N_1(\cdot)$, and $N_2(\cdot)$ of the system (1) are bounded. That is, the system (1) is the BIBS stable, and so is the BIBO stable, because $S(\cdot)$ is the system output.

(ii) We present a systematic procedure for choosing the values of some of the laser parameters and the input amplitudes for which all equilibrium points of the system (1) in \mathbb{R}_+^3 are unstable, and hence no constant steady-state output is achieved.

Note that (i) by itself is an interesting and important result. This result shows an inherent property of narrow-stripe semiconductor lasers that their outputs are bounded. By (i) and (ii), the laser has a chance to have a bounded and time-varying output, which can be a periodic train of pulses – the desirable output expected from the laser. Note that by (i) and (ii), there is a possibility of having quasi-periodic or chaotic outputs. The study of such outputs, however, is beyond the scope of this paper. In our study of the system (1), however, we did not observe such outputs.

4.1. BIBS (and BIBO) Stability

In this section, we prove the BIBS (and BIBO) stability of the system (1) by obtaining upper bounds on the norms of the system states and output. In the following, the L_∞ -norm of functions of time defined by $\|f\|_\infty := \sup_{t \geq 0} |f(t)|$ for a function $t \mapsto f(t)$ is used. A function $f(\cdot)$ is said to be bounded (more precisely L_∞ -bounded) when $|f(t)| < \infty$ for all $t \geq 0$, which implies that $\|f\|_\infty < \infty$.

The upper bounds on the system states and output are given in the following theorem.

Theorem 4.1: The states and output of the system (1) are bounded. More precisely,

$$\|S\|_{\infty} \leq S_0 + V_1 N_{10} + V_2 N_{20} + \frac{I}{e \min \{ G_{th}, (1-C)/T_s \}} , \quad (6a)$$

$$\|N_1\|_{\infty} \leq \left(\frac{1}{V_1} \right) [S_0 + V_1 N_{10} + V_2 N_{20} + \frac{I}{e \min \{ G_{th}, (1-C)/T_s \}}] , \quad (6b)$$

$$\|N_2\|_{\infty} \leq \left(\frac{1}{V_2} \right) [S_0 + V_1 N_{10} + V_2 N_{20} + \frac{I}{e \min \{ G_{th}, (1-C)/T_s \}}] . \quad (6c)$$

Proof: We define a scalar-valued function of time as

$$V(t) := S(t) + V_1 N_1(t) + V_2 N_2(t) , \quad (7)$$

for all $t \geq 0$, where $S(\cdot)$, $N_1(\cdot)$, and $N_2(\cdot)$ satisfy (1). By Lemma 3.1, $V(t) \geq 0$ for all $t \geq 0$. At $t = 0$

$$V(0) := S_0 + V_1 N_{10} + V_2 N_{20} > 0 . \quad (8)$$

From (7), we obtain

$$\dot{V}(t) := \dot{S}(t) + V_1 \dot{N}_1(t) + V_2 \dot{N}_2(t) , \quad (9)$$

for all $t \geq 0$. Using (1) and (2) in (9), we can obtain the linear differential inequality

$$\dot{V}(t) \leq -\xi V(t) + \frac{I}{e} , \quad (10)$$

for all $t \geq 0$, where $\xi := \min \{ G_{th}, (1-C)/T_s \}$. By a comparison theorem given in [1], we conclude that $V(\cdot)$ in (10) satisfies

$$V(t) \leq \exp(-\xi t) V(0) + \left(\frac{I}{e \xi} \right) [1 - \exp(-\xi t)] , \quad (11)$$

for all $t \geq 0$. Using (8) in (11), we obtain

$$\|V\|_{\infty} \leq S_0 + V_1 N_{10} + V_2 N_{20} + \frac{I}{e \xi} < \infty . \quad (12)$$

Having $V(\cdot)$ a bounded function of time, the boundedness of the states follows. Since the system states are nonnegative, from (7) we conclude that $S(t) \leq V(t)$ for all $t \geq 0$. Thus, (6a) holds for the state $S(\cdot)$ which is the laser output as well. The upper bounds on $\|N_1\|_{\infty}$ and $\|N_2\|_{\infty}$ in (6) are obtained similarly. \square

To this end, we have established the BIBS (and BIBO) stability of the system (1).

4.2. Destabilization of Equilibrium Points

The input to the system (1) is a step function (constant current) of amplitude I . Thus, the steady-state output of the system can possibly be a constant function of time when an equilibrium point of the system in \mathbb{R}_+^3 is either locally or globally stable. This output, however, is not desirable if the laser is supposed to self-pulsate. Therefore, in order to guarantee that no constant steady-state output is achieved, all equilibrium points of the system (1) in \mathbb{R}_+^3 should be destabilized. The next task is thus to determine where the equilibrium points are.

Lemma 4.2: Let

$$A_1 := \frac{a_1 \xi_1 (1 - C)}{T_s G_{th}}, \quad (13a)$$

$$B_1 := \frac{a_1 \xi_1 V_2}{T_s G_{th} V_1}, \quad (13b)$$

$$D_1 := -\left(\frac{a_1 \xi_1 I}{V_1 e G_{th}} + \frac{a_1 \xi_1 N_{g_1} (1 - C)}{T_s G_{th}} + \frac{1}{T_s} + \frac{1}{T_{12}} \right), \quad (13c)$$

$$E_1 := \frac{1}{T_{12}} - \frac{a_1 \xi_1 N_{g_1} V_2}{T_s G_{th} V_1}, \quad (13d)$$

$$F_1 := \frac{a_1 \xi_1 N_{g_1} I}{V_1 e G_{th}} + \frac{I}{e V_1}, \quad (13e)$$

$$B_2 := \frac{a_2 \xi_2 V_1 (1 - C)}{T_s G_{th} V_2}, \quad (14a)$$

$$C_2 := \frac{a_2 \xi_2}{T_s G_{th}}, \quad (14b)$$

$$D_2 := -\left(\frac{a_2 \xi_2 I}{V_2 e G_{th}} + \frac{a_2 \xi_2 N_{g_2}}{T_s G_{th}} + \frac{1}{T_s} + \frac{1}{T_{21}} \right), \quad (14c)$$

$$E_2 := \frac{1}{T_{21}} - \frac{a_2 \xi_2 N_{g_2} V_1 (1 - C)}{T_s G_{th} V_2}, \quad (14d)$$

$$F_2 := \frac{a_2 \xi_2 N_{g_2} I}{V_2 e G_{th}}. \quad (14e)$$

Consider the polynomial

$$P(x) = p_3 x^3 + p_2 x^2 + p_1 x + p_0, \quad (15)$$

with the real coefficients

$$p_3 = A_1 C_2 D_1 - A_1 (B_1 E_2 + B_2 E_1) + B_1^2 D_2, \quad (16a)$$

$$p_2 = C_2 D_1^2 + A_1 C_2 F_1 - (B_1 E_2 + B_2 E_1) D_1 - A_1 E_1 E_2 + 2 B_1 D_2 E_1 + B_1^2 F_2, \quad (16b)$$

$$p_1 = 2 C_2 D_1 F_1 - (B_1 E_2 + B_2 E_1) F_1 - D_1 E_1 E_2 + D_2 E_1^2 + 2 B_1 E_1 F_2, \quad (16c)$$

$$p_0 = C_2 F_1^2 - E_1 E_2 F_1 + E_1^2 F_2. \quad (16d)$$

The system (1) has equilibrium points at

$$X_e = (S_e, N_{1e}, N_{2e}), \quad (17)$$

where N_{1e} is the real solution of the polynomial equation

$$P(N_{1e}) = 0, \quad (18)$$

and

$$N_{2e} = -\frac{A_1 (N_{1e})^2 + D_1 N_{1e} + F_1}{B_1 N_{1e} + E_1}, \quad (19)$$

$$S_e = - \left[\frac{V_1 (1 - C)}{T_s G_{th}} \right] N_{1e} - \left(\frac{V_2}{T_s G_{th}} \right) N_{2e} + \frac{I}{e G_{th}}. \quad (20)$$

Proof: See Appendix. \square

Note that the polynomial equation in (18) can have up to three real solutions for N_{1e} . That is, there can be up to three equilibrium points X_e for the system (1). The equilibrium points, to which attention must be paid, are those in \mathbb{R}_+^3 . Firstly, because by Lemma 3.1, an $X_e \notin \mathbb{R}_+^3$ (even stable) cannot be attained. Secondly and more importantly, because an $X_e \in \mathbb{R}_+^3$ may prevent the laser from self-pulsating: Suppose that there is an $X_e \in \mathbb{R}_+^3$. If this equilibrium point is globally (respectively, locally) stable, then trajectories of the system (1) are (can possibly be) attracted to it. In this case, the steady-state output of the laser is a *constant* equal to $S_e \geq 0$. This output is certainly undesirable if the laser is supposed to self-pulsate, i.e., if the laser output should be a periodic train of pulses.

By the above argument, we conclude that the key to self-pulsation is the destabilization of every possible equilibrium point $X_e \in \mathbb{R}_+^3$ of the system (1) by appropriate choices of the laser parameters and the input amplitudes. When all $X_e \in \mathbb{R}_+^3$ are unstable, trajectories of the system (1) are repelled by them. On the other hand, by the boundedness result, the system states and output do not blow up. Thus, the system has no choice but having a time-varying output that can never settle to a constant value. When this time-varying output of the laser is periodic, the laser is self-pulsating.

The stability of an equilibrium point X_e is decided upon locally by the coefficient matrix of the linearized model of the system (1) around X_e , namely, the Jacobian matrix. This matrix is

$$J(X_e) = \begin{bmatrix} a_1 \xi_1 (N_{1e} - N_{g_1}) + a_2 \xi_2 (N_{2e} - N_{g_2}) - G_{th} & a_1 \xi_1 S_e + \frac{C V_1}{T_s} & a_2 \xi_2 S_e \\ -\left(\frac{a_1 \xi_1}{V_1}\right) (N_{1e} - N_{g_1}) & -\left(\frac{a_1 \xi_1}{V_1}\right) S_e - \left(\frac{1}{T_s} + \frac{1}{T_{12}}\right) & \frac{1}{T_{12}} \\ -\left(\frac{a_2 \xi_2}{V_2}\right) (N_{2e} - N_{g_2}) & \frac{1}{T_{21}} & -\left(\frac{a_2 \xi_2}{V_2}\right) S_e - \left(\frac{1}{T_s} + \frac{1}{T_{21}}\right) \end{bmatrix}, \quad (21)$$

where N_{1e} , N_{2e} , and S_e are given in (18), (19), and (20), respectively. From (18)-(20), it is clear that the eigenvalues of $J(X_e)$, and consequently the local stability of X_e , depend on the values of laser parameters and the input amplitude I . Having the matrix $J(X_e)$, we can systematically determine the laser parameters and the input amplitude I that make the system (1) self-pulsate.

Suppose that the laser parameters are known fixed values and a set of values of input amplitudes I is sought for which the laser would self-pulsate. Such a set of I can be determined conveniently by the following algorithm.

Algorithm 4.3: (Input Amplitudes for Self-Pulsation)

- (i) For an I compute X_e from (18)-(20);
- (ii) Use (21) to compute the eigenvalues of $J(X_e)$ at every $X_e \in \mathbb{R}_+^3$;
- (iii) Vary (increase and decrease) I by a small increment and repeat steps (i) and (ii). For every $X_e \in \mathbb{R}_+^3$ plot the loci of the eigenvalues of $J(X_e)$ as a function of I in the complex plane;
- (iv) From the loci obtained in step (iii) determine a set of input amplitudes I , such that for every I in this set the matrix $J(X_e)$ is not Hurwitz (i.e., some eigenvalues of $J(X_e)$ have positive real parts) at every $X_e \in \mathbb{R}_+^3$; denote this set by S_I . \square

Remarks: 1) The set S_I can be the union of disjoint sets.

2) The input amplitudes (currents) $I \in S_I$ should be physically reasonable. Thus, for instance, very large values of I that make the laser self-pulsate are not acceptable. If it turns out that the laser can self-pulsate only

for large values of I , then its parameters should be changed by a redesign, so that the self-pulsation occurs for reasonable values of I .

3) If the set S_I turns out to be an empty set, then the laser parameters should be changed by a redesign, so that for the new set of parameters there will be some I that will make the laser self-pulsate. \square

Now suppose that for a known set of laser parameters and an input amplitude I the laser self-pulsates. Let the values of any two parameters δ_1 and δ_2 in this set be δ_1^* and δ_2^* , respectively. Suppose that a set of values of δ_1 and δ_2 is sought for which the laser would self-pulsate. Such a set can be determined by the following algorithm.

Algorithm 4.4: (Parameters for Self-Pulsation)

(i) Let

$$\delta_1 = \delta_1^* + r \cos \theta, \quad \delta_2 = \delta_2^* + r \sin \theta, \quad (22)$$

where $r > 0$ is to be determined for different values of $\theta \in [0, 2\pi]$.

- (ii) Set $\theta = 0$;
- (iii) Set $r = 0$;
- (iv) For δ_1 and δ_2 in (22) compute X_e from (18)-(20);
- (v) Using (21) compute the eigenvalues of $J(X_e)$ at every $X_e \in \mathbb{R}_+^3$;
- (vi) Increase r by a small increment and repeat steps (iv) and (v). For every $X_e \in \mathbb{R}_+^3$ plot the loci of the eigenvalues of $J(X_e)$ as a function r in the complex plane;
- (vii) From the loci obtained in step (vi) determine an interval $[0, \bar{r}]$ such that for every $r \in [0, \bar{r}]$ the matrix $J(X_e)$ is not Hurwitz at every $X_e \in \mathbb{R}_+^3$;
- (viii) Increase θ by a small incremental and go to step (iii) and repeat up to $\theta = 2\pi - \varepsilon$, where $\varepsilon > 0$ is a small number.
- (ix) Consider those $\theta \in [0, 2\pi]$ at which \bar{r} has been computed. At those θ draw a ray of length \bar{r} . Connect the end points of the rays to obtain the set of parameters δ_1 and δ_2 for which the laser self-pulsates; denote this set by S_p . \square

Remark: For a fixed θ , step (vii) of Algorithm 4.4 provides an interval $[0, \bar{r}]$ such that for every $r \in [0, \bar{r}]$ the matrix $J(X_e)$ is not Hurwitz at every $X_e \in \mathbb{R}_+^3$, where X_e is computed for the parameters δ_1 and δ_2 in (22). In computing $[0, \bar{r}]$, Algorithm 4.4 does not take into account any physical constraints on δ_1 and δ_2 . Thus, an interval $[0, \bar{r}]$ can be computed such that for some r in it, δ_1 and δ_2 are physically unrealizable. This can happen, for instance, when a large \bar{r} is computed. Therefore, physical constraints should be considered in computing \bar{r} . Such constraints result in reasonable values for \bar{r} , δ_1 , and δ_2 , and can reduce the computational effort significantly. \square

Algorithms 4.3 and 4.4 will be used in an example given next.

5. Example

Consider the narrow-stripe semiconductor laser represented by (1) whose parameters are

$$a_1 = 3.08 \times 10^{-12} \text{ m}^3 \text{ sec}^{-1}, \quad a_2 = 1.5 \times 10^{-11} \text{ m}^3 \text{ sec}^{-1}, \quad (23a)$$

$$\xi_1 = 0.0948, \quad \xi_2 = 0.35, \quad (23b)$$

$$N_{g_1} = 1.4 \times 10^{24} \text{ m}^{-3}, \quad N_{g_2} = 1.6 \times 10^{24} \text{ m}^{-3}, \quad (23c)$$

$$G_{th} = 3.91 \times 10^{11} \text{ sec}^{-1}, \quad (23d)$$

$$C = 1.1 \times 10^{-5} \text{ m}^{-3}, \quad (23e)$$

$$V_1 = 48 \times 10^{-18} \text{ m}^3, \quad V_2 = 419.04 \times 10^{-18} \text{ m}^3, \quad (23f)$$

$$T_s = 3 \times 10^{-9} \text{ sec}, \quad T_{12} = 1.176 \times 10^{-9} \text{ sec}, \quad T_{21} = 10.2664 \times 10^{-9} \text{ sec}. \quad (23g)$$

Most of the values of parameters are given in [10]. Some parameters are not given explicitly, however, they can be easily computed using the information in [10]. The values of a_2 and ξ_2 in (23) are slightly different from those in [10].

First, by Algorithm 4.3, we determine a set of values of the input amplitudes I for which the laser would self-pulsate. In using this algorithm, we find out that for any $I \in (0.0475, 0.2) \text{ amp}$, there is only one equilibrium point $X_e \in \mathbb{R}_+^3$. The loci of the eigenvalues of the matrix $J(X_e)$ in (21) as a function of I are plotted in Figure 1. In this figure, we have designated points by π_1 and π_2 at which $I = 0.0475 \text{ amp}$ and $I = 0.1219 \text{ amp}$, respectively. Clearly, for any $I \in S_I = (0.0475, 0.1219) \text{ amp}$, the matrix $J(X_e)$ is not Hurwitz and hence the laser self-pulsates. We simulated the system (1) for $I = 0.1 \text{ amp}$ for a long period of time. The laser output $S(\cdot)$ is plotted in Figure 2. From this figure, it is evident that the laser output is a periodic train of pulses, i.e., the laser is self-pulsating.

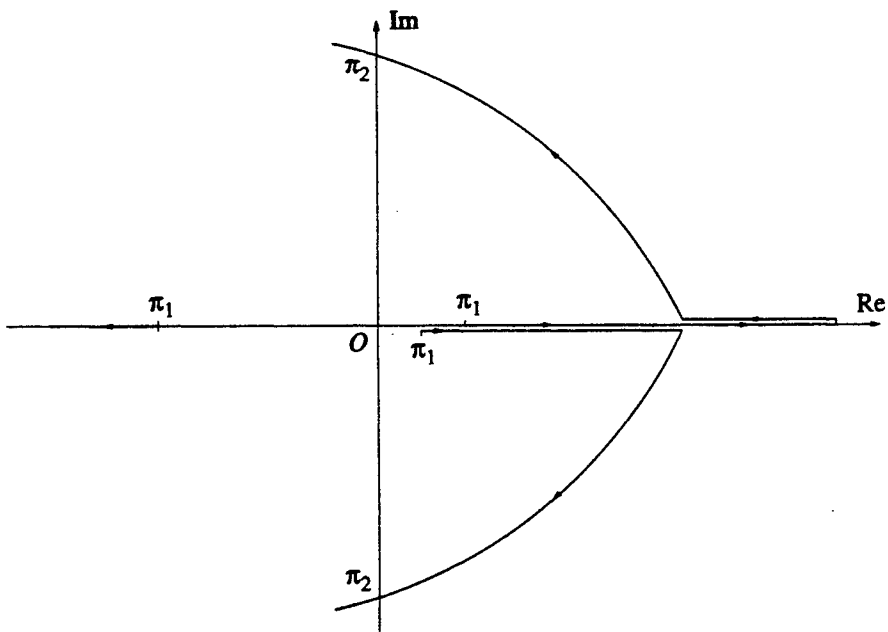


Figure 1. The loci of the eigenvalues of the matrix $J(X_e)$ in (21) as a function of the input amplitude I . For any $I \in S_I = (0.0475, 0.1219) \text{ amp}$, the matrix $J(X_e)$ is not Hurwitz and hence the laser self-pulsates.

Next, we fix $I = 0.1 \text{ amp}$ and by Algorithm 4.4 determine a set of values of ξ_1 and ξ_2 for which the laser would self-pulsate. In using this algorithm, we set $\xi_1^* = 0.0948$ and $\xi_2^* = 0.35$. We determine the interval $[0, \bar{r})$ in step (vii) of Algorithm 4.4 for $\theta = 0, 5, 10, \dots, 355 \text{ degrees}$. There are physical constraints $0 < \xi_1 < 1$ and $0 < \xi_2 < 1$ (see [10]) that we take into account to truncate the computation when these constraints are violated.

Having \bar{r} computed for $\theta = 0, 5, 10, \dots, 355 \text{ degrees}$, we can plot the set of parameters ξ_1 and ξ_2 for which the laser self-pulsates in the parameter space (ξ_1, ξ_2) . This set is shown in Figure 3. It turns out that for θ in the interval $[75, 95] \text{ degrees}$, \bar{r} is very large which results in $\xi_2 > 1$. Thus, we have truncated the set of parameters at $\xi_2 = 1$ for $\theta \in [75, 95] \text{ degrees}$. Note that the set in Figure 3 can be refined if \bar{r} is computed for more values of θ .

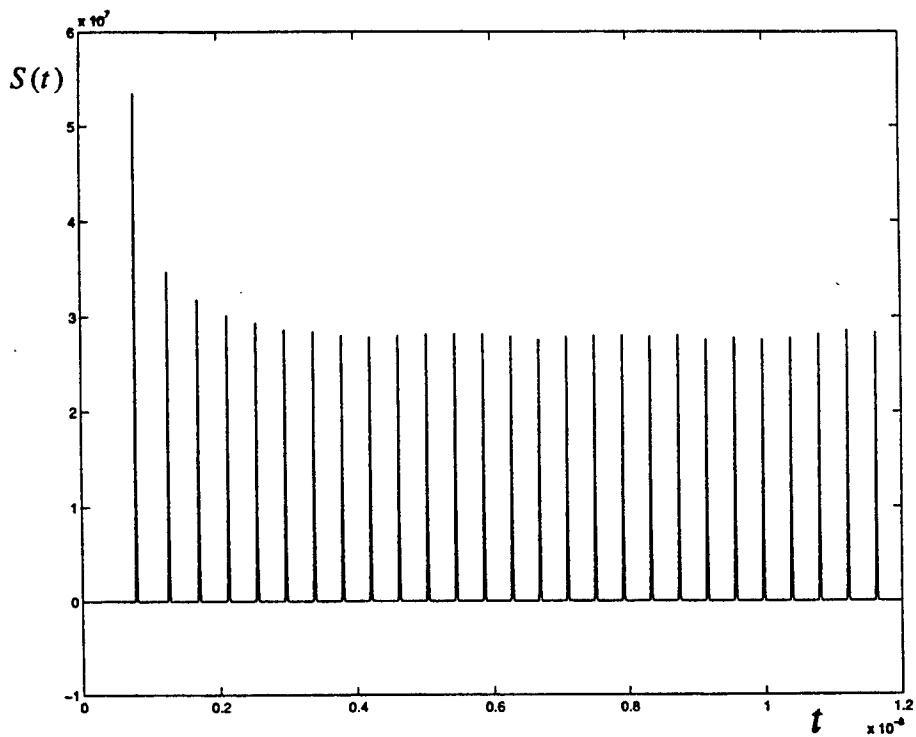


Figure 2. The output of the laser represented by the system (1) and (23) for a step input of amplitude $I = 0.1 \text{ amp}$ for a long period of time. It is evident that the output is a train of pulses, i.e., the laser is self-pulsating.

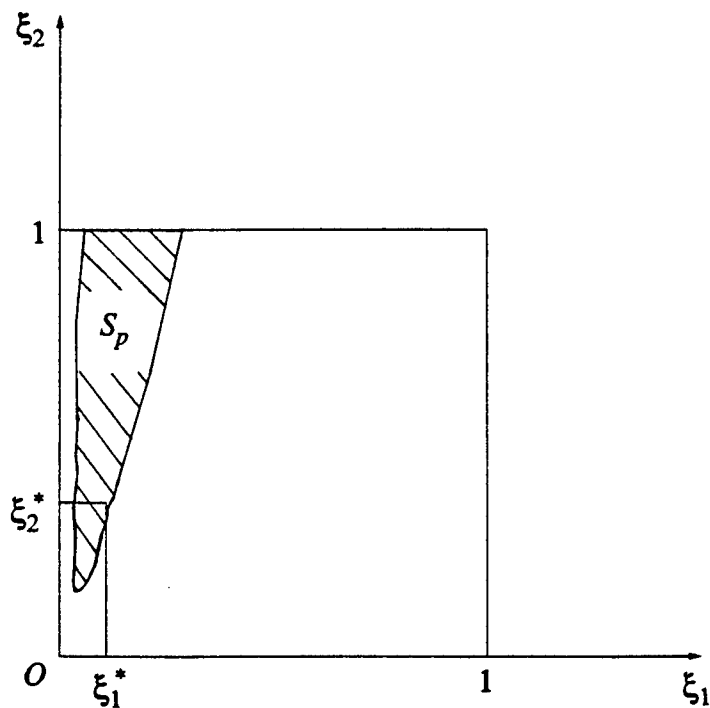


Figure 3. The set S_p of parameters ξ_1 and ξ_2 in the parameter space (ξ_1, ξ_2) when $I = 0.1 \text{ amp}$. For any ξ_1 and ξ_2 in S_p , the laser self-pulsates.

6. Conclusions

In this paper, we considered narrow-stripe semiconductor lasers. The dynamics of such lasers are very well represented by the system (1), known as the rate equations. For the system (1), we proved that the laser states and output are bounded. Furthermore, we presented a systematic procedure for choosing the amplitudes of step inputs and the values of laser parameters that destabilize all equilibrium points of the system (1). Thus, we were able to make the laser represented by (1) and (23) self-pulsate.

Our procedure of making lasers self-pulsate is quite general, easily applicable, and computationally straightforward. What are to be computed are the equilibrium points of the nonlinear system representing the laser and the eigenvalues of the Jacobian matrices of the system at the equilibrium points which are in the nonnegative orthant.

What we have presented in the paper is a way of determining when a nonlinear system can have the limit cycle behavior (periodic response). It should be reminded that it is not an easy task to determine when a three or a higher dimensional nonlinear system has the limit cycle behavior. The difficulty stems from the fact that almost all existing mathematical techniques by which the existence of limit cycles is established — such as Poincaré-Bendixon theorem or Poincaré-Andronov-Hopf bifurcation technique — are for two dimensional (planar) systems. There are generalizations of these techniques for three or higher dimensional nonlinear systems, however, they are either inapplicable to most systems or computationally demanding; see, e.g., [2], [4, pp. 119-123], and the references therein for difficulties in establishing the limit cycle behavior for three or higher dimensional nonlinear systems.

Appendix

Proof of Lemma 4.1: We set the right-hand side of the system (1) equal to zero to obtain the following set of nonlinear algebraic equations

$$a_1 \xi_1 (N_{1e} - N_{g_1}) S_e + a_2 \xi_2 (N_{2e} - N_{g_2}) S_e - G_{th} S_e + \left(\frac{C V_1}{T_s} \right) N_{1e} = 0, \quad (\text{A.1a})$$

$$- \left(\frac{a_1 \xi_1}{V_1} \right) (N_{1e} - N_{g_1}) S_e - \left(\frac{1}{T_s} + \frac{1}{T_{12}} \right) N_{1e} + \frac{N_{2e}}{T_{12}} + \frac{I}{e V_1} = 0, \quad (\text{A.1b})$$

$$- \left(\frac{a_2 \xi_2}{V_2} \right) (N_{2e} - N_{g_2}) S_e + \frac{N_{1e}}{T_{21}} - \left(\frac{1}{T_s} + \frac{1}{T_{21}} \right) N_{2e} = 0. \quad (\text{A.1c})$$

The unknowns in (A.1) are S_e , N_{1e} , and N_{2e} . In order to obtain them, we multiply (A.1b) and (A.1c) by V_1 and V_2 , respectively, and add the resulting equations to (A.1a) to obtain

$$S_e = - \left[\frac{V_1 (1 - C)}{T_s G_{th}} \right] N_{1e} - \left(\frac{V_2}{T_s G_{th}} \right) N_{2e} + \frac{I}{e G_{th}}, \quad (\text{A.2})$$

where in deriving (A.2), we used (2). Substituting (A.2) in (A.1b) and (A.1c), we obtain, respectively,

$$A_1 N_{1e}^2 + B_1 N_{1e} N_{2e} + D_1 N_{1e} + E_1 N_{2e} + F_1 = 0, \quad (\text{A.3a})$$

$$B_2 N_{1e} N_{2e} + C_2 N_{2e}^2 + D_2 N_{1e} + E_2 N_{2e} + F_2 = 0, \quad (\text{A.3b})$$

where the coefficients of the unknowns N_{1e} and N_{2e} are those in (13) and (14). From (A.3a), we obtain

$$N_{2e} = - \frac{A_1 N_{1e}^2 + D_1 N_{1e} + F_1}{B_1 N_{1e} + E_1}. \quad (\text{A.4})$$

We substitute N_{2e} from (A.4) into (A.3b) and use the fact that $A_1^2 C_2 - A_1 B_1 B_2 = 0$ to obtain $P(N_{1e}) = 0$, where $P(\cdot)$ is given in (15). \square

References

- [1] D. Bainov and P. Simeonov, *Integral Inequalities and Applications*. Dordrecht, The Netherlands: Kluwer Academic Publishers, 1992.
- [2] M. Farkas, *Periodic Motions*. New York, New York: Springer Verlag, 1994.
- [3] H. Kawaguchi, *Bistabilities and Nonlinearities in Laser Diodes*. Norwood, Massachusetts: Artech House, 1994.
- [4] G. A. Leonov, I. M. Burkin, and A. I. Shepeljavyi, *Frequency Methods in Oscillation Theory*. Dordrecht, The Netherlands: Kluwer Academic Publishers, 1996.
- [5] S. Matsui, H. Takiguchi, H. Hayashi, S. Yamamoto, S. Yano, and T. Hijikata, "Suppression of feedback-induced noise in short-cavity V-channeled substrate inner stripe lasers with self-oscillation," *Applied Physics Letters*, vol. 43, pp. 219-221, 1983.
- [6] K. Petermann, *Laser Diode Modulation and Noise*. Dordrecht, The Netherlands: Kluwer Academic Publishers, 1988.
- [7] S. M. Shahruz and T. A. Mahavaraha, "A System Theoretic Approach to the Stability of Passively Q-Switched Lasers," to appear in *IEEE Transactions on Control Systems Technology*.
- [8] P. Vasil'ev, *Ultrafast Diode Lasers: Fundamentals and Applications*. Norwood, Massachusetts: Artech House, 1995.
- [9] M. Yamada, "Transverse and Longitudinal Mode Control in Semiconductor Injection Lasers," *IEEE Journal of Quantum Electronics*, vol. QE-19, pp. 1365-1380, 1983.
- [10] M. Yamada, "A Theoretical Analysis of Self-Sustained Pulsation Phenomena in Narrow-Stripe Semiconductor Lasers," *IEEE Journal of Quantum Electronics*, vol. 29, pp. 1330-1336, 1993.
- [11] S. Yamashita, A. Ohishi, T. Kajimura, M. Inoue, and Y. Fukui, "Low-Noise AlGaAs Lasers Grown by Organo-Metallic Vapor Phase Epitaxy," *IEEE Journal of Quantum Electronics*, vol. 25, pp. 1483-1488, 1989.

Author Index

Abshire, James B., 20
Adams, M.J., 13
Affolderbach, C., 135
Aifer, E.H., 158
Allen, C. Ni., 175
Allendorf, Sarah W., 50

Baer, D.S., 22
Bamford, Douglas J., 119
Bellemare, Antoine, 186
Bewley, W.W., 158
Blake, Geoffrey A., 103
Blumenthal, Daniel J., 183
Bournes, P.A., 10
Brock, John, 16

Capasso, Federico, 156
Chen, Miin-Jang, 58
Chen, Pin, 103
Cheung, C.Y.L., 89, 161
Cho, S.H., 5
Chou, S.I., 22
Connolly, J.C., 158
Corvini, P.J., 10
Curl, R.F., 43

Dagenais, M., 5, 112
De Natale, P., 122
Deveaud, B., 178
Duan, Guang-Hua, 112
Duerksen, Gary L., 35

Eichler, Hans, J., 189

Fafard, S., 175
Fang, F., 10
Felix, C.L., 158
Finander, M., 10
Fishman, T., 147
Forbes, David, 16
Frish, Michael B., 32
Frost, J.E.F., 13

Ganière, J.-D., 178
Garbuzov, Dmirtri, 2
Ghosh, Abhik, 112
Gioannini, M., 192
Giusfredi, G., 122
Gmachl, Claire, 156

Gourgon, C., 178
Grealy, M.G., 13
Guja, V., 192

Hader, J., 92
Han, I.K., 5
Hanson, R.K., 22
Hardy, A., 147
Harris Jr., James S., 130
Heim, P.J.S., 5
Henningsen, Jes, 25, 47
Hinzer, K., 175
Hollberg, L., 106, 122
Hong, Y., 61
Hu, Y., 5

Ikonen, E., 56
Indik, R.A., 92

Jansen, M., 10
Johnson, F.G., 5

Kalluri, Srinath, 16
Kálna, K., 89
Kane, D.M., 64, 67, 73, 79, 86
Kapon, E., 147
Kemp, W., 135
Kennedy, Brian, 53
Kitching, J., 106
Knappe, S., 135
Koch, S.W., 92
Krainak, Michael A., 35
Kuittinen, M., 56
Ky, Nguyen Hong, 178

Laakkonen, P., 56
Lacey, Johanna, 16
Lancaster, D.G., 43
Larson, Michael, 130
Latrasse, Christine, 186
Lawrence, J.S., 64, 67
Lee, Bor-Lin, 58
Lee, H., 158
Lembo, Larry, 16
Lemieux, Jean-François, 186
Lin, Chien-Chung, 130
Lin, Chinh-Fuh, 58
Lodenkamper, Robert, 16

Ludowise, Peter D., 50
Martin, D., 178
Martin, Wayne, 130
Martinelli, R.U., 158
Masum, J., 13
Matsuura, Shuji, 103
Mazzotti, D., 122
McLaren, Ian A., 53
McNesby, Kevin L., 53
Merimaa, M., 56
Meyer, J.R., 158
Mirin, Richard P., 183
Mitchell, J., 122
Misolek, Andrzej W., 53
Moloney, J.V., 92
Montrosset, I., 192
Morris, Jeffrey B., 53
Muraviov, A.V., 96
Mustafa, N., 164

Nabiev, R.F., 10
Nagel, A., 135
Nesnidal, Michael, 16
Nurmikko, Arto V., 168

Olafsen, L.J., 158
Orsila, S., 10
Otteson, David K., 50

Paige, Mark, 141
Paldus, Barbara, 130
Pamulapati, J., 5
Patterson, Thomas, L., 119
Pavlov, S.G., 96
Peale, R.E., 96
Pearson, John C., 103
Pesquera, L., 144, 164
Petrov, Konstantin P., 119
Pickett, Herbert M., 103
Pier, H., 147
Pierce, I., 89, 161
Pogany, Peter, 189

Rees, P., 144, 161
Reinhart, F.K., 178
Richter, D., 43
Robadey, J., 178
Roberts, J.S., 13

Roth, Arti. P., 119
Saarinen, M., 10
Salokatve, A., 10
Sanders, S., 22
Santangelo, Philip J., 50
Savolainen, P., 10
Shaddix, Christopher R., 50
Shahruz, Shahram, 203
Shanabrook, B.V., 158
Shastin, V.N., 96
Shen, H., 5
Shine Jr., Robert, 40
Shore, K.A., 61, 70, 73, 79, 86, 89, 109, 144, 161, 164, 200
Simonsen, Harald, 25, 47
Sivaprakasam, S., 70
Skaggs, R. Reed, 53
Song, J.H., 5
Song, Y.-K., 168
Spencer, P.S., 67
Steer, M.J., 13
Stokes, D.W., 158
Stone, D.R., 5
Strijbos, R.C., 96
Sugg, A.R., 158
Sugihwo, Fred, 130
Sun, Guoxi, 112
Talvitie, H., 56
Tang, J.M., 109, 200
Tétu, Michel, 186
Tittel, F.K., 43
Tittonen, I., 56
Toivonen, M., 10
Uusimaa, P., 10
Valle, A., 144
Vang, Timothy, 16
Vukičević, N., 106
Vurgaftman, I., 158
Walls, F., 106
Wasilewski, Z.R., 175
Webber, M.E., 22
Wehe, S.D., 22
Wickham, Michael, 16
Widman, M., 10
Withers, S.H., 96
Woodhead, J., 13
Wynands, R., 135
Yang, M.J., 158
Zhou, W., 5
Zibrov, A.S., 106

Subject Index

Absorption, 22, 32
Air pollution monitoring, 25, 47
All-optical devices, 147
Bragg reflectors, 35, 186, 192
Bragg waveguide, 13
Chaos, 61, 70, 73
Chemical lasers, 168
Coherent optical effects, 135
Combustion diagnosis, 22, 32, 50
Detectors, 53
Diode lasers, 2, 10, 22, 40, 53, 61, 70, 86, 106, 135, 144, 175
Fiber optics amplifiers and oscillators, 43
FM operation, 79
Four-wave mixing, 112, 200
Frequency conversion, 43, 109, 112, 122
Frequency modulation, 73
Gratings, 56
Infrared and far-infrared lasers, 2, 89, 86, 158, 161, 164, 178
Instabilities and chaos, 92
Laser amplifiers, 96
Laser arrays, 147
Laser sensors, 43, 156
Lasers and laser optics, 192
Lasers, distributed-feedback, 178
Lasers, injection-locked, 35, 86, 147
Lasers, single-mode, 13, 40, 178
Lasers, tunable, 40, 58, 130, 175, 186, 192
Lidar, 20
Metrology, 135
Mode-locked lasers, 58, 96
Multi-quantum wells, 5
Nonlinear optics, 112
Nonlinear optics, four-wave mixing, 109
Optical amplifiers, 109
Optical communications, 61, 70, 86
Optical data processing, 70
Optical devices, 192
Optical feedback, 73, 79
Optical pulses, 73
Optical resonators, 158
Optical standards and testing, 186
Phase conjugation, 35
Phase modulation, 86
Photorefractive materials, 189
Picosecond phenomena, 109
Remote sensing, 47
Semiconductor lasers, 5, 13, 16, 58, 64, 67, 73, 79, 89, 92, 158, 161, 164, 175, 178, 203
Semiconductor optical amplifier, 112, 183, 200
Semiconductors, including MQW, 58, 92
Spectrometers and spectroscopic instrumentation, 32
Spectroscopy, diode lasers, 22, 32, 35, 40, 47, 50, 130
Spectroscopy, far infrared, 103
Spectroscopy, infrared, 43, 122
Spectroscopy, modulation, 25
Spectroscopy, molecular, 122
Spectroscopy, nonlinear, 135
Superluminescent diodes, 5
Ultrafast phenomena, 89, 164
Vertical cavity surface emitting lasers, 141, 144, 147, 168
Visible lasers, 175
Waveguides, 144
Waveguides, channeled, 119